Thermodynamic Programming of Erbium(III) Coordination Complexes for Dual Visible/Near-Infrared Luminescence

Bahman Golesorkhi, Laure Guénée, Homayoun Nozary, Alexandre Fürstenberg, Yan Suffren, Eliseeva V. Svetlana, Stéphane Petoud, Andreas Hauser, Claude Piguet

Thermodynamic Programming of Erbium(III) Coordination Complexes for Dual Visible/Near-Infrared Luminescence

Golesorkhi, Bahman; Guenee, Laure; Nozary, Homayoun; Fuerstenberg, Alexandre; Suffren, Yan Jonathan Mathieu; Eliseeva, Svetlana V.; Petoud, Stéphane; Hauser, Andreas; Piguet, Claude

How to cite

GOLESORKHI, Bahman et al. Thermodynamic Programming of Erbium(III) Coordination Complexes for Dual Visible/Near-Infrared Luminescence. In: Chemistry - A European Journal, 2018, vol. 24, n° 50, p. 13158–13169. doi: 10.1002/chem.201802277

This publication URL: https://archive-ouverte.unige.ch//unige:108196

Publication DOI: 10.1002/chem.201802277

Publication: Chemistry A European Journal 2018, 24, 13158-13169. DOI: 10.1002/chem.201802277.

Thermodynamic Programming of Erbium(III) Coordination Complexes for Dual Visible-Near Infrared Luminescence

---

Bahman Golesorkhi,[a] Laure Guénée,[b] Homayoun Nozary,[a] Alexandre Fürstenberg,[a] Yan Suffren,[c],[e] Svetlana V. Eliseeva,[d] Stéphane Petoud,*[d] Andreas Hauser*[c] and Claude Piguet*[a]

[a] *Mr. B, Golesorkhi, Dr. H. Nozary, Dr A. Fürstenberg, Prof. Dr C. Piguet Department of Inorganic and Analytical Chemistry University of Geneva, 30 quai E. Ansermet, CH-1211 Geneva 4, (Switzerland). E-mail: Claude.Piguet@unige.ch*

[b] *Dr L. Guénée Laboratory of Crystallography, University of Geneva, 24 quai E. Ansermet, CH-1211 Geneva 4 (Switzerland).*

[c] *Dr. Y. Suffren, Prof. Dr A. Hauser, Department of Physical Chemistry University of Geneva, 30 quai E. Ansermet, CH-1211 Geneva 4 (Switzerland). E-mail: Andreas.Hauser@unige.ch*

[d] *Dr S. V. Eliseeva, Prof. Dr S. Petoud, Centre de Biophysique Moléculaire, CNRS UPR 4301, Rue Charles Sadron, F-45071 Orléans Cedex 2 (France). E-mail : Stephane.Petoud@inserm.fr*

[e] *Current address: Université Rennes, INSA Rennes, CNRS, ISCR "Institut des Sciences Chimiques de Rennes", F-35708 Rennes (France).*

Supporting information and the ORCID identification number(s) for the author(s) of this article can be found under https://doi.org/10.1002/chemxxxxx

Abstract

Intrigued by the unexpected room-temperature dual visible-NIR luminescence observed for fast-relaxing erbium complexes embedded in triple-stranded helicates, this contribution explores a series of six tridentate *N*-donor receptors **L4-L9** with variable aromaticities and alkyl substituents for extricating the stereo-electronic requirements responsible for such scarce optical signatures. Detailed solid state (X-ray diffraction, differential scanning calorimetry, optical spectroscopy) and solution (speciations and thermodynamic stabilities, spectrophotometry, NMR and optical spectroscopy) studies of mononuclear unsaturated $[Er(\mathbf{Lk})_2]^{3+}$ and saturated triple-helical $[Er(\mathbf{Lk})_3]^{3+}$ model complexes reveal that the stereo-electronic changes induced by the organic ligands affect inter- and intra-molecular interactions to such an extent that (i) melting temperatures in solids, (ii) the affinity for trivalent erbium in solution, and (iii) optical properties in luminescent complexes can be rationally varied and controlled. With this toolkit in hand, mononuclear erbium complexes with low stabilities displaying only near-infrared (NIR) emission can be transformed into molecular-based dual Er-centered visible/NIR emitters operating at room temperature in solids and in solutions.

Introduction

Trivalent neodymium ($4f^3$), holmium ($4f^{10}$), but especially erbium ($4f^{11}$) are famous for possessing a series of regularly spaced $^{2S+1}L_J$ excited spectroscopic levels which cover the entire near-infrared (NIR), visible (VIS) and ultra-violet (UV) domains (Scheme 1).[1] The radiative relaxation processes taking place between the different levels, quantified by their radiative rate constants k_r and lifetimes $\tau_r = 1/k_r$ obey Einstein's probability $A_{J',J}$ (in s^{-1}) of spontaneous $J' \rightarrow J$ emission (Equation (1)), where h is Planck's constant, ν is the energy gap (in frequency unit) between the two incriminated J and J' states, c is the speed of light, g_J and $g_{J'}$ are the degeneracies of states J and J', respectively, and $B_{J,J'}$ is Einstein's coefficient giving the probability per unit time and per unit spectral energy density of the radiation field that an electron in state J absorbs a photon and jumps to state J'.[2]

$$k_r = \frac{1}{\tau_r} = A_{J',J} = \frac{8\pi h\nu^3}{c^3}\frac{g_J}{g_{J'}}B_{J,J'} \qquad (1)$$

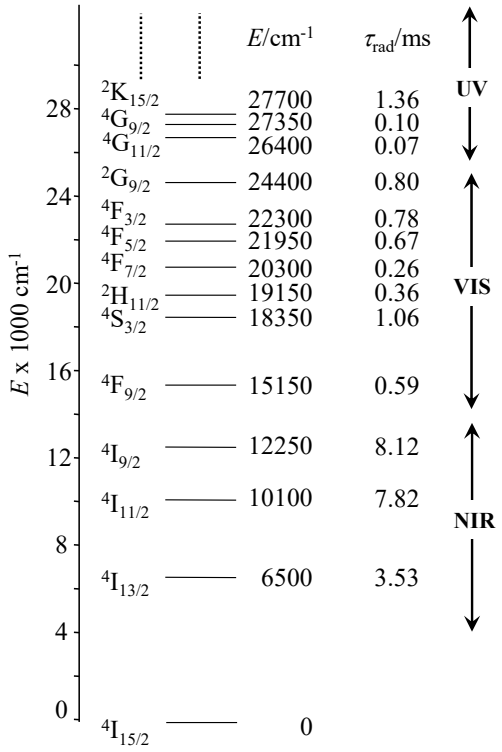

Scheme 1. Details of the near-infrared, visible, and near-ultra-violet parts of the energy-level diagram for Er^{3+} ions doped into yttrium orthoaluminate $YAlO_3$ including calculated radiative lifetimes.[8]

In quantum mechanics, $B_{J,J'}$ is proportional to the square of the transition moment $\langle \phi_J | \hat{H}_p | \phi_{J'} \rangle^2$, where ϕ_J and $\phi_{J'}$ are the wavefunctions of the J and J' states and $\hat{H}_p$ is the electromagnetic-induced perturbation hamiltonian, which involves electric and magnetic dipole components.[3] Within the framework of Judd and Ofelt theory of forced electric dipole intrashell 4f-4f transitions, Eq. (1) transforms into Eq. (2) for estimating the radiative rate constants in a lanthanide complex, where S_{ED} and S_{MD} are the electric-dipole and magnetic-dipole line strengths and n is the refractive index of the medium.[4]

$$k_r = A_{J',J} = \frac{64\pi^4 e^2 \nu^3}{3h(2J+1)} \left[\frac{n(n^2+2)^2}{9} S_{ED} + n^3 S_{MD} \right] \quad (2)$$

Since (i) the maximum energy gap between two adjacent energy levels in trivalent erbium compounds does not exceed $\tilde{\nu}$ = 4000 cm^{-1} (except for the maximum energy gap of 6500 cm^{-1} found between $Er(^4I_{13/2})$ and the ground state $Er(^4I_{15/2})$, Scheme 1) and (ii) the associated dipole line strengths S_{ED}

and S_{MD} are weak for f-f transitions,[4] Eq. (2) predicts small radiative rate constants, *i.e.* long radiative lifetimes spanning the 0.1-10 ms range (Scheme 1, right column).[3],[4] On the other hand, the competitive non-radiative relaxation pathways connecting states *J'* and *J* in trivalent lanthanides imply no significant displacement along any nuclear coordinates: a situation in line with the complete neglect of the Huang-Rhys factors[5] and the simple use of the energy gap law given in Eq. (3). The non-radiative rate constant, k_{nr}, thus decreases exponentially with increasing energy gaps $\Delta E = E_{J'} - E_J$, as measured by the numbers *p* of available high-vibrational modes $\hbar\omega_{max}$ required for filling these intervals (β is a constant of the material).[6]

$$k_{nr} \propto e^{-\beta \Delta E} = e^{-\beta p} \quad (3)$$

In erbium(III)-doped ionic solids or nanoparticles, the effective vibrational energy is low and amounts to $\hbar\omega_{eff} \approx$ 40-100 cm^{-1}, from which $p_{eff} \approx$ 40-100 can be deduced for matching $\Delta E \approx$ 4000 cm^{-1}. In these conditions, Eq. (3) predicts that non-radiative processes are poorly efficient ($k_{nr} \leq k_r$), thus producing long experimental excited lifetimes (close to the radiative lifetimes) and high quantum yields. In erbium(III) coordination complexes, the effective vibrational energy reaches $\hbar\omega_{eff} \approx$ 2000 cm^{-1},[6] and p_{eff} reduces to ≈ 2. Non-radiative relaxation dominates throughout ($k_{nr} >> k_r$) with no hope for detecting luminescence, except for the weak near-infrared Er($^4I_{13/2} \rightarrow {}^4I_{15/2}$) emission at 6500 cm^{-1}, which benefits from $p_{eff} \geq 3$.[7] Since the latter luminescent transition occurs at ca. 1.54 μm, a wavelength which is little attenuated by silica-based optical fibers and by biological tissues, Er^{3+} is attractive for working as activator in lasers, in optical amplifiers exploiting silica,[9] Al_2O_3[10] or $LiNbO_3$ ionic hosts,[11] in plastic waveguides,[12] in organometallic light-emitting diodes[7],[13] and in biological probes and sensors.[14] Major efforts were thus made for maximizing Er($^4I_{13/2} \rightarrow {}^4I_{15/2}$) emission quantum yield in molecular compounds[15] through the minimization of k_{nr} (*i.e.* maximization of the Er($^4I_{13/2}$) excited state lifetime) which accompanies the replacement of high-energy X-H oscillators (X = C, N, O) located close to the activator with heavier X-D and X-F analogues.[16] Such improvements open novel perspectives for inducing linear upconversion into

molecular complexes, a process during which two near-infrared photons are successively absorbed by the erbium activator, prior to be eventually emitted as a single photon of higher energy.[17] This mechanism, referred to as excited state absorption (ESA), was discovered during the late fifties in ionic erbium-doped solids because the millisecond-lived excited states observed in these low-phonon materials (see Scheme 1) are compatible with non-negligible probabilities for these intermediate excited states to catch a second photon leading to doubly excited levels.[18] Linear upconversion was significantly improved few years later by the demonstration that the indirect sensitization may greatly help in feeding the pertinent long-lived erbium-centered excited states (energy transfer upconversion: ETU),[19] and ETU is currently exploited for engineering functional solid materials and nanoparticles.[20]

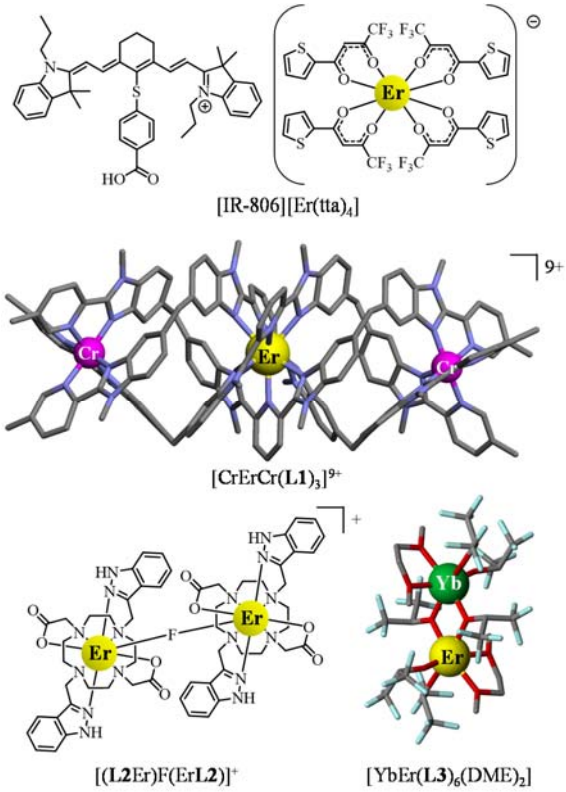

Scheme 2. Erbium-based coordination complexes exhibiting linear upconversion processes via the ETU mechanism. X-ray crystal structures are shown for [CrErCr(**L1**)$_3$](CF$_3$SO$_3$)$_9$ [23] and [YbEr(**L3**)$_6$(DME)$_2$] [25] (color code: C = grey, N = dark blue, O = red, F= light blue). Chemical structures deduced from spectroscopic data recorded in solution are depicted for [IR-806][Er(tta)$_4$] [22] and [(**L2**Er)F(**L2**Er)]$^+$.[24]

To the best of our knowledge, the unambiguous implementation of ESA in molecular complexes under reasonable incident pump intensities (i.e. below 1 kW/cm^2) is currently unknown,[21] and the few successful molecular erbium-centered upconverters reported so far exploit the ETU mechanism as found in [IR-806][Er(tta)$_4$] (use of a polyaromatic sensitizer),[22] [CrErCr(**L1**)$_3$]$^{9+}$(use of a d-block sensitizer),[23] [(**L2**Er)F(Er**L2**)]$^+$ [24] and [YbEr(**L3**)$_6$(DME)$_2$] (use of f-block sensitizers, Scheme 2).[25] Beyond some classical optimization of the sensitization in the latter complexes maximizing NIR absorption cross sections,[22] the ultimate induction of visible Er-centered emission, for instance the green Er(^{4}S$_{3/2}\rightarrow{}^4$I$_{15/2}$) signal, while at least one long-lived intermediate excited state relay of lower energy is available, for instance Er(^{4}I$_{13/2}$), represents a major impediment for the implementation of successful linear piling up of photons in these molecular systems. Looking at erbium chemistry, the latter requirement for multiple (at least dual) emission is commonly fulfilled in solid-state samples and nanoparticles,[17] and uponversion is therefore common in doped solids.[20],[26] The exact mechanism responsible for the feeding of the various emissive levels is still subject of lively debates.[27] On the contrary, molecular erbium complexes, when they are emissive upon ligand-centered UV excitations,[6] usually deliver a single weak near-infrared ^{4}I$_{13/2}\rightarrow{}^4$I$_{15/2}$ emission band, which is diagnostic for the existence of a single long-lived intermediate excited state.[7],[14],[15] In this context, the dual visible Er(^{4}S$_{3/2}\rightarrow{}^4$I$_{15/2}$) (545 nm, $\tau\left({}^4\mathrm{S}_{3/2}\right)$ = 40(2) ns) and near-infrared Er(^{4}I$_{13/2}\rightarrow{}^4$I$_{15/2}$) (1525 nm, $\tau\left({}^4\mathrm{I}_{13/2}\right)$ = 3.6(3) μs) emission bands arising from the pseudo-tricapped trigonal prismatic ErN$_9$ site in [CrErCr(**L1**)$_3$]$^{9+}$ (Scheme 2) appears to be particularly intriguing because no special care was taken for replacing H atoms with D or F atoms in the ligand strand.[23] We report here on our efforts for identifying, by structural 'dissection' in ligands **L4**-**L9** (Schemes 3-4), the chemical design required for the successful induction of room-temperature dual visible/near infrared emissions in stable ErN$_9$ coordination sites: a prerequisite for the design of erbium-containing molecular light-upconverters.

Results and Discussions

Tridentate receptors L4-L9: synthesis and substituent effects.

A careful look at the crystal structure of [CrErCr(**L1**)$_3$]$^{9+}$ cation (Scheme 2), suggests that the target central luminescent ErN$_9$ site could be reproduced in a mononuclear model *via* the helical wrapping of three 2,6-bis(benzimidazol-2-yl)pyridine ligands around a trivalent lanthanide cation as found in [Eu(**L4**)$_3$](ClO$_4$)$_3$,[28] [Eu(**L4'**)$_3$](ClO$_4$)$_3$ (**L4'** is identical to **L4**, except for the replacement of *N*-methyl groups with *N*-neopentyl analogues)[29] and [Eu(**L5'**)$_3$](ClO$_4$)$_3$ (**L5'** is identical to **L5** except for the replacement of *N*-methyl groups with *N*-ethyl analogues, see Scheme 3).[30] However, repulsive intramolecular inter-strand interactions produced by the tight wrapping of three ligands around the metallic cation in [Eu(**L4**)$_3$]$^{3+}$ is thought to be responsible for the unsuccessful isolation of related complexes using cations smaller than Eu(III) along the lanthanide series.[31]

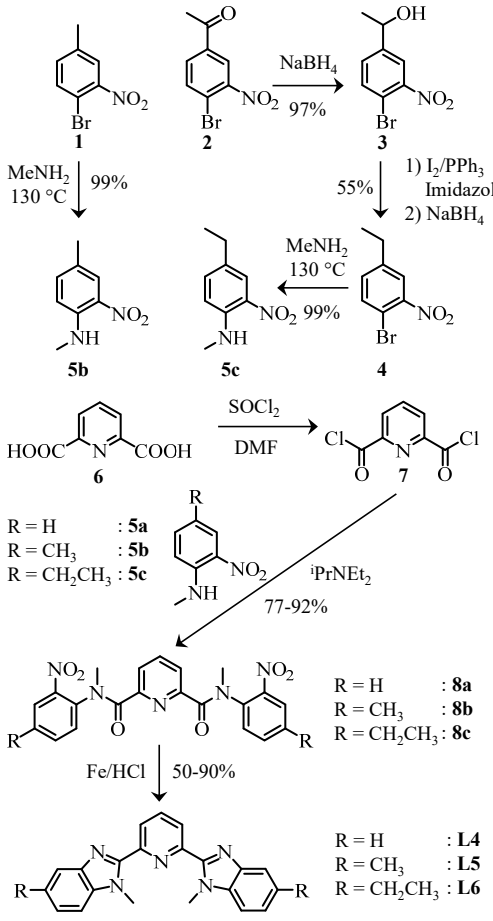

Scheme 3. Synthesis of 2,6-bis(5,5'-disubstituted-benzimidazol-2-yl)pyridine ligands **L4-L6**.

Since the ionic radius of the target Er^{3+} cation is significantly smaller than that of Eu^{3+}, we exploited compact *N*-methyl substituents for minimizing spatial expansion in ligands **L4-L6,** together with the connection of terminal alkyl substitution of increasing size R = H (**L4**) < R= CH_3 (**L5**) < R = CH_2CH_3 (**L6**) for preventing any infiltration of inner-sphere solvent molecules and/or counter-anions into the core of the target $[Ln(\mathbf{L}\boldsymbol{k})_3]^{3+}$ triple helices. The syntheses of the bis-benzimidazolpyridine series (bisbzimpy: **L4-L6**) rely on the well-established two-step reductive Philips-modified reaction of activated dipicolinic acid **7** with substituted ortho-nitroaminophenyl derivatives **5a-c**.[32] The synthesis of **L4**, which used commercially available **5a**, was previously reported.[28],[30] Analogous 5-methyl derivatives **5b** and the 5-ethyl derivative **5c** can be easily obtained by aryl nucleophilic substitution of adapted ortho-bromo-nitrophenyls **1** and **4**,[33] thus leading to ligands **L5** and **L6** (Scheme 3).

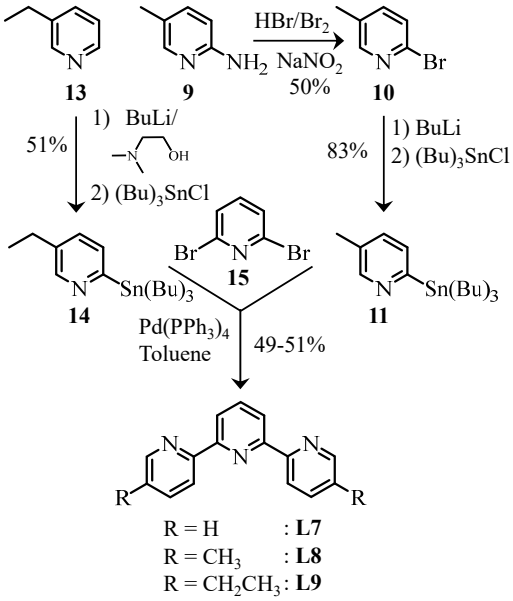

Scheme 4. Synthesis of 5,5''-disubstituted 2,2':6',2"-terpyridine ligands **L7**-**L9**.

Interestingly, the closely related, but less extended 2,2':6',2"-terpyridine ligand **L7** is known to produce stable triple-helical $[Ln(\mathbf{L7})_3]^{3+}$ along the complete lanthanide series, this without size-discriminating effects.[34] It would be highly desirable to prepare the analogous terpyridine series (terpy: **L7**-**L9**) for comparison purpose. Initial attempts to prepare the methyl (**L8**) and ethyl (**L9**) derivatives using catalyzed alkyl/aryl cross-coupling reactions with 5,5"-dichloroterpyridine[35] gave

only low yields (< 20%) in our hands. A more successful approach used double Stille-type cross-coupling reactions between 2,6-dibromopyridine **15**[36] and stannylated 5-methylpyridine **11**[37] and 5-ethylpyridine **14** (Scheme 4).[38]

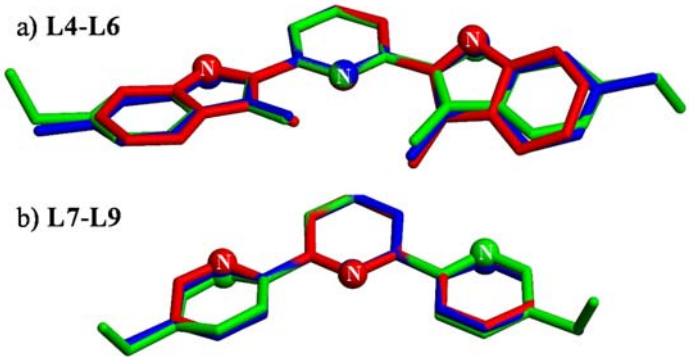

Figure 1. Superimposition of molecular structures of a) **L4** (red), **L5** (blue) and **L6** (green) and b) **L7** (red), **L8** (blue) and **L9** (green) as observed in their crystal structures. Hydrogen atoms are omitted for clarity and N-donor atoms are highlighted.

As previously observed in the crystal structures of **L4**[39] and **L7**,[40] the three connected heterocyclic units in **L5-L6** and **L8-L9** adopt pseudo-twofold *transoid-transoid* arrangements of the nitrogen donor atoms (Figure 1, Tables S1-S13 and Figure S1 in the Supporting Inofrmation). Variable interplanar angles between the connected aromatic heterocycles ($7.2 \leq \omega \leq 42.8°$) result from specific intermolecular inter-aromatic packing interactions observed in the crystals (Figure S2). A thorough thermodynamic analysis of the ligand melting processes (Figures S3-S8 and Appendix 1) within the framework of enthalpy/entropy compensation,[41] combined with cohesive free energy densities,[42] leads to the conclusion that the H→CH_3→CH_2CH_3 sequence implemented in **L4→L5→L6** and **L7→L8→L9** series produces two successive, but opposite changes in intermolecular cohesion in the solid state. The replacement of small hydrogen atoms with methyl groups improves the cohesion due the increase in molecular polarizability, while further extension provided by the introduction of additional methylene rotors to give non-linear ethyl substituents severely disrupts the inter-aromatic stacking. These three-dimensional substituent-induced packing effects, identified for the free ligand **L4-L9** in the solid state**,** have their molecular (*i.e.* zero-dimensional) counterpart in the target triple

helices $[Ln(\mathbf{Lk})_3]^{3+}$ where alkyl-modulated intramolecular inter-strand interactions are known to control metal protection and crystal-field parameters.[28]-[31]

Erbium complexes with receptors L4-L9: speciation, stabilities and solution structures. Electrospray-ionization mass spectroscopy (ESI-MS) titrations of ligands **L4** (bisbzimpy) and **L7** (terpy) with $Er(CF_3SO_3)_3$ in acetonitrile show the stepwise formation of $[Er(\mathbf{Lk})_n]^{3+}$ (n = 3-1) with some gas-phase adducts $[Er(\mathbf{Lk})_n(CF_3SO_3)_i]^{(3-i)+}$ in agreement with Equilibria (4)-(6) (Figures S9-S10, Supporting Information).

$$Er^{3+}_{solvated} + \mathbf{Lk} \rightleftharpoons \left[Er(\mathbf{Lk})\right]^{3+}_{solvated} \qquad \beta^{Er,\mathbf{Lk}}_{1,1} \qquad (4)$$

$$Er^{3+}_{solvated} + 2\ \mathbf{Lk} \rightleftharpoons \left[Er(\mathbf{Lk})_2\right]^{3+}_{solvated} \qquad \beta^{Er,\mathbf{Lk}}_{1,2} \qquad (5)$$

$$Er^{3+}_{solvated} + 3\ \mathbf{Lk} \rightleftharpoons \left[Er(\mathbf{Lk})_3\right]^{3+}_{solvated} \qquad \beta^{Er,\mathbf{Lk}}_{1,3} \qquad (6)$$

Beyond the ESI-MS signals observed for the protonated ligands $[\mathbf{Lk}+n\mathrm{H}]^{n+}$, the intensity of which are biased by their efficient gas-phase transfer coefficients,[43] only few faint ESI-MS signals can be detected. They correspond to traces of hydrolyzed dimeric complexes $[(\mathbf{Lk})_2Er(OH)_2Er(\mathbf{Lk})_2]^{4+}$ which will therefore not be considered further in the thermodynamic modeling of the speciation. ^{1}H NMR titrations of the methyl-substituted ligands **L5** and **L8**, which were selected for the simple first-order analysis of their spin systems upon complexation with diamagnetic $Y(CF_3SO_3)_3$ (the size of Y^{3+} is close to that of Er^{3+}) confirm Equilibria (4)-(6) and the formation of only three complexes $[Y(\mathbf{Lk})_n]^{3+}$ (n = 3-1) in acetonitrile at millimolar concentrations (Figures 2 and S11-S13). The strong downfield shifts observed for H3 ($\Delta\delta$ = 0.8-0.9 ppm), and to a lesser extend for the methyl groups H6 ($\Delta\delta$ = 0.5 ppm), between the free ligand and the 1:3 complexes $[Y(\mathbf{Lk})_3]^{3+}$ are diagnostic for the formation of a triple helix (magenta dashed traces in Figures 2 and S11-S13), which puts these protons in the shielding region of the terminal aromatic groups of the next ligand strands.[28],[30] As expected, this effect is stepwise relaxed with the successive loss of ligand strands when $[Y(\mathbf{Lk})_3]^{3+}$ transforms into $[Y(\mathbf{Lk})_2]^{3+}$ and $[Y(\mathbf{Lk})]^{3+}$ (orange dashed traces in Figures 2 and S11-S13).

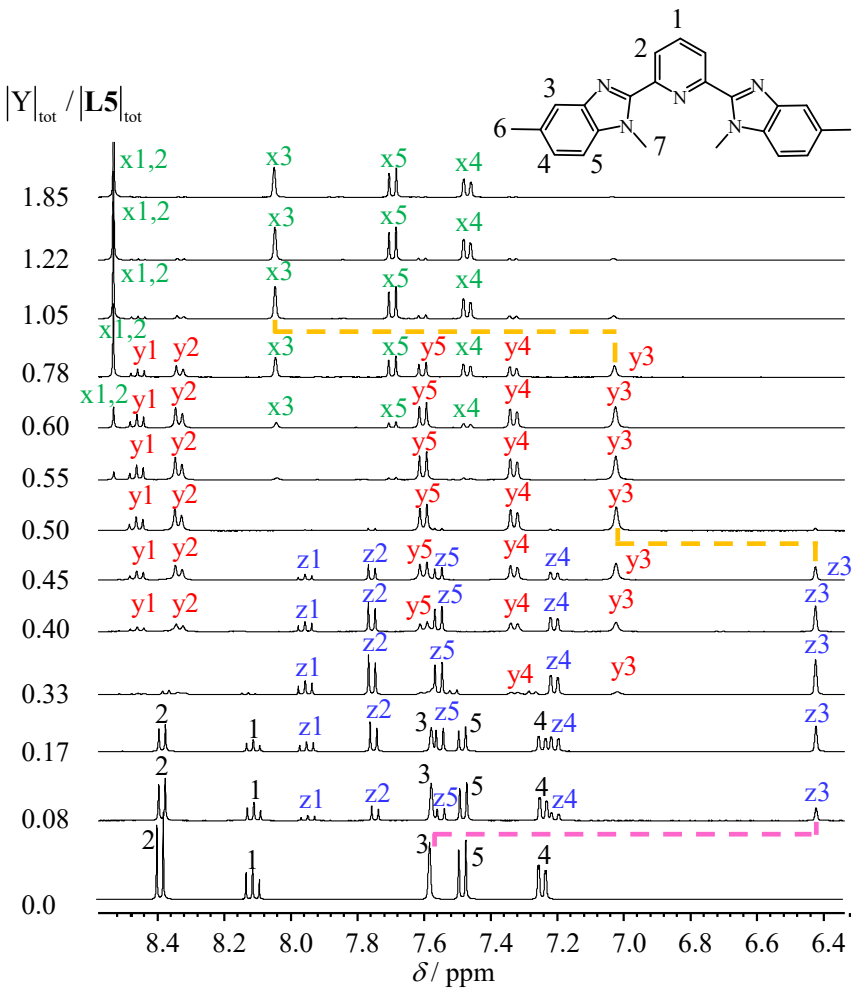

Figure 2. Aromatic parts of the ^{1}H NMR spectra with numbering scheme recorded upon titration of **L5** with $Y(CF_3SO_3)_3$ in CD_3CN at 298 K with numbering scheme. ($5\times10^{-3} \leq |\mathbf{L5}|_{tot} \leq 9\times10^{-3}$ M and $6\times10^{-4} \leq |Y|_{tot} \leq 8\times10^{-3}$ M). The letters x, y and z denote signals arising from the 1:1 (green), 1:2 (red) and 1:3 (blue) species, respectively.

The associated speciation (dots in Figures 3a and S14a) can be obtained by simple integration of the ^{1}H NMR signals of the same proton in ligands ($I_{\mathbf{L}k}$) and complexes ($I_{Y(\mathbf{L}k)n}$, Eq. (7) middle). Only partial binding isotherms could be obtained (occupancy factors $\theta_Y > 60\%$; diamonds in Figures 3b and S14b) because the NMR technique is not sensitive enough to fix total concentrations of metal and ligands low enough to limit binding-site saturation. Attempts to fit the available occupancy factors θ_Y with Eq. (7) gives only mere estimations of the stability constants $\beta_{1,n}^{\mathrm{Er},\mathbf{L}k}$ (gathered in the captions of Figures 3 and S14), which are then used for the calculation of the theoretical speciation curves and binding isotherms (full traces in Figures 3 and S14).

$$\theta_{Y} = \frac{1}{3}\frac{|\mathbf{Lk}|_{bound}}{|Y|_{tot}} = \frac{1}{3}\frac{(I_{YL\boldsymbol{k}} + I_{Y(L\boldsymbol{k})_2} + I_{Y(L\boldsymbol{k})_3})|\mathbf{Lk}|_{tot}}{(I_{L\boldsymbol{k}} + I_{YL\boldsymbol{k}} + I_{Y(L\boldsymbol{k})_2} + I_{Y(L\boldsymbol{k})_3})|Y|_{tot}} = \frac{1}{3}\frac{\sum_{n=1}^{3} n\beta_{1,n}^{Y,L\boldsymbol{k}}\left(|\mathbf{Lk}|\right)^n}{1+\sum_{n=1}^{3}\beta_{1,n}^{Y,L\boldsymbol{k}}\left(|\mathbf{Lk}|\right)^n} = \frac{1}{3}\frac{|\mathbf{Lk}|_{tot} - |\mathbf{Lk}|}{|Y|_{tot}} \quad (7)$$

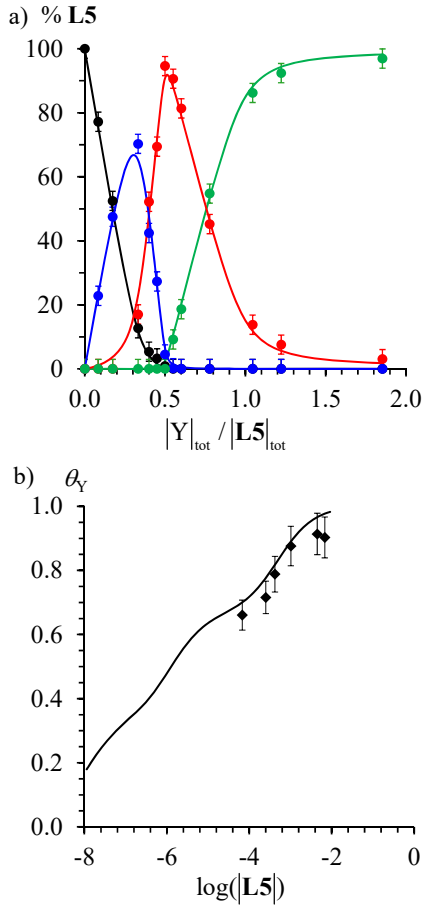

Figure 3. a) Macroscopic ligand speciations (dots) obtained by integration of ^{1}H NMR signals during the titration of **L5** (1.6×10^{-2} mol·dm^{-3}) with $Y(CF_3SO_3)_3$ in CD_3CN at 298 K (black = **L5**, blue = $[Y(\mathbf{L5})_3]^{3+}$, red = $[Y(\mathbf{L5})_2]^{3+}$ and green = $[Y(\mathbf{L5})]^{3+}$) and b) associated binding isotherm (Eq. (7); diamonds). The full traces correspond to the re-constructed a) distribution and b) binding isotherm computed using Equilibria (4)-(6) with $\beta_{1,1}^{Y,\mathbf{L5}} = 8.0$, $\beta_{1,2}^{Y,\mathbf{L5}} = 13.9$ and $\beta_{1,3}^{Y,\mathbf{L5}} = 17.2$.

As expected for ligand-metal association reactions (Eqs 4-6) monitored in weakly polar organic media, the disruption of the chemical potential of the solvent induces a dependence of the quotient of the reaction on the advance of the complexation process.[44] This prevents a simple determination of the true thermodynamic constants $\beta_{1,n}^{Er,L\boldsymbol{k}}$, which are then obtained as rough average values from the ^{1}H NMR data.[45] The associated binding isotherms depicted in Figures 3b and S14b therefore only

roughly fit the theoretical curves predicted with Eq. 7. Pertinent values for $\beta_{1,n}^{\mathrm{Er},\mathbf{Lk}}$ are restored when titrations are recorded at much lower concentrations by spectrophotometry (vide infra). Related ^{1}H NMR titrations with ethyl-substituted ligands **L6** and **L9** obviously give very similar results (Figures S15-S16), but the hydrogen atoms of the methylene probes are systematically enantiotopic (pure quartets). This results points to the presence of time-averaged symmetry planes on the NMR time scale for all complexes including, to our surprise, the D_3-symmetrical triple helical complexes $[Y(\mathbf{Lk})_3]^{3+}$. Making the assumption that a dynamic symmetry plane results from fast exchange between the two D_3-helical enantiomers on the NMR time scale, as previously reported for lanthanide tris-dipicolinates,[46] low-temperature NMR data were collected, but they did not improve the situation. However, it is worth reminding here that the experimentally accessible dynamic range of an exchange process as measured by two diastereotopic protons depends on the difference of the specific chemical shifts in absence of exchange $\Delta\nu$, which fixes the coalescence temperature T_c for a given free energy barrier $\Delta G^{\neq}$ (Eq. (8), k_B and h are respectively the *Boltzmann* and the *Planck* constants).[47] For diamagnetic yttrium complexes $[Y(\mathbf{Lk})_3]^{3+}$, the two hydrogen atoms of the methylene probe likely display very similar chemical environments (i.e $\Delta\nu$ is small) and T_c lies thus much below 233 K, the minimum accessible temperature in acetonitrile.

$$\Delta G^{\neq} = RT\ln\left(\frac{\sqrt{2}\cdot k_B\cdot T_c}{h\cdot\pi\cdot\Delta\nu}\right) \qquad (8)$$

Replacing Y(III) with paramagnetic Er(III) boosts the difference in chemical shifts between the methylene hydrogen atoms H6 and H6'. Two signals, separated by $\Delta\nu$ = 220 Hz, are now recorded for $[Er(\mathbf{L9})_3]^{3+}$ at room temperature, in agreement with the existence of a 'blocked' triple-helical arrangement in solution (Figure S17, Supporting Information). High-temperature ^{1}H NMR data combined with linear extrapolation give an estimation of T_c = 433(34) K, from which $\Delta G^{\neq}$ = 59(4) kJ/mol can be computed with Eq. (8) for the intramolecular helical interconversion. The latter values compares well with $\Delta G^{\neq}$(Tm) = 64(1) kJ/mole (T_c = 290 K) and $\Delta G^{\neq}$(Yb) = 60(1) kJ/mole (T_c = 303

K) previously reported for related intramolecular helical exchange processes occurring in D_3-symmetrical $[Ln(2,6\text{-dipicolinate})_3]^{3-}$ in D_2O.[46]

Having established that the speciation in solution obeys Equilibria (4)-(6), pertinent thermodynamic stability constants were obtained by spectrophotometric titrations of **L*k*** with $[ErX_3]$ (X = $CF_3SO_3^-$, ClO_4^- and $[Al(OC(CF_3)_3)_4]^-$) collected at low concentration in acetonitrile (Figures 4a,b and Figures S18-S22). Evolving factor analysis[48] confirms the existence of four absorbing species (Figure 4c), while non-linear least-square fit[49] to Equilibria (4)-(6) provide stability constants (Table 1) together with acceptable reconstructed absorption spectra (Figure 4d).

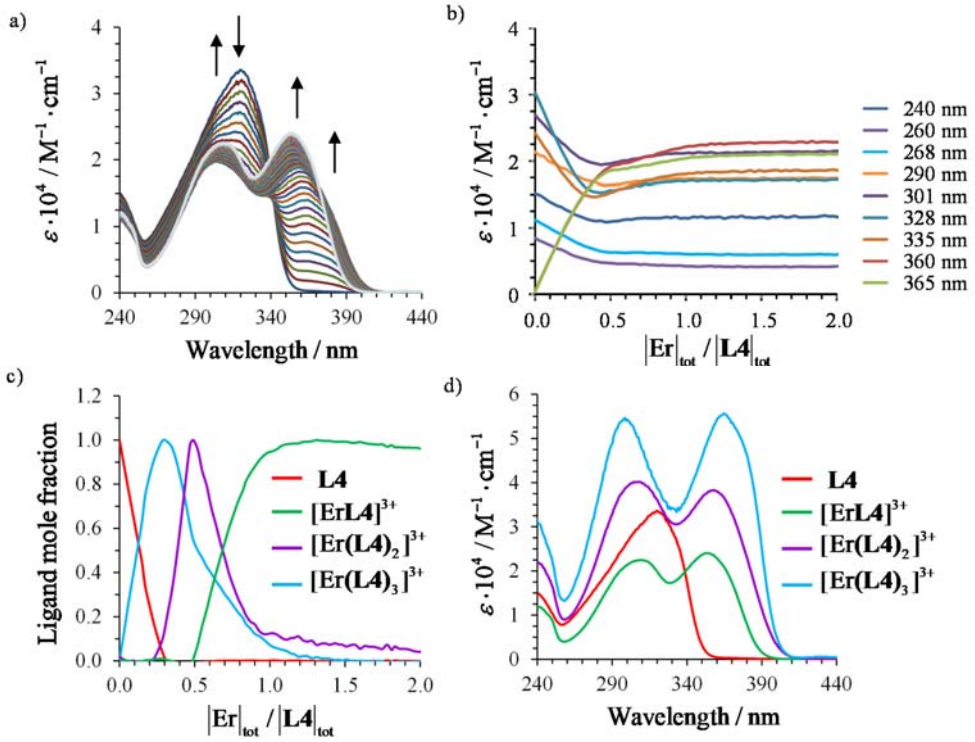

Figure 4. a) Variation of experimental absorption spectra and b) corresponding variation of molar extinction at different wavelengths observed for the spectrophotometric titration of **L4** with $Er(CF_3SO_3)_3$ (total ligand concentration: 3.0×10^{-4} M in acetonitrile, 298 K). c) Evolving factor analysis[48] using four absorbing eigenvectors and d) reconstructed individual electronic absorption spectra.

Since poorly coordinating triflate ($CF_3SO_3^-$) or perchlorate (ClO_4^-) anions are known to display similar affinities for Er^{3+},[50] the stability constants $\beta_{1,n}^{Er,Lk}$ obtained in the presence of these counter-anions for complexing **L4** and **L7** are logically similar (Table 1, entries 1-8). On the contrary, the use

of less-coordinating perfluoroalkoxyaluminate anions $[Al(OC(CF_3)_3)_4]^-$ [51] further increases the affinity of Er^{3+} for ligands **L4**-**L9** by one order of magnitude (Table 1, entries 9-14).

Table 1. Thermodynamic formation constants $\log(\beta_{1,n}^{Er,Lk})$ (Equations (4)-(6)) and associated microscopic parameters $\Delta G_{affinity}^{Er,Lk} = -RT\ln(f^{Er,Lk})$ and $\Delta E^{Lk,Lk} = -RT\ln(u^{Lk,Lk})$ (Equations (9)-(11) obtained for the spectrophotometric titrations of **L4**-**L9** with ErX_3 (X= $CF_3SO_3^-$, ClO_4^-, $[Al(OC(CF_3)_3)_4]^-$) in acetonitrile at 298 K.

L*k*	Anion	$\log(\beta_{1,1}^{Er,Lk})$	$\log(\beta_{1,2}^{Er,Lk})$	$\log(\beta_{1,3}^{Er,Lk})$	$\Delta G_{affinity}^{Er,Lk}$ kJ·mol^{-1}	$\Delta E^{Lk,Lk}$ kJ·mol^{-1}
L4	ClO_4^-	9.6(1)	17.4(4)	22.7(4)	-51(1)	10(1)
L7	ClO_4^-	9.8(1)	17.1(1)	22.5(1)	-50.7(3)	11(1)
L4	$CF_3SO_3^-$	9.2(1)	16.5(3)	20.9(3)	-49(1)	11(1)
L5	$CF_3SO_3^-$	10.9(4)	20.2(8)	24.8(8)	-60(3)	15(4)
L6	$CF_3SO_3^-$	11.6(5)	22(1)	26(1)	-66(5)	19(6)
L7	$CF_3SO_3^-$	10.5(2)	18.5(4)	23.0(4)	-56(1)	15(1)
L8	$CF_3SO_3^-$	9.9(1)	17.8(2)	22.7(2)	-53(1)	12(1)
L9	$CF_3SO_3^-$	9.2(1)	16.7(2)	21.8(2)	-49(1)	10(1)
L4	$[Al(OC(CF_3)_3)_4]^-$	10.4(3)	19.3(5)	25.7(7)	-56(1)	9(1)
L5	$[Al(OC(CF_3)_3)_4]^-$	12.0(2)	20.9(4)	27.1(4)	-63.9(1)	14.7(1)
L6	$[Al(OC(CF_3)_3)_4]^-$	12.9(3)	22.8(7)	29.5(8)	-69.6(5)	15.7(6)
L7	$[Al(OC(CF_3)_3)_4]^-$	11.2(2)	19.9(3)	26.8(5)	-59.1(4)	10.5(4)
L8	$[Al(OC(CF_3)_3)_4]^-$	10.4(1)	18.5(2)	24.8(3)	-54.7(2)	9.9(2)
L9	$[Al(OC(CF_3)_3)_4]^-$	10.1(1)	18.6(3)	24.7(3)	-54(1)	9(1)

A global thermodynamic analysis exploits the site-binding model, which considers the successive complexation of tridentate ligands to Er^{3+} within the frame of next-neighbor *Ising*-like interacting chains.[52] According to this simple approach, the purely entropic contributions produced by the

change in rotational entropies (*i.e.* the statistical factors) are safely estimated with the help of symmetry numbers to give the numerical values given in Equations (9)-(11) (see Figure S23 for calculations).[53] The free energy change accompanying the chemical reaction is then partitioned between the simple intermolecular affinity (including solvation effects) accompanying the complexation of Er^{3+} to a single ligand **L*k*** ($\Delta G_{\text{affinity}}^{\text{Er},\mathbf{Lk}} = -RT\ln(f^{\text{Er},\mathbf{Lk}})$), and the modulation of the latter affinity due to successive ligand binding in $[Er(\mathbf{Lk})_n]^{3+}$ ($n \geq 2$); a thermodynamic correction $\Delta E^{\mathbf{Lk},\mathbf{Lk}} = -RT\ln(u^{\mathbf{Lk},\mathbf{Lk}})$ often referred to as allosteric cooperativity (eqs 9-11).[54]

$$\beta_{1,1}^{\text{Er},\mathbf{Lk}} = 6f^{\text{Er},\mathbf{Lk}} \quad (9)$$

$$\beta_{1,2}^{\text{Er},\mathbf{Lk}} = 12\left(f^{\text{Er},\mathbf{Lk}}\right)^2 u^{\mathbf{Lk},\mathbf{Lk}} \quad (10)$$

$$\beta_{1,3}^{\text{Er},\mathbf{Lk}} = 16\left(f^{\text{Er},\mathbf{Lk}}\right)^3 \left(u^{\mathbf{Lk},\mathbf{Lk}}\right)^3 \quad (11)$$

Multi-linear least-square fits of the experimental successive stability constants $\log(\beta_{1,n}^{\text{Er},\mathbf{Lk}})$ to the logarithmic forms of Equations (9)-(11) provide $\Delta G_{\text{affinity}}^{\text{Er},\mathbf{Lk}} = -RT\ln(f^{\text{Er},\mathbf{Lk}})$ and $\Delta E^{\mathbf{Lk},\mathbf{Lk}} = -RT\ln(u^{\mathbf{Lk},\mathbf{Lk}})$ gathered in Table 1 (columns 6-7) and illustrated in Figure 5. As expected, the intrinsic metal-ligand affinities are favored when triflate anions are replaced with the less competitive counter-anion $[Al(OC(CF_3)_3)_4]^-$, but the successive connections of alkyl groups of larger sizes at the termini of the ligands induce surprising opposite trends when plotting $\Delta G_{\text{affinity}}^{\text{Er},\mathbf{Lk}}$ along the bisbzimpy series (**L4**-**L6**) and terpy (**L7**-**L9**) series (Figure 5a). The latter behavior is paralleled by the anti-cooperative interligand interactions $\Delta E^{\mathbf{Lk},\mathbf{Lk}}$ (Figure 5b). The regular dependence of both intrinsic affinities and interligand interactions on the molecular volumes[55] within each series suggests the prevalence of solvation effects in controlling the thermodynamic binding properties as previously established for helicate self-assemblies[56] and for the metal loading of linear polymers.[57] Pertinent Born-Haber cycles developed in Appendix 2 demonstrate that, whilst the thermodynamic stabilities of the $[Er(\mathbf{Lk})_n]^{3+}$ (n = 1-3) complexes in acetonitrile are globally comparable for all six ligands, the minor variations along the series observed in Figure 5 can be rationalized by a fine balance between

inductive effect and size-dependent solvation energies. Specific inter-strand interactions can be highlighted in $[Er(\mathbf{L5})_3]^{3+}$ and $[Er(\mathbf{L6})_3]^{3+}$ when three bulky extended aromatic ligands are wrapped around small Er^{3+}.

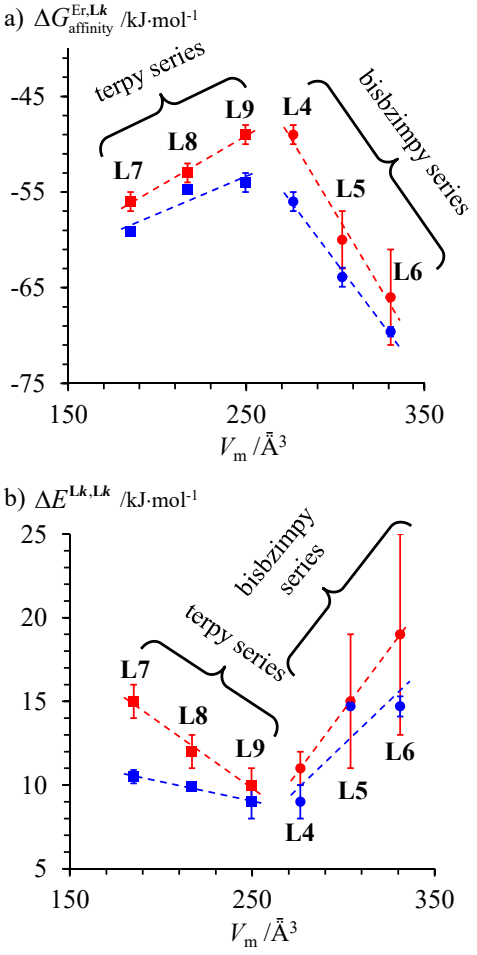

Figure 5. a) Intermolecular microscopic affinities $\Delta G^{Er,Lk}_{affinity} = -RT\ln(f^{Er,Lk})$ for inner sphere connection of $Er(CF_3SO_3)_3$ (red) and $Er([Al(OC(CF_3)_3)_4])_3$ (blue) to the tridentate binding sites in ligands **L4-L9** (CH_3CN, 298 K). b) Interligand interactions $\Delta E^{Lk,Lk} = -RT\ln(u^{Lk,Lk})$ operating upon successive binding of **L4-L9** to a single metallic center in $Er(CF_3SO_3)_3$ (red) and $Er([Al(OC(CF_3)_3)_4])_3$ (blue). V_m is the molecular volume of the ligand taken as its Connolly volume.[55] The dashed trendlines are only guides for the eyes.

Erbium complexes with receptors L4-L9: isolation and solid-state structures.

According to the stability constants collected in Table 1, we used close to molar concentrations of ligands and ErX_3 salts at 3:1 stoichiometric ratio for producing ≥ 98% of $[Er(\mathbf{Lk})_3]^{3+}$ in acetonitrile

(Figures S24-S25), prior to exposing resulting mixtures either to slow evaporation or to the diffusion of poorly polar volatile solvents for inducing crystallization. In the presence of triflate counter-anions (X = $CF_3SO_3^-$), only 1:2 complexes could be crystallized (Figure 6a, Tables S14-S20 and Figures S26-S28). Since the latter stoichiometry accounts for a maximum 2% of the ligand speciation in solution, these complexes are probably much less soluble than the lipophilic 1:3 adducts. Complexes $[Er(\mathbf{L4})_2(CF_3SO_3)_2](CF_3SO_3)$ (**1**) and $[Er(\mathbf{L7})_2(CF_3SO_3)_2](CF_3SO_3)$ (**2**)[21a] display eight-coordinate Er(III) centers, the coordination geometry of which can be assigned to slightly distorted square antiprisms. Trivalent erbium in $[Er(\mathbf{L8})_2(CF_3SO_3)_3]$ (**3**) is nine-coordinated in a pseudo-tricapped trigonal prismatic coordination sphere (Figure S29).

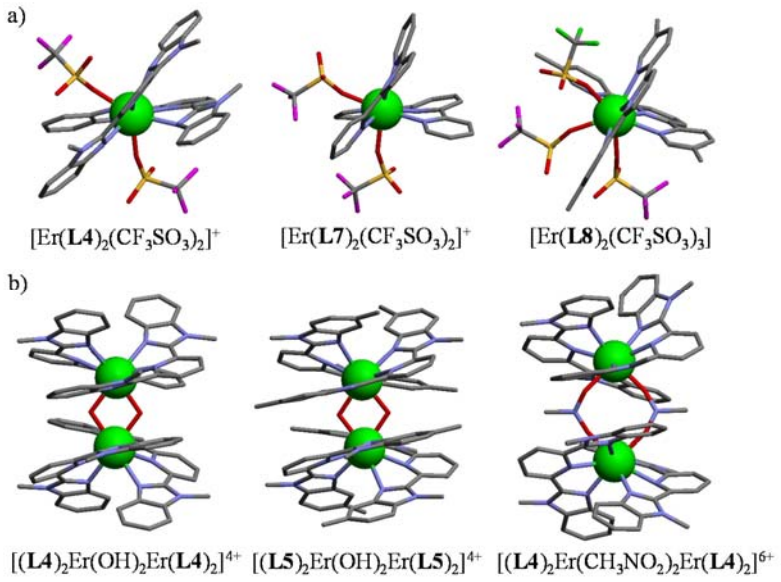

Figure 6. Molecular structures of a) mononuclear 1:2 complexes and b) dinuclear 2:4 complexes found in the crystal structures of $[Er(\mathbf{L4})_2(CF_3SO_3)_2](CF_3SO_3)\cdot 2CH_3CN$ (**1**), $[Er(\mathbf{L7})_2(CF_3SO_3)_2](CF_3SO_3)\cdot 1.5C_2H_5CN$ (**2**),[21a] $[Er(\mathbf{L8})_2(CF_3SO_3)_3]$ (**3**), $[(\mathbf{L4})_2Er(OH)_2Er(\mathbf{L4})_2](ClO_4)_4\cdot 2C_6H_5CN\cdot 4CH_3CN$ (**8**), $[(\mathbf{L5})_2Er(OH)_2Er(\mathbf{L5})_2](ClO_4)_4\cdot C_6H_5CN\cdot 8CH_3CN$ (**9**) and $[(\mathbf{L4})_2Er(CH_3NO_2)_2Er(\mathbf{L4})_2](ClO_4)_6\cdot CH_3NO_2$ (**10**). The counter-anions, solvent molecules and H atoms are omitted for clarity. Color code: C = grey, blue = N, red = O, yellow = S, magenta = F, green = Er.

Replacing triflate with perchlorate counter-anions reduces the solubility of the triple helices $[Er(\mathbf{L}\boldsymbol{k})_3]^{3+}$, which quantitatively crystallized to give $[Er(\mathbf{L6})_3](ClO_4)_3$ (**4**), $[Er(\mathbf{L7})_3](ClO_4)_3$ (**5**), $[Er(\mathbf{L8})_3](ClO_4)_3$ (**6**) and $[Er(\mathbf{L9})_3](ClO_4)_3$ (**7**, Figure 7, Tables S21-S29 and Figures S30-S33). The

nine-coordinate Er(III) sites in these complexes systematically adopt pseudo-tricapped trigonal prismatic geometries (Figure S34). The detailed analysis of Er-N bond distances within the framework of bond valence theory (Table S30)[58] logically confirms that the Er-N interactions in eight-coordinate $[Er(\mathbf{L4})_2(CF_3SO_3)_2]^+$ and $[Er(\mathbf{L7})_2(CF_3SO_3)_2]^+$ complexes are slightly stronger than those found in the corresponding nine-coordinated analogues $[Er(\mathbf{L8})_2(CF_3SO_3)_3]$, $[Er(\mathbf{L}k)_3]^{3+}$ (**L*k* = L6-L9**), $[Eu(\mathbf{L4})_3]^{3+}$ [28],[30] and $[Lu(\mathbf{L7})_3]^{3+}$.[34b] We also note that a significant intramolecular inter-strand packing[59] produced by the tight wrapping of the helical strands in $[Eu(\mathbf{L4})_3]^{3+}$ [28],[30] and $[Er(\mathbf{L6})_3]^{3+}$ (Figure 7 top left and Figure S36) are lacking for the terpy series.

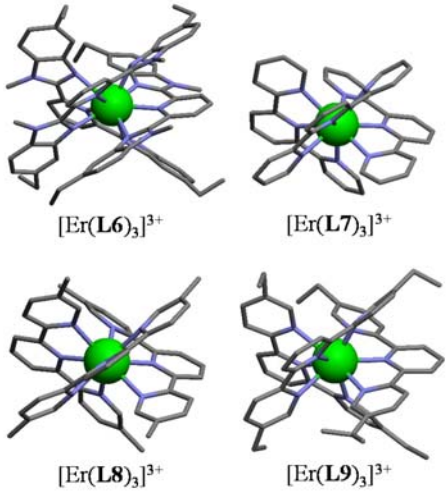

Figure 7. Molecular structures of mononuclear 1:3 complexes found in the crystal structures of $[Er(\mathbf{L6})_3](ClO_4)_3 \cdot 1.5CH_3CN$ (**4**), $[Er(\mathbf{L7})_3](ClO_4)_3$ (**5**), $[Er(\mathbf{L8})_3](ClO_4)_3$ (**6**) and $[Er(\mathbf{L9})_3](ClO_4)_3 \cdot 1.5CH_3CN$ (**7**). The counter-anions, solvent molecules and H atoms are omitted for clarity. Color code: C = grey, blue = N, green = Er.

In line with previous unsuccessful attempts to isolate Lu-based triple helical complexes with **L4** and **L5** in the solid state,[28],[30] we were unable to isolate $[Er(\mathbf{L}k)_3](ClO_4)_3$ with these two ligands. Slow evaporation of $Er(ClO_4)_3$/**L*k*** (1:3) mixtures (k = 4, 5) over several weeks provided only small quantities of dinuclear complexes $[(\mathbf{L4})_2Er(OH)_2Er(\mathbf{L4})_2](ClO_4)_4$ (**8**), $[(\mathbf{L5})_2Er(OH)_2Er(\mathbf{L5})_2](ClO_4)_4$ (**9**) and $[(\mathbf{L4})_2Er(CH_3NO_2)_2Er(\mathbf{L4})_2](ClO_4)_6$ (**10**), the stoichiometry of which is reminiscent of mononuclear 1:2 complexes (Figure 6b, Tables S31-S37 and Figures S36-S38). According to the fact that no identified thermodynamic effect specifically destabilizes $[Er(\mathbf{L}k)_3]^{3+}$ complexes with **L4** and

L5 (Table 1), we conclude that mass transfers at the solid/solution phase interfaces master solubility during the crystallization processes and the compositions of the resulting solid state samples do not mirror the thermodynamic speciation.

Erbium complexes with receptors L4-L9: dual visible/near-infrared luminescence.

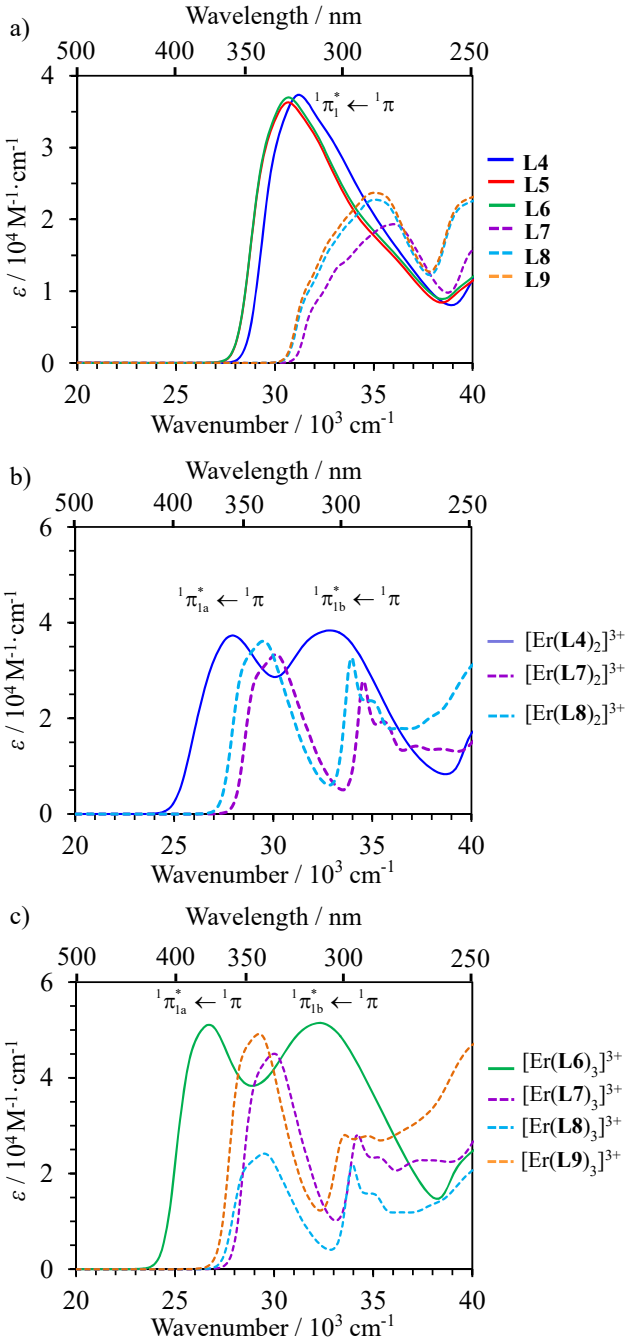

Figure 8. Absorption spectra of a) ligands **L4-L9** (0.3 mM), b) 1:2 complexes **1-3** (3.0 mM) and c) 1:3 complexes **4-7** (3.0 mM) in acetonitrile solution at 298K.

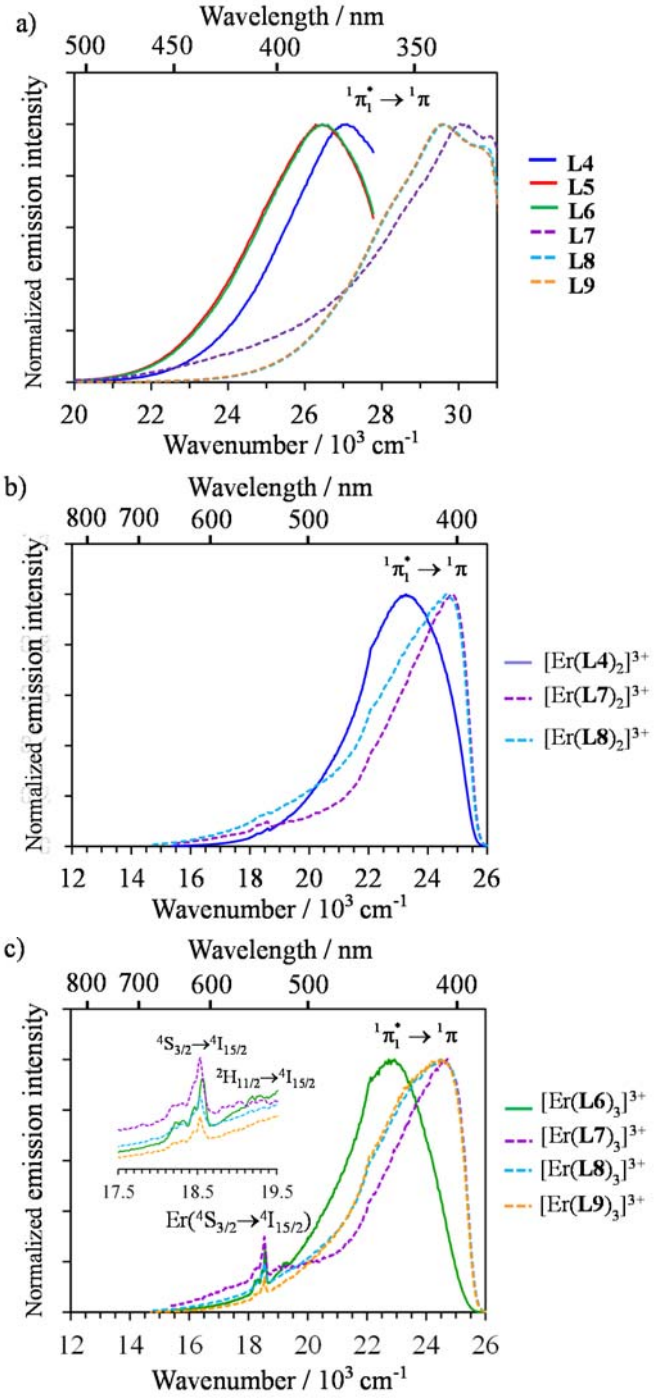

Figure 9. Emission spectra of a) ligands **L4**-**L6** (0.3 mM, λ_{exc} = 330 nm) and **L7**-**L9** (0.3 mM, λ_{exc} = 280 nm), b) 1:2 complexes **1**-**3** (3.0 mM) and c) 1:3 complexes **4**-**7** (3.0 mM) in acetonitrile solution at 298 K (λ_{exc} = 370 nm for complexes with **L4**-**L6** and λ_{exc} = 340 nm for complexes with **L7**-**L9**; a cutoff filter at 400 nm is used).

The electronic absorption spectra of the free ligands **L4**-**L9** in acetonitrile solution display the typical $\pi_1^* \leftarrow \pi$ transitions characteristic for the bisbzimpy (**L4**)[30],[60] and terpyridine (**L7**)[61] series (Figure

8a). The 4500 cm^{-1} red-shift combined with the doubling of the absorption coefficient resulting from the aromatic extension in going from the terpy series (**L7**-**L9**, dotted traces in Figure 8) to bisbzimpy (**L4**-**L6**, full traces in Figure 8) makes the latter ligands more efficient for acting as sensitizers for luminescent lanthanides in $[Ln(\mathbf{L}\boldsymbol{k})_n]^{3+}$ complexes.[62] The minor additional 400 cm^{-1} red-shift induced by the connection of methyl (**L5** and **L8**) or ethyl (**L6** and **L9**) groups to the distal aromatic rings are in line with the reduction of the HOMO-LUMO gap predicted by Extended Hückel Molecular Orbital calculations.[30] These global shifts toward lower energies are mirrored by similar trends observed in the associated emission spectra recorded in acetonitrile (298 K) upon excitation into the $\pi_1^* \leftarrow \pi$ transitions (Figure 9a). According to their nanosecond lifetimes (Table S38 and Figure S39), these emission bands can be safely assigned to singlet $^1\pi_1^* \rightarrow {}^1\pi$ transitions, the intensity of which can be magnified at lower temperature (77 K in frozen solution, Figure S40a) where the appearance of low-energy weak bands possessing longer lifetimes (> 1 μs, Figure S40b) can be attributed to the contribution of weak spin-forbidden $^3\pi_1^* \rightarrow {}^1\pi$ transitions. Upon complexation to Er^{3+} in $[Er(\mathbf{L}\boldsymbol{k})_n]^{3+}$ (n = 2, 3) at 3.0 mM concentration (> 90% of the ligand speciation corresponds to the target complex), the $\pi_1^* \leftarrow \pi$ transition undergoes the well-known $\pi_{1a},\pi_{1b}^* \leftarrow \pi$ splitting accompanying the *trans-trans* → *cis-cis* rearrangement of the aromatic tridentate ligand binding units: a spectral feature diagnostic for their meridional tri-coordination to a central metallic center (Figures 8b-c).[30],[60],[61] Concomitant measurements in the solid state (*i.e.* at higher concentration) confirm the latter splitting process (Figure S41) together with the detection of additional weak $Er(^{2S+1}L_J \leftarrow {}^4I_{15/2})$ absorption transitions covering the 6000-25000 cm^{-1} spectral window (Figure S42). Interestingly, the radiative lifetime associated to any emission transition terminating onto the ground $Er(^4I_{15/2})$ level can be estimated by its oscillator strength calculated with Eq. (12) where $\int \varepsilon(\tilde{\nu})\mathrm{d}\tilde{\nu}$ is the integrated spectrum of the incriminated absorption transition recorded in solution, J and J' refer to the ground (J = 15/2) and excited states, respectively, n is the refractive index of the medium, N_A is Avogadro's number, c is the speed of light in vacuum and $\tilde{\nu}_m$ is the barycenter of the transition (Table 2).[4]

$$\frac{1}{\tau_{\mathrm{rad}}} = 2303 \cdot \frac{8\pi c n^2 \tilde{\nu}_{\mathrm{m}}{}^2 (2J+1)}{N_{\mathrm{A}}(2J'+1)} \int \varepsilon(\tilde{\nu}) \mathrm{d}\tilde{\nu} \qquad (12)$$

Table 2 Radiative lifetimes calculated with Eq. (12) for selected Er(III) excited levels in the complexes **1**-**7** (acetonitrile, 298 K).

Compound	State / Solvent	$\tau_{\mathrm{Er,rad}}^{4}\mathrm{I}_{13/2}$ / ms	$\tau_{\mathrm{Er,rad}}^{4}\mathrm{I}_{11/2}$ / ms	$\tau_{\mathrm{Er,rad}}^{4}\mathrm{S}_{3/2}$ / μs	$\tau_{\mathrm{Er,rad}}^{2}\mathrm{H}_{11/2}$ / μs	$\tau_{\mathrm{Er,rad}}^{4}\mathrm{F}_{7/2}$ / μs
[Er(**L4**)$_2$(O$_3$SCF$_3$)$_2$](CF$_3$SO$_3$)	Solid[a]	6.3	4.3	546	177	246
	CH_3CN[b]	9.1	6.1	785	254	353
[Er(**L7**)$_2$(O$_3$SCF$_3$)$_2$](CF$_3$SO$_3$)	Solid[a]	6.1	5.6	515	301	269
	CH_3CN[b]	8.7	8.1	741	433	387
Er(**L8**)$_2$(O$_3$SCF$_3$)$_3$	Solid[a]	5.6	6.3	453	259	266
	CH_3CN[b]	8.0	9.0	651	372	382
[Er(**L6**)$_3$](ClO$_4$)$_3$	Solid[a]	6.3	5.4	716	282	405
	CH_3CN[b]	9.1	7.8	1029	406	582
[Er(**L7**)$_3$](ClO$_4$)$_3$	Solid[a]	6.4	4.4	476	442	352
	CH_3CN[b]	9.2	6.3	684	636	506
[Er(**L8**)$_3$](ClO$_4$)$_3$	Solid[a]	6.1	6.8	493	418	299
	CH_3CN[b]	8.8	9.8	709	602	430
[Er(**L9**)$_3$](ClO$_4$)$_3$	Solid[a]	6.1	6.9	495	435	299
	CH_3CN[b]	8.7	9.9	712	626	430

[a] For the solid-state samples, $\tau_{\mathrm{Er,rad}}$ was calculated assuming that the structures are similar in different media and taking into account a simple n^3 dependence (Eq. (2)) of the refractive index with $n_{\mathrm{solid}} = 1.517$ and $n_{\mathrm{CH3CN}} = 1.344$.[4b],[63] [b] $c = 3$ mM.

Excitation into the ligand-centered **L*k***($\pi_{1b}{}^{*} \leftarrow \pi$) transition in the unsaturated [Er(**L*k***)$_2$]$^{3+}$ complexes (**L*k*** = **L4**, **L7**, **L8**) in solution at room temperature shows the residual emission of the ligand-centered singlet emission (Figure 9b and Table S39). Upon freezing the solution at 77 K, additional very weak

green Er($^4S_{3/2}\rightarrow{}^4I_{15/2}$) emission bands ($\tau(^4S_{3/2})$ = 8-12 ns, Table S40) can be identified around 18450 cm^{-1} (Figure S43), the intensity of which further increases for solid-state samples measured at 7-11 K (Figure S44). Compared with natural radiative lifetimes of $540 < \tau_{Er,rad}^{^4S_{3/2}} < 750$ μs calculated for this transition in the corresponding 1:2 complexes (Table 2, column 5), the observed nanosecond Er($^4S_{3/2}\rightarrow{}^4I_{15/2}$) emission corresponds to small Er-centered quantum yields $Q_{Er}^{Er}\left(^4S_{3/2}\right) = \tau_{Er,exp}^{^4S_{3/2}} / \tau_{Er,rad}^{^4S_{3/2}}$ < 0.002% (Table S40). The latter visible Er-centered luminescence becomes more sizeable in the saturated triple-stranded helical $[Er(\mathbf{L}\boldsymbol{k})_3]^{3+}$ complexes (**L*k*** = **L6**-**L9**), where it can be now easily detected at room temperature in solution (Figure 9c) additionally to the residual ligand-centered singlet emission (Table S41). This observation mirrors the previous and rather surprising report of detectable upconverted green Er($^4S_{3/2}\rightarrow{}^4I_{15/2}$) emission implemented in $[CrErCr(\mathbf{L1})_3]^{9+}$, a coordination complex possessing high-energy oscillators.[23a] Taking $\tau_{Er,exp}^{^4S_{3/2}}$ = 40(2) ns measured in $[GaErGa(\mathbf{L1})_3](CF_3SO_3)_9$ at 3K[23c] as an upper limit of the experimental Er($^4S_{3/2}$) lifetimes in these $[ErN_9]$ chromophores, the intrinsic quantum yield of the Er($^4S_{3/2}\rightarrow{}^4I_{15/2}$) emission still remains limited ($Q_{Er}^{Er}\left(^4S_{3/2}\right) < 0.01\%$) in mononuclear triple-helical complexes, but still roughly one order of magnitude larger than in unsaturated complexes. This observation justifies the use of solid-state samples of $[Er(\mathbf{L}\boldsymbol{k})_3](ClO_4)_3$ complexes (**L*k*** = **L6**-**L9**), where local concentration and antenna effect are maximized, for getting well-resolved emission spectra both at room temperature (Figure 10) and at 77 K (Figure S45). Beyond the uncommon visible Er($^4S_{3/2}\rightarrow{}^4I_{15/2}$) luminescence observed upon ligand-centered excitation (main plot in Figure 10), the latter triple helical complexes additionally display standard Er-centered infrared emission associated with Er($^4I_{13/2}\rightarrow{}^4I_{15/2}$) transitions occurring around 6300 cm^{-1} (inset in Figure 10), the room temperature lifetimes of which $1 < \tau_{Er,exp}^{^4I_{13/2}} < 6$ μs corresponds to intrinsic $Q_{Er}^{Er}\left(^4I_{15/2}\right) \approx 0.1\%$ quantum yields for the best protected $[Er(\mathbf{L6})_3](ClO_4)_3$ triple helix. It is worth noting here that the induction of dual Er-centered $^4S_{3/2}\rightarrow{}^4I_{15/2}$ (Visible) and $^4I_{13/2}\rightarrow{}^4I_{15/2}$ (NIR) emission is exceptional in coordination complexes and the detailed investigation

of the less-protected hydroxyl-bridged analogous $[(\mathbf{L4})_2Er(OH)_2Er(\mathbf{L4})_2](ClO_4)_4$ (**8**) and $[(\mathbf{L5})_2Er(OH)_2Er(\mathbf{L5})_2](ClO_4)_4$ (**9**), or solvent-bridged $[(\mathbf{L4})_2Er(CH_3NO_2)_2Er(\mathbf{L4})_2](ClO_4)_6$ (**10**) dimers indeed show no trace of visible emission, even in the solid state even at low temperature (Figure S46).

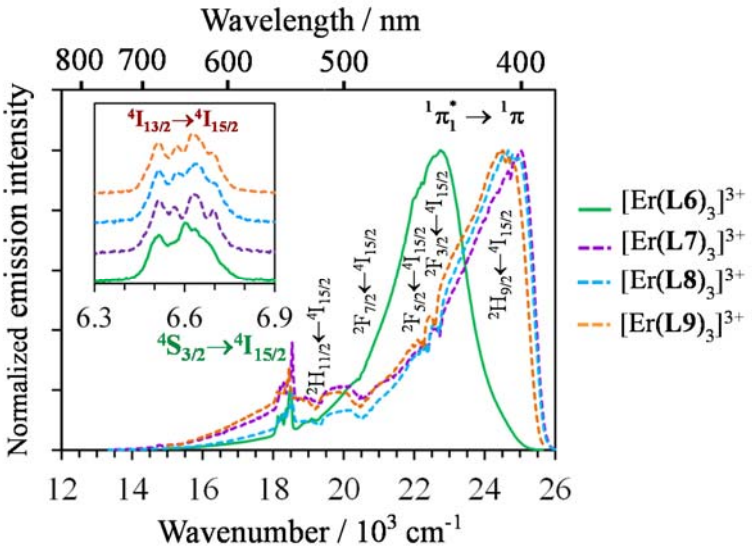

Figure 10. Dual visible (main plot) and near-infrared (inset) emission spectra recorded for the complexes **4** (λ_{exc} = 370 nm) and **5**-**7** (λ_{exc} = 340 nm) in the solid-state at room temperature. The dual emission is assigned using color fonts, while the dips (assigned using black fonts) correspond to Er-centered re-absorption of the residual ligand-centered $^1\pi^*\rightarrow\pi$ emission.

Conclusion

In our attempt to reproduce the intriguing luminescent properties of $[ErN_9]$ chromophores found in the self-assembled trinuclear d-f helicate $[CrErCr(\mathbf{L1})_3]^{9+}$ (Scheme 2), into simple, stable and tunable mononuclear triple-helical model complexes $[Er(\mathbf{L}\boldsymbol{k})_3]^{3+}$ ($\mathbf{L}\boldsymbol{k}$ = **L4**-**L9**), we discovered that the stereo-electronic requirements responsible for the uncommon room-temperature dual Er-centered visible/near-infrared emission essentially depend on the tight wrapping of the three polyaromatic strands around the metallic center. The Jablonski diagram shown in Figure 11 summarizes the established mechanisms responsible for the generation of the dual visible/near-infrared luminescence in the triple helical $[Er(\mathbf{L}\boldsymbol{k})_3]^{3+}$ complexes ($\mathbf{L}\boldsymbol{k}$ = **L6**-**L9**).

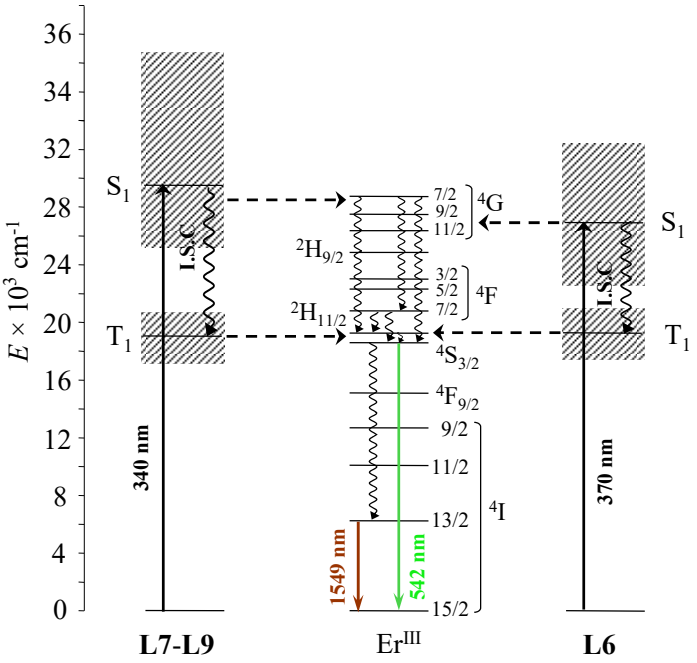

Figure 11. Jablonski diagram summarizing the excitation processes (straight upward arrows), energy transfers (dashed arrows), non-radiative multiphonon relaxation (undulating arrows) and radiative emission processes (straight downward arrows) operating in the triple-helical complexes $[Er(\mathbf{L}\boldsymbol{k})_3]^{3+}$ (**L*k*** = **6**-**9**). Ligand-to-metal energy transfers arising from both singlet and triplet states are considered.

The replacement of one ligand strand with low-frequency oscillators triflate counter-anions in $[Er(\mathbf{L}\boldsymbol{k})_2(CF_3SO_3)_n]^{(3-n)+}$ chromophores (n = 2, 3) is still compatible with the detection of very weak green $Er(^4S_{3/2}\rightarrow{}^4I_{15/2})$ emission at 542 nm, but only at low temperature. As soon as hydroxide anions (OH oscillators) or solvent molecules (CH oscillators) are bound in the Er(III) first coordination sphere in the dimers $[(\mathbf{L4})_2Er(OH)_2Er(\mathbf{L4})_2](ClO_4)_4$ (**8**), $[(\mathbf{L5})_2Er(OH)_2Er(\mathbf{L5})_2](ClO_4)_4$ (**9**) and $[(\mathbf{L4})_2Er(CH_3NO_2)_2Er(\mathbf{L4})_2](ClO_4)_6$ (**10**), the visible emission is totally quenched. The extension of the aromatic units in going from the terpy series (**L7**-**L9**, Scheme 4) to the bisbzimpy series (**L4**-**L6**, Scheme 3) shifts the ligand-centered absorption bands toward lower energies, a trend in line with potential visible sensitization of Er-centered luminescence in $[Er(\mathbf{L4})_3]^{3+}$, a process which is not accessible for $[Er(\mathbf{L7})_3]^{3+}$. A further red-shift accompanies the peripheral substitution with terminal methyl (**L5**, **L8**) or ethyl (**L6**, **L9**) groups, but no spectacular luminescence change results from the protection of the termini of the $[Er(\mathbf{L}\boldsymbol{k})_3]^{3+}$ triple-helix with these ligands. However, the systematic

(often tedious) preparation and analysis of the H→methyl→ethyl structural series demonstrates its pertinence for the rationalization of (i) the driving forces controlling the intermolecular interactions operating in the solid state, which are responsible for phase transition temperatures, and (ii) the solvation energies pertinent to thermodynamic association processes occurring in solution. To summarize, we are now fully equipped for the molecular design of stable erbium coordination complexes, the ErN_9 chromophore of which displays room temperature dual visible/near-infrared emission in solution and in the solid state at room temperature. Further use as activators for molecular-based excited state absorption (ESA) and energy-transfer (ETU) linear upconversion are currently under investigation.

Acknowledgements

Financial support from the Swiss National Science Foundation is gratefully acknowledged. The work performed in France was supported by La Ligue contre le Cancer, Cancéropôle Grand Ouest, Agence Nationale de la Recherche (ANR-13-BS08-0011) and INSERM.

Conflicts of interest

The authors declare no conflict of interest

Keywords: erbium complexes, thermodynamics, dual emission, solvation, triple helical

References

[1] a) C. Piguet, *Nature Chemistry* **2014**, *6***,** 370; b) C.-G. Ma, M. G. Brik, D.-X. Liu, B. Feng, Y. Tian, A. Suchocki, *J. Luminesc.* **2016**, *170*, 369-374.

[2] a) A. Einstein, *Phys. Z.* **1917**, *18*, 121–128; b) S. Strickler, S. J. Berg, *J. Chem. Phys.* **1962**, *37*, 814–822; c) J. B. Berks, D. J. Dyson, *R. London Soc. Ser. A* **1963**, *275*, 135–148.

[3] a) W. T. Carnall, *Handbook on the Physics and Chemistry of Rare Earths*, K. A. Gschneidner and L. Eyring, Eds. North-Holland Publishing Company: Amsterdam, New York, Oxford, 1979; Vol. 3, chap 24, pp 171-208; b) J.-C. G. Bünzli, S. V. Eliseeva, *Lanthanide*

Luminescence: Photophysical, Analytical and Biological Aspects, P. Hänninen and H. Härmä, H., Eds. Springer-Verlag: Berlin Heidelberg, 2010; Vol. 7, pp 1-45.

[4] a) L. D. Carlos, R. A. S. Ferreira, V. D. Bermudez, S. J. L. Ribeiro, *Adv. Mater.* **2009**, *21*, 509-534; b) J.-C. G. Bünzli, A.-S. Chauvin, H. K. Kim, E. Deiters, S. V. Eliseeva, *Coord. Chem. Rev.* **2010**, *254*, 2623-2633.

[5] T. C. Brunold, H. U. Güdel, *Inorganic Electronic Structures and Spectroscopy*; E. I. Solomon and A. B. P. Lever, Eds; Wiley: New York, 1999, pp 259-306.

[6] C. Reinhard, H. U. Güdel, *Inorg. Chem.* **2002**, *41*, 1048-1055.

[7] F. Artizzu, M. L. Mercuri, A. Serpe, P. Deplano, *Coord. Chem. Rev.* **2011**, *255*, 2514-2529.

[8] D. K. Sardar, S. Chandrasekharan, K. L. Nash, J. B. Gruber, *J. Appl. Phys.* **2008**, *104*, 023102.

[9] T. Feuchter, E. K. Mwarania, J. Wang, L. Reekie, J. S. Williams, *IEEE Photonics Technol. Lett.* **1992**, *4*, 542-544.

[10] G. N. van den Hoven, R. J. I. M. Koper, A. Polman, C. van Dam, J. W. M. Uffelen, K. M. Smit, *Appl. Phys. Lett.* **1996**, *68*, 1886-1888.

[11] P. Becker, R. Brinkmann, M. Dinand, W. Sohler, H. Suche, *Appl. Phys. Lett.* **1992**, *61*, 1257-1259.

[12] K. Kuriki, K. Koike, Y. Okamoto, *Chem. Rev.* **2002**, *102*, 2347-2356.

[13] a) J. Kido, Y. Okamoto, *Chem. Rev.* **2002**, *102*, 2357-2368; b) P. Martin-Ramos, C. Coya, A. L. Alvarez, M. Ramos Silva, C. Zaldo, J. A. Paixao, P. Chamorro-Posada, J. Martin-Gil, *J. Phys. Chem. C* **2013**, *117*, 10020-10030; c) H. Wei, G. Yu, Z. Zhao, Z. Liu, Z. Bian, C. Huang, *Dalton Trans.* **2013**, *42*, 8951-8960.

[14] a) J. W. Hofstraat, M. P. Oude Wolbers, F. C. J. M. Van Veggel, D. Reinhoudt, M. H. V. Werts, J. W. Verhoeven, *J. Fluoresc.* **1998**, *8*, 301-308; b) S. Quici, G. Marzanni, A. Forni, G. Accorsi, F. Barigelletti, *Inorg. Chem.* **2004**, *43*, 1294-1301; c) G. M. Davies, H. Adams, S. J. A. Pope, S. Faulkner, M. D. Ward, *Photochem. Photobiol. Sci.* **2005**, *4*, 829-834; d) S. Comby, D. Imbert, C. Vandevyver, J.-C. G. Bünzli, *Chem. Eur. J.* **2007**, *13*, 936-944.

[15] a) A. Mech, A. Monguzzi, F. Meinardi, J. Mezyk, G. Macchi, R. Tubino, *J. Am. Chem. Soc.* **2010**, *132*, 4574-4576; b) E. R. Triveldi, S. V. Eliseeva, J. Jankolovits, M. M. Olmstead, S. Petoud, V. L. Pecoraro, *J. Am. Chem. Soc.* **2014**, *136*, 1526-1534; c) B. L. Reid, S. Stagni, J. M. Malicka, M. Cocchi, A. N. Sobolev, B. W. Skelton, E. G. Moore, G. S. Hanan, M. I. Ogden, M. Massi, *Chem. Eur. J.* **2015**, *21*, 18354-18363; d) Y. Peng, J. X. Xu, H. Lu, R. M. Wilson, M. Motevalli, I. Hernandez, W. P. Gillin, P. B. Wyatt, H. Q. Ye, *RSC Adv.* **2017**, *7*, 128-131.

[16] a) G. Mancino, A. J. Ferguson, A Beeby, N. J. Long, T. S. Jones, *J. Am. Chem. Soc.* **2005**, *127*, 524-5251; b) P. B. Glover, A. P. Basset, P. Nockemann, B. M. Kariuki, R. Van Deun, Z. Pikramenou, *Chem. Eur. J.* **2007**, *13*, 6309-6320; c) L. Song, J. Hu, J. Wang, X. Liu, Z. Zhen, *Photochem. Photobiol. Sci.* **2008**, *7*, 689-693; d) C. Doffek, N., Alzakhem, M. Molon, M. Seitz, *Inorg. Chem.* **2012**, *51*, 4539-4545.

[17] a) F. Auzel, *Chem. Rev.* **2004**, *104*, 139-173; b) B. M. van der Ende, L. Aarts, A. Meijerink, *Phys. Chem. Chem. Phys.* **2009**, *11*, 11081-11095.

[18] N. Bloembergen, *Phys. Rev. Lett.* **1959**, *2*, 84-85,

[19] a) F. Auzel, *C. R. Acad. Sc. Paris* **1966**, *B262*, 1016-1019; b) F. Auzel, *C. R. Acad. Sc. Paris* **1966**, *B263*, 819-821.

[20] a) G. Chem, H. Qiu, P. N. Prasad, X. Chen, *Chem. Rev.* **2014**, *114*, 5161-5214; b) P. Ramasamy, P. Manivasakan, J. Y. Kim, *RSC Adv.* **2014**, *4*, 34873-34895; c) J. Zhou, Q. Liu, W. Feng, Y. Sun, F. Li, *Chem. Rev.* **2015**, *115*, 395-465; d) S. Ye, E.-H. Song, Q.-Y. Zhang, *Adv. Sci.* **2016**, *3*, 1600302; e) R. Medishetty, J. K. Zareba, D. Mayer, M. Samoc, R. A. Fischer, *Chem. Soc. Rev.* **2017**, *46*, 4976-5004; f) X.-Y. Wang, R. R. Valiev, T. Y. Ohulchanskyy, H. Agren, C. Yang, G. Chen, *Chem. Soc. Rev.* **2017**, *46*, 4150-4167.

[21] a) Y. Suffren, B. Golesorkhi, D. Zare, L. Guénée, H. Nozary, S. V. Eliseeva, S Petoud, A. Hauser, C. Piguet, *Inorg. Chem.* **2016**, *55*, 9964-9972; b) L. J. Charbonnière, *Dalton Trans.*, 2018 DOI 10.1039/c7dt04737a.

[22] I. Hyppänen, S. Lahtinen, T. Ääritalo, J. Mäkelä, J. Kankare, T. Soukka, *ACS Photonics* **2014**, *1*, 394-397.

[23] a) L. Aboshyan-Sorgho, C. Besnard, P. Pattison, K. R. Kittilstved, A. Aebischer, J.-C. G. Bünzli, A. Hauser, C. Piguet, *Angew. Chem. Int. Ed.* **2011**, *50*, 4108-4112; b) Y. Suffren, D. Zare, S. V. Eliseeva, L. Guénée, H. Nozary, T. Lathion, L. Aboshyan-Sorgho, S. Petoud, A. Hauser, C. Piguet, *J. Phys. Chem. C* **2013**, *117*, 26957-26963; c) D. Zare, Y. Suffren, L. Guénée, S. V. Eliseeva, H. Nozary, L. Aboshyan-Sorgho, S. Petoud, A. Hauser, C. Piguet, *Dalton Trans.* **2015**, *44*, 2529-2540.

[24] A. Nonat, C.F. Chan, C. Platas-Iglesias, Z. Liu, W.-T. Wong, W.-K. Wong, K.-L. Wong, L. J. Charbonnière, *Nature Commun.* **2016**, 11978.

[25] T. V. Balashova, A. P. Pushkarev, A. N. Yablonskiy, B. A. Andreev, I. D. Grishin, R. V. Rumyantcev, G. K. Fukin, M. N. Bochkarev, *J. Luminesc.* **2017**, *192*, 208-210.

[26] M. Haase, H. Schäfer, *Angew. Chem. Int. Ed.* **2011**, *50*, 5808-5829.

[27] a) M. T. Berry, P. S. May, *J. Phys. Chem. A* **2015**, *119*, 9805-9811; b) X. Shang, P. Chen, T. Jia, D. Feng, S. Zhang, Z.-M. Sun, J. Qiu, *Phys. Chem. Chem. Phys.* **2015**, *17*, 11481-11489; c) I. Hyppänen, N. Hoÿsniemi, R. Arppe, M. Schäferling, T. Soukka, *J. Phys. Chem. C* **2017**, *121*, 6924-6929.

[28] C. Piguet, J.-C. G. Bünzli, G. Bernardinelli, A. F. Williams, *Inorg. Chem.* **1993**, *32*, 4139-4149.

[29] G. Muller, J.-C. G. Bünzli, K. J. Schenk, C. Piguet, G. Hopfgartner, *Inorg. Chem.* **2001**, *40*, 2642-2651.

[30] C. Piguet, J.-C. G. Bünzli, G. Bernardinelli, C. G. Bochet, P. Froidevaux, *J. Chem. Soc.*, *Dalton Trans.* **1995**, 83-97.

[31] S. Petoud, J.-C. G. Bünzli, F. Renaud, C. Piguet, K. J. Schenk, G. Hopfgartner, *Inorg. Chem.* **1997**, *36*, 5750-5760.

[32] a) C. Piguet, B. Bocquet, G. Hopfgartner, *Helv. Chim. Acta* **1994**, *77*, 931-942; b) B. M. McKenzie, A. K. Miller, R. J. Wojtecki, J. C. Johnson, K. A. Burke, K. A. Tzeng, P. T. Mather S. J. Rowan, *Tetrahedron* **2008**, *64*, 8488-8495.

[33] L. F. Silva, M. V. Craveiro, *Org. Lett.* **2008**, *10*, 5417-5420.

[34] a) R. D. Chapman, R. T. Loda, J. P. Riehl, R. W. Schwartz, *Inorg. Chem.* **1984**, *23*, 1652-1657; b) L. I. Semenova, A. N. Sobolev, B. W. Skelton, A. H. White, *Aust. J. Chem.* **1999**, *52*, 519-529; c) M. G. B. Drew, P. B. Iveson, M. J. Hudson, J. O. Liljenzin, L. Spjuth, P.-Y. Cordier, A. Enarsson, C. Hill, C.; Madic, *J. Chem. Soc., Dalton Trans.* **2000**, 821-830; d) M. G. B. Drew, M. J. Hudson, P. B. Iveson, C. Madic, M. L. Russel, *J. Chem. Soc., Dalton Trans.* **2000**, 2711-2720; e) H.-R. Mürner, E. Chassat, R. P. Thummel, J.-C. G. Bünzli, *J. Chem. Soc., Dalton Trans.* **2000**, 2809-2816; f) L. Petit, C. Daul, C. Adamo, P. Maldivi, *New J. Chem.* **2007**, *31*, 1738-1745; g) J. M. Hamilton, M. J. Anhorn, K. A. Oscarson, J. H. Reibenspies, R. D. Hancock, *Inorg. Chem.* **2011**, *50*, 2764-2770.

[35] A. Fürstner, A. Leitner, M. Mendez, H. Krause, *J. Am. Chem. Soc.* **2002**, *124*, 13856-13863.

[36] R.-A. Fallahpour, M. Neuburger, M. Zehnder, *New J. Chem.* **1999**, 53-61.

[37] C. Bolm, M. Ewald, M. Felder, G. Schlingloff, *Chem. Ber.* **1992**, *125*, 1169-1190.

[38] J. Mathieu, P. Gros, Y. Fort, *Chem. Commun.* **2000**, 951-952.

[39] J.-M. Bénech, C. Piguet, G. Bernardinelli, J.-C. G.; Bünzli, G.; Hopfgartner, *J. Chem. Soc., Dalton Trans.* **2001**, 684-689.

[40] C. A. Bessel, R. F. See, D. L. Jameson, M. R. Churchill, K. J. Takeuchi, *J. Chem. Soc., Dalton Trans.* **1992**, 3223-3228.

[41] a) D. M. Ford, *J. Am. Chem. Soc.* **2005**, *127*, 16167-16170; b) O. A. Khakhel', *Chem. Phys. Lett.* **2006**, *421*, 464-468; c) O. A. Khakhel', T. P. Romashko, Y. E. Sakhno, *J. Phys. Chem. B.* **2007**, *111*, 7331-7335; d) C. Piguet, *Dalton Trans.* 2011, **40**, 8059-8071; e) O. A. Khakhel', T. P. Romashko, *J. Phys. Chem. A.* **2016**, *120*, 2035-2040.

[42] a) T. Dutronc, E. Terazzi, L. Guénée, K.-L. Buchwalder, A. Spoerri, D. Emery, J. Mareda, S. Floquet, C. Piguet, *Chem. Eur. J.* **2013**, *19*, 8447-8456; b) T. Dutronc, E. Terazzi, L. Guénée,

K.-L. Buchwalder, S. Floquet, C. Piguet, *Chem. Eur. J.* **2016**, *22*, 1385-1391; c) S. Guerra, T. Dutronc, E. Terazzi, L. Guénée, C. Piguet, *Phys. Chem. Chem. Phys.* **2016**, *18*, 14479-14494.

[43] a) C. Piguet, G. Hopfgartner, J. D. Henion, A. F. Williams, *Helv. Chim. Acta* **1993**, *76*, 1759-1766; b) R. Colton, A. D'Agostino, J. C. Traeger, *Mass Spectrom. Rev.* **1995**, *14*, 79-106; c) E. Leize, A. Jaffrezic, A. van Dorsselaer, *J. Mass Spectrom.* **1996**, *31*, 537-544.

[44] B. M. Castellano, D. K. Eggers, *J. Phys. Chem. B* **2013**, *117*, 8180-8188.

[45] b) K. Baudet, S. Guerra, C. Piguet, *Chem. Eur. J.* **2017**, *23*, 16787-16798.

[46] N. Ouali, B. Bocquet, S. Rigault, P.-Y. Morgantini, J. Weber, C. Piguet, *Inorg. Chem.* **2002**, *41*, 1436-1445.

[47] M. Pons, O. Millet, *Prog. Nucl. Magn. Reson. Spec.* **2001**, *38*, 267-324.

[48] a) E. R. Malinowski, D. G. Howery, *Factor Analysis in Chemistry*, Wiley, New York, Chichester, 1980; b) H. Gampp, M. Maeder, C. J. Meyer, A. Zuberbühler, *Talanta* **1986**, *33*, 943-951; c) B. R. Hall, L. E. Manck, I. S. Tidmarsh, A. Stephenson, B. F. Taylor, E. J. Blaikie, D. A. Vander Griend, M. D. Ward, *Dalton Trans.* **2011**, *40*, 12132-12145.

[49] a) H. Gampp, M. Maeder, C. J. Meyer, A. Zuberbühler, *Talanta* **1985**, *32***,** 1133-1139; b) M. Maeder, P. King, *Analysis of Chemical Processes, Determination of the Reaction Mechanism and Fitting of Equilibrium and Rate Constants*, in Chemometrics in Practical Applications, Dr. Kurt Varmuza (Ed.), ISBN: 978-953-51-0438-4, InTech, DOI: 10.5772/31896; c) Specfit/32 from ReactLab Equilibria : http://jplusconsulting.com/products/reactlab-equilibria/.

[50] J.-C. G. Bünzli, A. E. Merbach, R. M. Nielson, *Inorg. Chim. Acta* **1987**, *139*, 151-152.

[51] G. Bodizs, I. Raabe, R. Scopelliti, I. Krossing, L. Helm, *Dalton Trans.* **2009**, 5137-5147.

[52] a) M. Borkovec, G. J. M. Koper, *J. Phys. Chem. B* **1994**, *98*, 6038-6045; b) G. J. M. Koper, M. Borkovec, *J. Phys. Chem. B* **2001**, *105*, 6666-6674; c) M. Borkovec, G. J. M. Koper, C. Piguet, *Curr. Opinion in Coll. and Int. Science* **2006**, *11*, 280-289; d) G. J. M. Koper, M. Borkovec, *Polymer* **2010**, *51*, 5649-5662; e) C. Piguet, *Chem. Commun.* **2010**, *46*, 6209-6231.

[53] a) S. W. Benson, *J. Am. Chem. Soc.* **1958**, *80*, 5151-5154; b) G. Ercolani, C. Piguet, M. Borkovec, J. Hamacek, *J. Phys. Chem. B* **2007**, *111*, 12195-12203.

[54] G. Ercolani, L. Schiaffino, *Angew. Chem. Int. Ed.* **2011**, *50*, 1762-1768.

[55] The molecular volumes are taken as the Connolly volumes, which are obtained from the building of the Connolly surface around the molecular structures of complexes observed in their crystal structure and by using a probe radius of 1.4 Å for modelling water solvent molecule. a) M. L. Connolly, *Science* **1983**, *221*, 709-713; b) M. L. Connolly, *J. Appl. Cryst.* **1983**, *16*, 548-558.

[56] T. Riis-Johannessen, N. Dalla Favera, T. K. Todorova, S. M. Huber, L. Gagliardi, C. Piguet, *Chem. Eur. J.* **2009**, *15*, 12702-12718.

[57] L. Babel, L. Guénée, C. Besnard, S. V. Eliseeva, S. Petoud, C. Piguet, *Chem. Sci.* **2018**, *9*, 325-335.

[58] a) I. D. Brown, D. Altermatt, *Acta Cryst B* **1985**, *B41*, 244-247; b) N. E. Breese, M. O'Keeffe, *Acta Cryst. B* **1991**, *B47*, 192-197; c) I. D. Brown, *Acta Cryst B* **1992**, *B48*, 553-572; d) I. D. Brown, *The Chemical Bond in Inorganic Chemistry,* Oxford University Press, UK, 2002; e) A. Trzesowska, R. Kruszynski, T. J. Bartczak, *Acta Cryst B Structural Science* **2004**, *B60*, 174-178; f) A. Trzesowska, R. Kruszynski, T. J. Bartczak, *Acta Cryst B Structural Science* **2005**, *B61*, 429-434; g) A Trzesowska, R Kruszynski, T. J. Bartczak, *Acta Cryst B Structural Science* **2006**, *B62*, 745-753; h) F. Zocchi, *J. Mol. Struct. Theochem.* **2007**, *805*, 73-78; (*i*) I. D. Brown, *Chem. Rev.* **2009**, *109*, 6858-6919.

[59] a) C. A. Hunter, K. R. Lawson, J Perkins, C. J. Urch, *J. Chem. Soc., Perkin 2* **2001**, 651-669; b) S. Grimme, *Angew. Chem. Int. Ed.* **2008**, *47*, 3430-3434; c) K. E. Riley, P. Hobza, *Acc. Chem. Res.* **2013**, *46*, 927-936.

[60] a) C. Piguet, B. Bocquet, E. Müller, A. F. Williams, *Helv. Chim. Acta* **1989**, *72*, 323-337; b) E. Terazzi, L. Guénée, P.-Y. Morgantini, G. Bernardinelli, B. Donnio, D. Guillon, C. Piguet, *Chem. Eur. J.* **2007**, *13*, 1674-1691.

[61] a) K. Nakamoto, *J. Phys. Chem.* **1960**, *64*, 1420-1425; b) S. Xu, J. E. T. Smith, J. M. Weber, *Inorg. Chem.* **2016**, *55*, 11937-11943.

[62] C. Piguet, J.-C. G. Bünzli, *Handbook on the Physics and Chemistry of Rare Earths*, K. A. GschneidnerJr, J.-C. G. Bünzli, V. K. Pecharsky, Eds. Elsevier Science: Amsterdam, 2010; Vol. 40, pp 301-553.

[63] Z. Wang, T. Senden, A. Meijerink, *J. Phys. Chem. Lett.* **2017**, *8*, 5689-5694.

TOC

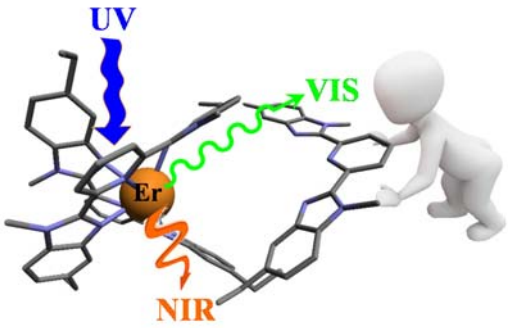

The thermodynamic assembly of three tridentate aromatic strands around trivalent erbium in triple-helical $[Er(\mathbf{L}\boldsymbol{k})_3]^{3+}$ complexes is the necessary condition for inducing some rare dual visible/near-infrared luminescence at room temperature in the solid state and in solution: a prerequisite for implementing lanthanide-based upconversion at the molecular level.

Supporting Information

(107 pages)

Appendix 1: Thermodynamics analysis of melting processes for L4-L9.

The influence of terminal substituents on the intermolecular cohesion in the solid state can be investigated by differential scanning calorimetry (Figures S3-S8). The traces of energy fluxes recorded at low scanning rate (0.5 K/min) reveal standard Ehrenfest first-order melting processes, from which the associated enthalpic (ΔH_m) and entropic (ΔS_m) contributions can be easily deduced by integration (columns 2-3 in Table A1-1).[42] Plots of enthalpic (ΔH_m) versus entropic (ΔS_m) contributions display approximate linear *H*/*S* compensations in agreement with the existence of a unique minimal intermolecular contact distance between polyaromatic entities in the solid state for both the bisbzimpy (**L4-L6**) and terpy (**L7-L9**) series (Figure A1-1a).[41]

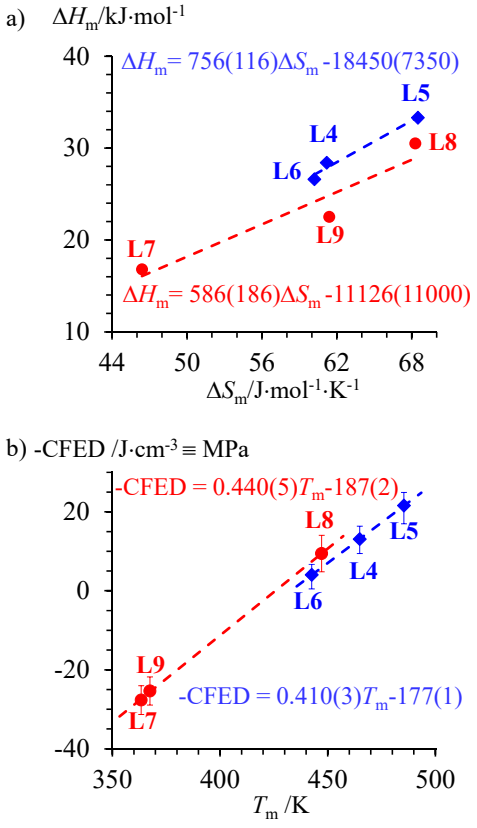

Figure A1-1 Plots of a) enthalpic *versus* entropic contributions for the melting processes modelled with eq. (A1-1) and b) cohesion free energy densities (-CFED computed at $T^{ref} = 428.5$ K) versus melting temperatures for ligands **L4-L9**. Local linear trendlines are shown together with their respective equations. The bisbzimpy series is plotted in blue and the terpy series in red.

Table A1-1 Thermodynamic parameters pertinent to the melting processes (ΔH_m, ΔS_m, T_m, $\Delta G_m^{T^{ref}}$),[42] molecular volumes (V_m), molar volumes (V_{mol}) and cohesion free energy densities (CFED, Eq. (A1-3)) for **L4**-**L9**.

L*k*	ΔH_m /kJ·mol^{-1}	ΔS_m /J·mol^{-1}·K^{-1}	T_m [a] /K	ΔG_m^{Tref} [b] /kJ·mol^{-1}	V_m [c] /Å^3	V_{mol} [d] /cm^3·mol^{-1}	CFED [e] /J·cm^{-3}
L4	28.4(1)	61(1)	464.9	2.2(5)	276.4	166.4	-13(3)
L5	33.3(2)	69(1)	485.4	3.9(6)	303.9	183.0	-21(3)
L6	26.6(1)	60(1)	442.6	0.8(5)	331.1	199.4	-4(3)
L7	16.8(1)	46(1)	363.4	-3.1(4)	185.0	111.4	28(4)
L8	30.5(2)	68(1)	447.2	1.2(6)	217.0	130.7	-9(5)
L9	22.5(1)	61(1)	367.5	-3.8(5)	249.6	150.3	25(4)

[a] Melting temperatures are taken at the onset of the DSC trace. [b] $\Delta G_m^{T^{ref}} = \Delta H_m - T^{ref}\Delta S_m$ are calculated at $T^{ref} = (1/N)\sum_{i=1}^{N} T_{m,i} = 428.5$ K. [c] Taken as the Connolly volume of the molecule in the solid state.[53] [d] $V_{mol} = N_A \cdot V_m$ where N_A is Avogadro's number. [e] $\mathrm{CFED} = -\Delta G_m^{T^{ref}} / V_{mol}$.

According to Eq. (A1-1),[41e] the different slopes displayed by the two red and blue *H*/*S* series in Figure A1-1a can be accounted for by the existence of two different phase volume expansions $\Delta\ln(\Omega_{1,2})$ accompanying the melting processes ($R\Delta\ln(\Omega_{1,2}^{bisbzimpy})$ = 24(10) J·mol^{-1}·K^{-1} and $R\Delta\ln(\Omega_{1,2}^{terpy})$ = 19(19) J·mol^{-1}·K^{-1}).

$$\Delta H_m = T_{comp}\Delta S_m - RT_{comp}\Delta\ln(\Omega_{1,2}) \quad \text{(A1-1)}$$

The magnitude of $1/\Omega$ can be then considered as a novel coordinate in the extended extra-thermodynamic relationship depicted in Eq. (A1-2) where *M* is some constant characterizing the system for which $p_\Omega^2/2M$ corresponds to its kinetic energy.[41]

$$\Delta H_m = T'_{comp}\left[\Delta S_m + R\Delta\ln(\Omega_{1,2})\right] - RT'_{comp}\Delta\ln(M_{1,2}) \quad \text{(A1-2)}$$

The restored straight line (within experimental uncertainties) observed for the plot of ΔH_m versus $\Delta S_m + R\Delta\ln(\Omega_{12})$ built for **L4**-**L9** (Figure A1-2) demonstrates that all ligands belong to the same

thermodynamic *H/S* family, for which the perturbation imposed by terminal alkyl substitutions of increasing sizes (R = H < CH_3 < CH_2CH_3) similarly affects the energy cohesion in the solid state; the only difference arises from minor changes in specific volume expansions.[41]

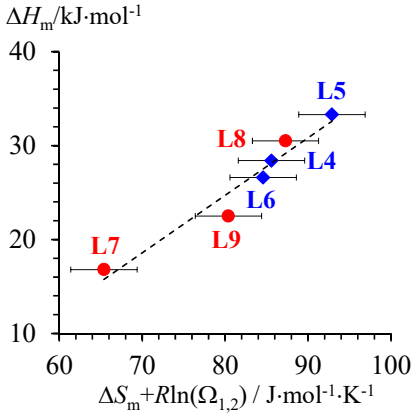

Figure A1-2 Plots of a) enthalpic *versus* entropic contributions to the melting processes modelled with Eq. (A1-2) for ligands **L4-L9**. The linear trendline is shown in black. The bisbzimpy series is plotted in red and the terpy series in blue.

The second step in the thermodynamic analysis consists in plotting in Figure A1-1b the cohesive Gibbs free energy densities (CFED) given in Eq. (A1-3), where V_{mol} is the molar volume and T^{ref} is a reference temperature taken as the average of the melting temperatures (columns 5-8 in Table A1-1) as a function of the transition temperatures (T_m).[42] The resulting pseudo-linear traces represents the phase boundaries produced by the 'chemical pressure' induced by successive perturbations within a *H/S* family (right part of Eq. (A1-3)).[42] The approximate single trace observed for ligands **L4-L9** points to similar dependence of the intermolecular energy cohesion on successive terminal alkylation for both series (Figure A1-1b).

$$\text{CFED} = \frac{\Delta G_{\text{cohesion}}^{T^{\text{ref}}}}{V_{\text{mol}}} = \frac{\Delta H_{\text{m}} - T^{\text{ref}}\Delta S_{\text{m}}}{V_{\text{mol}}} \approx \frac{\Delta V_{\text{melting}}}{V_{\text{mol}}}\Delta P_{\text{chemical}} \qquad \text{(A1-3)}$$

Moving along the boundary line, the connection of two terminal methyl groups (**L4**→**L5** or **L7**→**L8**), induces larger cohesive energies in the solid state as measured by the development of positive 'chemical pressures' ($\Delta P_{chemical}$ = CFED(**L4**)-CFED(**L5**) = 9(4) MPa or CFED(**L7**)-CFED(**L8**)

= 37(4) MPa) and the concomitant increase of the melting temperatures (Figure A1-1b). This behavior can be reasonably assigned to the increase of the molecular polarizability produced by the larger molar volume, this without significant disruption of the intermolecular packing interactions. On the contrary, the introduction of an additional methylene (CH_2) rotor in ethyl groups as found in **L6** and **L9**, provides non-linear three-carbon chains, the various conformations of which may notably affect intermolecular packing possibilities. The associated severe loss in 'chemical pressure' observed along the boundary (**L5**→**L6** or **L8**→**L9**) reduces the melting temperature of **L6** and **L9** despite their larger molecular weight and polarizabilities (Figure A1-1b). In other words, the H→CH_3→CH_2CH_3 sequence produces two successive, but opposite alterations of intermolecular cohesion. The introduction of methyl groups improves cohesion due the increase in molecular polarizability, while the extension by additional methylene rotors to give ethyl substituents severely disrupts inter-aromatic stacking.

Appendix 2: Thermodynamics analysis of Er-ligand affinities and interligand interactions in acetonitrile solutions for L4-L9.

Pertinent Born-Haber cycles allow the partition of the experimental Er-ligand affinities (Eq. (A2-1) and Scheme A2-1a) and interligand interactions (Eq. (A2-2) and Scheme A2-2b) measured in solution into their gas-phase counterpart modulated by the various solvation energies.[A2-1]

$$\Delta G^{\mathrm{Er},\mathbf{L}\boldsymbol{k}}_{\mathrm{affinity,solv}} = \Delta G^{\mathrm{Er},\mathbf{L}\boldsymbol{k}}_{\mathrm{affinity,gas}} + \Delta G^{\mathrm{Er}\mathbf{L}\boldsymbol{k}}_{\mathrm{solv}} - \left(\Delta G^{\mathrm{Er}}_{\mathrm{solv}} + \Delta G^{\mathbf{L}\boldsymbol{k}}_{\mathrm{solv}}\right) \quad \text{(A2-1)}$$

$$\Delta E^{\mathbf{L}\boldsymbol{k},\mathbf{L}\boldsymbol{k}}_{\mathrm{solv}} = \Delta E^{\mathbf{L}\boldsymbol{k},\mathbf{L}\boldsymbol{k}}_{\mathrm{gas}} + \left(\Delta G^{\mathrm{Er}}_{\mathrm{solv}} + \Delta G^{\mathrm{Er}(\mathbf{L}\boldsymbol{k})_2}_{\mathrm{solv}}\right) - 2\Delta G^{\mathrm{Er}\mathbf{L}\boldsymbol{k}}_{\mathrm{solv}} \quad \text{(A2-2)}$$

a) Intrinsic affinity

$$\begin{array}{ccc} \mathrm{Er}^{3+}_{(\mathrm{gas})} + \mathbf{L}\boldsymbol{k}_{(\mathrm{gas})} & \overset{\Delta G^{\mathrm{Er},\mathbf{L}\boldsymbol{k}}_{\mathrm{affinity,gas}}}{\rightleftharpoons} & [\mathrm{Er}(\mathbf{L}\boldsymbol{k})]^{3+}_{(\mathrm{gas})} \\ \Big\updownarrow \Delta G^{\mathrm{Er}}_{\mathrm{solv}} \quad \Big\updownarrow \Delta G^{\mathbf{L}\boldsymbol{k}}_{\mathrm{solv}} & & \Big\updownarrow \Delta G^{\mathrm{Er}\mathbf{L}\boldsymbol{k}}_{\mathrm{solv}} \\ [\mathrm{Er}]^{3+}_{(\mathrm{solv})} + \mathbf{L}\boldsymbol{k}_{(\mathrm{solv})} & \underset{\Delta G^{\mathrm{Er},\mathbf{L}\boldsymbol{k}}_{\mathrm{affinity,solv}}}{\rightleftharpoons} & [\mathrm{Er}(\mathbf{L}\boldsymbol{k})]^{3+}_{(\mathrm{solv})} \end{array}$$

b) Interligand interaction

$$\begin{array}{ccc} 2[\mathrm{Er}(\mathbf{L}\boldsymbol{k})]^{3+}_{(\mathrm{gas})} & \overset{\Delta E^{\mathbf{L}\boldsymbol{k},\mathbf{L}\boldsymbol{k}}_{\mathrm{gas}}}{\rightleftharpoons} & \mathrm{Er}^{3+}_{(\mathrm{gas})} + [\mathrm{Er}(\mathbf{L}\boldsymbol{k})_2]^{3+}_{(\mathrm{gas})} \\ \Big\updownarrow \Delta G^{\mathrm{Er}\mathbf{L}\boldsymbol{k}}_{\mathrm{solv}} & & \Big\updownarrow \Delta G^{\mathrm{Er}}_{\mathrm{solv}} \quad \Big\updownarrow \Delta G^{\mathrm{Er}(\mathbf{L}\boldsymbol{k})_2}_{\mathrm{solv}} \\ 2[\mathrm{Er}(\mathbf{L}\boldsymbol{k})]^{3+}_{(\mathrm{solv})} & \underset{\Delta E^{\mathbf{L}\boldsymbol{k},\mathbf{L}\boldsymbol{k}}_{\mathrm{solv}}}{\rightleftharpoons} & \mathrm{Er}^{3+}_{(\mathrm{solv})} + [\mathrm{Er}(\mathbf{L}\boldsymbol{k})_2]^{3+}_{(\mathrm{solv})} \end{array}$$

Scheme A2-1. Thermodynamic cycles used for rationalizing a) intrinsic Er-ligand **L*k*** affinities and b) interligand interactions.

The various solvation energies can be roughly estimated with the help of Born Eq. (A2-3),[A2-2] which is adapted for spherical ions of R_i radii and bearing z charges, and of Onsager Eq. (A2-4),[A2-3] which stands for neutral pseudo-spherical dipolar molecules possessing R_{vdw} van der Waals radii and μ dipole moments ($N_{Av} = 6.023 \cdot 10^{23}$ mol^{-1} is Avogadro's number, $e = 1.602 \cdot 10^{-19}$ C is the elementary charge, $\varepsilon_0 = 8.859 \cdot 10^{-12}$ C$^2 \cdot$N$^{-1} \cdot$m^{-2} is the vacuum permittivity, ε_r is the relative dielectric permittivity).

$$\Delta G^{0}_{\text{solv}} = -\frac{z^2 e^2 N_{\text{av}}}{8\pi\varepsilon_0 R_{\text{i}}} \cdot \left(1 - \frac{1}{\varepsilon_{\text{r}}}\right) \tag{A2-3}$$

$$\Delta G^{0}_{\text{solv}} = -\frac{\mu^2 N_{\text{av}}}{4\pi\varepsilon_0 \left(R_{\text{vdw}}\right)^3} \cdot \left(\frac{\varepsilon_{\text{r}} - 1}{2\varepsilon_{\text{r}} + 1}\right) \tag{A2-4}$$

Let's start with intrinsic affinities $\Delta G^{\text{Er,L}k}_{\text{affinity,solv}}$ modeled with Eq. (A2-1). Since the solvation energies of neutral dipolar molecules (Eq. (A2-4)) are several orders of magnitude smaller than those obtained for charged objects of similar size (Eq. (A2-3)),[A2-4] $\left|\Delta G^{\mathbf{L}k}_{\text{solv}}\right|$ is largely dominated by $\left|\Delta G^{\text{ErL}k}_{\text{solv}}\right|$ in Eq. (A2-1) and the stepwise increase in size accompanying the connection of alkyl groups along the series R=H (**L4** or **L7**) < R=CH_3 (**L5** or **L8**) < R=CH_2CH_3 (**L6** or **L9**) gradually limits the favorable contribution of $\Delta G^{\text{ErL}k}_{\text{solv}}$ to $\Delta G^{\text{Er,L}k}_{\text{affinity,solv}}$ (Eq. (A2-1)). This effect is leveled out by the inductive effects which boost the affinity of **L*k***$_{(\text{gas})}$ for $Er^{3+}_{(\text{gas})}$, and makes $\Delta G^{\text{Er,L}k}_{\text{affinity,gas}}$ more negative along the H < methyl < ethyl series. Considering the two latter opposite contributions, the effect of $\left|\Delta G^{\text{ErL}k}_{\text{solv}}\right|$ is magnified for the small ligands and it dominates the trend for the terpy series. The loss in solvation along **L7**→**L8**→**L9** therefore reduces their affinities for Er(III), and $\Delta G^{\text{Er,L}k}_{\text{affinity,solv}}$ becomes less negative (left part of Figure 5a). For the larger ligands of the bisbzimpy series, the solvation energies are significantly reduced and the inductive effect dominates. Consequently, $\Delta G^{\text{Er,L}k}_{\text{affinity,gas}}$ and $\Delta G^{\text{Er,L}k}_{\text{affinity,solv}}$ concomitantly become more negative along **L4**→**L5**→**L6** (right part of Figure 5a).

The analysis of interligand interactions $\Delta E^{\mathbf{L}k,\mathbf{L}k}_{\text{solv}}$ modeled with Eq. (A2-2) follows the same strategy with the initial neglect of weak dipole-dipole interactions responsible for $\Delta E^{\mathbf{L}k,\mathbf{L}k}_{\text{gas}}$,[A2-4] which leaves $\Delta G^{\text{Er}(\mathbf{L}k)_2}_{\text{solv}} - 2\Delta G^{\text{ErL}k}_{\text{solv}}$ as the dominant variable contributions upon successive alkyl substitution. Introducing Born Eq. (A2-3) into Eq. (A2-2) gives

$$\Delta G^{\text{Er}(\mathbf{L}k)_2}_{\text{solv}} - 2\Delta G^{\text{ErL}k}_{\text{solv}} = -\frac{z^2 e^2 N_{\text{av}}}{8\pi\varepsilon_0} \cdot \left(1 - \frac{1}{\varepsilon_{\text{r}}}\right)\left(\frac{1}{R^{\text{Er}(\mathbf{L}k)_2}} - \frac{1}{R^{\text{Er}(\mathbf{L}k)}}\right) > 0 \tag{A2-5}$$

The latter positive contribution ($R^{\mathrm{Er}(\mathbf{Lk})_2} > R^{\mathrm{Er}(\mathbf{Lk})}$) is maximized for small ligands and we therefore predict that $\Delta E_{\mathrm{solv}}^{\mathbf{Lk},\mathbf{Lk}}$ decreases when the molecular volume increases (**L7** > **L8** > **L9** > **L4** > **L5** > **L6**). This trend is experimentally detected for the first four members of the series (left part of Figure 5b), but **L5** and **L6** significantly deviate from the rule (right part of Figure 5b). This noticeable discrepancy is diagnostic for the operation of unusually strong repulsive and destabilizing interligand interactions in the triple-stranded helix $[\mathrm{Er}(\mathbf{L5})_3]^{3+}$ (methyl substituted), but especially in $[\mathrm{Er}(\mathbf{L6})_3]^{3+}$ where the ethyl substituents are known (see Appendix 1) to prevent interaromatic packing. To conclude, the thermodynamic stabilities of the $[\mathrm{Er}(\mathbf{Lk})_n]^{3+}$ (n = 1-3) complexes in acetonitrile are globally comparable for all six ligands, while minor variations along the series can be rationalized by a fine balance between inductive effect and size-dependent solvation energies. Specific inter-strand interactions can be highlighted in $[\mathrm{Er}(\mathbf{L5})_3]^{3+}$ and $[\mathrm{Er}(\mathbf{L6})_3]^{3+}$ when three bulky extended aromatic ligands are wrapped around small Er^{3+}.

References

[A2-1] a) C. J. Cramer, D. G. Truhlar, *Acc. Chem. Res.* **2008**, *41*, 760-768; b) S. A. Cotton, P. R. Raithby, *Coord. Chem. Rev.* **2017**, *340*, 220-231; c) G. Schreckenbach, *Chem. Eur. J.* **2017**, *23*, 3797-3803.

[A2-2] a) M. Born, *Zeit. Phys.* **1920**, *1*, 45-48; b) R. H. Stokes, *J. Phys. Chem.* **1964**, *86*, 979-982; c) P. W. Atkins, A. J. MacDermott, *J. Chem. Educ.* **1982**, *59*, 359-360; d) T. Abe, *Bull. Chem. Soc. Jpn* **1991**, *64*, 3035-3038.

[A2-3] a) L. Onsager, *J. Am. Chem. Soc.* **1936**, *58*, 1486-1492; b) D. V. Matyushov, *J. Chem. Phys.* **2004**, *120*, 1375-1382; c) L. E. Johnson, S. J. Benight, R. Barnes, B. H. Robinson, *J. Phys. Chem. B* **2015**, *119*, 5240-5250.

[A2-4] L. Babel, T. N. Y. Hoang, L. Guénée, C. Besnard, T. A. Wesolowski, M. Humbert-Droz, C. Piguet, *Chem. Eur. J.* **2016**, *22*, 8113-8123.

Appendix 3: Experimental section

Chemicals were purchased from Fluka AG, Aldrich or Acros and used without further purification unless otherwise stated. $Er(ClO_4)_3{\cdot}xH_2O$ and $Er(CF_3SO_3)_3{\cdot}xH_2O$ were prepared from the corresponding oxides (Aldrich, 99.99%).[S1] The Ln content of solid salts was determined by complexometric titrations with Titriplex III (Merck) in the presence of urotropine and xylene orange.[S2] The synthesis of $[Er(NCCH_3)_8][Al(OC(CF_3)_3)_4]$[49] was carried out with rigorous exclusion of air and water. Dry glove box or Schlenk techniques were employed, using purified nitrogen or argon (H_2O and O_2 < 1 ppm). Acetonitrile, dichloromethane and hexane were distilled over calcium hydride. Toluene and tetrahydrofuran were distilled under nitrogen over sodium.

Caution! *Dry perchlorates may explode and should be handled in small quantities and with the necessary precautions.*[S3]

Preparation of 2,6-bis(1′-methyl-benzimidazol-2′-yl)pyridine (L4). 2,6-bis(2-benzimidazolyl-2-yl)pyridine (2.0 g, 6.42 mmol, 1 eq)[S4] in DMF (60 mL) was slowly added to a suspension of NaH (0.5 g, 13.48 mmol, 2.1 eq) in DMF (40 mL) at rt. After 30 min, methyl iodide (0.82 mL, 1.9 g, 13.16 mmol, 2.05 eq) was added dropwise. The mixture was stirred at rt for 16 h and then quenched with ethanol (1.0 mL). Water (30 mL) was added and the crude product was extracted with ethyl acetate (3×100 mL). The combined organic phases were dried over anhydrous Na_2SO_4, filtered, and evaporated to dryness. The residue was purified by crystallization in hot acetonitrile to give white crystals of **L4** (1.8 g, yield: 82%). Mp: 192 °C. ^{1}H NMR (CD_3CN; 400 MHz), δ/ppm: 4.30 (s, 6H), 7.33-7.43 (m, 4H), 7.62 (d, ^3J = 8.0 Hz, 2H), 7.79 (d, ^3J = 8.0 Hz, 2H), 8.14 (t, ^3J = 8.0 Hz, 1H), 8.42 (d, ^3J = 8.0 Hz, 2H). Elem. analyses calcd for $C_{21}H_{17}N_5$: C 74.32, H 5.05, N 20.63; found C 74.80, H 5.46, N 19.78. ESI-MS ($CHCl_3$, soft positive mode): *m*/*z* 340.1 ($[M+H]^+$), 362.4 ($[M+Na]^+$), 679.5 ($[2M+H]^+$), 701.5 ($[2M+Na]^+$).

Preparation of 4-(*N*-methylamino)-3-nitrotoluene (5b). 4-Bromo-3-nitrotoluene (**1**, 10.0 g, 46.29 mmol, 1 eq) and methylamine (33% in methanol, 14.3 mL, 463.00 mmol, 10 eq) were heated at 130

°C for 24 h in an autoclave. The mixture was evaporated to dryness and the residual red oil shaken with concentrated hydrochloric acid (75 mL). The organic phase was separated, extracted with concentrated hydrochloric acid (3×30 mL) and the combined aqueous phases were neutralized (pH 9) with aqueous NaOH (5 M). The resulting solution was extracted with dichloromethane (3×300 mL) and the combined organic phases were dried over anhydrous Na_2SO_4, filtered, and evaporated to dryness. The residue was purified by crystallization in hot hexane to give orange crystals of **5b** (6.4 g, yield: 83%). ^{1}H NMR ($CDCl_3$; 400 MHz), δ/ppm: 2.30 (s, 3H), 3.04 (s, 3H), 6.79 (d, ^3J = 8.0 Hz, 1H), 7.32 (d, ^3J = 8.0 Hz, 1H), 8.01 (s, 1H). ESI-MS ($CHCl_3$, soft positive mode): *m*/*z* 167.1 ($[M+H]^+$)

Preparation of bis[*N*-methyl-*N*-(4′-methyl-2′-nitrophenyl)]-pyridine-2,6-dicarboxamide (8b). Pyridine-2,6-dicarboxylic acid (**6**, 1.0 g, 6.0 mmol, 1 eq) and DMF (100 μL) were refluxed in thionyl chloride (18 mL, 240 mmol, 40 eq) for 2 h. Excess thionyl chloride was distilled from the reaction mixture, which was then co-evaporated with dry CH_2Cl_2 (3 × 20 mL) and dried under vacuum. The solid was re-dissolved in freshly distilled CH_2Cl_2 (50 mL) and slowly added to a solution of 4-(*N*-methylamino)-3-nitrotoluene (**5b**, 2.1 g, 12.6 mmol, 2.1 eq) in CH_2Cl_2 (100 mL). The resulting mixture was refluxed for 24 h and the pH value was kept close to pH 9 by adding small amounts of *N,N*-diisopropylethylamine. The mixture was partitioned between CH_2Cl_2 (120 mL) and half-saturated aqueous NH_4Cl (60 mL). The organic phase was separated and the aqueous phase was further extracted with CH_2Cl_2 (2 × 150 mL). The combined organic phases were dried with anhydrous Na_2SO_4, filtered, and evaporated to dryness. The crude product was purified by column chromatography (Silicagel; CH_2Cl_2/Hexane, 30:70→100:0) to give **8b** as a yellow powder (2.6 g, yield: 92%). 1H NMR ($CDCl_3$; 400 MHz), δ/ppm: 2.19-2.50 (m, 6H, aryl CH_3), 3.19-3.52 (m, 6H, CH_3), 7.10-7.88 (m, 9H, aromatic). ESI-MS ($CHCl_3$, soft positive mode): *m*/*z* 464.0 ($[M+H]^+$).

Preparation of 2,6-bis(1′-methyl-5′-methylbenzimidazol-2′-yl)pyridine (L5). Compound **8b** (2.5 g, 5.48 mmol, 1 eq) was dissolved in ethanol-water (4:1, 600 mL). Activated iron powder (9.18 g, 164.4 mmol, 30 eq) and concentrated hydrochloric acid (37%, 15.3 mL, 180 mmol) were added and the mixture refluxed for 20 h. Water (100 mL) was then added, excess of iron filtered off and ethanol

was evaporated. The resulting mixture was poured into CH_2Cl_2 (100 mL), $Na_2(H_2edta)\cdot 2H_2O$ (H_4edta = N,N,N′,N′-ethylenediaminetetraacetic acid; 24.8 g, 66.7 mmol, 12.1 eq) dissolved in water (100 mL) was added and the resulting stirred mixture neutralized (pH > 9) with aqueous NH_4OH (12%). Concentrated hydrogen peroxide (30%, 10 mL) was added cautiously under vigorous stirring. After 15 min, the organic phase was separated and the aqueous phase extracted with CH_2Cl_2 (2 × 200 mL). The combined organic phases were dried over anhydrous Na_2SO_4, filtered, and evaporated to dryness. The residue was purified by crystallization in hot acetonitrile to give pale yellow crystals of **L5** (1.8 g, yield: 90%). Mp: 212 °C. ^{1}H NMR ($CDCl_3$; 400 MHz), δ/ppm: 2.55 (s, 6H), 4.24 (s, 6H), 7.22 (d, ^3J = 8.0 Hz, 2H), 7.36 (d, ^3J = 8.0 Hz, 2H), 7.67 (s, 2H), 8.05 (t, ^3J = 8.0 Hz, 1H), 8.41 (d, ^3J = 8.0 Hz, 2H). ^{13}C NMR ($CDCl_3$; 101 MHz), δ/ppm: 21.65 (2 CH_3), 32.53 (2 CH_3), 109.43 (2 CH), 119.86 (2 CH), 125.09 (2 CH), 125.23 (2 CH), 132.57 (2 C_{quat}), 135.36 (2 C_{quat}), 137.97 (CH), 142.92 (2 C_{quat}), 149.64 (2 C_{quat}), 150.14 (2 C_{quat}). Elem. analyses calcd for $C_{23}H_{21}N_5$: C 75.18, H 5.76, N 19.06; found C 74.78, H 5.73, N 19.03. ESI-MS ($CHCl_3$, soft positive mode): *m*/*z* 368.0 ($[M+H]^+$), 735.3 ($[2M+H]^+$).

Preparation of 1-(4-bromo-3-nitrophenyl)ethanol (3). Sodium borohydride (1.3 g, 33.8 mmol, 1.5 eq) was slowly added to a stirred solution of 4-bromo-3-nitroacetophenone (5.5 g, 22.54 mmol, 1 eq) in methanol (150 mL) at 0 °C, and the mixture was allowed to warm to rt. After stirring for 1 h. The reaction mixture was evaporated to dryness and water (50 mL) was added and the aqueous phase was extracted with ethyl acetate (2 × 100 mL). The combined organic phases were washed with brine and dried over anhydrous Na_2SO_4, filtered, and evaporated to dryness. The crude product was purified by column chromatography (Silicagel; CH_2Cl_2/methanol, 99:1) to give **3** as a pale yellow powder (5.4 g, yield: 97%). ^{1}H NMR ($CDCl_3$; 400 MHz), δ/ppm: 1.535 (d, ^3J = 4.0, 3H), 2.00 (s, br, OH), 4.98 (q, ^3J = 8.0 Hz, 1H), 7.46 (d, ^3J = 8.0 Hz, 1H), 7.72 (d, ^3J = 8.0 Hz, 1H), 7.89 (s, 1H). ESI-MS ($CHCl_3$, soft positive mode): *m*/*z* 246.4 ($[M+H]^+$).

Preparation of 1-bromo-4-ethyl-2-nitrobenzene (4). The crude alcohol **3** (5.4 g, 21.88 mmol, 1 eq) was dissolved in CH_2Cl_2 (150 mL). Triphenylphosphine (8.6 g, 32.82 mmol, 1.5 eq) and imidazole

(2.24 g, 32.94 mmol, 1.5 eq) were then added and the mixture was cooled to 0 °C. Molecular iodine (8.3 g, 32.70 mmol, 1.6 eq) was added, the cold bath was removed, and after stirring for 3 h, water (100 mL) was added. The organic phase was separated and the aqueous phase was extracted with CH_2Cl_2 (2 × 100 mL). The combined organic phases were washed with brine and dried over anhydrous Na_2SO_4, filtered, and evaporated to dryness and the crude product was dried at rt under high vacuum for 1.5 h. The product was then dissolved in DMSO (75 mL) and the solution was cooled to 0 °C. Sodium borohydride (1.7 g, 44.97 mmol, 2 eq) was slowly added, the reaction mixture was allowed to warm to rt and stirred for 30 min, and then cooled to 0 °C once more. Water (50 mL) was added and the mixture was extracted with ethyl acetate (3 × 50 mL). The combined organic phases were washed with brine and dried over anhydrous Na_2SO_4, filtered, and evaporated to dryness to afford the crude product as a yellow solid. This product was dissolved in a minimum volume of CH_2Cl_2 and then a mixture of hexane/Et_2O (1:1; 100 mL) was added. After gentle shaking, Ph_3PO started to precipitate. The mixture was then filtered through a silica pad, which was washed with Et_2O until no more product could be eluted, as monitored by TLC. This procedure removed most of the Ph_3PO formed as a byproduct. The eluent was collected and concentrated under reduced pressure, and the crude product was purified by column chromatography (Silicagel; hexane/ethyl acetate, 90:10) to give **4** (2.9 g, yield: 55%) as a yellow oil. ^{1}H NMR ($CDCl_3$; 400 MHz), δ/ppm: 1.29 (t, ^3J = 8.0, 3H), 2.72 (q, ^3J = 8.0 Hz, 2H), 7.29 (d, ^3J = 8.0 Hz, 1H), 7.65 (d, ^3J = 8.0 Hz, 1H), 7.70 (s, 1H). ESI-MS ($CHCl_3$, soft positive mode): m/z 230.3 ($[M+H]^+$).

Preparation of 4-ethyl-*N*-methyl-2-nitro-benzenamine (5c). Compound **4** (2.9 g, 12.5 mmol, 1 eq) and methylamine (33% in methanol, 20.0 mL, 161.1 mmol, 10 eq) were heated at 130 °C for 48 h in an autoclave. The mixture was evaporated to dryness and the residual red oil was shaken with concentrated hydrochloric acid (40 mL). The organic phase was separated, extracted with concentrated hydrochloric acid (3×40 mL) and the combined aqueous phases were neutralized (pH 9) with aqueous NaOH (5 M). The resulting solution was extracted with dichloromethane (3×100 mL) and the combined organic phases were dried over anhydrous Na_2SO_4, filtered, and evaporated

to dryness. The residue was purified by column chromatography (Silicagel; CH_2Cl_2/Hexane, 90:10) to give **5c** (2.2 g, yield: 99%). ^{1}H NMR ($CDCl_3$; 400 MHz), δ/ppm: 1.24 (t, ^3J = 8.0, 3H), 2.60 (q, ^3J = 8.0 Hz, 2H), 3.04 (s, 3H), 6.81 (d, ^3J = 12.0 Hz, 1H), 7.36 (d, ^3J = 8.0 Hz, 1H), 8.02 (s, 1H). ESI-MS ($CHCl_3$, soft positive mode): m/z 181.1 ($[M+H]^+$)

Preparation of bis[*N*-methyl-*N*-(4′-ethyl-2′-nitrophenyl)]-pyridine-2,6-dicarboxamide (8c). Pyridine-2,6-dicarboxylic acid (**6**, 1.0 g, 5.9 mmol, 1 eq) and DMF (100 μL) were refluxed in thionyl chloride (17.1 mL, 236.0 mmol, 40 eq) for 2 h. Excess thionyl chloride was distilled from the reaction mixture, which was then co-evaporated with dry CH_2Cl_2 (3 × 20 mL) and dried under vacuum. The solid was re-dissolved in freshly distilled CH_2Cl_2 (50 mL) and slowly added to a solution of 4-(*N*-methylamino)-3-nitrotoluene (**5c**, 2.2 g, 12.4 mmol, 2.1 eq) in CH_2Cl_2 (100 mL). The resulting mixture was heated to reflux for 24 h and the pH value was kept close to pH 9 by adding small amounts of *N,N*-diisopropylethylamine. The mixture was partitioned between CH_2Cl_2 (150 mL) and half-saturated aqueous NH_4Cl (60 mL). The organic phase was separated and the aqueous phase was further extracted with CH_2Cl_2 (2 × 150 mL). The combined organic phases were dried with anhydrous Na_2SO_4, filtered, and evaporated to dryness. The crude product was purified by column chromatography (Silicagel; CH_2Cl_2/methanol, 100: 0→98:2) to give **8c** (2.2 g, yield: 77%). 1H NMR ($CDCl_3$; 400 MHz), δ/ppm: 1.17-1.36 (m, 6H, aryl CH_3), 2.64-2.83 (m, 4H, aryl CH_2), 3.30-3.60 (m, 6H, CH_3), 7.10-7.89 (m, 9H, aromatic). ESI-MS ($CHCl_3$, soft positive mode): m/z 492.4 ($[M+H]^+$).

Preparation of 2,6-bis(1′-methyl-5′-ethylbenzimidazol-2′-yl)pyridine (L6). Compound **8c** (2.2 g, 4.48 mmol, 1 eq) was dissolved in ethanol-water (4:1, 600 mL). Activated iron powder (7.5 g, 134.4 mmol, 30 eq) and concentrated hydrochloric acid (37%, 13.0 mL, 147.8 mmol) were added and the mixture refluxed for 20 h. Water (100 mL) was then added, excess of iron filtered off and ethanol was evaporated. The resulting mixture was poured into CH_2Cl_2 (100 mL), $Na_2(H_2edta)\cdot 2H_2O$ (H_4edta = N,N,N′,N′-ethylenediaminetetraacetic acid, 20.1 g, 66.7 mmol, 12.1 eq) dissolved in water (100 mL) was added and the resulting stirred mixture was neutralized (pH > 9) with aqueous NH_4OH (12%). Concentrated hydrogen peroxide (30%, 10 mL) was added cautiously under vigorous stirring.

After 15 min, the organic phase was separated and the aqueous phase extracted with CH_2Cl_2 (2 × 200 mL). The combined organic phases were dried over anhydrous Na_2SO_4, filtered, and evaporated to dryness. The residue was purified by crystallization in hot acetonitrile to give pale orange needle crystals of L3 (0.9 g, yield: 50%). Mp: 169 °C. ^{1}H NMR ($CDCl_3$; 400 MHz), δ/ppm: 1.35 (t, ^3J = 8.0 Hz, 6H), 2.84 (q, ^3J = 8.0 Hz, 4H), 4.22 (s, 6H), 7.25 (d, ^3J = 8.0 Hz, 2H), 7.38 (d, ^3J = 8.0 Hz, 2H), 7.71 (s, 2H), 8.03 (t, ^3J = 8.0 Hz, 1H), 8.41 (d, ^3J = 8.0 Hz, 2H). ^{13}C NMR ($CDCl_3$; 101 MHz), δ/ppm: 16.32 (2 CH_3), 29.08 (2 CH_2), 32.50 (2 CH_3), 109.55 (2 CH), 118.63 (2 CH), 124.27 (2 CH), 125.06 (2 CH), 135.52 (2 C_{quat}), 137.94 (2 C_{quat}), 139.30 (CH), 142.92 (2 C_{quat}), 149.65 (2 C_{quat}), 150.14 (2 C_{quat}). Elem. analyses calcd for $C_{23}H_{21}N_5$: C 75.92, H 6.37, N 17.71; found C 75.41, H 6.34, N 17.49. ESI-MS ($CHCl_3$, soft positive mode): *m*/*z* 395.8 ($[M+H]^+$), 791.5 ($[2M+H]^+$).

Preparation of 2-bromo-5-methylpyridine (10). To a mechanically stirred mixture of HBr (48%, 40.4 mL, 357.1 mmol, 8 eq) and 2-amino-5-picoline (**9**, 10.0 g, 92.6 mmol, 1 eq), bromine (14.24 mL, 280.0 mmol, 3 eq) was added dropwise during 90 min at -5 °C. A 200 mL aqueous $NaNO_2$ solution (16.0 g, 231.0 mmol, 2.5 eq) was added dropwise during 2 h and the temperature was kept below 0 °C. The mixture was neutralized with aqueous NaOH while the temperature was kept below 0 °C, then warmed to rt and extracted with CH_2Cl_2 (2 × 200 mL). The combined organic phases were washed with aqueous $Na_2S_2O_3$ and dried over anhydrous Na_2SO_4, filtered, and evaporated to dryness. The crude product was purified by sublimation (40 °C, 0.05 mbar) to give **10** (8.1 g, yield: 50%) as a pale yellow crystals. ^{1}H NMR ($CDCl_3$; 400 MHz), δ/ppm: 2.49 (s, 3H), 7.74 (d, ^3J = 8.0 Hz, 1H), 7.89 (d, ^3J = 8.0 Hz, 1H), 8.52 (s, 1H). ESI-MS ($CHCl_3$, soft positive mode): *m*/*z* 172.4 and 174.4 ($[M+H]^+$).

Preparation of 5-methyl-2-tributylstannyl pyridine (11). A solution of 2-bromo-5-methylpyridine (**10**, 3.6 g, 20.84 mmol, 1 eq) in THF (90 mL) was cooled to -78 °C and *n*-BuLi (13.81 mL, 22.1 mmol, 1.06 eq) was added dropwise during 10 min. After stirring for 2 h at -78 °C, tributyltin chloride (7.9 g, 24.31 mmol, 1.1 eq) was added and the mixture was stirred for another 2 h at -78 °C. The mixture was allowed to warm to r.t. and then saturated aqueous NH_4Cl (40 mL) was added. The

resulting precipitate was dissolved by adding water, and the layers were separated. The aqueous layer was extracted with diethyl ether (3 × 100 mL). The combined organic phases were washed with brine and dried over anhydrous Na_2SO_4, filtered, and evaporated to dryness. The crude product was purified by column chromatography (Alumina; petroleum ether/ethyl acetate, 95: 5) to give **11** (6.7 g, yield: 83%) as a yellow oil. ^{1}H NMR ($CDCl_3$; 400 MHz), δ/ppm: 0.89 (t, ^3J = 8.0 Hz, 9H), 1.13 (t, ^3J = 8.0 Hz, 6H), 1.34 (tq, ^3J = 8.0 Hz, 6H), 1.58 (m, 6H), 2.29 (s, 3H), 7.31 (m, 2H), 8.61 (s, 1H). ESI-MS ($CHCl_3$, soft positive mode): *m*/*z* 384.5 ($[M+H]^+$), 326.1 ($[M-Bu]^+$), 268.3 ($[M-2Bu]^+$), 209.9 ($[M-3Bu]^+$).

Preparation of 5,5″-dimethyl-2,2′:6′,2″-terpyridine (L8). 2,6-Dibromopyridine (**14**, 1.9 g, 8.2 mmol, 1 eq), **11** (6.3 g, 16.5 mmol, 2.01 eq) and $Pd(PPh_3)_4$ (379 mg, 0.164 mmol, 0.04 eq) were heated in toluene (100 mL) for 16 h. After cooling to r.t, saturated NH_4Cl (40 mL) was added and the organic phase separated. The aqueous phase was extracted with toluene (3 × 50 mL). The combined organic phases were dried over anhydrous Na_2SO_4, filtered, and evaporated to dryness. Concentrated hydrochloric acid was added (30 mL) to the residue, and then washed with CH_2Cl_2 (3 × 200 mL). The aqueous phase was cautiously neutralized by solid sodium hydroxide. The aqueous phase was separated and extracted with CH_2Cl_2 (3 × 100 mL). The combined organic phases were dried with anhydrous Na_2SO_4, filtered, and evaporated to dryness. The crude product was purified by column chromatography (Silicagel; CH_2Cl_2/methanol, 100: 0→97:3) and crystallized in hot acetonitrile to give white needles of **L8** (1.4 g, yield: 51%). Mp: 174 °C. ^{1}H NMR ($CDCl_3$; 400 MHz), *δ*/ppm: 2.43 (s, 6H), 7.67 (d, ^3J = 8.0 Hz, 2H), 7.94 (t, ^3J = 8.0 Hz, 1H), 8.40 (d, ^3J = 8.0 Hz, 2H), 8.52 (d, ^3J = 8.0 Hz, 2H), 8.54 (s, 2H). ^{13}C NMR ($CDCl_3$; 101 MHz), *δ*/ppm: 18.42 (2 CH_3), 120.35 (2 CH), 120.69 (2 CH), 133.37 (2 C_{quat}), 137.34 (2 CH), 137.77 (CH), 149.54 (2 CH), 153.82 (2 C_{quat}), 155.40 (2 C_{quat}). Elem. analyses calcd for $C_{23}H_{21}N_5$: C 78.13, H 5.79, N 16.08; found C 77.70, H 5.76, N 15.96. ESI-MS ($CHCl_3$, soft positive mode): *m*/*z* 262.0 ($[M+H]^+$), 523.3 ($[2M+H]^+$).

Preparation of 5-ethyl-2-tributylstannyl pyridine (13). To a solution of 2-dimethylaminoethanol (6.5 g, 72.4 mmol, 3.1 eq) in hexane (15 mL) cooled at 0 °C, was added dropwise *n*-BuLi (1.6 M

solution in hexane, 90 mL, 144.7 mmol, 6.2 eq). After 15 min, a solution of 3-ethylpyridine (**12**, 2.5 g, 23.3 mmol, 1 eq) in hexane (15 mL) was added dropwise and the orange solution stirred for 1 h at 0 °C. After cooling at -78 °C, a solution of tributyltin chloride (28.5 g, 84.0 mmol, 3.6 eq) in THF (20 mL) was added dropwise. The reaction mixture was kept at -78 °C for 1 h and then allowed to warm to r.t. Hydrolysis at 0 °C with water (30 mL) was followed by extraction with diethyl ether (3 × 100 mL). The combined organic phases were dried with anhydrous Na_2SO_4, filtered, and the solvent was evaporated. The oily crude product was purified by Kugelrohr type distillation (150 °C, 1×10^{-3} Torr) to give **13** (4.7 g, yield: 51%) as a yellow oil. 1H NMR (DMSO-d_6; 400 MHz), δ/ppm: 0.84 (t, ^3J = 8.0 Hz, 9H), 1.05 (t, ^3J = 8.0 Hz, 6H), 1.18 (t, ^3J = 8.0 Hz, 3H) 1.28 (tq, ^3J = 8.0 Hz, 6H), 1.52 (m, 6H), 2.57 (q, ^3J = 8.0 Hz, 2H), 7.36 (d, ^3J = 8.0 Hz, 1H), 7.46 (d, ^3J = 8.0 Hz, 1H), 8.56 (s, 1H). ESI-MS ($CHCl_3$, soft positive mode): *m*/*z* 399.0 ($[M+H]^+$), 340.6 ($[M-Bu]^+$), 282.5 ($[M-2Bu]^+$), 226.6 ($[M-3Bu]^+$).

Preparation of 5,5″-diethyl-2,2′:6′,2″-terpyridine (L9). 2,6-Dibromopyridine (**14**, 1.3 g, 5.65 mmol, 1 eq), **13** (4.7 g, 11.9 mmol, 2.01 eq) and $Pd(PPh_3)_4$ (261 mg, 0.226 mmol, 0.04 eq) were heated in toluene (100 mL) for 16 h. After cooling to r.t, saturated NH_4Cl (40 mL) was added and the organic phase separated. The aqueous phase was extracted with toluene (3 × 50 mL). The combined organic phases were dried over anhydrous Na_2SO_4, filtered, and evaporated to dryness. Concentrated hydrochloric acid was added (30 mL) to the residue, and then washed with CH_2Cl_2 (3 × 200 mL). The aqueous phase was cautiously neutralized with solid sodium hydroxide. The aqueous phase was separated and extracted with CH_2Cl_2 (3 × 100 mL). The combined organic phases were dried with anhydrous Na_2SO_4, filtered, and evaporated to dryness. The crude product was purified by column chromatography (Silicagel; CH_2Cl_2/methanol, 100: 0→97:3) and crystalized in hot acetonitrile to give white needles of **L9** (0.8 g, yield: 49%). Mp: 94 °C. ^{1}H NMR ($CDCl_3$; 400 MHz), *δ*/ppm: 1.33 (t, ^3J = 8.0 Hz, 6H), 2.76 (q, ^3J = 8.0 Hz, 6H), 7.70 (d, ^3J = 8.0 Hz, 2H), 7.95 (t, ^3J = 8.0 Hz, 1H), 8.41 (d, ^3J = 8.0 Hz, 2H), 8.55 (d, ^3J = 8.0 Hz, 2H), 8.57 (s, 2H). ^{13}C NMR ($CDCl_3$; 101 MHz), *δ*/ppm: 15.36 (2 CH_3), 26.02 (2 CH_2), 120.37 (2 CH), 120.84 (2 CH), 136.18 (2 C_{quat}), 137.76 (2 CH), 139.58

(CH), 148.84 (2 CH), 154.08 (2 C_{quat}), 155.44 (2 C_{quat}). Elem. analyses calcd for $C_{23}H_{21}N_5$: C 78.86, H 6.62, N 14.52; found C 78.71, H 6.62, N 14.61. ESI-MS ($CHCl_3$, soft positive mode): *m*/*z* 290.8 ($[M+H]^+$), 313.8 ($[M+Na]^+$).

Preparation of $[Er(L4)_2(O_3SCF_3)_2](CF_3SO_3)$, $[Er(L7)_2(O_3SCF_3)_2](CF_3SO_3)$ and $Er(L8)_2(O_3SCF_3)_3$. Reaction **L*k*** (*k* = 3, 7 and 8, 3.0 eq) with $[Er(CF_3SO_3)_3]$ (1.0 eq) in acetonitrile followed by crystallization induced by slow diffusion of diethyl ether into a saturated acetonitrile solution of the complex provided crystals of $[Er(\mathbf{L4})_2(CF_3SO_3)_2](CF_3SO_3)\cdot 2CH_3CN$ (**1**), $[Er(\mathbf{L7})_2(CF_3SO_3)_2](CF_3SO_3)\cdot 1.5C_2H_5CN$ (**2**, recristallized from propionitrile), $[Er(\mathbf{L8})_2(CF_3SO_3)_3]$ (**3**) suitable for X-ray diffraction. Separation from the mother liquor followed by air drying gave satisfying elemental analysis for $[Er(\mathbf{L4})_2(O_3SCF_3)_2](CF_3SO_3)\ 0.4CH_3CN\cdot 1.2H_2O$ (calcd for C 41.29, H 2.85, N 10.93; found C 41.37, H 3.11, N 10.83), $[Er(\mathbf{L7})_2(CF_3SO_3)_2](CF_3SO_3)\cdot 0.6CH_3CN$ (calcd for C 37.12, H 2.18, N 8.41; found C 37.14, H 2.35, N 8.23; $[Er(\mathbf{L8})_2(CF_3SO_3)_3]$ (calcd for C 39.08, H 2.66, N 7.39; found C 38.87, H 2.61, N 7.26. ESI-MS (CH_3CN, positive mode) for: **1** *m*/*z* 1144.8 ($[Er(\mathbf{L4})_2(O_3SCF_3)_2]^+$), 498.2 ($[Er(\mathbf{L4})_2(O_3SCF_3)]^{2+}$), 395.3 ($[Er(\mathbf{L4})_3]^{3+}$), 340.5 ($[\mathbf{L4}+H]^+$), 282.1 ($[Er(\mathbf{L4})_2]^{3+}$); **2** *m*/*z* 931.7 ($[Er(\mathbf{L7})_2(O_3SCF_3)_2]^+$), 391.6 ($[Er(\mathbf{L7})_2(O_3SCF_3)]^{2+}$), 326.3 ($[Er(\mathbf{L7})_2(F)]^{2+}$), 346.4 ($[Er(\mathbf{L7})_2(F)(CH_3CN)]^{2+}$), 234.3 ($[\mathbf{L7}+H]^+$), 211.1 ($[Er(\mathbf{L7})_2]^{3+}$); **3** *m*/*z* 988.6 ($[Er(\mathbf{L8})_2(O_3SCF_3)_2]^+$), 419.2 ($[Er(\mathbf{L8})_2(O_3SCF_3)]^{2+}$), 374.3 ($[Er(\mathbf{L8})_2(F)(CH_3CN)]^{2+}$), 317.2 ($[Er(\mathbf{L8})_3]^{3+}$), 262.2 ($[\mathbf{L8}+H]^+$), 230.2 ($[Er(\mathbf{L8})_2]^{3+}$).

Preparation of $[Er(L\mathit{k})_3](ClO_4)_3$ (*k* = 6-9): Reaction **L*k*** (3.0 eq) with $[Er(ClO_4)_3]\cdot xH_2O$ (1.0 eq) in acetonitrile for **L7** and **L9**, or acetonitrile/propionitrile/dichloromethane for **L6** and **L9,** followed by crystallization induced by slow evaporation provided crystals of $[Er(\mathbf{L6})_3](ClO_4)_3\cdot 1.5CH_3CN$ (**4**), $[Er(\mathbf{L7})_3](ClO_4)_3$ (**5**), $[Er(\mathbf{L8})_3](ClO_4)_3$ (**6**), $[Er(\mathbf{L9})_3](ClO_4)_3\cdot 1.5CH_3CN$ (**7**) suitable for X-ray diffraction studies. Separation from the mother liquor followed by air drying gave satisfying elemental analysis for $[Er(\mathbf{L6})_3](ClO_4)_3\cdot 1.5CH_3CN$ calcd for: (calcd C 54.91, H 4.37, N 13.78; found C 54.55, H 4.86, N 13.52), $[Er(\mathbf{L7})_3](ClO_4)_3$ (calcd C 46.38, H 2.85, N 10.82; found C 46.38, H 2.88,

N 10.87), [Er(**L8**)$_3$](ClO$_4$)$_3$ (calcd C 49.02, H 3.63, N 10.09; found C 48.96, H 3.65, N 10.15) and [Er(**L9**)$_3$](ClO$_4$)$_3$·0.8CH$_3$CN·2.6H$_2$O (calcd C 49.02, H 4.50, N 9.57; found C 49.70, H 4.25, N 9.75. ESI-MS (CH$_3$CN, positive mode) for: **4** *m*/*z* 1552.98 ([Er(L3)$_3$(ClO$_4$)$_2$]$^+$), 726.51 ([Er(**L6**)$_3$(ClO$_4$)]$^{2+}$), 529.2 ([Er(**L6**)$_2$(ClO$_4$)]$^{2+}$), 451.88 ([Er(**L6**)$_3$]$^{3+}$); **5** *m*/*z* 832.3 ([Er(**L7**)$_2$(ClO$_4$)$_2$]$^+$), 366.6 ([Er(**L7**)$_2$(ClO$_4$)]$^{2+}$), 289.1 ([Er(**L7**)$_3$]$^{3+}$), 234.3 ([**L7**+H]$^+$); **6** *m*/*z* 888.5 ([Er(**L8**)$_2$(ClO$_4$)$_2$]$^+$), 394.7 ([Er(**L8**)$_2$(ClO$_4$)]$^{2+}$), 317.2 ([Er(**L8**)$_3$]$^{3+}$), 262.2 ([**L8**+H]$^+$); **7** *m*/*z* 944.7 ([Er(**L9**)$_2$(ClO$_4$)$_2$]$^+$), 423.0 ([Er(**L9**)$_2$(ClO$_4$)]$^{2+}$), 345.1 ([Er(**L9**)$_3$]$^{3+}$), 290.3 ([**L9**+H]$^+$).

Preparation of [(L*k*)$_2$Er(OH)$_2$Er(L*k*)$_2$](ClO$_4$)$_4$ (*k* = 4 and 5). Reaction of **L*k*** (3.0 eq) with [Er(ClO$_4$)$_3$]·*x*H$_2$O (1.0 eq) in a mixture of acetonitrile/ propionitrile/ benzonitrile (4:2:1) followed by crystallization induced by slow evaporation provided crystals of [(**L4**)$_2$Er(OH)$_2$Er(**L4**)$_2$](ClO$_4$)$_4$·2C$_6$H$_5$CN·4CH$_3$CN (**8**) and [(**L5**)$_2$Er(OH)$_2$Er(**L5**)$_2$](ClO$_4$)$_4$·C$_6$H$_5$CN ·7.5CH$_3$CN (**9**) suitable for X-ray diffraction studies. Separation from the mother liquor followed by air drying gave satisfying elemental analysis for [(**L4**)$_2$Er(OH)$_2$Er(**L4**)$_2$](ClO$_4$)$_4$ ·1.6CH$_3$CN·1.5C$_6$H$_5$CN (calcd C 50.01, H 3.51, N 13.79; found C 50.13, H 3.58, N 13.81) and [(**L5**)$_2$Er(OH)$_2$Er(**L5**)$_2$](ClO$_4$)$_4$·0.8CH$_3$CN·4.4C$_6$H$_5$CN (calcd C 54.83, H 4.05, N 12.96; found C 54.90, H 4.17, N 12.97. ESI-MS (CH$_3$CN, positive mode) for: **8** *m*/*z* 679.3 ([2**L4**+H]$^+$), 472.5 ([Er(**L4**)$_2$(ClO$_4$)]$^{2+}$), 395.0 ([Er(**L4**)$_3$]$^{3+}$), 431.5 ([Er(**L4**)$_2$(OH)]$^{2+}$), 340.3 ([**L4**+H]$^+$); **9** *m*/*z* 1019.1 ([(**L5**)$_2$Er(OH)$_2$Er(**L5**)$_2$(ClO$_4$)$_2$]$^{2+}$), 735.2 ([2**L5**+H]$^+$), 645.6 ([(**L5**)$_2$Er(OH)$_2$Er(**L5**)$_2$(ClO$_4$)]$^{3+}$), 500.7 ([Er(**L5**)$_2$(ClO$_4$)]$^{2+}$), 459.5 ([Er(**L5**)$_2$(OH)]$^{2+}$), 423.0 ([Er(**L5**)$_3$]$^{3+}$), 368.2 ([**L5**+H]$^+$).

Preparation of [(L4)$_2$Er(O(CH$_3$)NO)$_2$Er(L4)$_2$](ClO$_4$)$_6$. Reaction **L4** (3.0 eq) with [Er(ClO$_4$)$_3$]·*x*H$_2$O (1.0 eq) in a mixture of acetonitrile/ propionitrile/ nitromethane (2:2:1) followed by crystallization induced by slow evaporation provided crystals of [(**L4**)$_2$Er(CH$_3$NO$_2$)$_2$Er(**L4**)$_2$](ClO$_4$)$_6$·CH$_3$NO$_2$ (**10**) suitable for X-ray diffraction studies. Separation from the mother liquor followed by air drying gave satisfying elemental analysis for [(**L1**)$_2$Er(O(CH$_3$)NO)$_2$Er(**L1**)$_2$](ClO$_4$)$_6$·2.2C$_2$H$_5$CN (calcd C 43.88, H 3.36, N 13.38; found C 44.2,

H 3.23, N 13.30. ESI-MS (CH_3CN, positive mode) *m*/*z* 1004.6, 665.5, 451.9, 340.5 ([**L4**+H]$^+$), 282.5 ([Er(**L4**)$_2$]$^{3+}$), 170.8 ([**L4**+2H]$^{2+}$).

Preparation of K[Al(OC(CF$_3$)$_3$)$_4$].[S5] $LiAlH_4$ (purified by several successive extractions with dry diethyl ether and then dried at 80 °C under high vacuum, 1.5 g, 39.9 mmol, 1 eq) was suspended in dry toluene (100 mL). Perfluoro-tert-butanol (22.8 mL, 163.6 mmol, 4.1 eq) was added at 0 °C during 30 min. The reaction mixture was then stirred for 1 h at 0 °C and another 1 h at r.t. The mixture was heated to reflux overnight (use two reflux condensers). Cooling this solution for one hour to -20 °C led to the precipitation of a colorless powder. The supernatant solution was decanted and all the volatiles were removed (at least 1 h under high vacuum). The crude residue was carefully suspended in dry diethyl ether (60 mL) and a saturated aqueous KCl (60 mL) was added dropwise. The mixture was stirred vigorously for 2 h at r.t and then the organic phase separated. The aqueous phase was extracted with toluene (3 × 50 mL). The combined organic phases were washed by saturated aqueous KCl (40 mL) and evaporated to dryness. The residue was re-dissolved in diethyl ether and filtered. The filtrate was evaporated to dryness and the residue was exposed to high vacuum for at least 2 h to give K[Al(OC(CF$_3$)$_3$)$_4$] (18.1 g, yield: 45%) as a pale yellow powder.

Preparation of [Ag(NCCH$_3$)$_4$][Al(OC(CF$_3$)$_3$)$_4$].[S6] K[Al(OC(CF$_3$)$_3$)$_4$] (5.0 g, 5.0 mmol, 1 eq) and silver nitrate (844 mg, 4.7 mmol, 1 eq) were mixed in acetonitrile (40 mL) in the dark. The mixture was stirred for 20 min and then diethyl ether (40 mL) was added. The solvent and volatiles were removed in vacuum and the residue was dissolved in CH_2Cl_2 (40 mL) and filtered. The filtrate was evaporated to dryness and the residue was exposed to high vacuum for at least 2 h to give [Ag(NCCH$_3$)$_4$][Al(OC(CF$_3$)$_3$)$_4$] (3.0 g, yield: 49%) as a light sensitive off-white powder. ^{1}H NMR (CD_3CN; 400 MHz), *δ*/ppm: 1.99 (s, CH_3). ^{19}F NMR (CD_3CN; 376.5 MHz), *δ*/ppm: -76.01 (s). Elem. analyses calcd for [Ag(NCCH$_3$)$_4$][Al(OC(CF$_3$)$_3$)$_4$]·4.8CH_2Cl_2: C 23.26, H 0.98, N 4.52; found C 20.89, H 1.10, N 3.51.

Preparation of $[Er(NCCH_3)_8][Al(OC(CF_3)_3)_4]$.[49] Anhydrous $ErCl_3$ (137 mg, 0.5 mmol, 1 eq) and $[Ag(NCCH_3)_4][Al(OC(CF_3)_3)_4]$ (1.9 g, 1.55 mmol, 3.1 eq) were mixed in acetonitrile (50 mL) in the darkness at r.t. The reaction mixture was stirred for 10 min and the precipitate was allowed to settle down. After cautious filtration, the filtrate was evaporated to dryness under vacuum. The residue was washed several times with CH_2Cl_2 (7 × 15 mL), dried in vacuum to give $[Er(NCCH_3)_8][Al(OC(CF_3)_3)_4]$ (1.0 g, yield: 58%) as an off-white powder. ^{1}H NMR (CD_3CN; 400 MHz), *δ*/ppm: 1.99 (s, CH_3). 13C NMR ($CDCl_3$; 101 MHz), δ/ppm: 117.26 (CN). ^{19}F NMR (CD_3CN; 376.5 MHz), *δ*/ppm: -76.0 (s). Elem. analyses calcd for $[Er(NCCH_3)_8][Al(OC(CF_3)_3)_4]\cdot 19.9CH_2Cl_2\cdot 3.2CH_3CN$: C 20.77, H 1.42, N 3.00; found C 20.58, H 1.17, N 3.28.

Spectroscopic and analytical measurements

^{1}H, ^{19}F and ^{13}C NMR spectra were recorded at 293 K on Bruker Avance 400 MHz and Bruker DRX-300 MHz spectrometers. Chemical shifts are given in ppm with respect to TMS (^{1}H) or C_6F_6 (^{19}F). Spectrophotometric titrations were performed with a J&M diode array spectrometer (Tidas series) connected to an external computer. In a typical experiment, 20 cm^3 of ligand in acetonitrile (10^{-4} M) were titrated at 293 K with a solution of erbium salt (10^{-3} M) in acetonitrile under an inert atmosphere. After each addition of 0.1 mL, the absorbance was recorded using Hellma optrodes (optical path length 0.1 cm) immersed in the thermostated titration vessel and connected to the spectrometer. Mathematical treatment of the spectrophotometric titrations was performed with factor analysis[46] and with the SPECFIT program.[47] Pneumatically-assisted electrospray (ESIMS) mass spectra were recorded from 10^{-4} M (ligands) and 10^{-3} M (complexes) solutions on an Applied Biosystems API 150EX LC/MS System equipped with a Turbo Ionspray source. Elemental analyses were performed by K. L. Buchwalder from the Microchemical Laboratory of the University of Geneva. Electronic spectra in the UV-Vis region were recorded at 293 K from solutions in CH_3CN with a Perkin-Elmer Lambda 1050 using quartz cells of 0.1 or 1.0 mm path length. Solid-state diffuse reflectance spectra were recorded using UV/Vis/NIR Perkin-Elmer Lambda 900 in reflectance (*R*) mode fitted with an

integrating sphere. The pure or MgO-diluted samples were placed between two 1.0 mm path length quartz cells whose background cell was filled with pure MgO. The signal of pure MgO was used as the baseline. The spectra were then converted into absorbance using *Kubelka-Munk* function ($(1-R)^2/2R$). Solid-state luminescence data were collected on samples either mounted directly onto copper plates using conductive silver glue or placed in quartz suprasil certified capillaries and tubes. Solution emission spectra were recorded on CH_3CN solution sample of compounds using quartz suprasil certified tubes. Emission spectra were measured on a Horiba Scientific Fluorolog 3 spectrofluorimeter equipped with a visible photomultiplier tube (PMT) (220-850 nm, R928P or 185-1010 nm, R2658P; Hamamatsu). The infrared luminescence spectra were recorded either on a Horiba Scientific Fluorolog 3 spectrofluorimeter equipped with a NIR solid-state InGaAs detector cooled to 77 K (800-1600 nm, DSSIGA020L; Horiba Scientific), a NIR PMT (950-1650 nm, H10330-75; Hamamtsu) or a Bruker IFS 66/S spectrometer equipped with an InGaAs diode (780-1725 nm; D424). High resolution NIR emission spectra were recorded upon excitation with a 447 nm diode laser. The low temperature emission spectra were recorded using either a FL-1013 liquid nitrogen dewar Horiba Scientific Fluorolog 3 accessory or an optical closed-cycle cryostat capable of reaching low temperatures down to 5 K in an helium atmosphere (Oxford Instruments CCC1100T, or Sumitono SHI-950/Janis Research CCS-500/204). Luminescence lifetimes were determined under excitation at 355 nm provided by a Nd:YAG laser (YG 980; Quantel). Signals were detected with help of either a CCD detector (in the visible region) or a Hamamatsu H10330-75 PMT (in the NIR region). The output signals from the detectors were fed into a bandpass digital oscilloscope (TDS-724C or 754-C; Tektronix), transferred to a PC for data analysis. Appropriate filters were utilized to remove the laser light, the Rayleigh scattered light and associated harmonics from the emission spectra. Emission spectra were corrected for instrumental functions. Fluorescence lifetimes on the nanosecond timescale were measured using the time-correlated single-photon counting (TCSPC) technique. Excitation was performed at 320 nm at a repetition rate between 8.46 and 78.8 MHz with the output of the Extend-UV module of a picosecond pulsed SuperK Extreme supercontinuum laser (NKT

Photonics). Fluorescence was collected at 90° and focused into an optical fiber guiding the light to the entrance of a Horiba Triax 190 monochromator set at 380 nm (for L1-L3) or 370 nm (for L4-L6) with fully open slits. The fluorescence was then detected on a photomultiplier (PicoQuant PMA 192) connected to a TCSPC lifetime analysis module (PicoQuant PicoHarp 300). The full-width at half maximum of the instrument response function (IRF) was about 180 ps. All measurements were performed in a 1-cm quartz cell at a sample concentration of 10 μM in acetonitrile. The fluorescence decays were analysed by iterative reconvolution of a trial mono- or biexponential function with the measured IRF. The accuracy on the extracted lifetimes is about 0.1 ns.

X-ray crystallography

Summary of crystal data, intensity measurements and structure refinements for were collected in Tables S1, S14, S21, S31. The crystals were mounted on MiTeGen kapton cryoloops with protection oil. X-ray data collections were performed with an Agilent SuperNova Dual diffractometer equipped with a CCD Atlas detector (Cu[Kα] radiation). The structures were solved by using direct methods.[S8] Full-matrix least-square refinements on F^2 were performed with SHELX2014.[S8] CCDC 1834821-1834833 contains the supplementary crystallographic data. The cif files can be obtained free of charge via www.ccdc.cam.ac.uk/conts/retrieving.html (or from the Cambridge Crystallographic Data Centre, 12 Union Road, Cambridge CB2 1EZ, UK; fax: (+ 44) 1223-336-033; or deposit@ccdc.cam.ac.uk).

References

[S1] J. F. Desreux, in *Lanthanide Probes in Life, Chemical and Earth Sciences*; J.-C. G. Bünzli and G. R. Choppin, Eds., Elsevier: Amsterdam, 1989; chap. 2.

[S2] G. Schwarzenbach, *Complexometric Titrations*; Chapman & Hall: London, 1957 p. 8.

[S3] a) W. C. Wolsey, *J. Chem. Educ.* **1973**, *50*, A335-A337; b) J.-L. Pascal, F. Favier, *Coord. Chem. Rev.* **1998**, *178-180*, 865-902.

[S4] a) A. W. Addison, T. N. Rao, C. G. Wahlgren, *J. Heterocyl. Chem.* **1983**, *20*, 1481-1484; b) C. Piguet, B. Bocquet, E. Müller, A. F. Williams, *Helv. Chim. Acta* **1989**, *72*, 323-337.

[S5] I. Krossing, *Chem. Eur. J.* **2001**, *7*, 490-502.

[S6] Y. Li, F. E. Kühn, *J. Organomet. Chem.* **2008**, *693*, 2465-2467.

[S7] SHELXS97 G. M. Sheldrick, *Acta Crystallogr. A* **2008**, *64*, 112–122.

[S8] G. M. Sheldrick, *Acta Crystallogr. Sect. C Struct. Chem.* **2015**, *71*, 3–8.

Table S1 Summary of Crystal Data, Intensity Measurements and Structure Refinements for Ligands **L5**, **L6**, **L8** and **L9**.

	L5	**L6**	**L8**	**L9**
Empirical formula	C23H21N5	C25H25N5	C17H15N3	C19H19N3
Formula weight	367.45	395.50	261.32	289.37
Temperature	180(2) K	240(2)K	180(2)K	180(2)K
Wavelength	1.54184 Å	1.54184 Å	1.54184 Å	1.54184 Å
Crystal System, Space group	Monoclinic, $P2_1/c$	Monoclinic, $I2/a$	Monoclinic, $I2/a$	Monoclinic, $C2/c$
Unit cell dimensions	a = 14.0739(4) Å b = 7.0564(2) Å c = 18.7071(6) Å α = 90° β = 94.384(3)° γ = 90°	a = 8.4966(3) Å b = 12.8837(5) Å c = 19.7197(7) Å α = 90° β = 101.540(4)° γ = 90°	a = 17.0585(5) Å b = 6.47731(18) Å c = 24.6079(7) Å α = 90° β = 90.616(3)° γ = 90°	a = 15.2924(2) Å b = 6.48765(11) Å c = 31.7533(5) Å α = 90° β = 92.2110(14)° γ = 90°
Volume in Å^3	1852.38(11)	2115.03(13)	2718.86(14)	3147.96(9)
Z, Calculated density	4, 1.318 Mg/m^3	4, 1.242 Mg/m^3	8, 1.277 Mg/m^3	8, 1.221 Mg/m^3
Absorption coefficient	0.636 mm^{-1}	0.592 mm^{-1}	0.605 mm^{-1}	0.569 mm^{-1}
F(000)	776	840	1104	1232
Theta range for data collection	4.74 to 73.73°	4.577 to 73.10 °	3.59 to 73.25 °	5.58 to 73.37 °
Limiting indices	-14<=h<=17, -8<=k<=4, -23<=l<=21	-6<=h<=10, -15<=k<=11, -23<=l<=24	-20<=h<=9, -7<=k<=8, -30<=l<=29	-18<=h<=18, -7<=k<=7, -38<=l<=27
Reflections collected / unique	6561 / 3627 [R(int) = 0.0211]	3797 / 2061 [R(int) = 0.0191]	4941 / 2508 [R(int) = 0.0182]	5450 / 3066 [R(int) = 0.0153]
Completeness to theta	67.50°/ 99.8 %	67.50°/ 99.5%	67.50°/ 94.6 %	67.50°/ 99.8 %
Data / restraints / parameters	3627 / 0 / 258	2061 / 0 / 144	2508 / 0 / 184	3066 / 0 / 202
Goodness-of-fit on $F2$	1.033	1.063	1.037	1.077
Final R indices [$I>2\sigma(I)$]	$R1$ = 0.0407, $\omega R2$ = 0.1056	$R1$ = 0.0543, $\omega R2$ = 0.1497	$R1$ = 0.0423, $\omega R2$ = 0.1151	$R1$ = 0.0447, $\omega R2$ = 0.1226
R indices (all data)	$R1$ = 0.0499, $\omega R2$ = 0.1129	$R1$ = 0.0627, $\omega R2$ = 0.1597	$R1$ = 0.0525, $\omega R2$ = 0.1235	$R1$ = 0.0503, $\omega R2$ = 0.1279
Largest diff. peak and hole	0.236 and -0.188 e·Å^{-3}	0.201 and -0.205 e·Å^{-3}	0.193 and -0.158 e·Å^{-3}	0.217 and -0.218 e·Å^{-3}

Table S2 Selected bond distances (Å) and bond angles (°) for ligand **L4**.[39]

Bond distances (Å)

Atom 1	Atom 2	Distance	Atom 1	Atom 2	Distance
C(1)	N(1)	1.341(2)	C(5)	N(1)	1.347(2)
C(6)	N(2)	1.323(2)	C(7)	N(2)	1.392(2)
C(6)	N(3)	1.375(2)	C(12)	N(3)	1.378(2)
C(13)	N(3)	1.459(2)	C(14)	N(4)	1.327(2)
C(15)	N(4)	1.387(2)	C(14)	N(5)	1.381(2)
C(20)	N(5)	1.379(2)	C(21)	N(5)	1.463(2)
C(1)	C(2)	1.397(3)	C(1)	C(14)	1.437(2)
C(2)	C(3)	1.375(3)	C(3)	C(4)	1.383(3)
C(4)	C(5)	1.389(3)	C(5)	C(6)	1.475(2)
C(7)	C(8)	1.396(3)	C(7)	C(12)	1.401(3)
C(8)	C(9)	1.382(3)	C(9)	C(10)	1.401(3)
C(10)	C(11)	1.378(3)	C(11)	C(12)	1.400(3)
C(15)	C(16)	1.400(3)	C(15)	C(20)	1.401(3)
C(16)	C(17)	1.382(3)	C(17)	C(18)	1.398(3)
C(18)	C(19)	1.375(3)	C(19)	C(20)	1.395(3)

Angles (°)

At. 1	At. 2	At. 3	Angle	At. 1	At. 2	At. 3	Angle
C(1)	N(1)	C(5)	118.0(1)	C(6)	N(2)	C(7)	104.6(1)
C(6)	N(3)	C(12)	106.6(1)	C(6)	N(3)	C(13)	129.7(2)
C(12)	N(3)	C(13)	123.4(2)	C(14)	N(4)	C(15)	105.2(1)
C(14)	N(5)	C(20)	106.4(1)	C(14)	N(5)	C(21)	131.4(1)
C(20)	N(5)	C(1)	122.2(1)	N(1)	C(1)	C(2)	122.3(2)
N(6)	C(1)	C(14)	118.4(1)	C(2)	C(1)	C(14)	119.3(2)
C(1)	C(2)	C(3)	119.0(2)	C(2)	C(3)	C(4)	119.3(2)
C(3)	C(4)	C(5)	118.5(2)	N(1)	C(5)	C(4)	122.8(2)
N(1)	C(5)	C(6)	116.9(1)	C(4)	C(5)	C(6)	120.3(2)
N(2)	C(6)	N(3)	113.1(1)	N(2)	C(6)	C(5)	123.1(1)
N(3)	C(6)	C(5)	123.7(2)	N(2)	C(7)	C(8)	130.4(2)
N(2)	C(7)	C(12)	110.0(2)	C(8)	C(7)	C(12)	119.4(2)
C(7)	C(8)	C(9)	118.3(2)	C(8)	C(9)	C(10)	121.5(2)
C(9)	C(10)	C(11)	121.4(2)	C(10)	C(11)	C(12)	116.6(2)
N(3)	C(12)	C(7)	105.7(1)	N(3)	C(12)	C(11)	131.5(2)
C(7)	C(12)	C(11)	122.7(2)	N(4)	C(14)	N(5)	112.6(1)
N(4)	C(14)	C(1)	122.0(1)	N(5)	C(14)	C(1)	125.4(1)
N(4)	C(15)	C(16)	130.5(2)	N(4)	C(15)	C(20)	109.8(2)
C(16)	C(15)	C(20)	119.6(2)	C(15)	C(16)	C(17)	117.7(2)
C(16)	C(17)	C(18)	121.8(2)	C(17)	C(18)	C(19)	121.5(2)
C(18)	C(19)	C(20)	116.8(2)	N(5)	C(20)	C(15)	106.1(1)
N(5)	C(20)	C(19)	131.3(2)	C(15)	C(20)	C(19)	122.6(2)

Table S3 Selected least-squares planes data for ligand **L4**.

Least-squares planes

Least-squares planes description	Abbreviation	Max. deviation/Å	Atom
Benzimidazole 1 C(7) C(8) C(9) C(10) C(11) C(12) N(3) C(6) N(2)	Bz1	0.046	C(13)
Pyridine N(1) C(1) C(2) C(3) C(4) C(5)	Py	0.025	C(7)
Benzimidazole 2 C(15) C(16) C(17) C(18) C(19) C(20) N(5) C(14) N(4)	Bz2	0.019	N(6)

Interplanar angles (°)

	Bz1	Py	Bz2
Bz1		36.80(6)	42.75(5)
Py			7.11(6)
Bz2			

Table S4 Selected bond distances (Å) and bond angles (°) for ligand **L5**.

Bond distances (Å)

Atom 1	Atom 2	Distance	Atom 1	Atom 2	Distance
C(9)	N(1)	1.3220(19)	C(3)	C(5)	1.411(2)
C (1)	N(1)	1.3818(18)	C(3)	C(4)	1.508(2)
C (9)	N(2)	1.3744(18)	C(5)	C(6)	1.380(2)
C(7)	N(2)	1.3779(18)	C(6)	C(7)	1.3997(19)
C(8)	N(2)	1.4574(18)	C(9)	C(10)	1.4790(18)
C(10)	N(3)	1.3430(18)	C(10)	C(11)	1.3931(19)
C(14)	N(3)	1.3443(17)	C(11)	C(12)	1.382(2)
C(15)	N(4)	1.3247(17)	C(12)	C(13)	1.384(2)
C(16)	N(4)	1.3830(19)	C(14)	C(15)	1.473(2)
C(15)	N(5)	1.3727(17)	C(16)	C(17)	1.400(2)
C(22)	N(5)	1.3797(18)	C(17)	C(18)	1.380(2)
C(23)	N(5)	1.4569(16)	C(18)	C(20)	1.410(2)
C(1)	C(7)	1.397(2)	C(18)	C(19)	1.510(2)
C(1)	C(2)	1.400(2)	C(20)	C(21)	1.383(2)
C(2)	C(3)	1.387(2)	C(21)	C(22)	1.393(2)

Angles (°)

At. 1	At. 2	At. 3	Angle	At. 1	At. 2	At. 3	Angle
C(9)	N(1)	C(1)	104.96(12)	N(3)	C(10)	C(11)	123.14(13)
C(9)	N(2)	C(7)	105.83(11)	N(3)	C(10)	C(9)	119.51(12)
C(9)	N(2)	C(8)	130.80(12)	C(11)	C(10)	C(9)	117.34(13)
C(7)	N(2)	C(8)	123.37(12)	C(12)	C(11)	C(10)	118.57(13)
C(10)	N(3)	C(14)	117.37(12)	C(11)	C(12)	C(13)	119.30(13)
C(15)	N(4)	C(16)	104.90(11)	C(12)	C(13)	C(14)	118.36(13)
C(15)	N(5)	C(22)	106.44(11)	N(3)	C(14)	C(13)	123.25(13)
C(15)	N(5)	C(23)	129.07(12)	N(3)	C(14)	C(15)	118.43(12)
C(22)	N(5)	C(23)	124.37(12)	C(13)	C(14)	C(15)	118.31(12)
N(1)	C(1)	C(7)	109.76(12)	N(4)	C(15)	N(5)	112.95(12)
N(1)	C(1)	C(2)	129.94(13)	N(4)	C(15)	C(14)	122.00(12)
C(7)	C(1)	C(2)	120.30(13)	N(5)	C(15)	C(14)	125.04(12)
C(3)	C(2)	C(1)	118.51(14)	N(4)	C(16)	C(17)	130.19(13)
C(2)	C(3)	C(5)	119.79(14)	N(4)	C(16)	C(22)	110.04(12)
C(2)	C(3)	C(4)	120.50(15)	C(17)	C(16)	C(22)	119.77(14)
C(5)	C(3)	C(4)	119.71(14)	C(18)	C(17)	C(16)	119.22(14)
C(6)	C(5)	C(3)	122.91(13)	C(17)	C(18)	C(20)	119.59(14)
C(5)	C(6)	C(7)	116.26(14)	C(17)	C(18)	C(19)	120.56(15)
N(2)	C(7)	C(1)	106.29(12)	C(20)	C(18)	C(19)	119.84(15)
N(2)	C(7)	C(6)	131.47(14)	C(21)	C(20)	C(18)	122.61(14)
C(1)	C(7)	C(6)	122.23(13)	C(20)	C(21)	C(22)	116.74(14)
N(1)	C(9)	N(2)	113.16(12)	N(5)	C(22)	C(21)	132.26(13)
N(1)	C(9)	C(10)	120.72(13)	N(5)	C(22)	C(16)	105.67(12)
N(2)	C(9)	C(10)	126.11(12)	C(21)	C(22)	C(16)	122.07(13)

Table S5 Selected least-squares planes data for ligand **L5**.

Least-squares planes

Least-squares planes description	Abbreviation	Max. deviation/Å	Atom
Benzimidazole 1 C(1) C(2) C(3) C(5) C(6) C(7) N(2) C(9) N(1)	Bz1	0.012	N(2)
Pyridine N(3) C(10) C(11) C(12) C(13) C(14)	Py	0.003	C(11)
Benzimidazole 2 C(16) C(17) C(18) C(20) C(21) C(22) N(5) C(15) N(4)	Bz2	0.006	C(16) C(22)

Interplanar angles (°)

	Bz1	Py	Bz2
Bz1		13.25(4)	34.72(4)
Py			25.54(4)
Bz2			

Table S6 Selected bond distances (Å) and bond angles (°) for ligand **L6**.

Bond distances (Å)

Atom 1	Atom 2	Distance	Atom 1	Atom 2	Distance
N(1)	C(4)	1.317(2)	C(3)#1	C(4)#1	1.476(2)
N(1)#1	C(4)#1	1.317(2)	C(5)	C(6)	1.394(2)
N(1)	C(5)	1.379(2)	C(5)#1	C(6)#1	1.394(2)
N(1)#1	C(5)#1	1.379(2)	C(5)	C(12)	1.397(2)
N(2)	C(4)	1.376(2)	C(5)#1	C(12)#1	1.397(2)
N(2)#1	C(4)#1	1.376(2)	C(6)	C(7)	1.379(2)
N(2)	C(12)	1.378(2)	C(6)#1	C(7)#1	1.379(2)
N(2)#1	C(12)#1	1.378(2)	C(7)	C(10)	1.408(3)
N(2)	C(13)	1.456(2)	C(7)#1	C(10)#1	1.408(3)
N(2)#1	C(13)#1	1.456(2)	C(8)	C(9B)	1.476(19)
N(3)	C(3)	1.3381(19)	C(8)#1	C(9B)#1	1.476(19)
N(3)	C(3)#1	1.3381(19)	C(8)	C(9A)	1.488(4)
C(1)	C(2)	1.370(2)	C(8)#1	C(9A)#1	1.488(4)
C(1)	C(2)#1	1.370(2)	C(10)	C(11)	1.381(3)
C(2)	C(3)	1.397(2)	C(10)#	C(11)#1	1.381(3)
C(2)#1	C(3)#1	1.397(2)	C(11)	C(12)	1.395(2)
C(3)	C(4)	1.476(2)	C(11)#1	C(12)#1	1.395(2)

Symmetry operation #1 $-x+1/2,y,-z+2$

Angles (°)

At. 1	At. 2	At. 3	Angle	At. 1	At. 2	At. 3	Angle
C(4)	N(1)	C(5)	105.48(14)	N(1)#1	C(5)#1	C(12)#1	109.71(15)
C(4)#1	N(1)#1	C(5)#1	105.48(14)	C(6)	C(5)	C(12)	119.83(15)
C(4)	N(2)	C(12)	106.14(13)	C(6)#1	C(5)#1	C(12)#1	119.83(15)
C(4)#1	N(2)#1	C(12)#1	106.14(13)	C(7)	C(6)	C(5)	119.55(17)
C(4)	N(2)	C(13)	129.96(14)	C(7)#1	C(6)#1	C(5)#1	119.55(17)
C(4)	N(2)	C(13)	129.96(14)	C(6)	C(7)	C(10)	119.59(17)
C(12)	N(2)	C(13)	123.85(14)	C(6)#1	C(7)#1	C(10)#1	119.59(17)
C(12)	N(2)	C(13)	123.85(14)	C(6)	C(7)	C(8)	120.27(17)
C(3)#1	N(3)	C(3)	117.78(19)	C(6)#1	C(7)#1	C(8)#1	120.27(17)
C(2)	C(1)	C(2)#1	119.5(2)	C(10)	C(7)	C(8)	120.13(17)
C(1)	C(2)	C(3)	118.66(18)	C(10)#1	C(7)#1	C(8)#1	120.13(17)
C(1)	C(2)#1	C(3)#1	118.66(18)	C(9B)	C(8)	C(9A)	49.0(8)
N(3)	C(3)	C(2)	122.67(16)	C(9B)#1	C(8)#1	C(9A)#1	49.0(8)
N(3)	C(3)#1	C(2)#1	122.67(16)	C(9B)	C(8)	C(7)	117.4(6)
N(3)	C(3)	C(4)	120.94(15)	C(9B)#1	C(8)#1	C(7)#1	117.4(6)
N(3)	C(3)#1	C(4)#1	120.94(15)	C(9A)	C(8)	C(7)	113.60(19)
C(2)	C(3)	C(4)	116.39(15)	C(9A)#1	C(8)#1	C(7)#1	113.60(19)
C(2)#1	C(3)#1	C(4)#1	116.39(15)	C(11)	C(10)	C(7)	122.13(17)
N(1)	C(4)	N(2)	112.67(14)	C(11)#1	C(10)#1	C(7)#1	122.13(17)
N(1)#1	C(4)#1	N(2)#1	112.67(14)	C(10)	C(11)	C(12)	117.20(17)
N(1)	C(4)	C(3)	120.64(15)	C(10)#1	C(11)#1	C(12)#1	117.20(17)
N(1)#1	C(4)#1	C(3)#1	120.64(15)	N(2)	C(12)	C(11)	132.30(16)
N(2)	C(4)	C(3)	126.69(14)	N(2)#1	C(12)#1	C(11)#1	132.30(16)
N(2)#1	C(4)#	C(3)#1	126.69(14)	N(2)	C(12)	C(5)	105.99(14)
N(1)	C(5)	C(6)	130.46(16)	N(2)#1	C(12)#1	C(5)#1	105.99(14)
N(1)#1	C(5)#1	C(6)#1	130.46(16)	C(11)	C(12)	C(5)	121.71(16)
N(1)	C(5)	C(12)	109.71(15)	C(11)#1	C(12)#1	C(5)#1	121.71(16)

Symmetry operation #1 $-x+1/2,y,-z+2$

Table S7 Selected least-squares planes data for ligand **L6**.

Least-Squares Planes

Least-squares planes description	Abbreviation	Max. deviation/Å	Atom
Benzimidazole 1 C(5) C(6) C(7) C(10) C(11) C(12) N(2) C(4) N(1)	Bz1	0.006	C(4)
Pyridine N(3) C(1) C(2) C(3) C(2)#1 C(3)#1	Py	0.003	C(2), C(3), C(2)#1, C(3)#1
Benzimidazole 2 C(5)#1 C(6)#1 C(7)#1 C(10)#1 C(11)#1 C(12)#1 N(2)#1 C(4)#1 N(1)#1	Bz2	0.006	C(7)#1

Interplanar angles (°)

	Bz1	Py	Bz2
Bz1		10.09(4)	18.48(6)
Py			10.09(4)
Bz2			

Table S8 Selected bond distances (Å) and bond angles (°) for ligand **L7**.[40]

Bond distances (Å)

Atom 1	Atom 2	Distance	Atom 1	Atom 2	Distance
C(1)	N(1)	1.317(7)	C(5)	N(1)	1.339(9)
C(1)	C(2)	1.349(8)	C(1)	C(6)	1.488(8)
C(2)	C(3)	1.388(9)	C(3)	C(4)	1.351(10)
C(4)	C(5)	1.391(10)	C(6)	N(2)	1.353(8)
C(10)	N(2)	1.349(7)	C(6)	C(7)	1.398(9)
C(7)	C(8)	1.376(9)	C(8)	C(9)	1.380(9)
C(9)	C(10)	1.396(8)	C(10)	C(11)	1.439(8)
C(11)	N(3)	1.350(8)	C(15)	N(3)	1.344(9)
C(11)	C(12)	1.391(9)	C(12)	C(13)	1.386(9)
C(13)	C(14)	1.366(10)	C(14)	C(15)	1.360(10)

Angles (°)

At. 1	At. 2	At. 3	Angle	At. 1	At. 2	At. 3	Angle
C(1)	N(1)	C(5)	118.4(5)	N(1)	C(1)	C(2)	123.3(5)
N(1)	C(1)	C(6)	116.1(5)	C(2)	C(1)	C(6)	120.5 (5)
C(1)	C(2)	C(3)	118.2(6)	C(2)	C(3)	C(4)	120.1(6)
C(3)	C(4)	C(5)	117.8(6)	N(1)	C(5)	C(4)	122.0(6)
C(6)	N(2)	C(10)	117.5(5)	C(1)	C(6)	N(2)	117.3(5)
C(1)	C(6)	C(7)	120.2(5)	N(2)	C(6)	C(7)	122.5(5)
C(6)	C(7)	C(8)	119.6(6)	C(7)	C(8)	C(9)	118.2(6)
C(8)	C(9)	C(10)	120.0(5)	N(2)	C(10)	C(9)	122.3(5)
N(2)	C(10)	C(11)	116.7(5)	C(9)	C(10)	C(11)	121.1(5)
C(11)	N(3)	C(15)	115.4(5)	C(10)	C(11)	N(3)	114.8(5)
C(10)	C(11)	C(12)	121.7(5)	N(3)	C(11)	C(12)	123.5(5)
C(11)	C(12)	C(13)	118.7(6)	C(12)	C(13)	C(14)	118.0(6)
C(13)	C(14)	C(15)	119.8(6)	N(3)	C(15)	C(14)	124.4(6)

Table S9 Selected least-squares planes data for ligand **L7**.

Least-squares planes

Least-squares planes description	Abbreviation	Max. deviation/Å	Atom
Pyridine 1 C(1) C(2) C(3) C(4) C(5) N(1)	Py1	0.023	C(4)
Pyridine 2 C(6) C(7) C(8) C(9) C(10) N(2)	Py2	0.012	C(6)
Pyridine 3 C(11) C(12) C(13) C(14) C(15) N(3)	Py3	0.027	C(14)

Interplanar angles (°)

	Py1	Py2	Py3
Py1		5.1(2)	7.2(8)
Py2			7.10(11)
Py3			

Table S10 Selected bond distances (Å) and bond angles (°) for ligand **L8**.

Bond distances (Å)

Atom 1	Atom 2	Distance	Atom 1	Atom 2	Distance
N(1)	C(1)	1.3357(19)	C(6)	C(7)	1.4857(18)
N(1)	C(6)	1.3423(16)	C(7)	C(8)	1.3944(19)
N(2)	C(11)	1.3403(16)	C(8)	C(9)	1.380(2)
N(2)	C(7)	1.3426(16)	C(9)	C(10)	1.3832(19)
N(3)	C(17)	1.3349(18)	C(10)	C(11)	1.3969(19)
N(3)	C(12)	1.3422(17)	C(11)	C(12)	1.4897(18)
C(1)	C(2)	1.385(2)	C(12)	C(13)	1.3949(19)
C(2)	C(4)	1.387(2)	C(13)	C(14)	1.3848(18)
C(2)	C(3)	1.503(2)	C(14)	C(15)	1.387(2)
C(4)	C(5)	1.3826(19)	C(15)	C(17)	1.394(2)
C(5)	C(6)	1.394(2)	C(15)	C(16)	1.5076(19)

Angles (°)

At. 1	At. 2	At. 3	angle	At. 1	At. 2	At. 3	angle
C(1)	N(1)	C(6)	117.44(13)	C(9)	C(8)	C(7)	119.04(12)
C(11)	N(2)	C(7)	118.14(11)	C(8)	C(9)	C(10)	119.04(13)
C(17)	N(3)	C(12)	117.81(12)	C(9)	C(10)	C(11)	118.63(13)
N(1)	C(1)	C(2)	125.04(13)	N(2)	C(11)	C(10)	122.71(12)
C(1)	C(2)	C(4)	116.56(13)	N(2)	C(11)	C(12)	116.82(11)
C(1)	C(2)	C(3)	121.72(14)	C(10)	C(11)	C(12)	120.47(12)
C(4)	C(2)	C(3)	121.72(15)	N(3)	C(12)	C(13)	121.97(12)
C(5)	C(4)	C(2)	119.96(14)	N(3)	C(12)	C(11)	116.84(12)
C(4)	C(5)	C(6)	118.98(12)	C(13)	C(12)	C(11)	121.19(12)
N(1)	C(6)	C(5)	122.01(12)	C(14)	C(13)	C(12)	118.99(12)
N(1)	C(6)	C(7)	116.72(12)	C(13)	C(14)	C(15)	119.96(13)
C(5)	C(6)	C(7)	121.26(11)	C(14)	C(15)	C(17)	116.61(12)
N(2)	C(7)	C(8)	122.43(12)	C(14)	C(15)	C(16)	122.34(14)
N(2)	C(7)	C(6)	117.14(11)	C(17)	C(15)	C(16)	121.05(13)
C(8)	C(7)	C(6)	120.42(12)	N(3)	C(17)	C(15)	124.66(13)

Table S11 Selected least-squares planes data for ligand **L8**.

Least-squares planes

Least-squares planes description	Abbreviation	Max. deviation/Å	Atom
Pyridine 1 C(1) C(2) C(4) C(5) C(6) N(1)	Py1	0.004	C(5), C(6)
Pyridine 2 C(7) C(8) C(9) C(10) C(11) N(2)	Py2	0.006	N(2)
Pyridine 3 C(12) C(13) C(14) C(15) C(17) N(3)	Py3	0.006	C(14), C(15)

Interplanar angles (°)

	Py1	Py2	Py3
Py1		9.79(5)	11.26(5)
Py2			8.49(5)
Py3			

Table S12 Selected bond distances (Å) and bond angles (°) for ligand **L9**.

Bond distances (Å)

Atom 1	Atom 2	Distance	Atom 1	Atom 2	Distance
N(1)	C(7)	1.3331(18)	C(6)	C(8)	1.4901(17)
N(1)	C(6)	1.3436(15)	C(8)	C(9)	1.3908(19)
N(2)	C(12)	1.3410(16)	C(9)	C(10)	1.3822(19)
N(2)	C(8)	1.3423(15)	C(10)	C(11)	1.3857(18)
N(3)	C(17)	1.3387(17)	C(11)	C(12)	1.3935(19)
N(3)	C(13)	1.3394(16)	C(12)	C(13)	1.4872(17)
C(1)	C(2)	1.495(2)	C(13)	C(14)	1.388(2)
C(2)	C(3)	1.5078(18)	C(14)	C(15)	1.3792(19)
C(3)	C(4)	1.3852(19)	C(15)	C(16)	1.3877(19)
C(3)	C(7)	1.389(2)	C(16)	C(17)	1.387(2)
C(4)	C(5)	1.3845(19)	C(16)	C(18)	1.5062(17)
C(5)	C(6)	1.3901(19)	C(18)	C(19)	1.498(2)

Angles (°)

At. 1	At. 2	At. 3	angle	At. 1	At. 2	At. 3	angle
C(7)	N(1)	C(6)	117.55(12)	C(10)	C(9)	C(8)	118.63(12)
C(12)	N(2)	C(8)	118.25(11)	C(9)	C(10)	C(11)	119.26(12)
C(17)	N(3)	C(13)	117.19(12)	C(10)	C(11)	C(12)	118.59(12)
C(1)	C(2)	C(3)	113.37(13)	N(2)	C(12)	C(11)	122.54(11)
C(4)	C(3)	C(7)	116.38(12)	N(2)	C(12)	C(13)	116.57(12)
C(4)	C(3)	C(2)	122.39(14)	C(11)	C(12)	C(13)	120.89(11)
C(7)	C(3)	C(2)	121.22(12)	N(3)	C(13)	C(12)	117.05(12)
C(5)	C(4)	C(3)	120.05(14)	C(14)	C(13)	C(12)	121.02(11)
C(4)	C(5)	C(6)	119.02(12)	C(15)	C(14)	C(13)	119.73(12)
N(1)	C(6)	C(5)	121.97(12)	C(14)	C(15)	C(16)	119.48(13)
N(1)	C(6)	C(8)	116.68(12)	C(17)	C(16)	C(15)	116.47(12)
C(5)	C(6)	C(8)	121.36(11)	C(17)	C(16)	C(18)	121.87(13)
N(1)	C(7)	C(3)	125.04(12)	C(15)	C(16)	C(18)	121.66(14)
N(2)	C(8)	C(9)	122.69(11)	N(3)	C(17)	C(16)	125.17(12)
N(2)	C(8)	C(6)	116.50(11)	C(19)	C(18)	C(16)	113.02(12)
C(9)	C(8)	C(6)	120.81(11)				

Table S13 Selected least-squares planes data for ligand **L9**.

Least-squares planes

Least-squares planes description	Abbreviation	Max. deviation/Å	Atom
Pyridine 1 C(3) C(4) C(5) C(6) C(7) N(1)	Py1	0.005	C(3)
Pyridine 2 C(8) C(9) C(10) C(11) C(12) N(2)	Py2	0.011	C(9), C(12)
Pyridine 3 C(13) C(14) C(15) C(16) C(17) N(3)	Py3	0.012	C(15)

Interplanar angles (°)

	Py1	Py2	Py3
Py1		4.03(4)	20.84(5)
Py2			20.25(5)
Py3			

Table S14 Summary of crystal data, intensity measurements and structure refinements for complexes $[Er(\mathbf{L4})_2(CF_3SO_3)_2](CF_3SO_3)\cdot 2CH_3CN$ (**1**), $[Er(\mathbf{L7})_2(CF_3SO_3)_2](CF_3SO_3)\cdot 1.5C_2H_5CN$ (**2**) and $[Er(\mathbf{L8})_2(CF_3SO_3)_3]$ (**3**).

	$[Er(\mathbf{L4})_2(O_3SCF_3)_2](CF_3SO_3)$	$[Er(\mathbf{L7})_2(O_3SCF_3)_2](CF_3SO_3)$	$Er(\mathbf{L8})_2(O_3SCF_3)_3$
Empirical formula	$C_{49}H_{40}ErF_9N_{12}O_9S_3$	$C_{37.5}H_{29.5}ErF_9N_{7.5}O_9S_3$	$C_{37}H_{30}ErF_9N_6O_9S_3$
Formula weight	1375.37	1163.63	1137.11
Temperature	180(2)K	180(2)K	180(2)K
Wavelength	1.54184 Å	1.54184 Å	1.54184 Å
Crystal System, Space group	Triclinic, *P* -1	Orthorhombic, *P nnm*	Triclinic, *P* -1
Unit cell dimensions	*a* = 11.6161(3) Å *b* = 15.2976(4) Å *c* = 16.1008(4) Å α = 87.341(2)° β = 75.733(3)° γ = 72.947(3)°	*a* = 11.5807(2) Å *b* = 14.2430(3) Å *c* = 27.0122(5) Å α = 90° β = 90° γ = 90°	*a* = 11.5993(7) Å *b* = 11.7864(6) Å *c* = 15.9722(9) Å α = 87.379(5)° β = 88.132(5)° γ = 76.233(5)°
Volume in Å^3	2649.90(13)	4455.52(14)	2118.2(2)
Z, Calculated density	2, 1.724 Mg/m^3	4, 1.735 Mg/m^3	2, 1.783 Mg/m^3
Absorption coefficient	4.931 mm^{-1}	5.702 mm^{-1}	5.969 mm^{-1}
F(000)	1374	2304	1126
Theta range for data collection	3.02 to 73.68 °	3.27 to 73.51°	3.86 to 73.69 °
Limiting indices	-14<=*h*<=9, -18<=*k*<=18, -20<=*l*<=19	-12<=*h*<=13, -11<=*k*<=17, -33<=*l*<=29	-12<=*h*<=14, -13<=*k*<=14, -18<=*l*<=19
Reflections collected / unique	17866 / 10348 [*R*(int) = 0.0245]	10914 / 4476 [*R*(int) = 0.0344]	14024 / 8244 [*R*(int) = 0.0213]
Completeness to theta	67.50°/ 99.9 %	67.50°/ 99.9 %	67.50°/ 99.8 %
Data / restraints / parameters	10348 / 0 / 754	4476 / 0 / 282	8244 / 0 / 590
Goodness-of-fit on F^2	1.037	1.037	1.050
Final *R* indices [$I>2\sigma(I)$]	R_1 = 0.0277, ωR_2 = 0.0703	R_1 = 0.0378, ωR_2 = 0.0981	R_1 = 0.0264, ωR_2 = 0.0690
R indices (all data)	R_1 = 0.0318, ωR_2 = 0.0739	R_1 = 0.0430, ωR_2 = 0.1027	R_1 = 0.0274, ωR_2 = 0.0698
Largest diff. peak and hole	0.739 and -0.710 e.Å^{-3}	0.625 and -1.499 e·Å^{-3}	0.609 and -1.093 e.Å^{-3}

Table S15 Selected bond distances (Å) and bond angles (°) for complex [Er(**L4**)$_2$(O$_3$SCF$_3$)$_2$](CF$_3$SO$_3$) (**1**).

Bond distances (Å)

Atom 1	Atom 2	Distance	Atom 1	Atom 2	Distance
Er(1)	O(1)	2.285(2)	Er(1)	N(4)	2.447(2)
Er(1)	O(4)	2.329(2)	Er(1)	N(3)	2.479(2)
Er(1)	N(1)	2.414(2)	Er(1)	N(8)	2.489(2)
Er(1)	N(9)	2.446(2)	Er(1)	N(6)	2.498(2)

Angles (°)

At. 1	At. 2	At. 3	angle	At. 1	At. 2	At. 3	angle
O(1)	Er(1)	O(4)	128.62(6)	N(4)	Er(1)	N(3)	65.62(6)
O(1)	Er(1)	N(1)	75.41(6)	O(1)	Er(1)	N(8)	76.23(6)
O(4)	Er(1)	N(1)	77.24(6)	O(4)	Er(1)	N(8)	128.69(6)
O(1)	Er(1)	N(9)	76.64(7)	N(1)	Er(1)	N(8)	150.30(6)
O(4)	Er(1)	N(9)	77.12(6)	N(9)	Er(1)	N(8)	65.64(6)
N(1)	Er(1)	N(9)	115.37(6)	N(4)	Er(1)	N(8)	75.53(6)
O(1)	Er(1)	N(4)	149.58(6)	N(3)	Er(1)	N(8)	127.96(6)
O(4)	Er(1)	N(4)	78.93(8)	O(1)	Er(1)	N(6)	80.41(6)
N(1)	Er(1)	N(4)	129.54(6)	O(4)	Er(1)	N(6)	147.93(6)
N(9)	Er(1)	N(4)	101.50(7)	N(1)	Er(1)	N(6)	101.63(6)
O(1)	Er(1)	N(3)	127.01(6)	N(9)	Er(1)	N(6)	128.97(6)
O(4)	Er(1)	N(3)	76.77(6)	N(4)	Er(1)	N(6)	77.59(6)
N(1)	Er(1)	N(3)	65.94(6)	N(3)	Er(1)	N(6)	73.78(6)
N(9)	Er(1)	N(3)	152.70(6)	N(8)	Er(1)	N(6)	64.89(6)

Table S16 Selected least-squares planes data for complex $[Er(\mathbf{L4})_2(O_3SCF_3)_2](CF_3SO_3)$ (**1**).

Least-squares planes

Least-squares planes description	Abbreviation	Max. deviation/Å	Atom
Pyridine 1 N(3) C(9) C(10) C(11) C(12) C(13)	Py1	0.027	C(9)
Benzimidazole 1 C(1) C(2) C(3) C(4) C(5) C(6) N(1) C(8) N(2)	Bz1	0.018	C(3), C(1)
Benzimidazole 2 C(16) C(17) C(18) C(19) C(20) C(21) N(4) C(14) N(5)	Bz2	0.030	C(14)
Pyridine 2 N(8) C(30) C(31) C(32) C(33) C(34)	Py2	0.015	C(34)
Benzimidazole 3 C(22) C(23) C(24) C(25) C(26) C(27) N(6) C(29) N(7)	Bz3	0.042	N(6)
Benzimidazole 4 C(37) C(38) C(39) C(40) C(41) C(42) N(9) C(35) N(10)	Bz4	0.020	N(10)

Interplanar angles (°)

	Py1	Bz1	Bz2	Py2	Bz3	Bz4
Py1		16.143(1)	16.86(1)	43.991(1)	28.487(1)	44.020(1)
Bz1			25.715(1)	35.595(1)	30.941(1)	29.623(1)
Bz2				35.744(1)	13.590(1)	43.873(1)
Py2					24.645(1)	19.579(1)
Bz3						37.907(1)
Bz4						

Table S17 Selected bond distances (Å), bond angles (°) for complex [Er(**L7**)$_2$(O$_3$SCF$_3$)$_2$](CF$_3$SO$_3$) (**2**).

Bond distances (Å)

Atom 1	Atom 2	Distance	Atom 1	Atom 2	Distance
Er(1)	O(1)	2.264(2)	Er(1)	N(3)#1	2.479(3)
Er(1)	O(1)#1	2.264(2)	Er(1)	N(3)	2.479(3)
Er(1)	N(2)#1	2.476(2)	Er(1)	N(1)	2.519(3)
Er(1)	N(2)	2.476(2)	Er(1)	N(1)#1	2.519(3)

Symmetry operation (#1) -x,-y+1,z

Angles (°)

At. 1	At. 2	At. 3	Angle	At. 1	At. 2	At. 3	Angle
O(1)	Er(1)	O(1)#1	105.76(12)	N(3)#1	Er(1)	N(3)	92.10(12)
O(1)	Er(1)	N(2)#1	135.03(9)	O(1)	Er(1)	N(1)	76.22(9)
O(1)#1	Er(1)	N(2)#1	83.97(8)	O(1)#1	Er(1)	N(1)	75.03(9)
O(1)	Er(1)	N(2)	83.97(8)	N(2)#1	Er(1)	N(1)	146.89(9)
O(1)#1	Er(1)	N(2)	135.04(8)	N(2)	Er(1)	N(1)	64.73(8)
N(2)#1	Er(1)	N(2)	120.12(11)	N(3)#1	Er(1)	N(1)	87.68(9)
O(1)	Er(1)	N(3)#1	157.06(8)	N(3)	Er(1)	N(1)	127.71(8)
O(1)#1	Er(1)	N(3)#1	85.22(9)	O(1)	Er(1)	N(1)#1	75.03(9)
N(2)#1	Er(1)	N(3)#1	65.00(8)	O(1)#1	Er(1)	N(1)#1	76.22(9)
N(2)	Er(1)	N(3)#1	74.33(8)	N(2)#1	Er(1)	N(1)#1	64.73(8)
O(1)	Er(1)	N(3)	85.22(9)	N(2)	Er(1)	N(1)#1	146.89(9)
O(1)#1	Er(1)	N(3)	157.06(8)	N(3)#1	Er(1)	N(1)#1	127.71(8)
N(2)#1	Er(1)	N(3)	74.33(8)	N(3)	Er(1)	N(1)#1	87.68(9)
N(2)	Er(1)	N(3)	65.00(8)	N(1)	Er(1)	N(1)#1	131.41(12)

Table S18 Selected least-squares planes data for complex [Er(**L7**)$_2$(O$_3$SCF$_3$)$_2$](CF$_3$SO$_3$) (**2**).

Least-squares planes

Least-squares planes description	Abbreviation	Max. deviation/Å	Atom
Pyridine 1	Py1		
N(1) C(1) C(2) C(3) C(4) C(5)		0.004	N(1), C(3)
Pyridine 2	Py2		
N(2) C(6) C(7) C(8) C(9) C(10)		0.032	N(2)
Pyridine 3	Py3		
N(3) C(11) C(12) C(13) C(14) C(15)		0.009	N(3)
Pyridine 1#1	Py1#1		
N(1)#1 C(1)#1 C(2)#1 C(3)#1 C(4)#1 C(5)#1		0.004	N(1), C(3)
Pyridine 2#1	Py2#1		
N(2)#1 C(6)#1 C(7)#1 C(8)#1 C(9)#1 C(10)#1		0.032	N(2)
Pyridine 3#1	Py3#1		
N(3)#1 C(11)#1 C(12)# C(13)#1 C(14)#1 C(15)#1		0.009	N(3)

Interplanar angles (°)

	Py1	Py2	Py3	Py1#1	Py2#1	Py3#1
Py1		21.29(11)	31.24(11)	44.52(15)	48.07(12)	65.87(11)
Py2			17.81(11)	48.07(12)	40.72(16)	57.16(11)
Py3				65.87(11)	57.16(11)	72.16(17)
Py1#1					21.29(11)	31.24(11)
Py2#1						17.81(11)
Py3#1						

Table S19 Selected bond distances (Å), bond angles (°) for complex Er(**L8**)$_2$(O_3SCF_3)$_3$ (**3**)

Bond distances (Å)

Atom 1	Atom 2	Distance	Atom 1	Atom 2	Distance
Er(1)	O(1)	2.3333(17)	Er(1)	N(5)	2.5272(19)
Er(1)	O(7)	2.3458(17)	Er(1)	N(2)	2.5395(19)
Er(1)	O(4)	2.4254(16)	Er(1)	N(4)	2.552(2)
Er(1)	N(6)	2.496(2)	Er(1)	N(3)	2.554(2)
Er(1)	N(1)	2.500(2)			

Angles (°)

At. 1	At. 2	At. 3	Angle	At. 1	At. 2	At. 3	Angle
O(1)	Er(1)	O(7)	144.50(6)	N(6)	Er(1)	N(2)	137.00(6)
O(1)	Er(1)	O(4)	73.73(6)	N(1)	Er(1)	N(2)	64.27(6)
O(7)	Er(1)	O(4)	70.93(6)	N(5)	Er(1)	N(2)	118.72(6)
O(1)	Er(1)	N(6)	93.01(7)	O(1)	Er(1)	N(4)	72.11(6)
O(7)	Er(1)	N(6)	79.27(6)	O(7)	Er(1)	N(4)	138.47(6)
O(4)	Er(1)	N(6)	71.73(6)	O(4)	Er(1)	N(4)	140.64(6)
O(1)	Er(1)	N(1)	77.79(6)	N(6)	Er(1)	N(4)	128.72(7)
O(7)	Er(1)	N(1)	88.72(6)	N(1)	Er(1)	N(4)	81.12(6)
O(4)	Er(1)	N(1)	73.04(6)	N(5)	Er(1)	N(4)	64.51(6)
N(6)	Er(1)	N(1)	144.76(6)	N(2)	Er(1)	N(4)	70.35(6)
O(1)	Er(1)	N(5)	70.98(6)	O(1)	Er(1)	N(3)	140.43(6)
O(7)	Er(1)	N(5)	131.87(6)	O(7)	Er(1)	N(3)	72.62(6)
O(4)	Er(1)	N(5)	120.58(6)	O(4)	Er(1)	N(3)	136.81(6)
N(6)	Er(1)	N(5)	64.24(6)	N(6)	Er(1)	N(3)	79.46(6)
N(1)	Er(1)	N(5)	138.94(6)	N(1)	Er(1)	N(3)	128.37(7)
O(1)	Er(1)	N(2)	129.57(6)	N(5)	Er(1)	N(3)	70.81(6)
O(7)	Er(1)	N(2)	68.98(6)	N(2)	Er(1)	N(3)	64.10(7)
O(4)	Er(1)	N(2)	120.66(6)	N(4)	Er(1)	N(3)	82.55(6)

Table S20 Selected least-squares planes data for complex Er(**L8**)$_2$(O_3SCF_3)$_3$ (**3**).

Least-squares planes

Least-squares planes description	Abbreviation	Max. deviation/Å	Atom
Pyridine 1	Py1		
N(1) C(1) C(2) C(3) C(4) C(5)		0.012	C(3)
Pyridine 2	Py2		
N(2) C(6) C(7) C(8) C(9) C(1AA)		0.007	C(6)
Pyridine 3	Py3		
N(3) C(10) C(11) C(12) C(13) C(14)		0.019	N(3), C(10)
Pyridine 4	Py4		
N(4) C(17) C(18) C(19) C(20) C(21)		0.036	N(4)
Pyridine 5	Py5		
N(5) C(22) C(23) C(24) C(25) C(26)		0.020	N(5)
Pyridine 6	Py6		
N(6) C(27) C(28) C(29) C(30) C(31)		0.012	N(6)

Interplanar angles (°)

	Py1	Py2	Py3	Py4	Py5	Py6
Py1		7.31(8)	18.20(9)	115.61(9)	100.01(8)	90.49(8)
Py2			10.89(9)	120.61(8)	103.39(8)	95.23(8)
Py3				127.31(9)	107.90(9)	102.03(9)
Py4					22.03(8)	25.42(9)
Py5						15.54(9)
Py6						

Table S21 Summary of crystal data, intensity measurements and structure refinements for complexes [Er(**L6**)$_3$](ClO$_4$)$_3$·2CH$_3$CN (**4**), [Er(**L7**)$_3$](ClO$_4$)$_3$ (**5**), [Er(**L8**)$_3$](ClO$_4$)$_3$ (**6**) and [Er(**L9**)$_3$](ClO$_4$)$_3$·1.5CH$_3$CN (**7**).

	[Er(**L6**)$_3$](ClO$_4$)$_3$	[Er(**L7**)$_3$](ClO$_4$)$_3$	[Er(**L8**)$_3$](ClO$_4$)$_3$	[Er(**L9**)$_3$](ClO$_4$)$_3$
Empirical formula	$C_{79}H_{81}Cl_3ErN_{17}O_{12}$	$C_{45}H_{33}Cl_3ErN_9O_{12}$	$C_{102}H_{90}C_{l6}Er_2N_{18}O_{24}$	$C_{60}H_{61.5}Cl_3ErN_{10.5}O_{12}$
Formula weight	1734.21	1165.41	2499.14	1395.31
Temperature	180(2)K	180(2)K	180(2) K	180(2)K
Wavelength	1.54184 Å	1.54184 Å	1.54184 Å	1.54184 Å
Crystal System, Space group	Orthorhombic, *P bcm*	Monoclinic, *C* 2/*c*	Monoclinic, *P* 2/*c*	Hexagonal, *P* 6$_3$
Unit cell dimensions	*a* = 15.00938(15) Å *b* = 18.4400(2) Å *c* = 29.3855(4) Å α = 90° β = 90° γ = 90°	*a* = 17.5447(4) Å *b* = 20.7433(5) Å *c* = 12.2263(3) Å α = 90° β = 94.638(2)° γ = 90°	*a* = 22.8203(3) Å *b* = 12.70104(15) Å *c* = 18.9988(3) Å α = 90° β = 110.6651(16)° γ = 90°	*a* = 12.77903(19) Å *b* = 12.77903 (19) Å *c* = 24.2818(4) Å α = 90° β = 90° γ = 120°
Volume in Å^3	8133.11(17)	4435.00(19)	5152.35(12)	3434.05(9)
Z, Calculated density	4, 1.416 Mg/m^3	4, 1.745 Mg/m^3	2, 1.611 Mg/m^3	2, 1.349 Mg/m^3
Absorption coefficient	3.402 mm^{-1}	5.835 mm^{-1}	5.065 mm^{-1}	3.862 mm^{-1}
F(000)	3556	2324	2516	1420
Theta range for data collection	3.80 to 73.30 °	3.31 to 73.57 °	4.05 to 73.35°	3.99 to 73.37 °
Limiting indices	-18<=*h*<=18, -22<=*k*<=22, -35<=*l*<=36	-21<=*h*<=17, -24<=*k*<=25, -13<=*l*<=14	-22<=*h*<=28, -14<=*k*<=15, -23<=*l*<=22	-11<=*h*<=15, -15<=*k*<=15, -24<=*l*<=29
Reflections collected / unique	20324 / 8154 [*R*(int) = 0.0317]	8622 / 4340 [*R*(int) = 0.0244]	20072 / 10096 [*R*(int) = 0.0309]	8289 / 3926 [*R*(int) = 0.0293]
Completeness to theta	67.50°/ 99.9 %	67.50°/ 99.9 %	67.50°/ 99.9 %	67.50°/ 100.0%
Data / restraints / parameters	8154 / 10 / 531	4340 / 0 / 318	10096 / 0 / 708	3926 / 8 / 287
Goodness-of-fit on F^2	1.076	1.042	1.010	1.224
Final *R* indices [$I>2\sigma(I)$]	R_1 = 0.0630, ωR_2 = 0.1651	R_1 = 0.0353, ωR_2 = 0.0934	R_1 = 0.0375, ωR_2 = 0.0969	R_1 = 0.0506, ωR_2 = 0.1495
R indices (all data)	R_1 = 0.0796, ωR_2 = 0.1778	R_1 = 0.0362, ωR_2 = 0.0944	R_1 = 0.0416, ωR_2 = 0.1009	R_1 = 0.0519, ωR_2 = 0.1513
Largest diff. peak and hole	0.925 and -0.925 e.Å^{-3}	1.184 and -1.900 e.Å^{-3}	1.049 and -1.855 e.Å^{-3}	0.700 and -0.742 e.Å^{-3}

Table S22 Selected bond distances (Å) and bond angles (°) for complex $[Er(\mathbf{L6})_3](ClO_4)_3$ (**4**).

Bond distances (Å)

Atom 1	Atom 2	Distance	Atom 1	Atom 2	Distance
Er(1)	N(4)	2.476(5)	Er(1)	N(5)	2.547(4)
Er(1)	N(2)#1	2.482(4)	Er(1)	N(5)#1	2.547(4)
Er(1)	N(2)	2.482(4)	Er(1)	N(7)#1	2.606(4)
Er(1)	N(1)	2.489(4)	Er(1)	N(7)	2.606(4)
Er(1)	N(1)#1	2.489(4)			

Symmetry operation (#1) x,-y+1/2,-z+1

Angles (°)

At. 1	At. 2	At. 3	angle	At. 1	At. 2	At. 3	angle
N(4)	Er(1)	N(2)#1	73.69(8)	N(1)	Er(1)	N(5)#1	74.62(13)
N(4)	Er(1)	N(2)	73.69(8)	N(1)#1	Er(1)	N(5)#1	142.95(13)
N(2)#1	Er(1)	N(2)	147.37(17)	N(5)	Er(1)	N(5)#1	129.07(18)
N(4)	Er(1)	N(1)	128.29(9)	N(4)	Er(1)	N(7)#1	132.24(9)
N(2)#1	Er(1)	N(1)	139.15(13)	N(2)#1	Er(1)	N(7)#1	76.66(12)
N(2)	Er(1)	N(1)	65.90(13)	N(2)	Er(1)	N(7)#1	127.47(13)
N(4)	Er(1)	N(1)#1	128.29(9)	N(1)	Er(1)	N(7)#1	63.34(13)
N(2)#1	Er(1)	N(1)#1	65.90(13)	N(1)#1	Er(1)	N(7)#1	67.40(13)
N(2)	Er(1)	N(1)#1	139.15(13)	N(5)	Er(1)	N(7)#1	139.29(12)
N(1)	Er(1)	N(1)#1	103.42(18)	N(5)#1	Er(1)	N(7)#1	79.63(12)
N(4)	Er(1)	N(5)	64.54(9)	N(4)	Er(1)	N(7)	132.23(9)
N(2)#1	Er(1)	N(5)	74.93(13)	N(2)#1	Er(1)	N(7)	127.48(13)
N(2)	Er(1)	N(5)	91.06(13)	N(2)	Er(1)	N(7)	76.66(12)
N(1)	Er(1)	N(5)	142.95(13)	N(1)	Er(1)	N(7)	67.40(13)
N(1)#1	Er(1)	N(5)	74.61(13)	N(1)#1	Er(1)	N(7)	63.34(13)
N(4)	Er(1)	N(5)#1	64.53(9)	N(5)	Er(1)	N(7)	79.63(12)
N(2)#1	Er(1)	N(5)#1	91.06(13)	N(5)#1	Er(1)	N(7)	139.29(12)
N(2)	Er(1)	N(5)#1	74.93(13)	N(7)#1	Er(1)	N(7)	95.53(19)

Table S23 Selected least-squares planes data for complex $[Er(\mathbf{L6})_3](ClO_4)_3$ (**4**).

Least-squares planes

Least-squares planes description	Abbreviation	Max. deviation/Å	Atom
Pyridine 1 N(1) C(2) C(3) C(26) C(27) C(28)	Py1	0.016	C(2)
Benzimidazole 1 C(5) C(6) C(7) C(8) C(9) C(10) N(2) C(1) N(3)	Bz1	0.027	N(2)
Benzimidazole 3#1 C(31)#1 C(32)#1 C(33)#1 C(34)#1 C(35)#1 C(36)#1 N(7)#1 C(36)#1 N(8)#1	Bz3#1	0.055	N(7)#1
Pyridine 2 N(4) C(13) C(14) C(15) C(14)#1 C(15)#1	Py2	0.005	C(14) C(15) C(14)#1 C(15)#1
Benzimidazole 2 C(18) C(19) C(20) C(21) C(22) C(23) N(5) C(16) N(6)	Bz2	0.043	C(16)
Benzimidazole 2#1 C(18)#1 C(19)#1 C(20)#1 C(21)#1 C(22)#1 C(23)#1 N(5)#1 C(16)#1 N(6)#1	Bz2#1	0.043	C(16)
Pyridine 1#1 N(1)#1 C(2)#1 C(3)#1 C(26)#1 C(27)#1 C(28)#1	Py1#1	0.016	C(2)#1
Benzimidazole 3 C(31) C(32) C(33) C(34) C(35) C(36) N(7) C(36) N(8)	Bz3	0.055	N(7)
Benzimidazole 1#1 C(5)#1 C(6)#1 C(7)#1 C(8)#1 C(9)# C(10)#1 N(2)#1 C(1)#1 N(3)#1	Bz1#1	0.027	N(2)
F1 N(2), N(5), N(7)	F1		
F2 N(1), N(1)#1, N(4)	F2		
F3 N(2)#1, N(5)#1, N(7)#1	F3		

Interplanar angles (°)

	Py1	Bz1	Bz3#1	Py2	Bz2	Bz2#1	Py1#1	Bz3	Bz1#1	F1	F2	F3
Py1		23.03(16)	22.94(16)	56.8(2)	65.63(18)	43.8(2)	39.4(3)	21.37(17)	55.13(16)			
Bz1			44.48(12)	43.51(15)	63.25(13)	22.02(18)	55.13(16)	43.22(12)	62.24(12)			
Bz3#1				64.7(2)	61.14(14)	62.02(14)	21.37(17)	1.7(2)	43.22(12)			
Py2					28.31(15)	28.31(15)	56.8(2)	64.7(2)	43.51(15)			
Bz2						54.9(3)	43.8(2)	62.02(14)	22.02(18)			
Bz2#1							65.63(18)	61.14(14)	63.25(13)			
Py1#1								22.87(17)	23.10(16)			
Bz3									44.48(12)			
Bz1#1												
F1											8.8(1)	17.4(2)
F2												8.8(1)
F3												

Table S24 Selected bond distances (Å) and bond angles (°) for complex $[Er(\mathbf{L7})_3](ClO_4)_3$ (**5**).

Bond distances (Å)

Atom 1	Atom 2	Distance	Atom 1	Atom 2	Distance
Er(1)	N(5)	2.460(3)	Er(1)	N(4)#1	2.521(2)
Er(1)	N(3)#1	2.516(2)	Er(1)	N(4)	2.521(2)
Er(1)	N(3)	2.516(2)	Er(1)	N(1)#1	2.555(2)
Er(1)	N(2)	2.516(2)	Er(1)	N(1)	2.555(2)
Er(1)	N(2)#1	2.516(2)			

Symmetry operation (#1) -x+1,y,-z+3/2.

Angles (°)

At. 1	At. 2	At. 3	Angle	At. 1	At. 2	At. 3	Angle
N(5)	Er(1)	N(3)#1	138.39(5)	N(2)	Er(1)	N(4)	136.94(8)
N(5)	Er(1)	N(3)	138.39(6)	N(2)#1	Er(1)	N(4)	72.00(8)
N(3)#1	Er(1)	N(3)	83.23(11)	N(4)#1	Er(1)	N(4)	130.32(12)
N(5)	Er(1)	N(2)	120.12(6)	N(5)	Er(1)	N(1)#1	71.01(5)
N(3)#1	Er(1)	N(2)	71.42(8)	N(3)#1	Er(1)	N(1)#1	127.86(8)
N(3)	Er(1)	N(2)	64.42(8)	N(3)	Er(1)	N(1)#1	82.69(8)
N(5)	Er(1)	N(2)#1	120.12(5)	N(2)	Er(1)	N(1)#1	140.62(8)
N(3)#1	Er(1)	N(2)#1	64.42(8)	N(2)#1	Er(1)	N(1)#1	63.49(8)
N(3)	Er(1)	N(2)#1	71.42(8)	N(4)#1	Er(1)	N(1)#1	81.85(8)
N(2)	Er(1)	N(2)#1	119.76(11)	N(4)	Er(1)	N(1)#1	82.44(8)
N(5)	Er(1)	N(4)#1	65.16(6)	N(5)	Er(1)	N(1)	71.01(5)
N(3)#1	Er(1)	N(4)#1	143.39(8)	N(3)#1	Er(1)	N(1)	82.69(8)
N(3)	Er(1)	N(4)#1	79.94(8)	N(3)	Er(1)	N(1)	127.86(8)
N(2)	Er(1)	N(4)#1	72.00(8)	N(2)	Er(1)	N(1)	63.49(8)
N(2)#1	Er(1)	N(4)#1	136.94(8)	N(2)#1	Er(1)	N(1)	140.62(8)
N(5)	Er(1)	N(4)	65.16(6)	N(4)#1	Er(1)	N(1)	82.43(8)
N(3)#1	Er(1)	N(4)	79.94(8)	N(4)	Er(1)	N(1)	81.85(8)
N(3)	Er(1)	N(4)	143.39(8)	N(1)#1	Er(1)	N(1)	142.02(11)

Table S25 Selected least-squares planes data for complex $[Er(\mathbf{L7})_3](ClO_4)_3$ (**5**).

	Least-squares planes		
Least-squares planes description	Abbreviation	Max. deviation/Å	Atom
Pyridine 1 N(1) C(1) C(2) C(3) C(4) C(5)	Py1	0.021	N(1)
Pyridine 2 N(2) C(6) C(7) C(8) C(9) C(10)	Py2	0.010	N(2)
Pyridine 3 N(3) C(11) C(12) C(13) C(14) C(15)	Py3	0.049	C(11)
Pyridine 4 N(4) C(16) C(17) C(18) C(19) C(20)	Py4	0.024	C(20)
Pyridine 5 N(5) C(21) C(22) C(23) C(22)#1 C(23)#1	Py5	0.009	C(21), C(22), C(21)#1, C(22)#1
Pyridine 4#1 N(4)#1 C(16)#1 C(17)#1 C(18)#1 C(19)#1 C(20)#1	Py4#1	0.024	C(20)#1
Pyridine 1#1 N(1)#1 C(1)#1 C(2)#1 C(3)#1 C(4)#1 C(5)#1	Py1#1	0.021	N(1)#1
Pyridine 2#1 N(2)#1 C(6)#1 C(7)#1 C(8)#1 C(9)#1 C(10)#1	Py2#1	0.010	N(2)#1
Pyridine 3#1 N(3)#1 C(11)#1 C(12)#1 C(13) #1 C(14)#1 C(15)#1	Py3#1	0.049	C(11)#1
F1 N(1)#1, N(3), N(4)	F1		
F2 N(2), (2)#1, N(5)	F2		
F3 N(1), N(3)#1, N(4)	F3		

Interplanar angles (°)

	Py1	Py2	Py3	Py4	Py5	Py4#1	Py1#1	Py2#1	Py3#1	F1	F2	F3
Py1		11.49(11)	38.30(11)	67.23(11)	51.70(10)	40.04(11)	74.85(15)	69.83(11)	60.57(11)			
Py2			26.82(10)	70.48(11)	57.29(11)	48.73(10)	69.83(11)	63.01(14)	50.19(10)			
Py3				79.98(11)	73.34(13)	71.07(11)	60.57(11)	50.19(10)	27.94(14)			
Py4					18.20(90)	36.29(17)	40.04(11)	48.73(10)	71.07(11)			
Py5						18.20(90)	51.70(10)	57.29(11)	73.34(13)			
Py4#1							67.23(11)	70.48(11)	79.98(11)			
Py1#1								11.49(11)	38.30(11)			
Py2#1									26.82(10)			
Py3#1												
F1											1.80(8)	0.4(1)
F2												1.80(8)
F3												

Table S26 Selected bond distances (Å) and bond angles (°) for complex [Er(**L8**)$_3$](ClO$_4$)$_3$ (**6**).

Bond distances (Å)

Atom 1	Atom 2	Distance	Atom 1	Atom 2	Distance
Er(1)	N(2)	2.505(2)	Er(2)	N(7)	2.453(2)
Er(1)	N(2)#1	2.505(2)	Er(2)	N(7)#2	2.453(2)
Er(1)	N(4)	2.523(3)	Er(2)	N(9)	2.491(3)
Er(1)	N(1)	2.525(2)	Er(2)	N(6)	2.525(2)
Er(1)	N(1)#1	2.525(2)	Er(2)	N(6)#2	2.525(2)
Er(1)	N(3)	2.532(2)	Er(2)	N(10)	2.532(2)
Er(1)	N(3)#1	2.532(2)	Er(2)	N(10)#2	2.532(2)
Er(1)	N(5)	2.554(2)	Er(2)	N(8)	2.544(2)
Er(1)	N(5)#1	2.554(2)	Er(2)	N(8)#2	2.544(2)

Symmetry operation (#1) -x+1,y,-z+3/2 (#2) -x,y,-z+1/2.

Angles (°)

At. 1	At. 2	At. 3	Angle	At. 1	At. 2	At. 3	Angle
N(2)	Er(1)	N(2)#1	119.48(10)	N(7)#2	Er(2)	N(7)	123.34(11)
N(2)	Er(1)	N(4)	120.26(5)	N(7)#2	Er(2)	N(9)	118.33(6)
N(2)#1	Er(1)	N(4)	120.26(5)	N(7)	Er(2)	N(9)	118.33(6)
N(2)	Er(1)	N(1)#1	138.42(7)	N(7)#2	Er(2)	N(6)	137.11(8)
N(2)#1	Er(1)	N(1)#1	64.30(7)	N(7)	Er(2)	N(6)	65.29(8)
N(4)	Er(1)	N(1)#1	71.83(5)	N(9)	Er(2)	N(6)	70.64(6)
N(2)	Er(1)	N(1)	64.30(7)	N(7)#2	Er(2)	N(6)#2	65.29(8)
N(2)#1	Er(1)	N(1)	138.42(7)	N(7)	Er(2)	N(6)#2	137.11(8)
N(4)	Er(1)	N(1)	71.83(5)	N(9)	Er(2)	N(6)#2	70.64(6)
N(1)#1	Er(1)	N(1)	143.66(10)	N(6)	Er(2)	N(6)#2	141.28(11)
N(2)	Er(1)	N(3)	64.50(7)	N(7)#2	Er(2)	N(10)	70.20(7)
N(2)#1	Er(1)	N(3)	71.26(7)	N(7)	Er(2)	N(10)	138.17(8)
N(4)	Er(1)	N(3)	138.24(5)	N(9)	Er(2)	N(10)	64.64(5)
N(1)#1	Er(1)	N(3)	80.71(7)	N(6)	Er(2)	N(10)	79.07(7)
N(1)	Er(1)	N(3)	128.80(7)	N(6)#2	Er(2)	N(10)	84.58(7)
N(2)	Er(1)	N(3)#1	71.26(7)	N(7)#2	Er(2)	N(10)#2	138.17(8)
N(2)#1	Er(1)	N(3)#1	64.50(7)	N(7)	Er(2)	N(10)#2	70.21(7)
N(4)	Er(1)	N(3)#1	138.24(5)	N(9)	Er(2)	N(10)#2	64.64(5)
N(1)#1	Er(1)	N(3)#1	128.80(7)	N(6)	Er(2)	N(10)#2	84.59(7)
N(1)	Er(1)	N(3)#1	80.71(7)	N(6)#2	Er(2)	N(10)#2	79.07(7)
N(3)	Er(1)	N(3)#1	83.53(10)	N(10)	Er(2)	N(10)#2	129.28(10)
N(2)	Er(1)	N(5)#1	70.83(7)	N(7)#2	Er(2)	N(8)#2	64.88(8)
N(2)#1	Er(1)	N(5)#1	141.60(7)	N(7)	Er(2)	N(8)#2	71.85(8)
N(4)	Er(1)	N(5)#1	63.14(5)	N(9)	Er(2)	N(8)#2	140.86(5)
N(1)#1	Er(1)	N(5)#1	83.81(7)	N(6)	Er(2)	N(8)#2	82.64(8)
N(1)	Er(1)	N(5)#1	79.98(7)	N(6)#2	Er(2)	N(8)#2	129.97(8)
N(3)	Er(1)	N(5)#1	83.50(7)	N(10)	Er(2)	N(8)#2	82.95(7)
N(3)#1	Er(1)	N(5)#1	141.93(7)	N(10)#2	Er(2)	N(8)#2	141.92(7)
N(2)	Er(1)	N(5)	141.60(7)	N(7)#2	Er(2)	N(8)	71.85(8)
N(2)#1	Er(1)	N(5)	70.83(7)	N(7)	Er(2)	N(8)	64.88(8)
N(4)	Er(1)	N(5)	63.14(5)	N(9)	Er(2)	N(8)	140.86(5)
N(1)#1	Er(1)	N(5)	79.98(7)	N(6)	Er(2)	N(8)	129.97(8)
N(1)	Er(1)	N(5)	83.81(7)	N(6)#2	Er(2)	N(8)	82.64(8)
N(3)	Er(1)	N(5)	141.93(7)	N(10)	Er(2)	N(8)	141.91(7)
N(3)#1	Er(1)	N(5)	83.50(7)	N(10)#2	Er(2)	N(8)	82.95(7)
N(5)#1	Er(1)	N(5)	126.28(10)	N(8)#2	Er(2)	N(8)	78.28(11)

Table S27 Selected least-squares planes data for complex $[Er(\mathbf{L8})_3](ClO_4)_3$ (**6**).[a]

Least-squares planes

Least-squares planes description	Abbreviation	Max. deviation/Å	Atom
Pyridine 1 N(1) C(1) C(2) C(4) C(5) C(6)	Py1	0.027	C(6)
Pyridine 2 N(2) C(7) C(8) C(9) C(10) C(11)	Py2	0.009	C(8)
Pyridine 3 N(3) C(12) C(13) C(14) C(15) C(17)	Py3	0.030	N(3)
Pyridine 4 N(5) C(18) C(19) C(21) C(22) C(23)	Py4	0.027	N(5)
Pyridine 5 N(4) C(24) C(25) C(26) C(25)#1 C(24)#1	Py5	0.024	C(24), C(25), C(24)#1, C(25)#1
Pyridine 4#1 N(5)#1 C(18)#1 C(19)#1 C(21)#1 C(22)#1 C(23)#1	Py4#1	0.027	N(5)#1
Pyridine 1#1 N(1)#1 C(1)#1 C(2)#1 C(4)#1 C(5)#1 C(6)#1	Py1#1	0.027	C(6)#1
Pyridine 2#1 N(2)#1 C(7)#1 C(8)#1 C(9)#1 C(10)#1 C(11)#1	Py2#1	0.009	C(8)#1
Pyridine 3#1 N(3)#1 C(12)#1 C(13)#1 C(14)#1 C(15)#1 C(17)#1	Py3#1	0.030	N(3)#1
F1(Er1) N(1)#1, N(3), N(5)#1	F1(Er1)		
F2(Er1) N(2), N(2)#1, N(4)	F2(Er1)		
F3(Er1) N(1), N(3)#1, N(5)	F3(Er1)		

Least-squares planes

Least-squares planes description	Abbreviation	Max. deviation/Å	Atom
Pyridine 6 N(6) C(27) C(28) C(30) C(31) C(32)	Py6	0.042	N(6)
Pyridine 7 N(7) C(33) C(34) C(35) C(36) C(37)	Py7	0.008	C(36)
Pyridine 8 N(8) C(38) C(39) C(40) C(41) C(43)	Py8	0.020	N(8)
Pyridine 9 N(10) C(44) C(45) C(47) C(48) C(49)	Py9	0.023	N(10)
Pyridine 10 N(9) C(50) C(51) C(52) C(51)#2 C(52)#2	Py10	0.006	C(50), C(51), C(50)#2, C(51)#2
Pyridine 9#2 N(10)#2 C(44)#2 C(45)#2 C(47)#2 C(48)#2 C(49)#2	Py9#2	0.023	N(10)#2
Pyridine 6#2 N(6)#2 C(27)#2 C(28)#2 C(30)#2 C(31)#2 C(32)#2	Py6#2	0.042	N(6)#2
Pyridine 7#2 N(7)#2 C(33)#2 C(34)#2 C(35)#2 C(36)#2 C(37)#2	Py7#2	0.007	C(36)#2
Pyridine 8#2 N(8)#2 C(38)#2 C(39)#2 C(40)#2 C(41)#2 C(43)#2	Py8#2	0.020	N(8)#2
F1(Er2) N(6), N(8)#2, N(10)	F1(Er2)		
F2(Er2) N(7), N(7)#2, N(9)	F2(Er2)		
F3(Er2) N(6)#2, N(8), N(10)#2	F3(Er2)		

[a] The asymmetric unit in the crystal structure of 6 contains two slightly different cations of $[Er(\mathbf{L8})_3]^{3+}$.

Interplanar angles (°)[a]

	Py1	Py2	Py3	Py4	Py5	Py4#1	Py1#1	Py2#1	Py3#1	F1(Er1)	F2(Er1)	F3(Er1)
Py1		13.7(1)	34.5(1)	69.0(1)	50.4(8)	29.8(1)	83.3(1)	75.5(1)	62.4(1)			
Py2			20.8(1)	67.7(1)	53.3(1)	37.2(1)	75.5(1)	65.8(1)	50.5(1)			
Py3				65.5(1)	59.5(1)	51.3(1)	62.7(1)	50.5(1)	32.0(2)			
Py4					22.9(7)	45.1(1)	29.8(1)	37.2(1)	51.3(1)			
Py5						22.9(7)	50.4(8)	50.3(1)	59.5(1)			
Py4#1							69.0(1)	67.7(1)	65.5(1)			
Py1#1								13.7(1)	34.5(1)			
Py2#1									20.8(1)			
Py3#1												
F1(Er1)											1.84(6)	2.49(9)
F2(Er1)												1.84(6)
F3(Er1)												

	Py6	Py7	Py8	Py9	Py10	Py9#2	Py6#2	Py7#2	Py8#2	F1(Er2)	F2(Er2)	F3(Er2)
Py6		27.4(1)	46.0(1)	48.7(1)	33.8(9)	19.5(1)	58.2(1)	65.2(1)	64.2(1)			
Py7			20.2(1)	65.1(1)	55.2(1)	45.5(1)	65.2(1)	57.5(2)	64.2(1)			
Py8				71.4(1)	66.7(1)	61.7(1)	64.2(1)	47.0(1)	31.0(2)			
Py9					16.9(7)	33.8(1)	19.5(1)	45.5(1)	61.7(1)			
Py10						16.9(7)	33.8(9)	55.2(1)	66.7(1)			
Py9#2							48.7(1)	65.1(1)	71.4(1)			
Py6#2								27.4(1)	46.0(1)			
Py7#2									20.2(1)			
Py8#2												
F1(Er2)											2.08(8)	3.7(1)
F2(Er2)												2.08(8)
F3(Er2)												

[a] The asymmetric unit in the crystal structure of 6 contains two slightly different cations of $[Er(\mathbf{L8})_3]^{3+}$.

Table S28 Selected bond distances (Å) and bond angles (°) for complex $[Er(\mathbf{L9})_3](ClO_4)_3$ (**7**).

Bond distances (Å)

Atom 1	Atom 2	Distance	Atom 1	Atom 2	Distance
Er(1)	N(2)#1	2.488(5)	Er(1)	N(1)	2.529(7)
Er(1)	N(2)#2	2.488(5)	Er(1)	N(3)#1	2.543(6)
Er(1)	N(2)	2.488(5)	Er(1)	N(3)#2	2.543(6)
Er(1)	N(1)#1	2.529(7)	Er(1)	N(3)	2.543(6)
Er(1)	N(1)#2	2.529(7)			

Symmetry operation (#1) -x,-y,-z+1 (#2) -y,x-y,z

Angles (°)

At. 1	At. 2	At. 3	Angle	At. 1	At. 2	At. 3	Angle
N(2)#1	Er(1)	N(2)#2	120.000(3)	N(1)#1	Er(1)	N(3)#1	128.56(14)
N(2)#1	Er(1)	N(2)	120.000(2)	N(1)#2	Er(1)	N(3)#1	142.94(14)
N(2)#2	Er(1)	N(2)	119.999(2)	N(1)	Er(1)	N(3)#1	82.52(13)
N(2)#1	Er(1)	N(1)#1	64.61(16)	N(2)#1	Er(1)	N(3)#2	71.57(15)
N(2)#2	Er(1)	N(1)#1	71.38(16)	N(2)#2	Er(1)	N(3)#2	63.96(15)
N(2)	Er(1)	N(1)#1	138.69(19)	N(2)	Er(1)	N(3)#2	138.79(18)
N(2)#1	Er(1)	N(1)#2	138.69(19)	N(1)#1	Er(1)	N(3)#2	82.52(13)
N(2)#2	Er(1)	N(1)#2	64.61(16)	N(1)#2	Er(1)	N(3)#2	128.56(14)
N(2)	Er(1)	N(1)#2	71.37(16)	N(1)	Er(1)	N(3)#2	142.94(14)
N(1)#1	Er(1)	N(1)#2	81.38(18)	N(3)#1	Er(1)	N(3)#2	81.87(16)
N(2)#1	Er(1)	N(1)	71.38(15)	N(2)#1	Er(1)	N(3)	138.79(18)
N(2)#2	Er(1)	N(1)	138.69(18)	N(2)#2	Er(1)	N(3)	71.57(15)
N(2)	Er(1)	N(1)	64.61(16)	N(2)	Er(1)	N(3)	63.96(15)
N(1)#1	Er(1)	N(1)	81.38(18)	N(1)#1	Er(1)	N(3)	142.94(14)
N(1)#2	Er(1)	N(1)	81.38(18)	N(1)#2	Er(1)	N(3)	82.52(13)
N(2)#1	Er(1)	N(3)#1	63.96(15)	N(1)	Er(1)	N(3)	128.56(14)
N(2)#2	Er(1)	N(3)#1	138.79(18)	N(3)#1	Er(1)	N(3)	81.87(16)
N(2)	Er(1)	N(3)#1	71.57(15)	N(3)#2	Er(1)	N(3)	81.87(16)

Table S29 Selected least-squares planes data for complex [Er(**L9**)$_3$](ClO$_4$)$_3$ (**7**).

Least-squares planes

Least-squares planes description	Abbreviation	Max. deviation/Å	Atom
Pyridine 1 N(1) C(1) C(2) C(3) C(4) C(5)	Py1	0.028	C(3)
Pyridine 2 N(2) C(6) C(7) C(8) C(9) C(10)	Py2	0.009	C(9)
Pyridine 3 N(3) C(11) C(12) C(13) C(14) C(15)	Py3	0.034	C(11)
Pyridine 1#1 N(1)#1 C(1)#1 C(2)#1 C(3)#1 C(4)#1 C(5)#1	Py1#1	0.028	C(3)#1
Pyridine 2#1 N(2)#1 C(6)#1 C(7)#1 C(8)#1 C(9)#1 C(10)#1	Py2#1	0.009	C(9)#1
Pyridine 3#1 N(3)#1 C(11)#1 C(12)#1 C(13)#1 C(14)#1 C(15)#1	Py3#1	0.034	C(11)#1
Pyridine 1#2 N(1)#2 C(1)#2 C(2)#2 C(3)#2 C(4)#2 C(5)#2	Py1#2	0.028	C(3)#2
Pyridine 2#2 N(2)#2 C(6)#2 C(7)#2 C(8)#2 C(9)#2 C(10)#2	Py2#2	0.009	C(9)#2
Pyridine 3#2 N(3)#2 C(11)#2 C(12)#2 C(13)#2 C(14)#2 C(15)#2	Py3#2	0.034	C(11)#2
F1 N(1), N(1)#1, N(1)#2	F1		
F2 N(2), N(2)#1, N(2)#2	F2		
F3 N(3), N(3)#1, N(3)#2	F3		

Interplanar angles (°)

	Py1	Py2	Py3	Py1#1	Py2#1	Py3#1	Py1#2	Py2#2	Py3#2	F1	F2	F3
Py1		19.1(3)	38.9(3)	63.7(3)	69.6(2)	76.2(2)	63.7(3)	48.1(2)	33.0(3)			
Py2			19.8(3)	48.1(2)	58.7(3)	70.8(3)	69.6(2)	58.7(3)	48.7(3)			
Py3				33.0(3)	48.7(3)	65.6(3)	76.2(2)	70.8(3)	65.6(3)			
Py1#1					19.1(3)	38.9(3)	63.7(3)	69.6(2)	76.2(2)			
Py2#1						19.8(3)	48.1(2)	58.7(3)	70.8(3)			
Py3#1							33.0(3)	48.1(2)	33.0(3)			
Py1#2								19.1(3)	38.9(3)			
Py2#2									19.8(3)			
Py3#2												
F1											0.0	0.0
F2												0.0
F3												

Table S30 Average bond distances $\delta_{Ln,N}$ and $\delta_{Ln,O}$ (Å), average of bond valences (v_{ij}) [a] and bond valence sums (V_i) [b] in the crystal structures of 1:2 and 1:3 complexes of ligands **L4-L9** with Ln(III) (Ln = Er, Eu and Lu).

Complexes	Ln	Ln/**L*k***	Avg. $\delta_{Ln,N}$ / Å	Avg. $\delta_{Ln,O}$ / Å	Avg. $v_{Ln,N}$	Avg. $v_{Ln,O}$	V_{Ln}
[Er(**L4**)$_2$(O$_3$SCF$_3$)$_2$](CF$_3$SO$_3$)	Er	1:2	2.46(3)	2.31(3)	0.36(3)	0.41(4)	2.99(4)
[Er(**L7**)$_2$(O$_3$SCF$_3$)$_2$](CF$_3$SO$_3$)	Er	1:2	2.49(2)	2.26	0.33(2)	0.46	2.92(4)
Er(**L8**)$_2$(O$_3$SCF$_3$)$_3$	Er	1:2	2.53(2)	2.37(5)	0.32(2)	0.35(5)	2.95(4)
[Er(**L6**)$_3$](ClO$_4$)$_3$	Er	1:3	2.52(5)	-	0.32(4)	-	2.88(4)
[Eu(**L7**)$_3$](ClO$_4$)$_3$ [c]	Eu	1:3	2.57(3)	-	0.30(1)	-	2.88(4)
[Er(**L7**)$_3$](ClO$_4$)$_3$	Er	1:3	2.52(3)	-	0.32(2)	-	2.91(4)
[Lu(**L7**)$_3$](ClO$_4$)$_3$ [c]	Lu	1:3	2.50(3)	-	0.31(1)	-	2.84(4)
[Er(**L8**)$_3$](ClO$_4$)$_3$ [d]	Er	1:3	2.53(2)	-	0.31(1)	-	2.84(4)
[Er(**L8**)$_3$](ClO$_4$)$_3$ [d]	Er	1:3	2.51(4)	-	0.33(3)	-	2.98(4)
[Er(**L9**)$_3$](ClO$_4$)$_3$	Er	1:3	2.52(2)	-	0.32(2)	-	2.90(4)

[a] $v_{ij} = e^{[(R_{ij} - d_{ij})/b]}$, whereby d_{ij} is the Ln-donor atom j distance.[60] The valence bond parameters R_{ij} was taken from references 60e and 60f and b = 0.37 Å. [c] $V_i = \sum_j v_{ij}$. [c] Crystal data were taken from reference 34b. [d] The crystal structure of **6** shows that the asymmetric unit contains two slightly different molecules.

Table S31 Summary of crystal data, intensity measurements and structure refinements for dimer complexes [(**L4**)$_2$Er(OH)$_2$Er(**L4**)$_2$](ClO$_4$)$_4$ ·2C$_6$H$_5$CN·4CH$_3$CN (**8**), [(**L5**)$_2$Er(OH)$_2$Er(**L5**)$_2$](ClO$_4$)$_4$·C$_6$H$_5$CN·7.5CH$_3$CN (**9**) and [(**L4**)$_2$Er((CH$_3$)NO$_2$)$_2$Er(**L4**)$_2$](ClO$_4$)$_6$·CH$_3$NO$_2$ (**10**).

	[(**L4**)$_2$Er(OH)$_2$Er(**L4**)$_2$](ClO$_4$)$_4$	[(**L5**)$_2$Er(OH)$_2$Er(**L5**)$_2$](ClO$_4$)$_4$	[(**L4**)$_2$Er((CH$_3$)NO$_2$)$_2$Er(**L4**)$_2$](ClO$_4$)$_6$
Empirical formula	$C_{106}H_{92}Cl_4Er_2N_{26}O_{18}$	$C_{115}H_{115}Cl_4Er_2N_{29}O_{18}$	$C_{87}H_{77}Cl_6Er_2N_{23}O_{30}$
Formula weight	2494.38	2662.67	2471.93
Temperature	180(2)K	180(2)K	180(2)K
Wavelength	1.54184 Å	1.54184 Å	1.54184 Å
Crystal System, Space group	Monoclinic, *C* 2/*c*	Monoclinic, *C* 2/*c*	Monoclinic, *P* 2$_1$/*c*
Unit cell dimensions	*a* = 27.5175(4) Å *b* = 14.45677(19) Å *c* = 27.0356(5) Å α = 90° β = 107.1147(17)° γ = 90°	*a* = 24.0649(19) Å *b* = 30.860(2) Å *c* = 16.5690(11) Å α = 90° β = 107.371(8)° γ = 90°	*a* = 27.2009(5) Å *b* = 23.2822(5) Å *c* = 15.2320(2) Å α = 90° β = 94.6614(16)° γ = 90°
Volume in Å^3	10278.9(3)	11743.7(15)	9614.5(3)
Z, Calculated density	4, 1.612 Mg/m^3	4, 1.506 Mg/m^3	4, 1.708 Mg/m^3
Absorption coefficient	4.589 mm^{-1}	4.062 mm^{-1}	5.484 mm^{-1}
F(000)	5032	5424	4952
Theta range for data collection	3.42 to 73.33 °	3.849 to 67.404 °	3.260 to 73.573 °
Limiting indices	-32<=*h*<=33, -11<=*k*<=17, -31<=*l*<=33	-28<=*h*<=24, -18<=*k*<=36, -19<=*l*<=19	-33<=*h*<=22, -28<=*k*<=19, -18<=*l*<=18
Reflections collected / unique	18745 / 10046 [*R*(int) = 0.0229]	20752 / 10556 [*R*(int) = 0.0410]	34420 / 18724 [*R*(int) = 0.0490]
Completeness to theta	67.50°/ 99.7 %	67.50°/ 99.8 %	67.50°/ 99.6 %
Data / restraints / parameters	10046 / 1 / 689	10556 / 1 / 712	18724 / 1 / 1246
Goodness-of-fit on F^2	1.039	1.112	1.018
Final *R* indices [$I>2\sigma(I)$]	R_1 = 0.0363, ωR_2 = 0.0944	R_1 = 0.0654, ωR_2 = 0.1819	R_1 = 0.0571, ωR_2 = 0.1403
R indices (all data)	R_1 = 0.0401, ωR_2 = 0.0982	R_1 = 0.0736, ωR_2 = 0.1896	R_1 = 0.0812, ωR_2 = 0.1563
Largest diff. peak and hole	0.872 and -1.347 e.Å^{-3}	2.099 and -2.708 e.Å^{-3}	1.450 and -0.966 e.Å^{-3}

Table S32 Selected bond distances (Å), bond angles (°) in $[(\mathbf{L4})_2Er(OH)_2Er(\mathbf{L4})_2](ClO_4)_4$ (**8**).

Bond distances (Å)

Atom 1	Atom 2	Distance	Atom 1	Atom 2	Distance
Er(1)	O(1)	2.2375(18)	Er(2)	O(1)	2.2414(18)
Er(1)	O(1)#1	2.2376(18)	Er(2)	O(1)#1	2.2414(18)
Er(1)	N(1)#1	2.492(2)	Er(2)	N(9)	2.486(2)
Er(1)	N(1)	2.492(2)	Er(2)	N(9)#1	2.486(2)
Er(1)	N(3)	2.548(2)	Er(2)	N(8)#1	2.528(2)
Er(1)	N(3)#1	2.548(2)	Er(2)	N(8)	2.528(2)
Er(1)	N(4)	2.552(2)	Er(2)	N(6)	2.533(3)
Er(1)	N(4)#1	2.552(2)	Er(2)	N(6)#1	2.533(3)

Symmetry operation (#1) -x+1,y,-z+1/2

Angles (°)

At. 1	At. 2	At. 3	Angle	At. 1	At. 2	At. 3	Angle
O(1)	Er(1)	O(1)#1	70.60(9)	O(1)	Er(2)	N(9)	87.77(7)
O(1)	Er(1)	N(1)#1	82.46(7)	O(1)#1	Er(2)	N(9)	82.31(8)
O(1)#1	Er(1)	N(1)#1	87.05(7)	O(1)	Er(2)	N(9)#1	82.31(7)
O(1)	Er(1)	N(1)	87.05(7)	O(1)#1	Er(2)	N(9)#1	87.77(7)
O(1)#1	Er(1)	N(1)	82.46(7)	N(9)	Er(2)	N(9)#1	167.87(11)
N(1)#1	Er(1)	N(1)	167.15(11)	O(1)	Er(2)	N(8)#1	134.83(7)
O(1)	Er(1)	N(3)	77.32(7)	O(1)#1	Er(2)	N(8)#1	78.80(7)
O(1)#1	Er(1)	N(3)	134.45(7)	N(9)	Er(2)	N(8)#1	120.46(8)
N(1)#1	Er(1)	N(3)	120.16(8)	N(9)#1	Er(2)	N(8)#1	63.84(8)
N(1)	Er(1)	N(3)	64.12(8)	O(1)	Er(2)	N(8)	78.80(7)
O(1)	Er(1)	N(3)#1	134.45(7)	O(1)#1	Er(2)	N(8)	134.83(7)
O(1)#1	Er(1)	N(3)#1	77.32(7)	N(9)	Er(2)	N(8)	63.84(8)
N(1)#1	Er(1)	N(3)#1	64.12(8)	N(9)#1	Er(2)	N(8)	120.46(8)
N(1)	Er(1)	N(3)#1	120.16(8)	N(8)#1	Er(2)	N(8)	143.57(11)
N(3)	Er(1)	N(3)#1	145.74(10)	O(1)	Er(2)	N(6)	108.16(8)
O(1)	Er(1)	N(4)	104.32(7)	O(1)#1	Er(2)	N(6)	157.90(8)
O(1)#1	Er(1)	N(4)	157.10(7)	N(9)	Er(2)	N(6)	119.79(8)
N(1)#1	Er(1)	N(4)	70.07(8)	N(9)#1	Er(2)	N(6)	70.33(8)
N(1)	Er(1)	N(4)	120.07(8)	N(8)#1	Er(2)	N(6)	88.53(8)
N(3)	Er(1)	N(4)	61.85(7)	N(8)	Er(2)	N(6)	63.38(8)
N(3)#1	Er(1)	N(4)	92.87(7)	O(1)	Er(2)	N(6)#1	157.90(8)
O(1)	Er(1)	N(4)#1	157.10(7)	O(1)#1	Er(2)	N(6)#1	108.15(8)
O(1)#1	Er(1)	N(4)#1	104.31(7)	N(9)	Er(2)	N(6)#1	70.33(8)
N(1)#1	Er(1)	N(4)#1	120.07(8)	N(9)#1	Er(2)	N(6)#1	119.79(8)
N(1)	Er(1)	N(4)#1	70.07(8)	N(8)#1	Er(2)	N(6)#1	63.38(8)
N(3)	Er(1)	N(4)#1	92.87(7)	N(8)	Er(2)	N(6)#1	88.53(8)
N(3)#1	Er(1)	N(4)#1	61.85(7)	N(6)	Er(2)	N(6)#1	81.45(12)
N(4)	Er(1)	N(4)#1	88.58(11)	Er(1)	O(1)	Er(2)	109.47(7)
O(1)	Er(2)	O(1)#1	70.46(9)	Er(1)	O(1)#1	Er(2)	109.47(7)

Table S33 Selected least-squares planes data for [(**L4**)$_2$Er(OH)$_2$Er(**L4**)$_2$](ClO$_4$)$_4$ (**8**).

Least-squares planes

Least-squares planes description	Abbreviation	Max. deviation/Å	Atom
Pyridine 1 N(3) C(9) C(10) C(11) C(12) C(13)	Py1	0.018	N(3)
Benzimidazole 1 C(1) C(2) C(3) C(4) C(5) C(6) N(1) C(8) N(2)	Bz1	0.035	C(6)
Benzimidazole 2 C(15) C(16) C(17) C(18) C(19) C(20) N(4) C(14) N(5)	Bz2	0.046	C(14)
Pyridine 2 N(8) C(30) C(31) C(32) C(33) C(34)	Py2	0.029	C(34)
Benzimidazole 3 C(22) C(23) C(24) C(25) C(26) C(27) N(6) C(29) N(7)	Bz3	0.036	C(29)
Benzimidazole 4 C(36) C(37) C(38) C(39) C(40) C(41) N(9) C(35) N(10)	Bz4	0.026	C(35)
Pyridine 1#1 N(3)#1 C(9)#1 C(10)#1 C(11)#1 C(12)#1 C(13)#1	Py1#1	0.018	N(3)#1
Benzimidazole 1#1 C(1)#1 C(2)#1 C(3)#1 C(4)#1 C(5)#1 C(6)#1 N(1)#1 C(8)#1 N(2)#1	Bz1#1	0.035	C(6)#1
Benzimidazole 2#1 C(15)#1 C(16)#1 C(17)#1 C(18)#1 C(19)#1 C(20)#1 N(4)#1 C(14)#1 N(5)#1	Bz2#1	0.046	C(14)#1
Pyridine 2#1 N(8)#1 C(30)#1 C(31)#1 C(32)#1 C(33)#1 C(34)#1	Py2#1	0.029	C(34)#1
Benzimidazole 3#1 C(22)#1 C(23)#1 C(24)#1 C(25)#1 C(26)#1 C(27)#1 N(6)#1 C(29)#1 N(7)#1	Bz3#1	0.036	C(29)#1
Benzimidazole 4#1 C(36)#1 C(37)#1 C(38)#1 C(39)#1 C(40)#1 C(41)#1 N(9)#1 C(35)#1 N(10)#1	Bz4#1	0.026	C(35)#1

Interplanar angles (°)

	Py1	Bz1	Bz2	Py2	Bz3	Bz4	Py1#1	Bz1#1	Bz2#1	Py2#1	Bz3#1	Bz4#1
Py1		26.92(10)	18.40(8)	31.63(11)	15.73(9)	26.39(9)	37.38(14)	26.92(10)	18.40(8)	34.63(11)	42.80(8)	15.96(9)
Bz1			43.78(8)	44.50(11)	40.09(9)	26.25(7)	22.54(8)	33.27(12)	21.77(8)	11.39(11)	18.06(7)	10.97(9)
Bz2				23.60(11)	4.14(7)	31.64(9)	46.92(9)	21.77(8)	61.06(10)	52.69(10)	56.97(7)	33.12(8)
Py2					21.37(10)	19.89(11)	34.63(11)	11.39(11)	52.69(10)	55.81(18)	49.37(11)	37.59(10)
Bz3						27.62(8)	42.80(8)	18.06(7)	56.97(7)	49.37(11)	52.9(1)	29.61(8)
Bz4							15.96(9)	10.97(9)	33.12(8)	37.59(10)	29.61(8)	22.76(9)
Py1#1								26.92(10)	18.40(8)	31.63(11)	15.73(9)	26.39(9)
Bz1#1									43.78(8)	44.50(11)	40.09(9)	26.25(7)
Bz2#1										23.60(11)	4.14(7)	31.64(9)
Py2#1											21.37(10)	19.89(11)
Bz3#1												27.62(8)
Bz4#1												

Table S34 Selected bond distances (Å), bond angles (°) in $[(\mathbf{L5})_2Er(OH)_2Er(\mathbf{L5})_2](ClO_4)_4$ (**9**).

Bond distances (Å)

Atom 1	Atom 2	Distance	Atom 1	Atom 2	Distance
Er(1)	O(1)	2.221(4)	Er(1)#1	O(1)	2.256(4)
Er(1)	O(1)#1	2.256(4)	Er(1)#1	O(1)#1	2.221(4)
Er(1)	N(6)	2.466(4)	Er(1)#1	N(6)#1	2.466(4)
Er(1)	N(4)	2.468(5)	Er(1)#1	N(4)#1	2.468(5)
Er(1)	N(9)	2.481(5)	Er(1)#1	N(9)#1	2.481(5)
Er(1)	N(8)	2.495(5)	Er(1)#1	N(8)#1	2.495(4)
Er(1)	N(3)	2.500(5)	Er(1)#1	N(3)#1	2.500(5)
Er(1)	N(1)	2.586(4)	Er(1)#1	N(1)#1	2.586(4)

Symmetry operation (#1) -x+1,y,-z+3/2.

Angles (°)

At. 1	At. 2	At. 3	Angle	At. 1	At. 2	At. 3	Angle
O(1)	Er(1)	O(1)#1	71.30(16)	O(1)	Er(1)#1	N(6)#1	95.67(14)
O(1)	Er(1)	N(6)	95.67(14)	O(1)#1	Er(1)#1	N(6)#1	154.98(14)
O(1)#1	Er(1)	N(6)	154.98(14)	O(1)	Er(1)#1	N(4)#1	84.37(14)
O(1)	Er(1)	N(4)	84.37(14)	O(1)#1	Er(1)#1	N(4)#1	82.10(14)
O(1)#1	Er(1)	N(4)	82.10(14)	N(6)#1	Er(1)#1	N(4)#1	75.27(15)
N(6)	Er(1)	N(4)	75.27(15)	O(1)	Er(1)#1	N(9)#1	94.37(15)
O(1)	Er(1)	N(9)	94.37(15)	O(1)#1	Er(1)#1	N(9)#1	79.03(14)
O(1)#1	Er(1)	N(9)	79.03(14)	N(6)#1	Er(1)#1	N(9)#1	124.21(16)
N(6)	Er(1)	N(9)	124.21(16)	N(4)#1	Er(1)#1	N(9)#1	160.44(17)
N(4)	Er(1)	N(9)	160.44(17)	O(1)	Er(1)#1	N(8)#1	77.07(14)
O(1)	Er(1)	N(8)	77.07(14)	O(1)#1	Er(1)#1	N(8)#1	129.49(14)
O(1)#1	Er(1)	N(8)	129.49(14)	N(6)#1	Er(1)#1	N(8)#1	64.20(15)
N(6)	Er(1)	N(8)	64.20(15)	N(4)#1	Er(1)#1	N(8)#1	132.89(16)
N(4)	Er(1)	N(8)	132.89(16)	N(9)#1	Er(1)#1	N(8)#1	65.07(17)
N(9)	Er(1)	N(8)	65.07(17)	O(1)	Er(1)#1	N(3)#1	140.85(13)
O(1)	Er(1)	N(3)	140.85(13)	O(1)#1	Er(1)#1	N(3)#1	80.56(14)
O(1)#1	Er(1)	N(3)	80.56(14)	N(6)#1	Er(1)#1	N(3)#1	98.97(15)
N(6)	Er(1)	N(3)	98.97(15)	N(4)#1	Er(1)#1	N(3)#1	64.88(16)
N(4)	Er(1)	N(3)	64.88(16)	N(9)#1	Er(1)#1	N(3)#1	106.62(17)
N(9)	Er(1)	N(3)	106.62(17)	N(8)#1	Er(1)#1	N(3)#1	141.72(14)
N(8)	Er(1)	N(3)	141.72(14)	O(1)	Er(1)#1	N(1)#1	156.80(14)
O(1)	Er(1)	N(1)	156.80(14)	O(1)#1	Er(1)#1	N(1)#1	119.90(14)
O(1)#1	Er(1)	N(1)	119.90(14)	N(6)#1	Er(1)#1	N(1)#1	80.39(14)
N(6)	Er(1)	N(1)	80.39(14)	N(4)#1	Er(1)#1	N(1)#1	116.14(14)
N(4)	Er(1)	N(1)	116.14(14)	N(9)#1	Er(1)#1	N(1)#1	70.03(14)
N(9)	Er(1)	N(1)	70.03(14)	N(8)#1	Er(1)#1	N(1)#1	80.70(15)
N(8)	Er(1)	N(1)	80.70(15)	N(3)#1	Er(1)#1	N(1)#1	62.08(15)
N(3)	Er(1)	N(1)	62.08(15)	Er(1)	O(1)	Er(1)#1	108.32(16)
O(1)	Er(1)#1	O(1)#1	71.30(16)	Er(1)	O(1)#1	Er(1)#1	108.32(16)

Table S35 Selected least-squares planes data for [(**L5**)$_2$Er(OH)$_2$Er(**L5**)$_2$](ClO$_4$)$_4$ (**9**).

Least-squares planes

Least-squares planes description	Abbreviation	Max. deviation/Å	Atom
Pyridine 1 N(3) C(10) C(11) C(12) C(13) C(14)	Py1	0.035	N(3)
Benzimidazole 1 C(1) C(2) C(3) C(5) C(6) C(7) N(1) C(9) N(2)	Bz1	0.049	N(1)
Benzimidazole 2 C(16) C(17) C(18) C(20) C(21) C(22) N(4) C(15) N(5)	Bz2	0.043	C(15)
Pyridine 2 N(8) C(33) C(34) C(35) C(36) C(37)	Py2	0.017	C(37)
Benzimidazole 3 C(24) C(25) C(26) C(28) C(29) C(30) N(6) C(32) N(7)	Bz3	0.023	C(32)
Benzimidazole 4 C(39) C(40) C(41) C(43) C(44) C(45) N(9) C(38) N(10)	Bz4	0.010	C(43)
Pyridine 1#1 N(3)#1 C(10)#1 C(11)#1 C(12)#1 C(13)#1 C(14)#1	Py1#1	0.035	N(3)#1
Benzimidazole 1#1 C(1)#1 C(2)#1 C(3)#1 C(5)#1 C(6)#1 C(7)#1 N(1)#1 C(9)#1 N(2)#1	Bz1#1	0.049	N(1)#1
Benzimidazole 2#1 C(16)#1 C(17)#1 C(18)#1 C(20)#1 C(21)#1 C(22)#1 N(4)#1 C(15)#1 N(5)#1	Bz2#1	0.043	C(15)#1
Pyridine 2#1 N(8)#1 C(33)#1 C(34)#1 C(35)#1 C(36)#1 C(37)#1	Py2#1	0.017	C(37)#1
Benzimidazole 3#1 C(24)#1 C(25)#1 C(26)#1 C(28)#1 C(29)#1 C(30)#1 N(6)#1 C(32)#1 N(7)#1	Bz3#1	0.023	C(32)#1
Benzimidazole 4#1 C(39)#1 C(40)#1 C(41)#1 C(43)#1 C(44)#1 C(45)#1 N(9)#1 C(38)#1 N(10)#1	Bz4#1	0.010	C(43)#1

Interplanar angles (°)

	Py1	Bz1	Bz2	Py2	Bz3	Bz4	Py1#1	Bz1#1	Bz2#1	Py2#1	Bz3#1	Bz4#1
Py1		13.94(16)	26.01(16)	44.3(2)	50.76(16)	26.43(16)	44.4(3)	45.91(15)	18.51(16)	26.29(19)	14.49(17)	34.13(17)
Bz1			30.01(12)	36.93(17)	41.73(11)	17.17(15)	45.91(15)	42.67(15)	23.97(10)	13.08(17)	5.05(10)	27.10(15)
Bz2				29.50(16)	27.88(13)	24.35(12)	18.51(16)	23.97(10)	7.53(19)	32.99(17)	34.35(14)	22.66(10)
Py2					16.22(16)	19.78(19)	26.29(19)	13.08(17)	32.92(17)	27.8(3)	41.68(16)	44.4(2)
Bz3						18.35(18)	14.49(17)	5.05(10)	34.35(14)	41.68(16)	52.75(14)	21.91(14)
Bz4							34.13(17)	27.10(15)	22.66(10)	10.24(19)	21.91(14)	10.3(3)
Py1#1								13.94(16)	26.01(16)	44.3(2)	50.76(16)	26.43(16)
Bz1#1									30.01(12)	36.93(17)	47.71(11)	17.17(15)
Bz2#1										29.50(16)	27.88(13)	24.35(12)
Py2#1											16.22(16)	19.78(19)
Bz3#1												31.99(14)
Bz4#1												

Table S36 Selected bond distances (Å), bond angles (°) in $[(\mathbf{L4})_2Er((CH_3)NO_2)_2Er(\mathbf{L4})_2](ClO_4)_6$ (**10**).

Bond distances (Å)

Atom 1	Atom 2	Distance	Atom 1	Atom 2	Distance
Er(1)	O(3)	2.207(4)	Er(2)	O(2)	2.228(4)
Er(1)	O(1)	2.240(4)	Er(2)	O(4)	2.239(4)
Er(1)	N(4)	2.446(4)	Er(2)	N(16)	2.463(5)
Er(1)	N(9)	2.470(4)	Er(2)	N(19)	2.467(5)
Er(1)	N(6)	2.477(4)	Er(2)	N(14)	2.473(5)
Er(1)	N(1)	2.481(5)	Er(2)	N(11)	2.482(4)
Er(1)	N(8)	2.518(5)	Er(2)	N(13)	2.535(5)
Er(1)	N(3)	2.525(5)	Er(2)	N(18)	2.540(5)

Angles (°)

At. 1	At. 2	At. 3	angle	At. 1	At. 2	At. 3	angle
O(1)	Er(1)	N(1)	96.68(15)	O(2)	Er(2)	N(13)	139.97(15)
O(1)	Er(1)	N(3)	69.73(15)	O(2)	Er(2)	N(14)	155.64(16)
O(1)	Er(1)	N(4)	82.21(15)	O(2)	Er(2)	N(16)	88.14(17)
O(1)	Er(1)	N(6)	74.97(15)	O(2)	Er(2)	N(18)	69.75(15)
O(1)	Er(1)	N(8)	136.97(14)	O(2)	Er(2)	N(19)	89.30(17)
O(1)	Er(1)	N(9)	156.84(15)	O(4)	Er(2)	N(11)	80.52(16)
O(3)	Er(1)	O(1)	90.24(15)	O(4)	Er(2)	N(13)	71.21(16)
O(3)	Er(1)	N(1)	153.42(16)	O(4)	Er(2)	N(14)	100.22(17)
O(3)	Er(1)	N(3)	141.10(16)	O(4)	Er(2)	N(16)	155.98(16)
O(3)	Er(1)	N(4)	80.42(16)	O(4)	Er(2)	N(18)	137.32(16)
O(3)	Er(1)	N(6)	83.14(15)	O(4)	Er(2)	N(19)	77.58(17)
O(3)	Er(1)	N(8)	71.97(16)	N(11)	Er(2)	N(13)	64.48(16)
O(3)	Er(1)	N(9)	94.55(15)	N(11)	Er(2)	N(18)	128.17(16)
N(1)	Er(1)	N(3)	64.65(16)	N(13)	Er(2)	N(18)	145.33(16)
N(1)	Er(1)	N(8)	85.78(16)	N(14)	Er(2)	N(11)	125.32(17)
N(4)	Er(1)	N(1)	125.88(17)	N(14)	Er(2)	N(13)	64.38(16)
N(4)	Er(1)	N(3)	64.47(16)	N(14)	Er(2)	N(18)	87.56(16)
N(4)	Er(1)	N(6)	151.71(16)	N(16)	Er(2)	N(11)	75.91(15)
N(4)	Er(1)	N(8)	130.04(15)	N(16)	Er(2)	N(13)	94.21(17)
N(4)	Er(1)	N(9)	76.30(16)	N(16)	Er(2)	N(14)	89.81(17)
N(6)	Er(1)	N(1)	74.04(15)	N(16)	Er(2)	N(18)	64.23(16)
N(6)	Er(1)	N(3)	120.51(15)	N(16)	Er(2)	N(19)	126.40(16)
N(6)	Er(1)	N(8)	64.44(15)	N(19)	Er(2)	N(11)	154.14(17)
N(8)	Er(1)	N(3)	144.29(15)	N(19)	Er(2)	N(13)	119.75(17)
N(9)	Er(1)	N(1)	89.10(15)	N(19)	Er(2)	N(14)	72.54(18)
N(9)	Er(1)	N(3)	92.97(15)	N(19)	Er(2)	N(18)	64.82(17)
N(9)	Er(1)	N(6)	128.08(16)	N(21)	O(1)	Er(1)	146.1(3)
N(9)	Er(1)	N(8)	65.65(15)	N(21)	O(2)	Er(2)	146.8(4)
O(2)	Er(2)	O(4)	91.25(16)	N(22)	O(3)	Er(1)	161.4(4)
O(2)	Er(2)	N(11)	77.55(16)	N(22)	O(4)	Er(2)	155.9(4)

Table S37 Selected least-squares planes data for [(**L4**)$_2$Er((CH$_3$)NO$_2$)$_2$Er(**L4**)$_2$](ClO$_4$)$_6$ (**10**).

Least-squares planes

Least-squares planes description	Abbreviation	Max. deviation/Å	Atom
Pyridine 1 N(3) C(9) C(10) C(11) C(12) C(13)	Py1	0.021	C(9)
Benzimidazole 1 C(1) C(2) C(3) C(4) C(5) C(6) N(1) C(8) N(2)	Bz1	0.030	C(2)
Benzimidazole 2 C(16) C(17) C(18) C(19) C(20) C(21) N(4) C(14) N(5)	Bz2	0.046	C(14)
Pyridine 2 N(8) C(30) C(31) C(32) C(33) C(34)	Py2	0.025	N(8)
Benzimidazole 3 C(22) C(23) C(24) C(25) C(26) C(27) N(6) C(29) N(7)	Bz3	0.046	C(27) C(29)
Benzimidazole 4 C(37) C(38) C(39) C(40) C(41) C(42) N(9) C(35) N(10)	Bz4	0.025	N(9)
Pyridine 3 N(13) C(72) C(73) C(74) C(75) C(76)	Py3	0.015	N(13)
Benzimidazole 5 C(71) C(72) C(73) C(74) C(75) C(76) N(11) C(71) N(12)	Bz5	0.030	C(64)
Benzimidazole 6 C(79) C(80) C(81) C(82) C(83) C(84) N(14) C(77) N(15)	Bz6	0.020	C(83)
Pyridine 4 N(18) C(51) C(52) C(53) C(54) C(55)	Py4	0.022	C(51)
Benzimidazole 7 C(43) C(44) C(45) C(46) C(47) C(48) N(16) C(50) N(17)	Bz7	0.019	C(50)
Benzimidazole 8 C(58) C(59) C(60) C(61) C(62) C(63) N(19) C(56) N(20)	Bz8	0.027	C(63)

Interplanar angles (°)

	Py1	Bz1	Bz2	Py2	Bz3	Bz4	Py3	Bz5	Bz6	Py4	Bz7	Bz8
Py1		15.95(17)	16.17(17)	61.7(2)	33.67(16)	97.83(16)	51.3(2)	29.28(17)	56.76(17)	13.9(2)	9.97(19)	25.9(2)
Bz1			21.60(13)	52.81(18)	20.94(15)	112.28(13)	43.94(19)	29.92(11)	54.15(14)	13.12(17)	13.99(12)	12.39(19)
Bz2				48.64(19)	27.84(12)	105.35(13)	37.74(19)	13.39(15)	40.90(14)	27.97(19)	25.04(16)	23.45(15)
Py2					32.6(2)	33.31(19)	11.0(2)	36.8(2)	20.40(19)	65.9(2)	65.91(18)	40.8(2)
Bz3						48.62(13)	25.4(2)	25.50(14)	39.22(18)	33.97(18)	34.81(13)	8.5(2)
Bz4							42.2(2)	66.06(16)	53.37(15)	79.16(16)	98.60(11)	56.30(19)
Py3								25.8(2)	16.2(2)	56.8(2)	56.32(19)	32.7(2)
Bz5									27.53(15)	39.54(18)	37.30(15)	25.56(14)
Bz6										65.77(18)	64.15(15)	44.89(18)
Py4											4.27(19)	25.4(2)
Bz7												26.29(18)
Bz8												

Table S38 Photophysical data for ligands **L4**-**L9** in the solid-state and in acetonitrile solution (0.3 mM) at various temperatures.

Compounds	State / solvent	*T* / K	*E* /cm^{-1} [a] Absorption ($^1\pi^* \leftarrow {}^1\pi$)	*E* /cm^{-1} [a] Emission ($^1\pi^* \rightarrow {}^1\pi$)	$\tau(^1\pi^*)$ / ns
L4	Solid	77		27317 sh 25966 24575 23109 sh 21597 sh	
		293		25448 21201	
	CH_3CN^a	77		27333 sh 26481 25053 sh	
		293	48808 45044 sh 40807 sh 31056 29851 sh	26991	1.6 (100%)
L5	Solid	77		25664 24735 23257 sh 21437 19983 sh	
		293		25522 sh 24487 23223	
	CH_3CN	77		26918 sh 25608 24096 sh	
		293	48870 45045 sh 41152 sh 36232 sh 31056 29940 sh	26455	2.0 (100%)

L6	Solid	77		26270 sh 25511 sh 24802 sh 23865 22410	
		293	43809 37339 sh 29597 26222 sh 22638 sh	25331 sh 24013 21027[d]	
	CH_3CN	77	47847 44053 sh 40650 sh	26248 sh 24654 23353 sh	
		293	36232 sh 30581 29326 sh	26497	1.9 (100%)
L7	Solid	77		25895 24537 sh 23311 21757 19735	
		293	46508 sh 40869 35889 32148, 29561 sh 21491	27021 26056 sh 23273 21863 sh 20687 19197 sh	
	CH_3CN[a]	77		30573, 29605, 28801 sh 28801 sh 26993	< 0.3 (100%)
		293	42194 39841 sh 36232 33113, 31949 sh	24831 sh 30817 sh 29985 28531 sh	

L8	Solid	77		29168 27709 sh 26160 25195 sh 21481	
		293		28860 sh 27704 26385 sh	
	CH_3CN	77		30187 sh 29066 27626 26245	
		293	42918 sh 40984 39062 sh 34843 32680 sh 31348 sh	30817 sh 29586 28129 sh	< 0.3 (83%) 1.7 (17%)
L9	Solid	77		29090 sh 27675 sh 26424 25682,24293, 22988 sh 21375	
		293		20804 28656 sh 27436 24096 sh	
	CH_3CN	77		22820 sh 30110 sh 28977 27531	
		293	42918 sh 40816 39062 sh 34843 32680, 31348 sh	26493 sh 30769 sh 29499 28050 sh	< 0.3 (91%) 0.6 (9%)

[a] Maximum of the band envelope.

Table S39 Photophysical data recorded for the complexes **1**-**3** in acetonitrile solution (3.0 mM) at different temperatures.

Compounds	*T* / K	*E* /cm^{-1} [a] Absorption ($^1\pi^* \leftarrow {}^1\pi$)	*E* /cm^{-1} [a] Emission ($^1\pi^* \rightarrow {}^1\pi$)
[Er(**L4**)$_2$(O$_3$SCF$_3$)$_2$](CF$_3$SO$_3$) (**1**)	77		24331 sh
			23613
	293	49330 sh	23669
		44682 sh	
		40462 sh	
		32921	
		27701	
[Er(**L7**)$_2$(O$_3$SCF$_3$)$_2$](CF$_3$SO$_3$) (**2**)	77		27663 sh
			26882
			25211 sh
			24323 sh
	293	35714 sh	28011 sh
		34602	26991
		30211	
		29070 sh	
Er(**L8**)$_2$(O$_3$SCF$_3$)$_3$ (**3**)	77		27027 sh
			26042
			24752
	293	25088 sh	27397 sh
		33898	26385
		29499	
		28571 sh	

[a] Maximum of the band envelope.

Table S40 Experimental lifetimes, radiative lifetimes and intrinsic quantum yields of the complexes **1**-**7** in the solid state at room temperature.

Compound	$\tau_{\mathrm{Er,obs}}^{^4\mathrm{I}_{13/2}}$ /μs	$\tau_{\mathrm{Er,rad}}^{^4\mathrm{I}_{13/2}}$ /ms [a]	$Q_{\mathrm{Er}}^{\mathrm{Er}}\left(^4\mathrm{I}_{13/2}\right)$ /% [b]	$\tau_{\mathrm{Er,obs}}^{^4\mathrm{S}_{3/2}}$ /ns	$\tau_{\mathrm{Er,rad}}^{^4\mathrm{S}_{3/2}}$ /μs [a]	$Q_{\mathrm{Er}}^{\mathrm{Er}}\left(^4\mathrm{S}_{3/2}\right)$ /% [b]
[Er(**L4**)$_2$(O_3SCF_3)$_2$](CF_3SO_3) (**1**)	4.06(2)	6.3	0.064	10.9(5)	546	0.0020
[Er(**L7**)$_2$(O_3SCF_3)$_2$](CF_3SO_3) (**2**)	1.61(1)	6.1	0.026	8.9(4)	515	0.0017
Er(**L8**)$_2$(O_3SCF_3)$_3$ (**3**)	2.76(2)	5.6	0.049	9.0(3)	453	0.0020
[Er(**L6**)$_3$](ClO_4)$_3$ (**4**)	5.57(6)	6.3	0.088		716	
[Er(**L7**)$_3$](ClO_4)$_3$ (**5**)	1.88(2)	6.4	0.029		476	
[Er(**L8**)$_3$](ClO_4)$_3$ (**6**)	2.18(1)	6.1	0.036		493	
[Er(**L9**)$_3$](ClO_4)$_3$ (**7**)	1.94(2)	6.1	0.032		495	

[a]Taken from Table 2. [b] $Q_{\mathrm{Er}}^{\mathrm{Er}}\left(^{2S+1}L_J\right)=\tau_{\mathrm{Er,exp}}^{^{2S+1}\mathrm{L}_J}\Big/\tau_{\mathrm{Er,rad}}^{^{2S+1}\mathrm{L}_J}$.

Table S41 Photophysical data for the complexes **4**-**7** in acetonitrile solution (3.0 mM) and in the solid-state at various temperatures.

Compounds	State / solvent	T / K	E /cm^{-1} [a] Absorption ($^1\pi^* \leftarrow {}^1\pi$)	E /cm^{-1} [a] Emission ($^1\pi^* \rightarrow {}^1\pi$)
[Er(**L6**)$_3$](ClO$_4$)$_3$ (**4**)	Solid	293	29176 24402	
	CH_3CN	77		23950 22849 sh 21275 sh
		293	44586 sh 39776 sh 32354 26653	24063 sh 23154
[Er(**L7**)$_3$](ClO$_4$)$_3$ (**5**)	Solid	293	42085 35527 33457 sh	27866 sh 26139
	CH_3CN	77	27821	27610 sh 26681 25339 sh 23225 sh
		293	42918 sh 37453 35461 sh 34130 30120 29170 sh	27854 sh 26792
[Er(**L8**)$_3$](ClO$_4$)$_3$ (**6**)	Solid	293		27076 sh 25596
	CH_3CN	77		27401 sh 26050 24488 sh
		293	47847 40161 sh 37879 sh 35088 sh 33898 29499 28571 sh	27173 sh 26359 23189 sh
[Er(**L9**)$_3$](ClO$_4$)$_3$ (**7**)	CH_3CN	77		26678 sh 25958 24582 sh
		293	49504 40000 sh 33445 29412 28329 sh	27208 26119 sh 23158 sh

[a] Maximum of the band envelope.

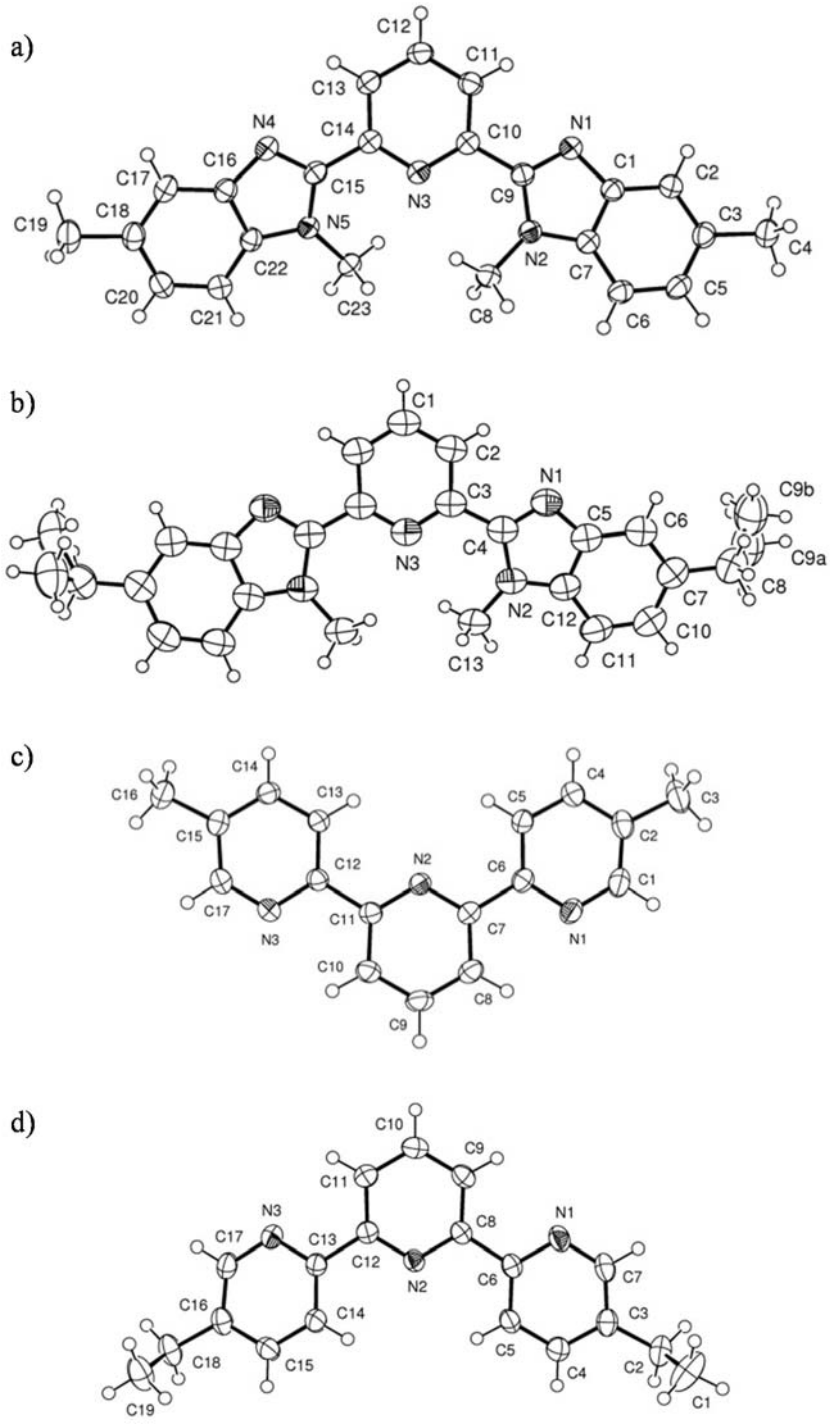

Figure S1 Molecular structures with numbering scheme of the asymmetric units of a) **L5**, b) **L6**, c) **L8** and d) **L9**. The thermal ellipsoids are represented at the 50% probability level.

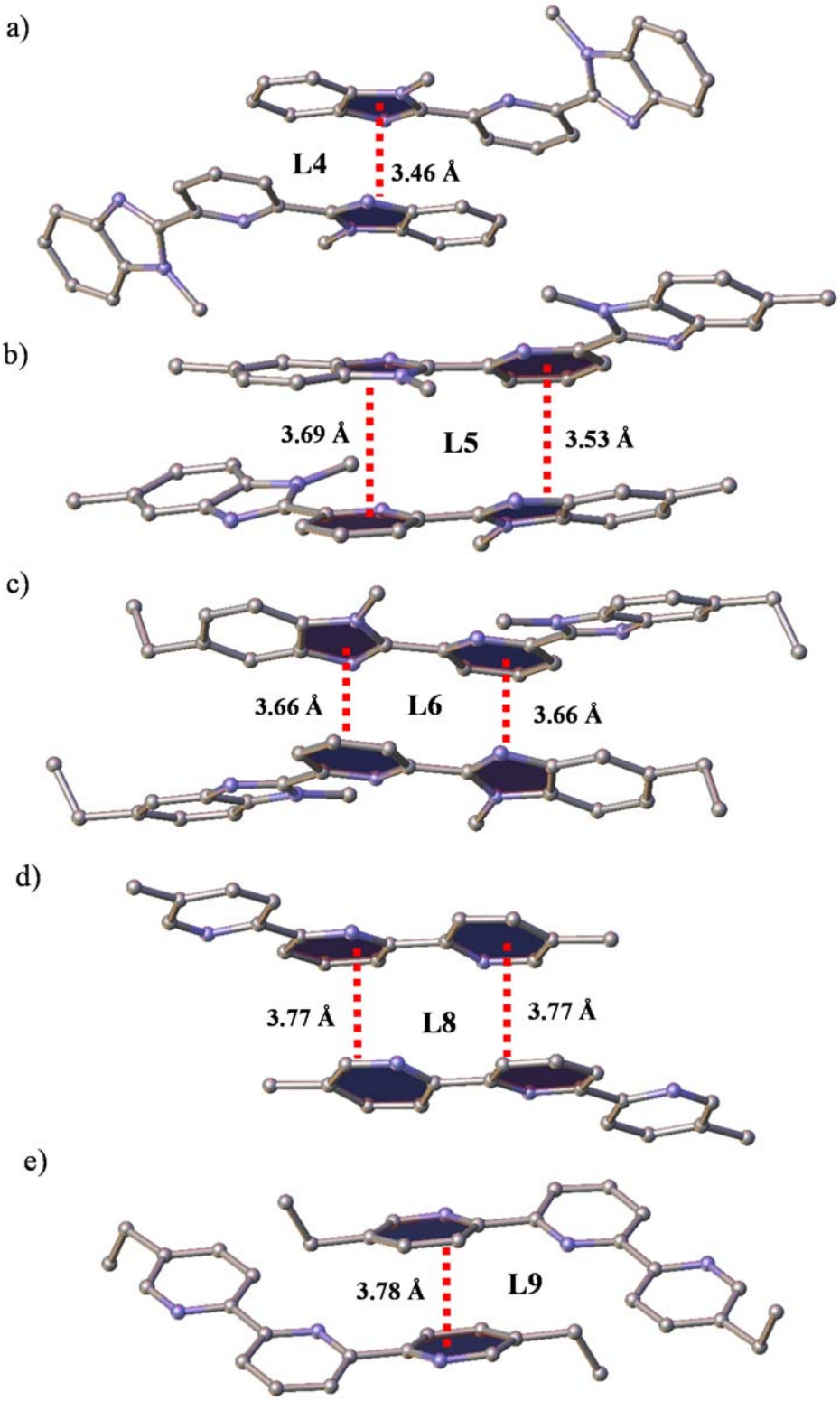

Figure S2 Perspective views of ligands a) **L4**, b) **L5**, c) **L6**, d) **L8** and e) **L9** showing the shortest intermolecular π-π interactions occurring between parallel aromatic units in the crystals.

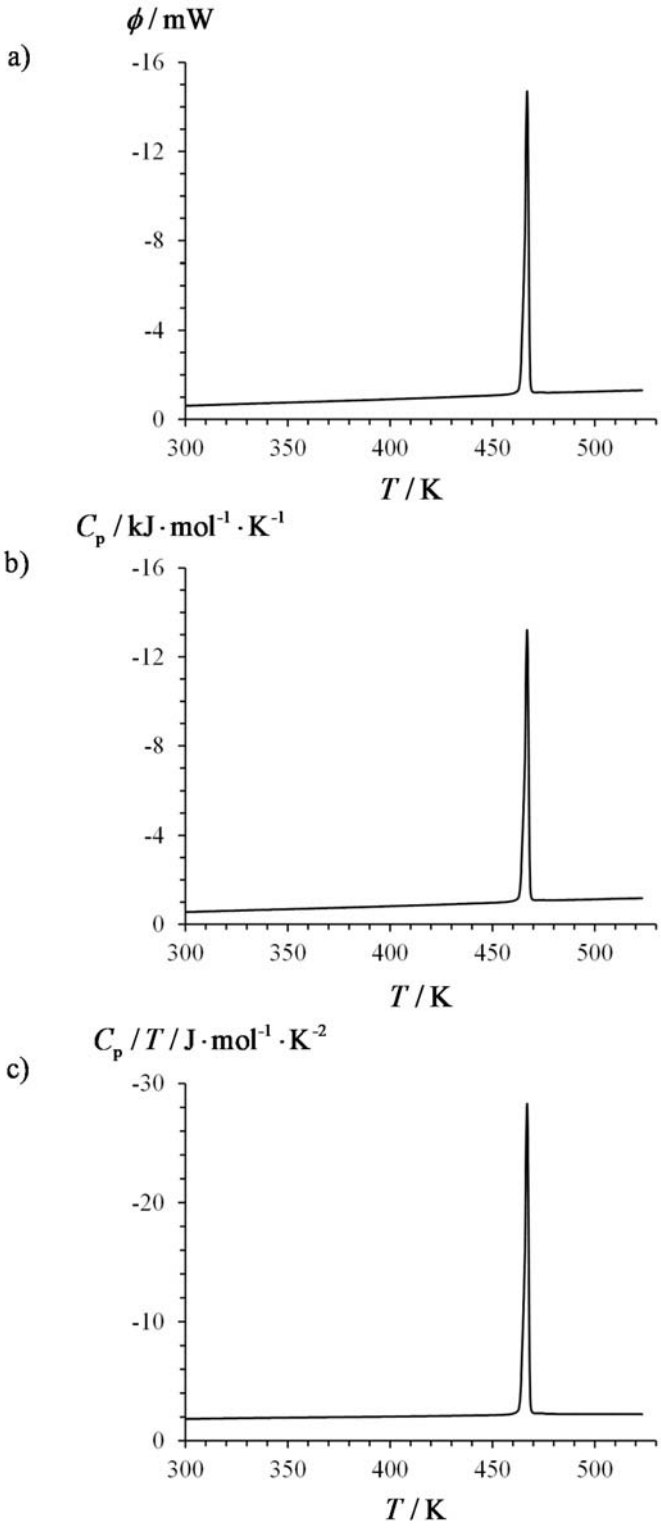

Figure S3 a) DSC traces recorded at 0.5 K/min for the ligand **L4** and its transformation into b) molar heat capacity ($\phi = \frac{\Delta W}{\Delta t} = \frac{nC_p\Delta T}{\Delta t} = nC_p\nu \Rightarrow C_p = \frac{\phi}{n\nu}$ with $\nu = \frac{\Delta T}{\Delta t}$ being the scanning rate and n the number of moles)[42a] and c) molar capacity per temperature unit.

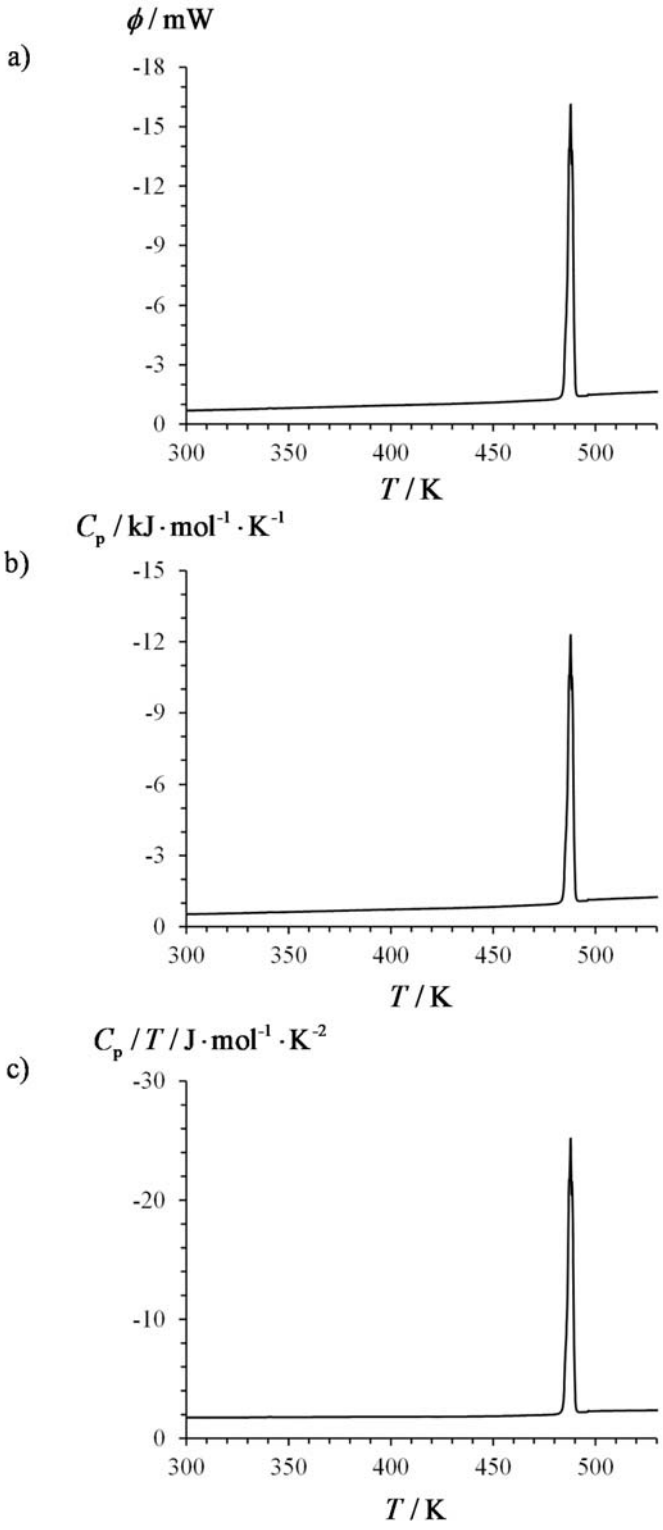

Figure S4 a) DSC traces recorded at 0.5 K/min for the ligand **L5** and its transformation into b) molar heat capacity ($\phi = \frac{\Delta W}{\Delta t} = \frac{nC_p\Delta T}{\Delta t} = nC_p\nu \Rightarrow C_p = \frac{\phi}{n\nu}$ with $\nu = \frac{\Delta T}{\Delta t}$ being the scanning rate and n the number of moles)[42a] and c) molar capacity per temperature unit.

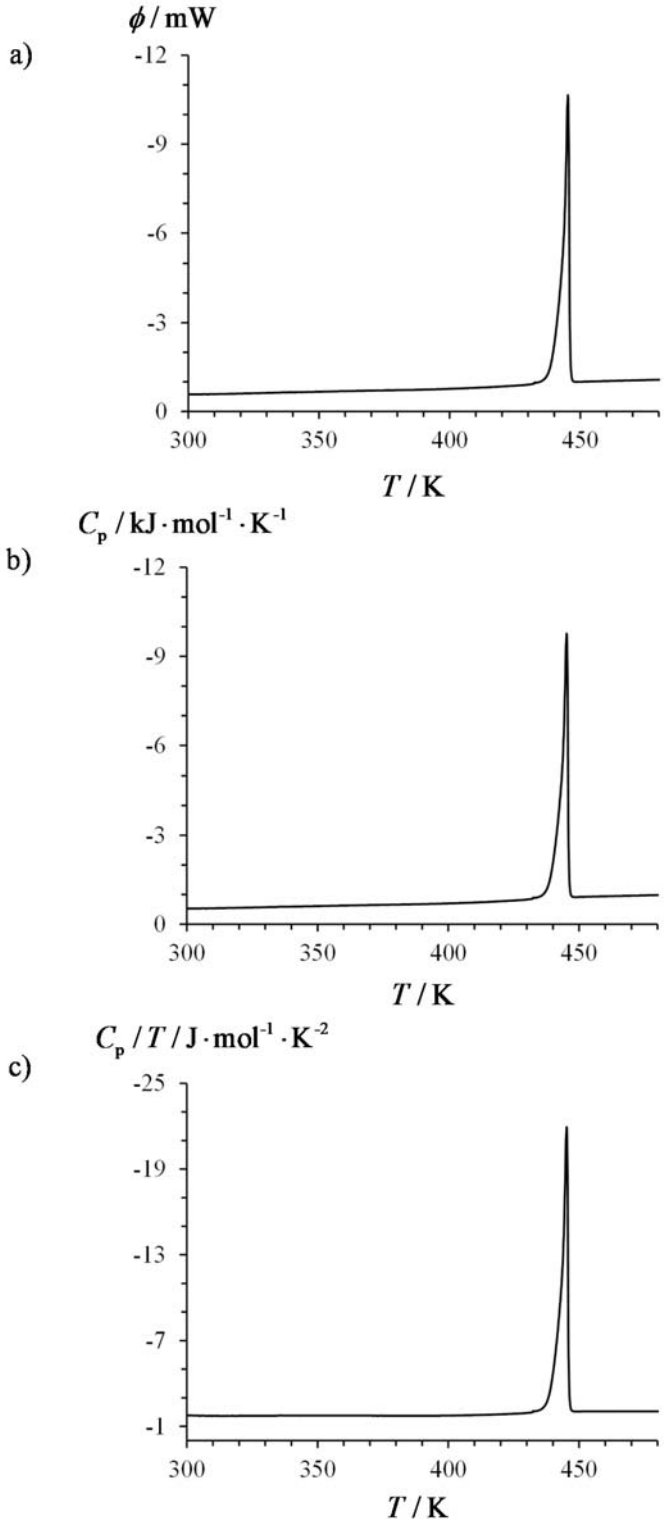

Figure S5 a) DSC traces recorded at 0.5 K/min for the ligand **L6** and its transformation into b) molar heat capacity ($\phi = \frac{\Delta W}{\Delta t} = \frac{nC_p\Delta T}{\Delta t} = nC_p\nu \Rightarrow C_p = \frac{\phi}{n\nu}$ with $\nu = \frac{\Delta T}{\Delta t}$ being the scanning rate and n the number of moles)[42a] and c) molar capacity per temperature unit.

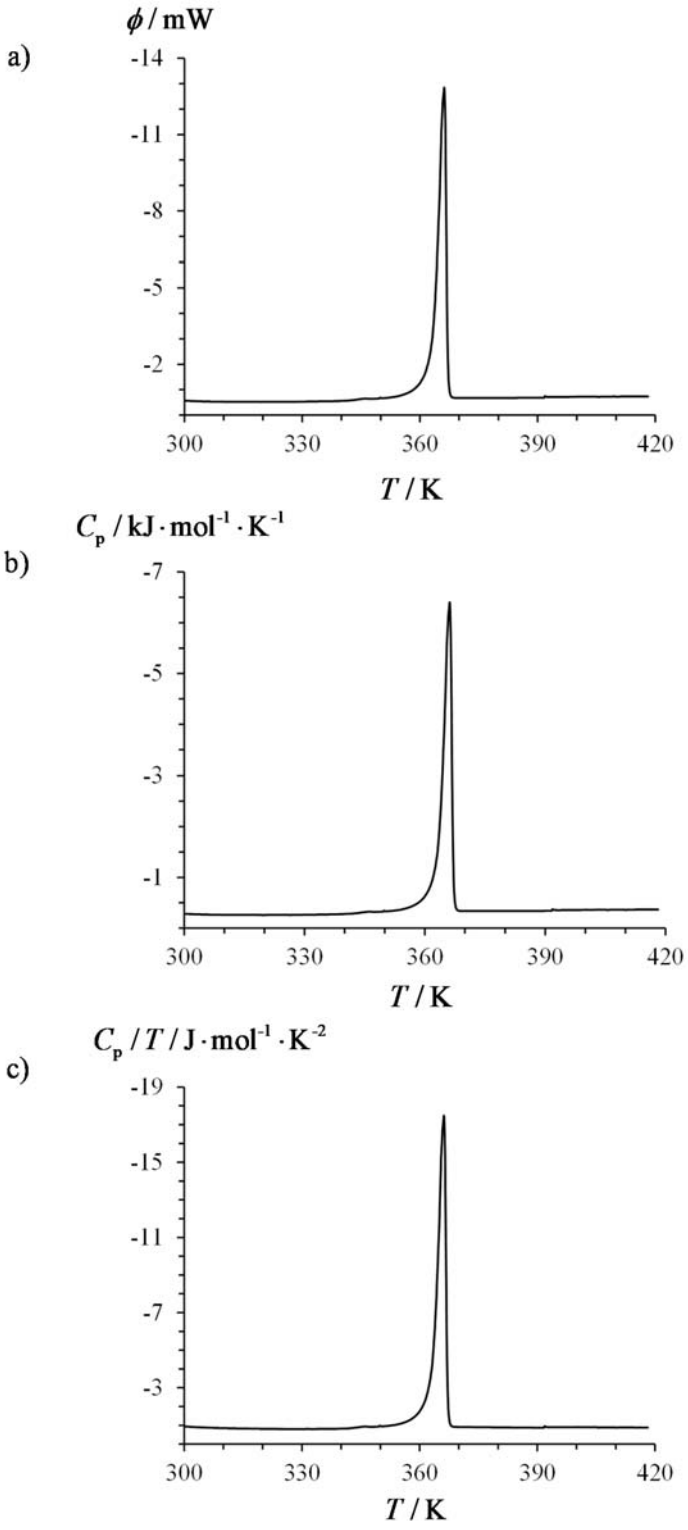

Figure S6 a) DSC traces recorded at 0.5 K/min for the ligand **L7** and its transformation into b) molar heat capacity ($\phi = \frac{\Delta W}{\Delta t} = \frac{nC_p\Delta T}{\Delta t} = nC_p\nu \Rightarrow C_p = \frac{\phi}{n\nu}$ with $\nu = \frac{\Delta T}{\Delta t}$ being the scanning rate and n the number of moles)[42a] and c) molar capacity per temperature unit.

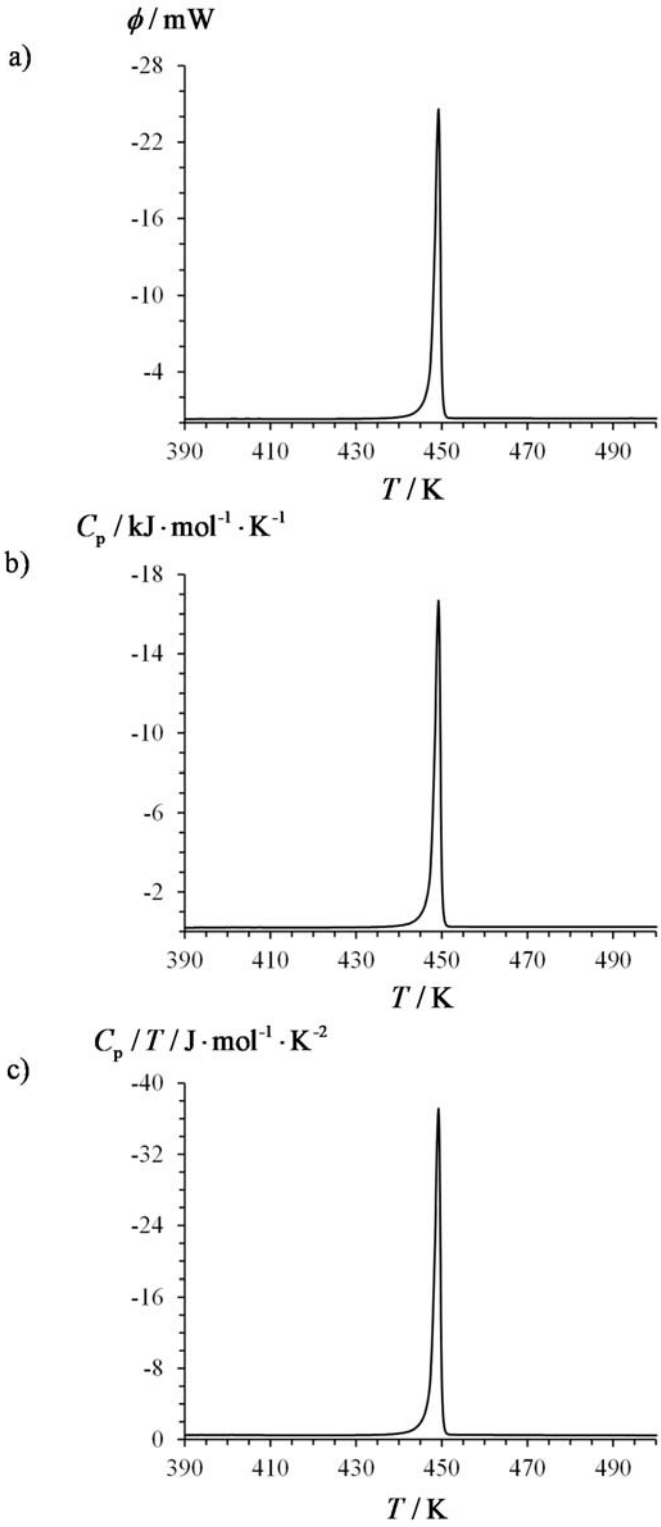

Figure S7 a) DSC traces recorded at 0.5 K/min for the ligand **L8** and its transformation into b) molar heat capacity ($\phi = \frac{\Delta W}{\Delta t} = \frac{nC_p\Delta T}{\Delta t} = nC_p\nu \Rightarrow C_p = \frac{\phi}{n\nu}$ with $\nu = \frac{\Delta T}{\Delta t}$ being the scanning rate and n the number of moles)[42a] and c) molar capacity per temperature unit.

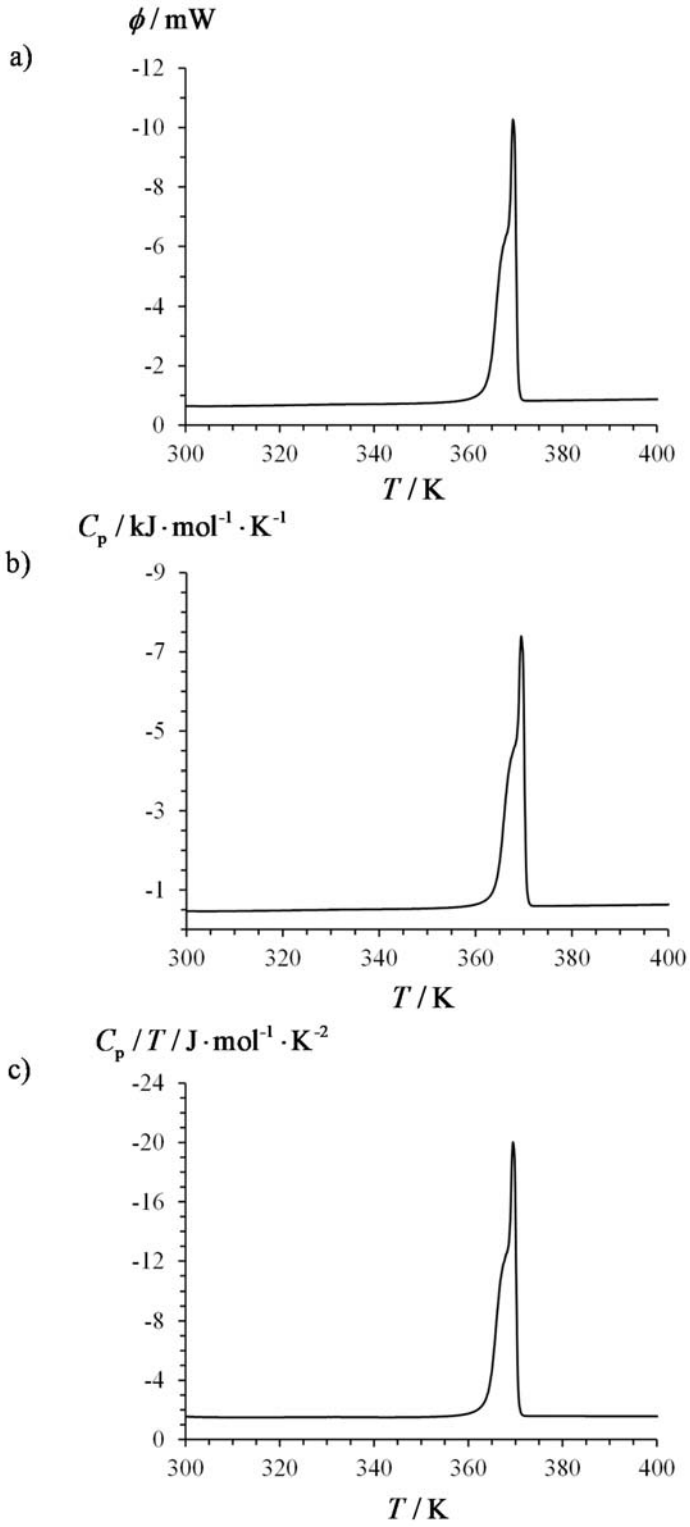

Figure S8 a) DSC traces recorded at 0.5 K/min for the ligand **L9** and its transformation into b) molar heat capacity ($\phi = \frac{\Delta W}{\Delta t} = \frac{nC_p\Delta T}{\Delta t} = nC_p\nu \Rightarrow C_p = \frac{\phi}{n\nu}$ with $\nu = \frac{\Delta T}{\Delta t}$ being the scanning rate and n the number of moles)[42a] and c) molar capacity per temperature unit.

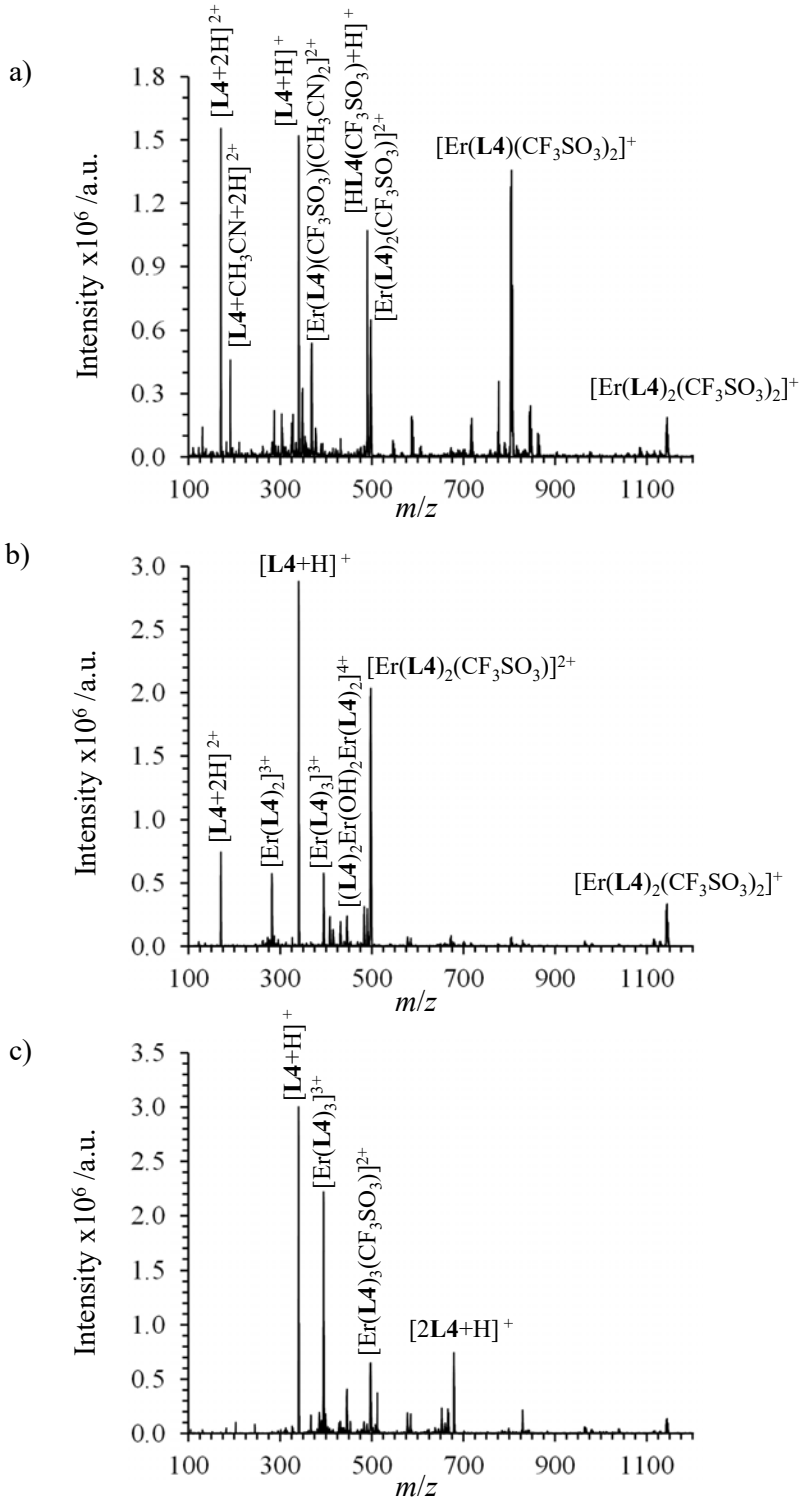

Figure S9 ESI-MS spectra recorded upon titration of **L4** with $Er(CF_3SO_3)_3$ (total ligand concentration: 2.0×10^{-3} M in acetonitrile, 298 K) for stoichiometric ratios a) $[Er]_{tot}/[\mathbf{L4}]_{tot} = 1.00$, b) $[Er]_{tot}/[\mathbf{L4}]_{tot} = 0.50$ and c) $[Er]_{tot}/[\mathbf{L4}]_{tot} = 0.33$.

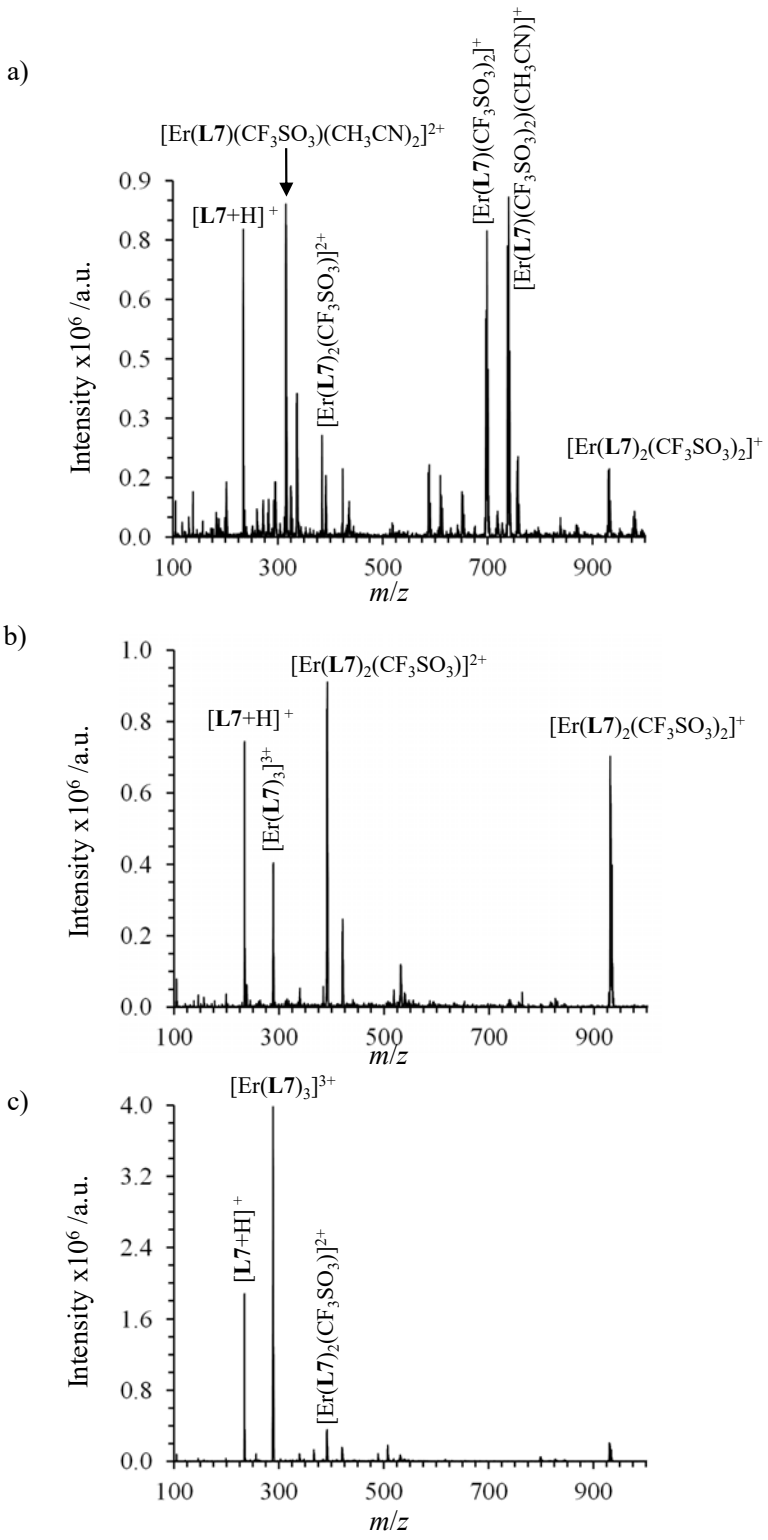

Figure S10 ESI-MS spectra upon titration of **L7** with $Er(CF_3SO_3)_3$ (total ligand concentration: 2.0×10^{-3} M in acetonitrile, 298 K) at stoichiometric ratios a) $[Er]_{tot}/\ [\mathbf{L7}]_{tot} = 1.00$, b) $[Er]_{tot}/\ [\mathbf{L7}]_{tot} = 0.50$ and c) $[Er]_{tot}/\ [\mathbf{L7}]_{tot} = 0.33$.

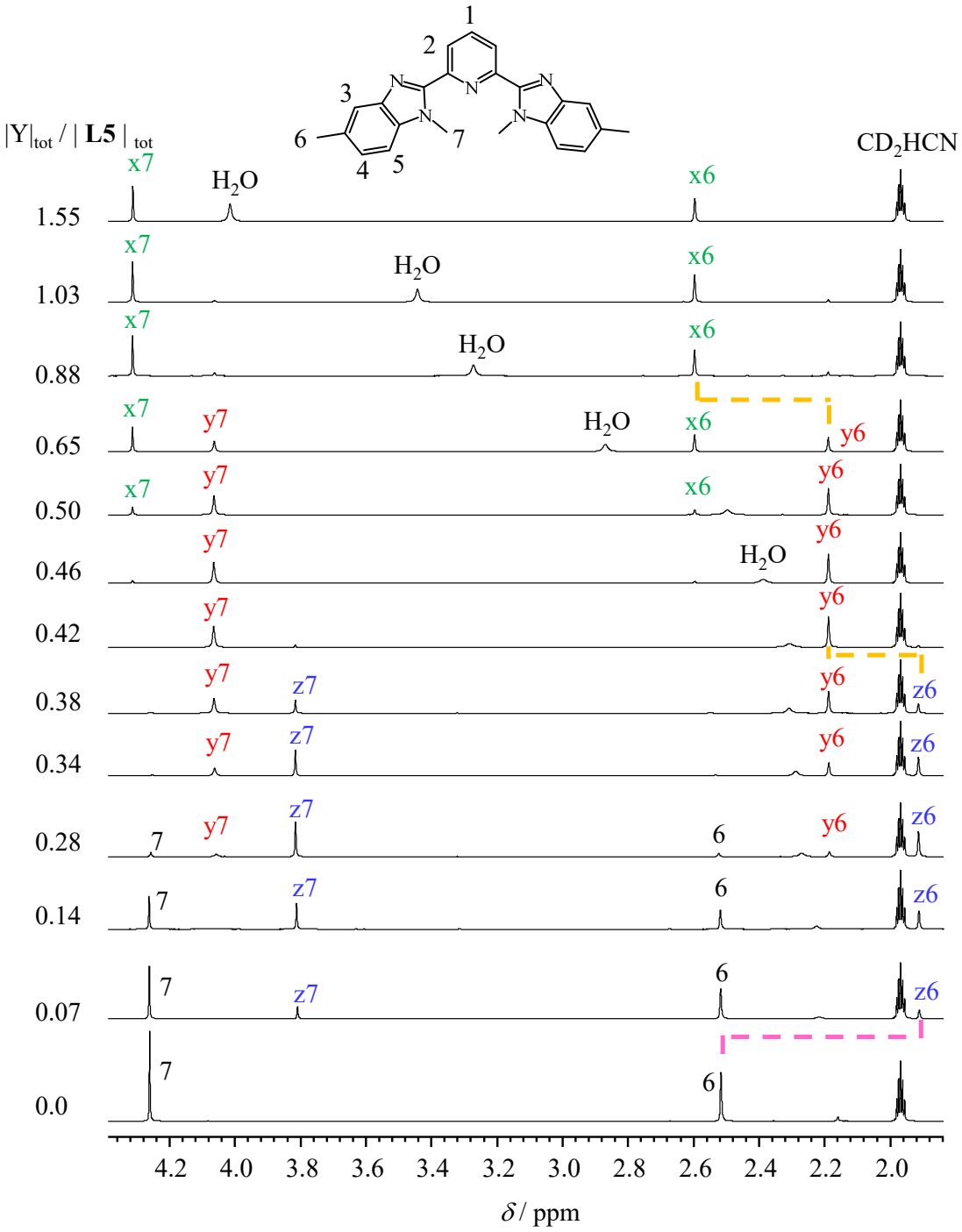

Figure S11 Aliphatic parts of the ^{1}H NMR spectra with numbering scheme recorded upon titration of **L5** with $Y(CF_3SO_3)_3$ in CD_3CN at 298 K with numbering scheme. ($5\times10^{-3} \leq |\mathbf{L5}|_{tot} \leq 9\times10^{-3}$ M and $6\times10^{-4} \leq |Y|_{tot} \leq 8\times10^{-3}$ M). The letters x, y and z denote signals arising from the 1:1 (green), 1:2 (red) and 1:3 (blue) species, respectively.

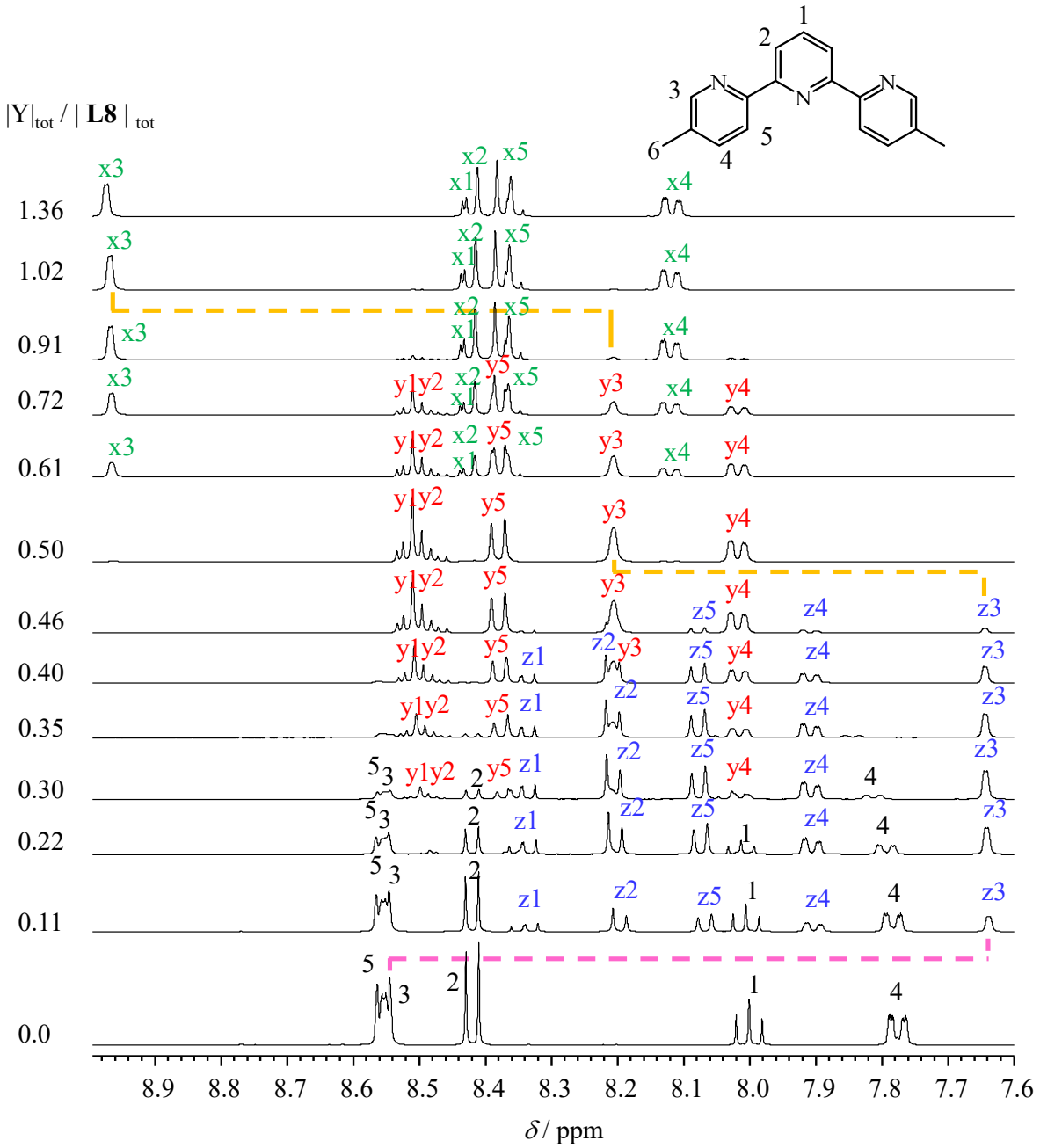

Figure S12 Aromatic parts of the ^{1}H NMR spectra with numbering scheme recorded upon titration of **L8** with $Y(CF_3SO_3)_3$ in CD_3CN at 298 K with numbering scheme. ($5\times10^{-3} \leq |\mathbf{L8}|_{tot} \leq 9\times10^{-3}$ M and $6\times10^{-4} \leq |Y|_{tot} \leq 8\times10^{-3}$ M). The letters x, y and z denote signals arising from the 1:1 (green), 1:2 (red) and 1:3 (blue) species, respectively.

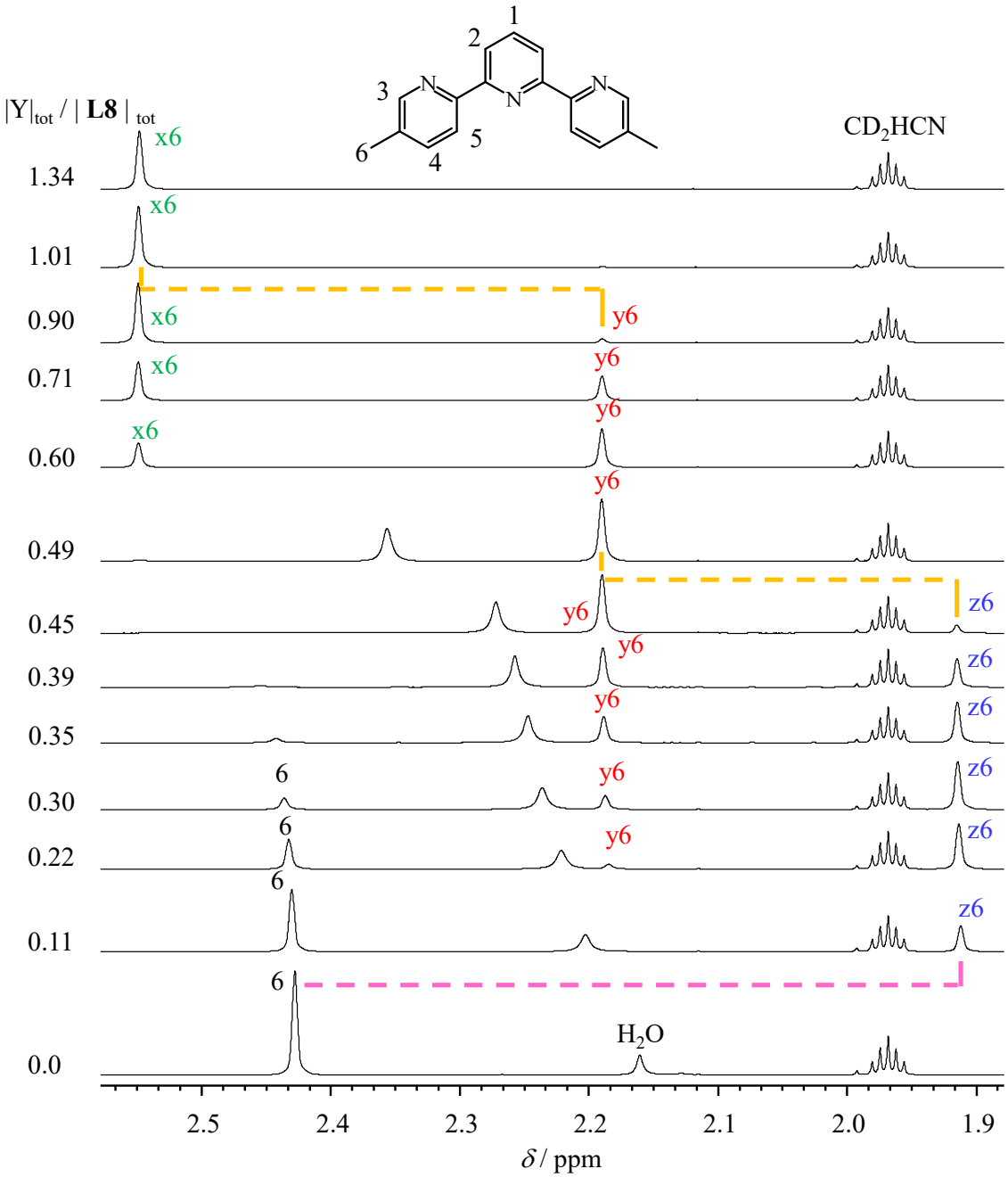

Figure S13 Aliphatic parts of the ^{1}H NMR spectra with numbering scheme recorded upon titration of **L8** with $Y(CF_3SO_3)_3$ in CD_3CN at 298 K with numbering scheme. ($5\times10^{-3} \leq |\mathbf{L8}|_{tot} \leq 9\times10^{-3}$ M and $6\times10^{-4} \leq |Y|_{tot} \leq 8\times10^{-3}$ M). The letters x, y and z denote signals arising from the 1:1 (green), 1:2 (red) and 1:3 (blue) species, respectively.

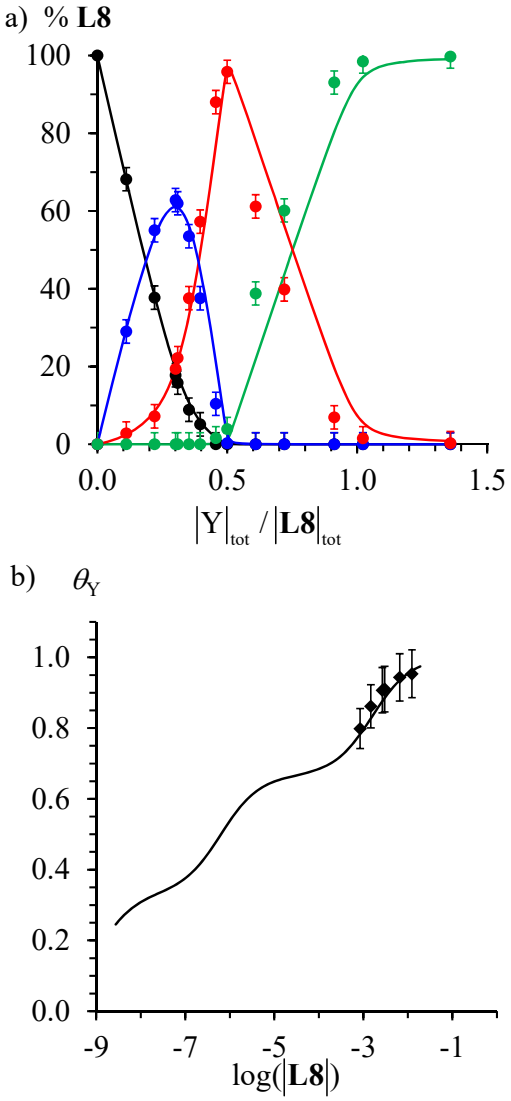

Figure S14 a) Macroscopic ligand speciations obtained by integration of ^{1}H NMR signals during the titration of **L8** (1.8×10^{-2} M) with $Y(CF_3SO_3)_3$ in CD_3CN at 298 K (discs, color code: black = **L8**, blue = $[Y(\mathbf{L8})_3]^{3+}$, red = $[Y(\mathbf{L8})_2]^{3+}$ and green = $[Y(\mathbf{L8})]^{3+}$) and b) associated binding isotherm (diamonds, Eq. (7)). The full traces correspond to the re-constructed a) distribution and b) binding isotherm computed for equilibria (4)-(6) with $\beta_{1,1}^{Y,\mathbf{L8}} = 9.0$, $\beta_{1,2}^{Y,\mathbf{L8}} = 15.2$ and $\beta_{1,3}^{Y,\mathbf{L8}} = 18.0$.

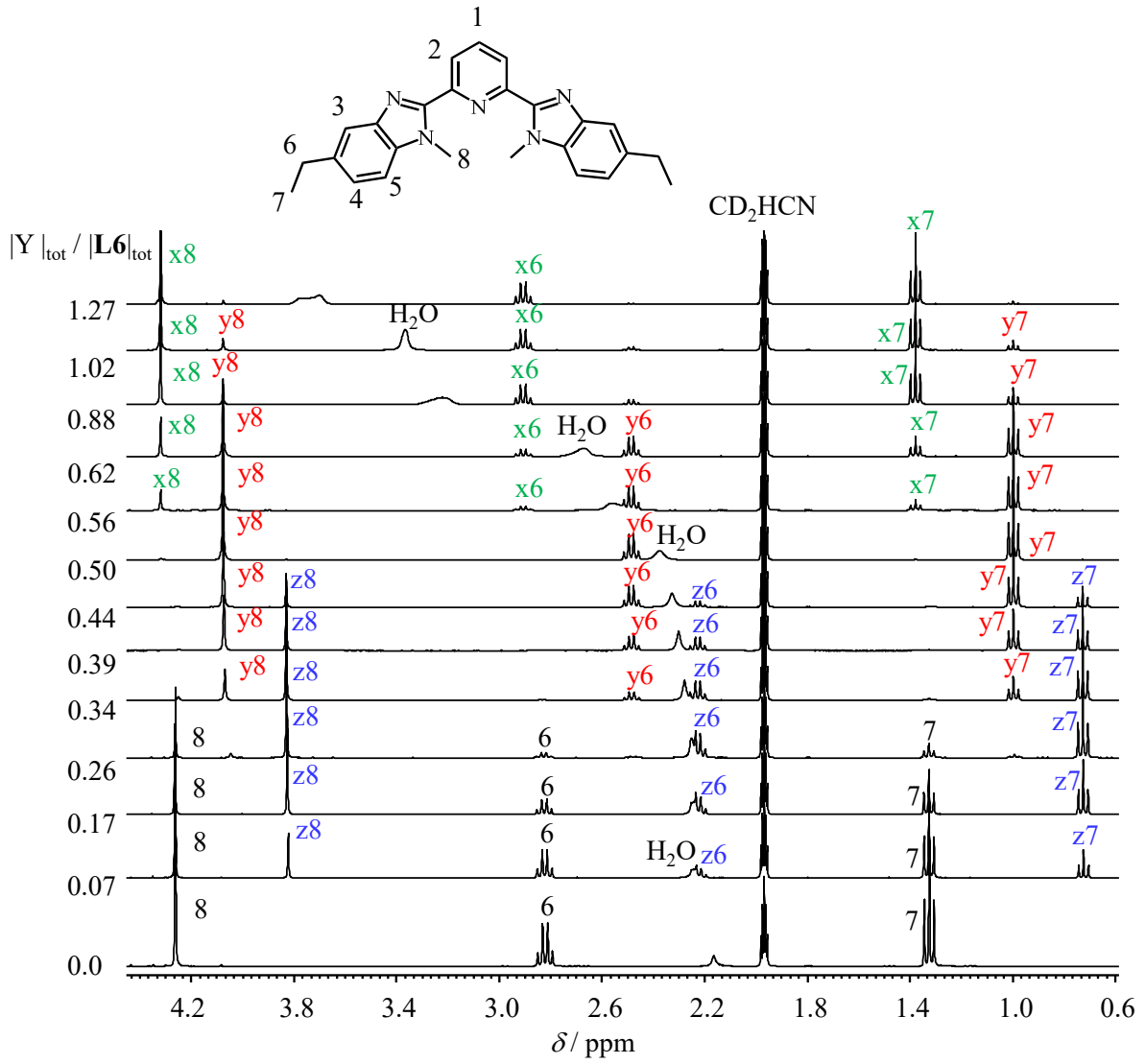

Figure S15 Aliphatic parts of the ^{1}H NMR spectra with numbering scheme recorded upon titration of **L6** with $Y(CF_3SO_3)_3$ in CD_3CN at 298 K with numbering scheme. ($5\times10^{-3} \leq |\mathbf{L6}|_{tot} \leq 9\times10^{-3}$ M and $6\times10^{-4} \leq |Y|_{tot} \leq 8\times10^{-3}$ M). The letters x, y and z denote signals arising from the 1:1 (green), 1:2 (red) and 1:3 (blue) species, respectively.

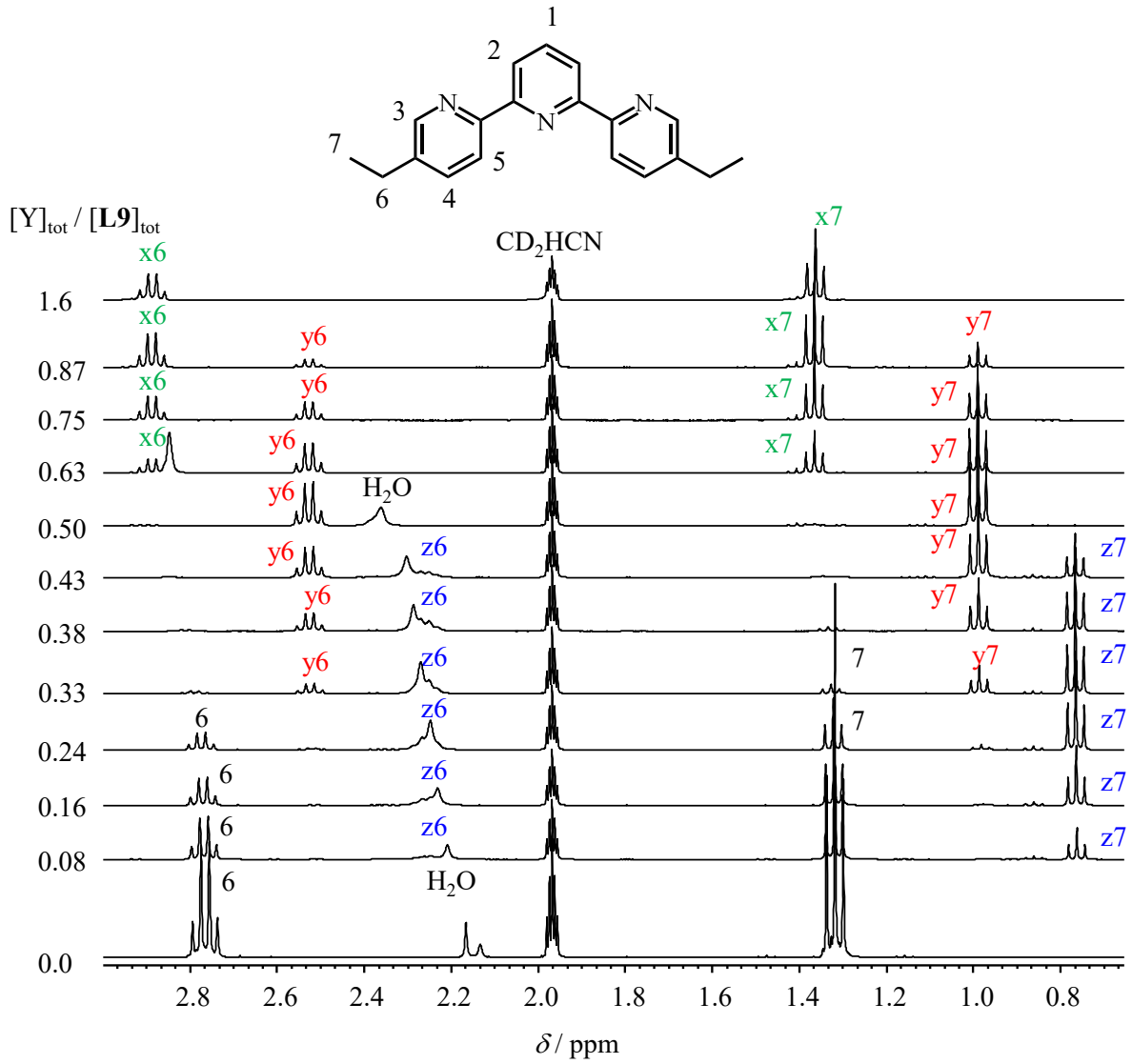

Figure S16 Aliphatic parts of the ^{1}H NMR spectra with numbering scheme recorded upon titration of **L9** with $Y(CF_3SO_3)_3$ in CD_3CN at 298 K with numbering scheme. ($5\times10^{-3} \leq |\mathbf{L9}|_{tot} \leq 9\times10^{-3}$ M and $6\times10^{-4} \leq |Y|_{tot} \leq 8\times10^{-3}$ M). The letters x, y and z denote signals arising from the 1:1 (green), 1:2 (red) and 1:3 (blue) species, respectively.

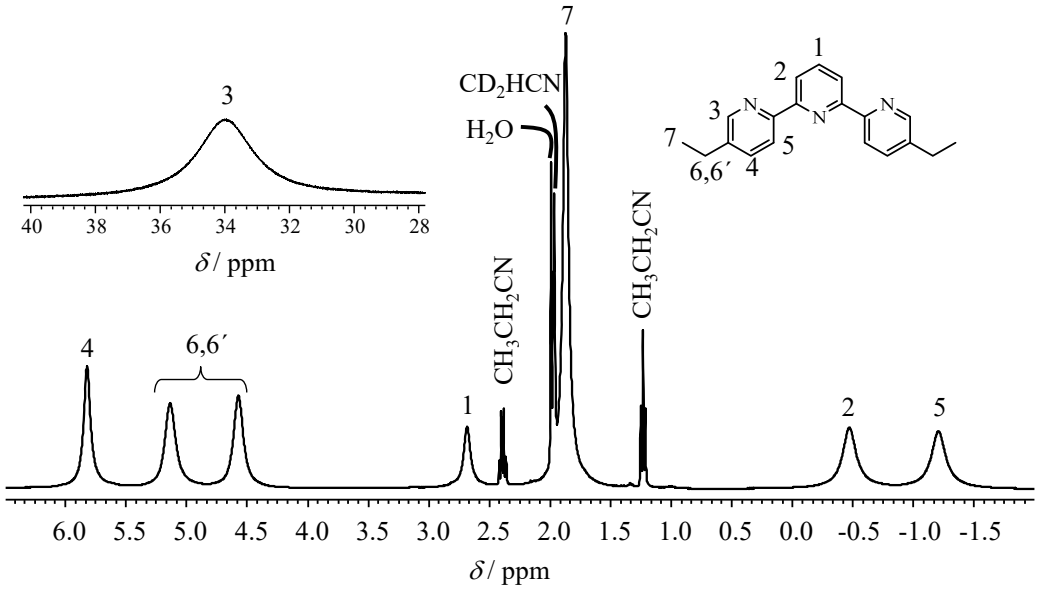

Figure S17 ^{1}H NMR spectrum with numbering scheme of $[Er(\mathbf{L9})_3](ClO_4)_3 \cdot 0.05CH_3CH_2CN \cdot 0.7H_2O$ in CD_3CN ($4.5 \cdot 10^{-2}$ M) at 298 K.

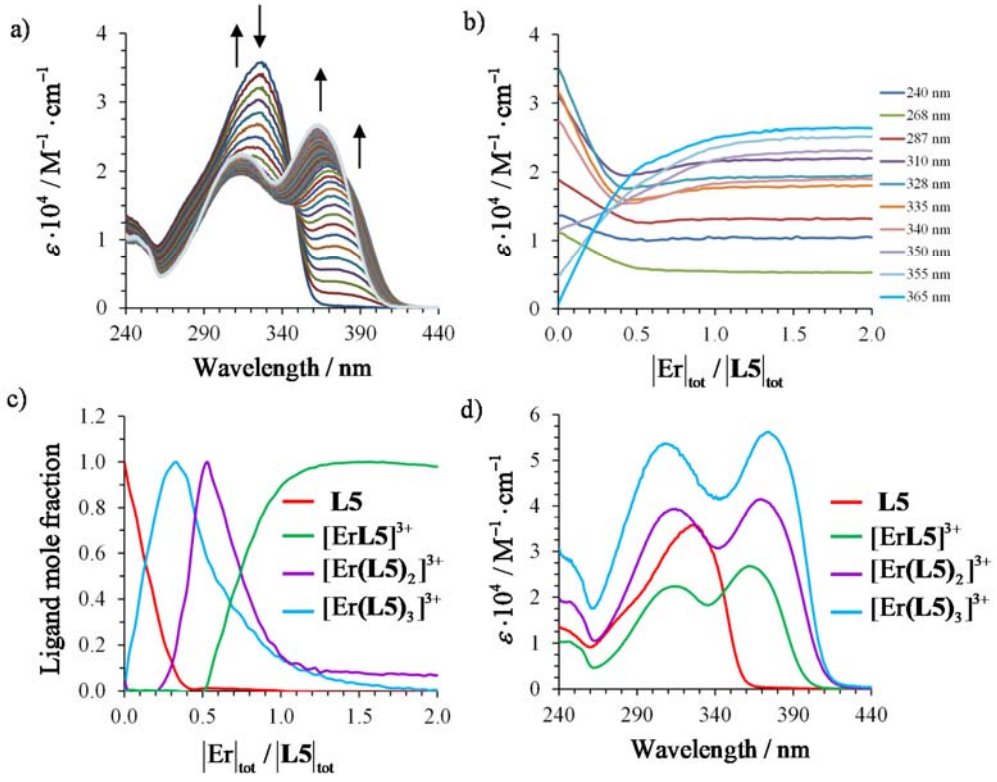

Figure S18. a) Variation of absorption spectra and b) corresponding variation of molar extinction at different wavelengths observed for the spectrophotometric titration of **L5** with $Er(CF_3SO_3)_3$ (total ligand concentration: $2.5 \cdot 10^{-4}$ mol·dm^{-3} in acetonitrile, 298 K). c) Evolving factor analysis[46] using four absorbing eigenvectors and d) reconstructed individual electronic absorption spectra.

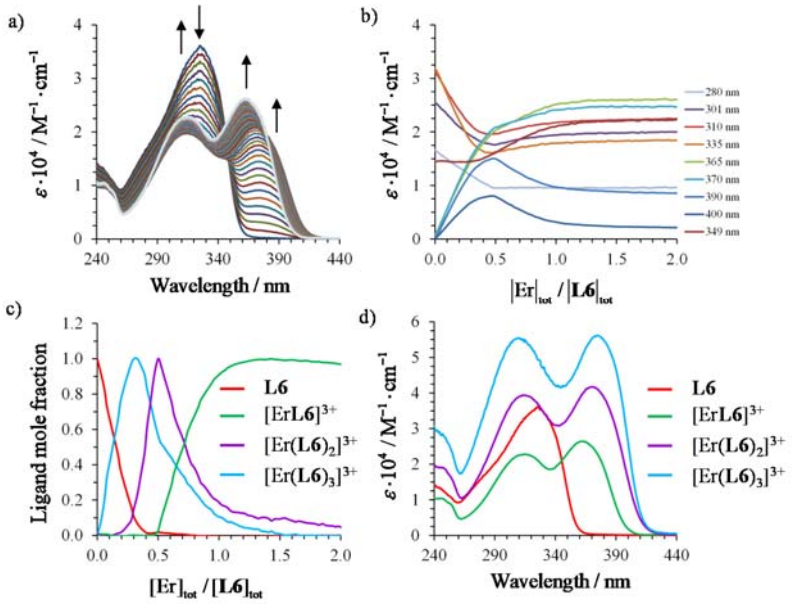

Figure S19. a) Variation of absorption spectra and b) corresponding variation of molar extinction at different wavelengths observed for the spectrophotometric titration of **L6** with $Er(CF_3SO_3)_3$ (total ligand concentration: $3.0 \cdot 10^{-4}$ mol·dm^{-3} in acetonitrile, 298 K). c) Evolving factor analysis[46] using four absorbing eigenvectors and d) reconstructed individual electronic absorption spectra.

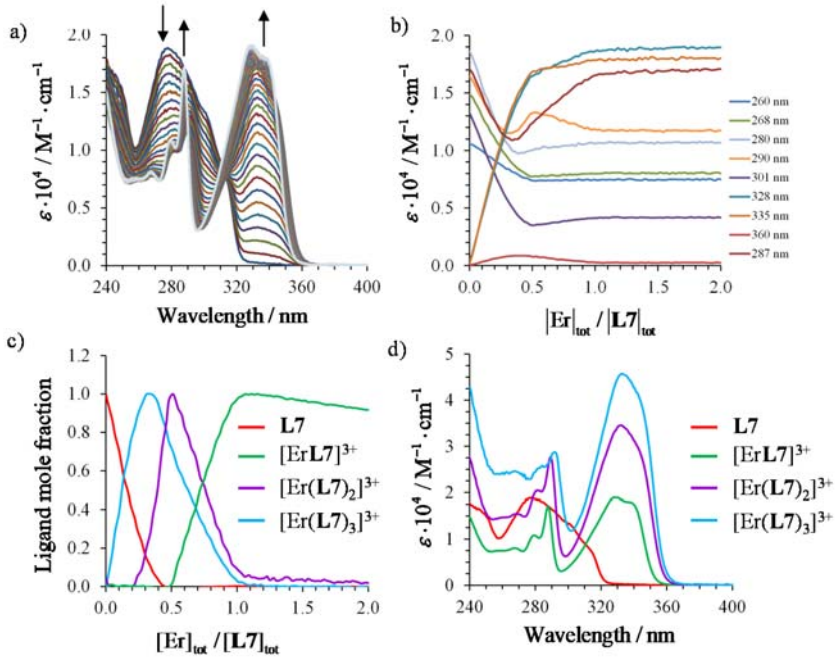

Figure S20. a) Variation of absorption spectra and b) corresponding variation of molar extinction at different wavelengths observed for the spectrophotometric titration of **L7** with $Er(CF_3SO_3)_3$ (total ligand concentration: $3.5 \cdot 10^{-4}$ mol·dm^{-3} in acetonitrile, 298 K). c) Evolving factor analysis[46] using four absorbing eigenvectors and d) reconstructed individual electronic absorption spectra.

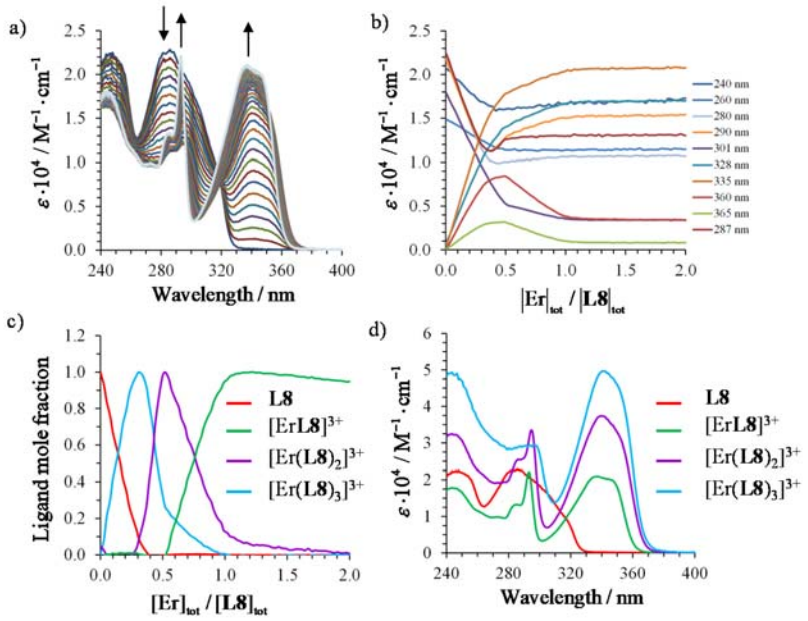

Figure S21. a) Variation of absorption spectra and b) corresponding variation of molar extinction at different wavelengths observed for the spectrophotometric titration of **L8** with $Er(CF_3SO_3)_3$ (total ligand concentration: $3.2 \cdot 10^{-4}$ mol·dm^{-3} in acetonitrile, 298 K). c) Evolving factor analysis[46] using four absorbing eigenvectors and d) reconstructed individual electronic absorption spectra.

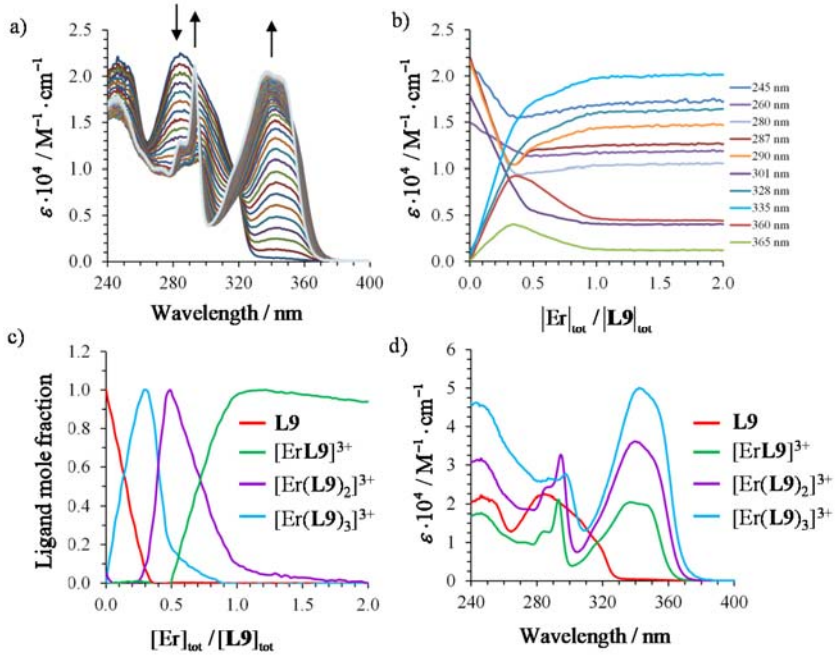

Figure S22. a) Variation of absorption spectra and b) corresponding variation of molar extinction at different wavelengths observed for the spectrophotometric titration of **L9** with $Er(CF_3SO_3)_3$ (total ligand concentration: $3.5 \cdot 10^{-4}$ mol·dm^{-3} in acetonitrile, 298 K). c) Evolving factor analysis[46] using four absorbing eigenvectors and d) reconstructed individual electronic absorption spectra.

a)

$$[Er(CH_3CN)_9]^{3+} + \textbf{L4} \xrightleftharpoons{\beta_{1,1}^{Er,\textbf{L4}}} [Er(\textbf{L4})(CH_3CN)_6]^{3+} + 3\ CH_3CN$$

Point group	D_{3h}	C_{2v}	C_{2v}	C_{3v}
σ_{ext}	6	2	2	3
σ_{int}	3^9	3^2	$3^2 \times 3^6$	1
σ_{mix}	1	1	1	1

$$\omega_{1,1}^{chiral} = \frac{1\times 1}{1\times (1)^3} = 1,\ \omega_{1,1}^{Er,\textbf{L4}} = \frac{6\times 3^9 \times 2\times 3^2}{2\times 3^2 \times 3^6 \times (3)^3} = 6 \Rightarrow K_{1,1}^{stat} = \omega_{1,1}^{chiral} \cdot \omega_{1,1}^{Er,\textbf{L4}} = 6$$

b)

$$[Er(CH_3CN)_9]^{3+} + 2\ \textbf{L4} \xrightleftharpoons{\beta_{1,2}^{Er,\textbf{L4}}} [Er(\textbf{L4})_2(CH_3CN)_3]^{3+} + 6\ CH_3CN$$

Point group	D_{3h}	C_{2v}	C_{2v}	C_{3v}
σ_{ext}	6	2	2	3
σ_{int}	3^9	3^2	$3^4 \times 3^3$	1
σ_{mix}	1	1	1	1

$$\omega_{1,2}^{chiral} = \frac{1\times 1^2}{1\times (1)^6} = 1,\ \omega_{1,2}^{Er,\textbf{L4}} = \frac{6\times 3^9 \times (2)^2 \times (3^2)^2}{2\times 3^4 \times 3^3 \times (3)^6} = 12 \Rightarrow K_{1,2}^{stat} = \omega_{1,2}^{chiral} \cdot \omega_{1,2}^{Er,\textbf{L4}} = 12$$

c)

$$[Er(CH_3CN)_9]^{3+} + 3\ \textbf{L4} \xrightleftharpoons{\beta_{1,3}^{Er,\textbf{L4}}} [Er(\textbf{L4})_3]^{3+} + 9\ CH_3CN$$

Point group	D_{3h}	C_{2v}	D_3	C_{3v}
σ_{ext}	6	2	6	3
σ_{int}	3^9	3^2	3^6	1
σ_{mix}	1	1	$\frac{1}{2}$	1

$$\omega_{1,3}^{chiral} = \frac{1\times 1^3}{\frac{1}{2}\times (1)^9} = 2,\ \omega_{1,3}^{Er,\textbf{L4}} = \frac{6\times 3^9 \times (2)^3 \times (3^2)^3}{6\times 3^6 \times (3)^9} = 8 \Rightarrow K_{1,3}^{stat} = \omega_{1,3}^{chiral} \cdot \omega_{1,3}^{Er,\textbf{L4}} = 16$$

Figure S23 Symmetry numbers obtained by *Benson*'s method and associated statistical factors computed for the formation of a) $[Er(\textbf{L4})]^{+3}$, b) $[Er(\textbf{L4})_2]^{+3}$ and c) $[Er(\textbf{L4})_3]^{+3}$.

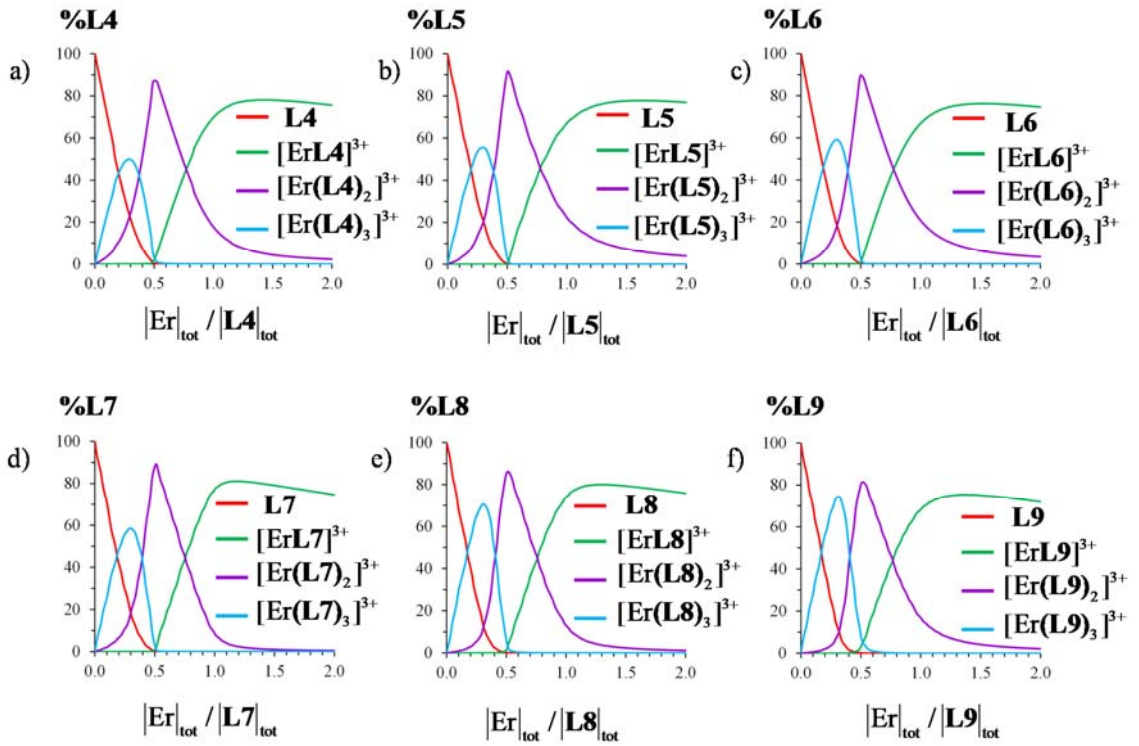

Figure S24 Macroscopic speciation curves computed for the spectrophotometric titrations of ligands **L4-L9** with $Er(CF_3SO_3)_3$ ($|\mathbf{Lk}|_{tot} \approx 3\times10^{-4}$ M in acetonitrile, 298 K).

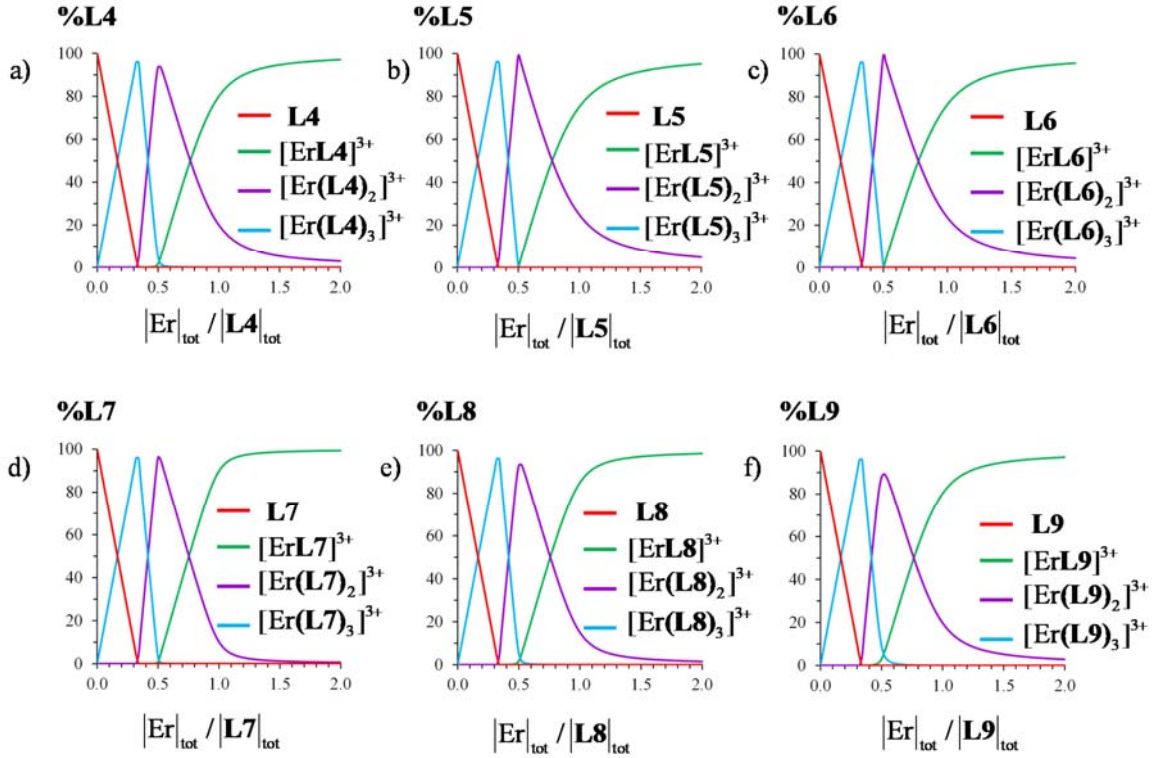

Figure S25 Macroscopic speciation curves computed for the spectrophotometric titrations of ligands **L4-L9** with $Er(CF_3SO_3)_3$ ($|\mathbf{Lk}|_{tot} \approx 1$M in acetonitrile, 298 K).

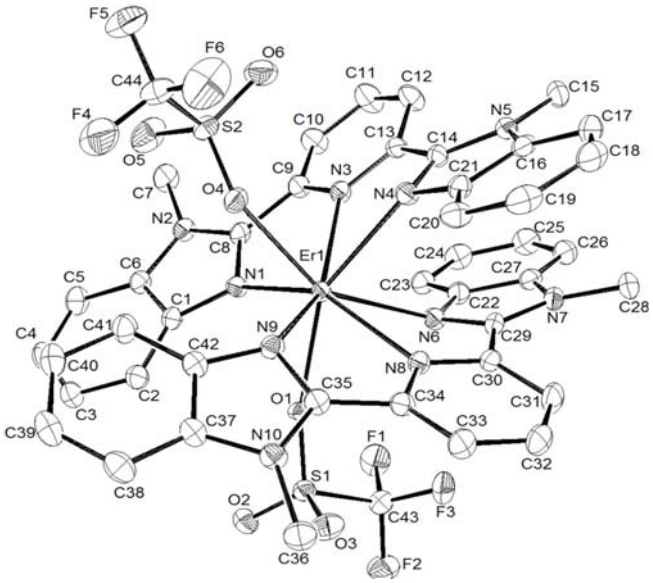

Figure S26 ORTEP molecular view with numbering scheme of the asymmetric unit for $[Er(\mathbf{L4})_2(O_3SCF_3)_2]^+$ in the crystal structure of **1**. Thermal ellipsoids are represented at the 40% probability level and hydrogen atoms are omitted for clarity.

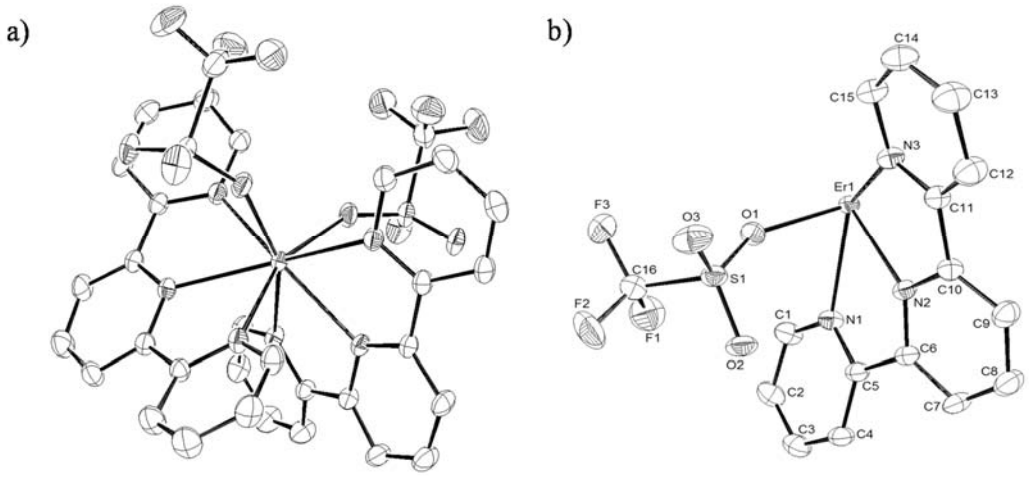

Figure S27 ORTEP molecular view of a) $[Er(\mathbf{L7})_2(O_3SCF_3)_2]^+$ in the crystal structure of **2** and b) numbering scheme of the asymmetric unit. Thermal ellipsoids are represented at the 40% probability level and hydrogen atoms are omitted for clarity.

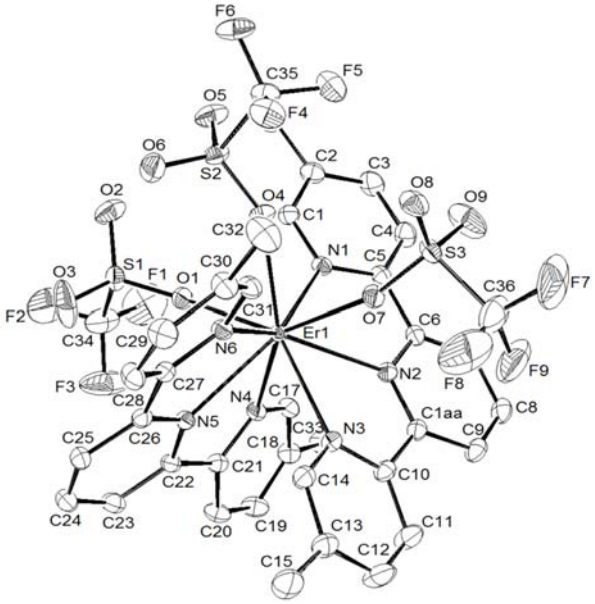

Figure S28 ORTEP molecular view with numbering scheme of the asymmetric unit for Er(**L8**)$_2$(O$_3$SCF$_3$)$_3$ in the crystal structure of **3**. Thermal ellipsoids are represented at the 40% probability level and hydrogen atoms are omitted for clarity.

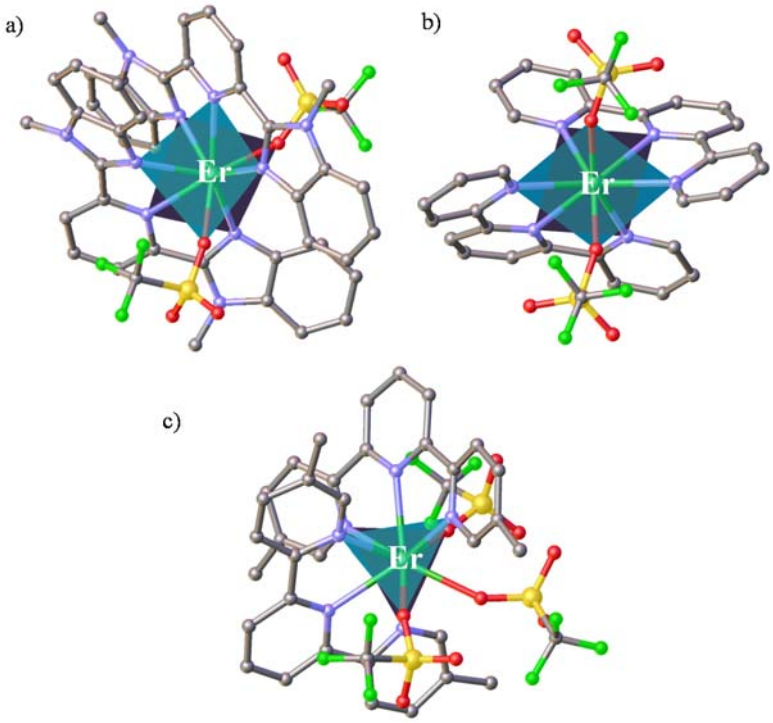

Figure S29 Perspective views of complexes a) [Er(**L4**)$_2$(O$_3$SCF$_3$)$_2$]$^+$ (**1**), b) [Er(**L7**)$_2$(O$_3$SCF$_3$)$_2$]$^+$ (**2**) and c) Er(**L8**)$_2$(O$_3$SCF$_3$)$_3$ (**3**) showing the pseudo-square antiprismatic (for complexes **1** and **2**) and distorted tricapped trigonal-prismatic (for complex **3**) arrangements around trivalent erbium.

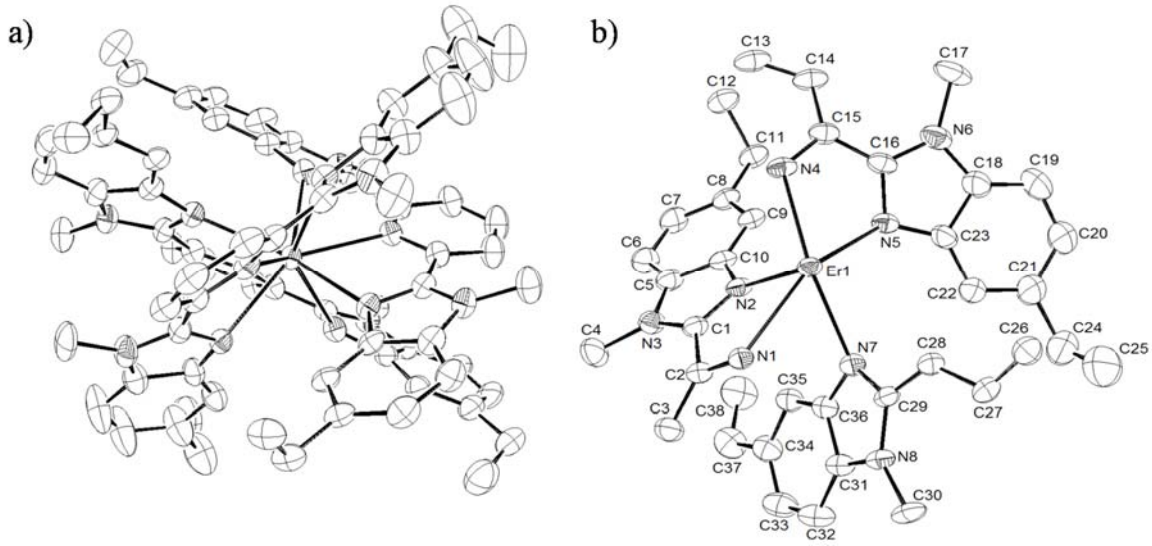

Figure S30 ORTEP molecular view of a) $[Er(\mathbf{L6})_3]^{3+}$ in the crystal structure of **4** and b) numbering scheme of the asymmetric unit. Thermal ellipsoids are represented at the 40% probability level and hydrogen atoms are omitted for clarity.

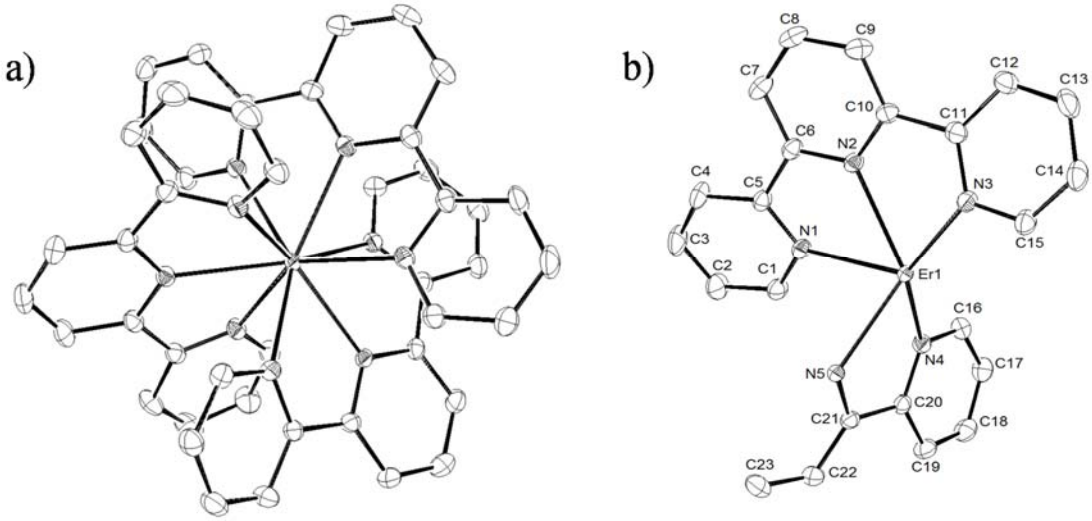

Figure S31 ORTEP molecular view of a) $[Er(\mathbf{L7})_3]^{3+}$ in the crystal structure of **5** and b) numbering scheme of the asymmetric unit. Thermal ellipsoids are represented at the 40% probability level and hydrogen atoms are omitted for clarity.

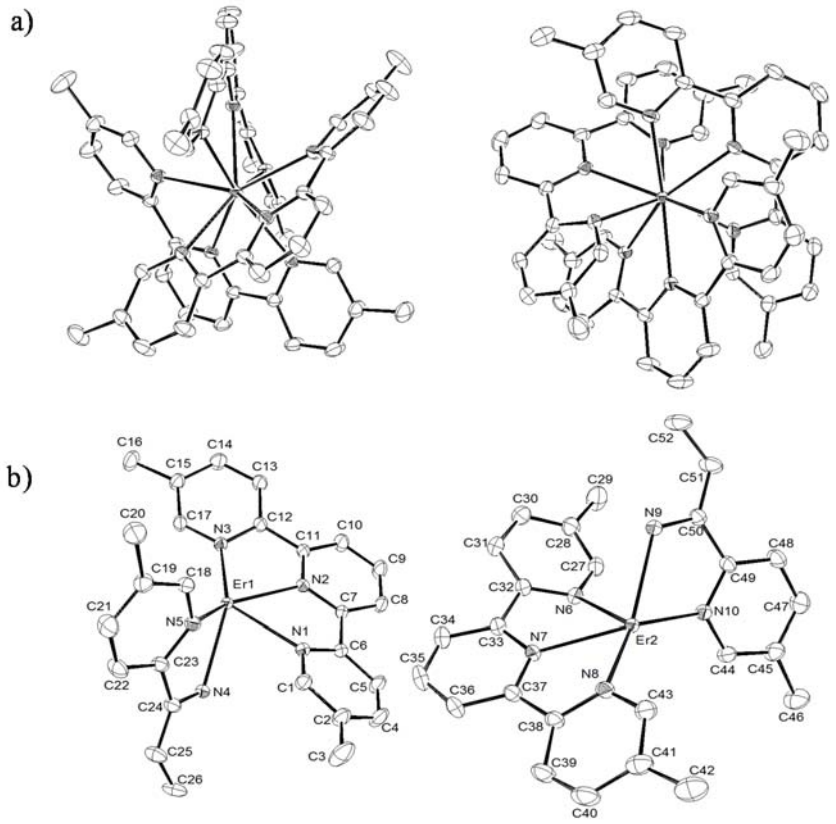

Figure S32 ORTEP molecular view of a) $[Er(\mathbf{L8})_3]^{3+}$ in the crystal structure of **6** and b) numbering scheme of the asymmetric unit (the asymmetric unit in the crystal structure of **6** contains two slightly different $[Er(\mathbf{L8})_3]^{3+}$ cations). Thermal ellipsoids are represented at the 40% probability level and hydrogen atoms are omitted for clarity.

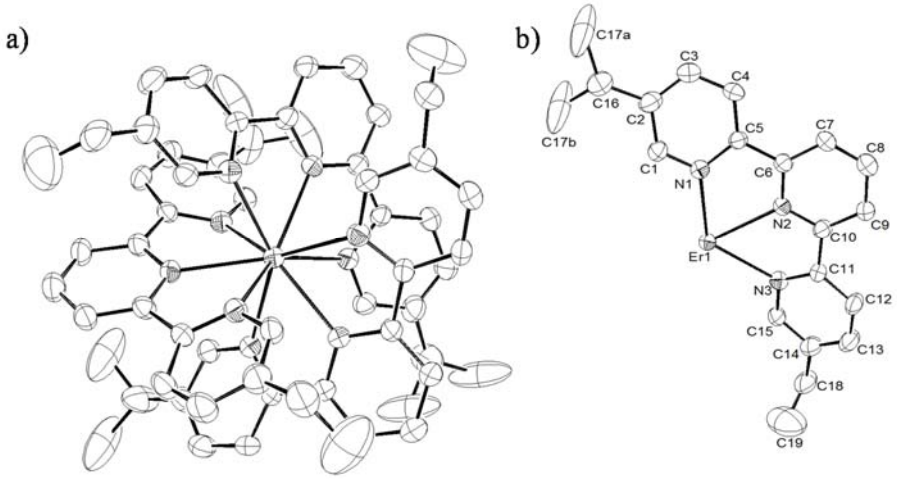

Figure S33 ORTEP molecular view of a) $[Er(\mathbf{L9})_3]^{3+}$ in the crystal structure of **7** and b) numbering scheme of the asymmetric unit. Thermal ellipsoids are represented at the 40% probability level and hydrogen atoms are omitted for clarity.

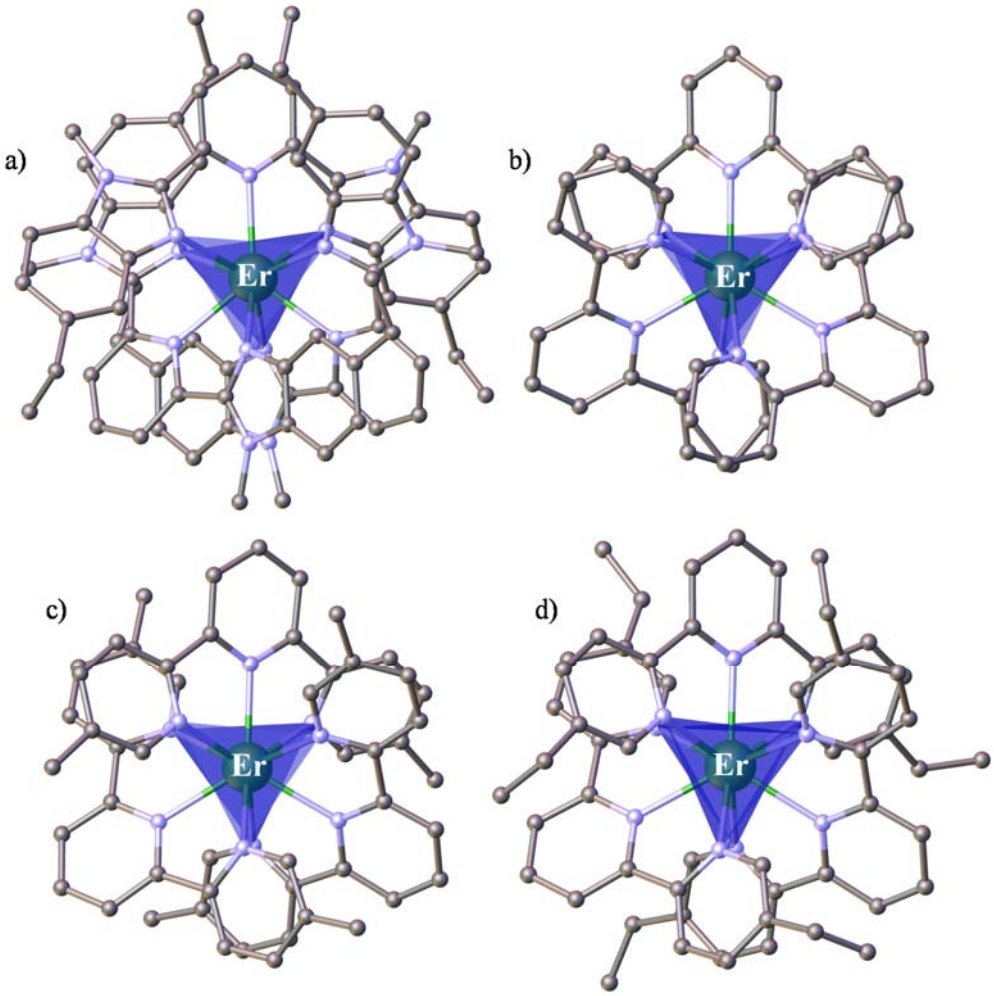

Figure S34 Perspective views of complexes a) $[Er(\mathbf{L6})_3]^{3+}$, b) $[Er(\mathbf{L7})_3]^{3+}$, c) $Er(\mathbf{L8})_3]^{3+}$ and d) $[Er(\mathbf{L9})_3]^{3+}$ along the pseudo-C_3 axis which highlight the distorted tricapped trigonal-prismatic arrangements around trivalent erbium.

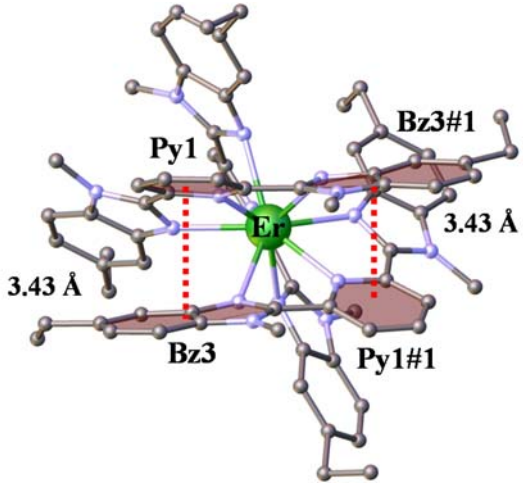

Figure S35 Perspective view of complex $[Er(\mathbf{L6})_3]^{3+}$ perpendicular to the pseudo-C_3 axis showing the intramolecular π-π interactions.

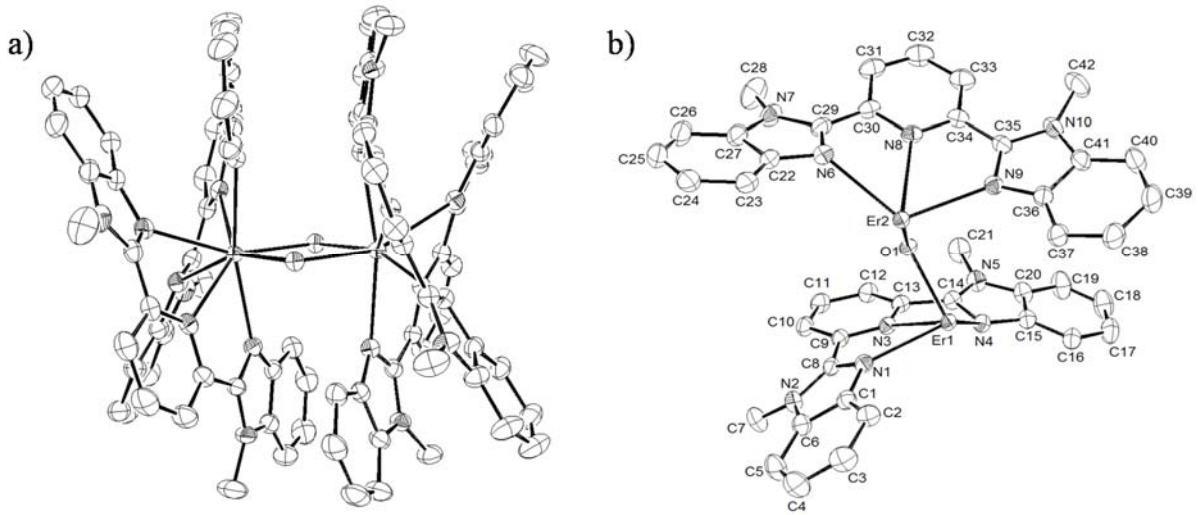

Figure S36 ORTEP molecular view of a) $[(\mathbf{L4})_2Er(OH)_2Er(\mathbf{L4})_2]^{4+}$ in the crystal structure of **8** and b) numbering scheme of the asymmetric unit. Thermal ellipsoids are represented at the 40% probability level and hydrogen atoms are omitted for clarity.

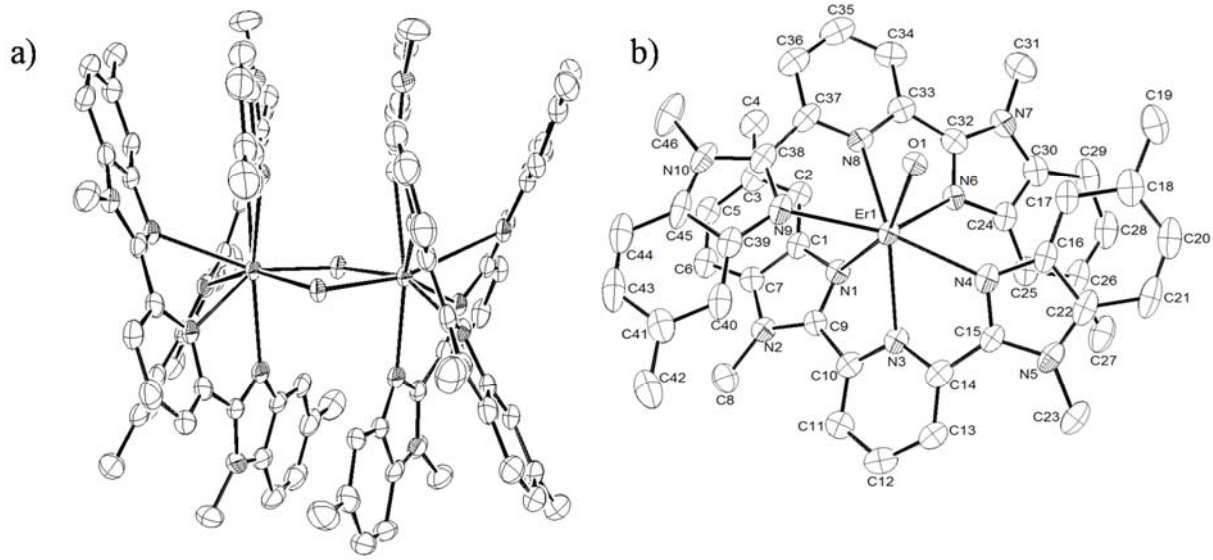

Figure S37 ORTEP molecular view of a) $[(\mathbf{L5})_2Er(OH)_2Er(\mathbf{L5})_2]^{4+}$ in the crystal structure of **9** and b) numbering scheme of the asymmetric unit. Thermal ellipsoids are represented at the 40% probability level and hydrogen atoms are omitted for clarity.

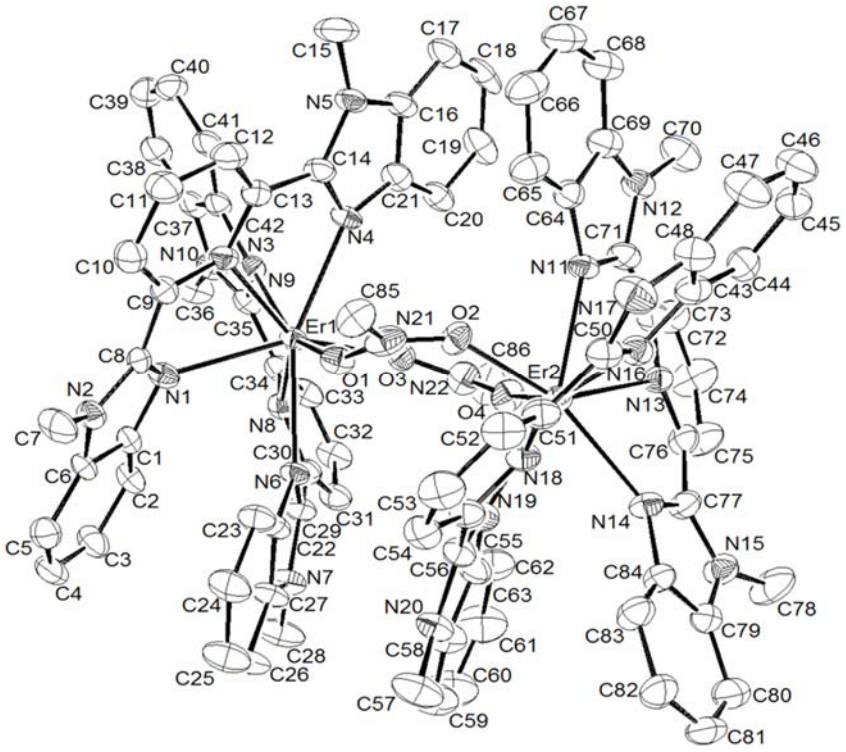

Figure S38 ORTEP molecular view with numbering scheme of the asymmetric unit for $[(\mathbf{L4})_2Er((CH_3)NO_2)_2Er(\mathbf{L4})_2]^{6+}$ in the crystal structure of **10**. Thermal ellipsoids are represented at the 40% probability level and hydrogen atoms are omitted for clarity.

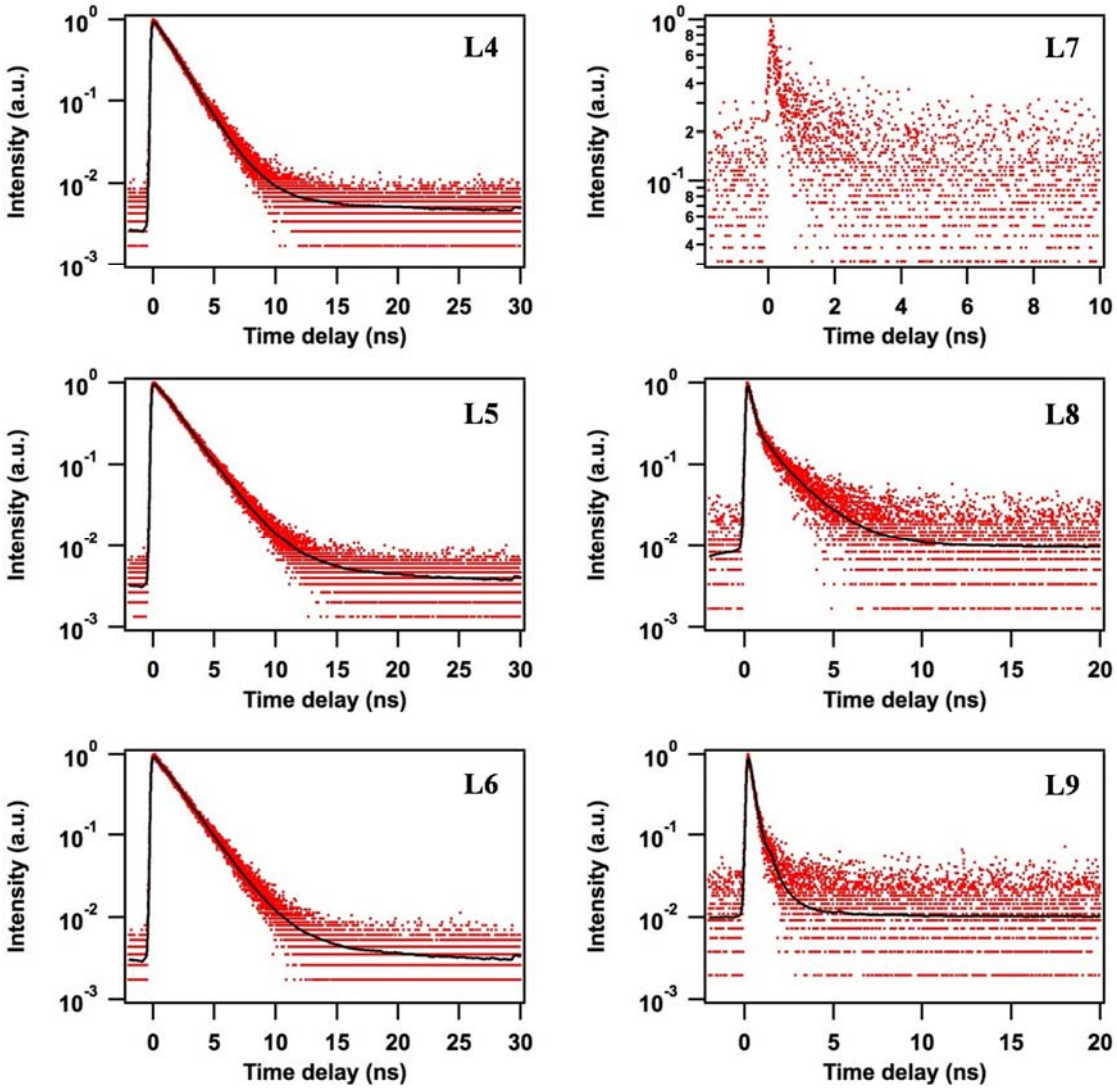

Figure S39 Fluorescence time profiles of **L4-L9** in acetonitrile upon excitation at 320 nm. The black solid traces represent best fits to the data points. The quality of the experimental data obtained with **L7** (extremely low signal) prevented from an exponential fit to the data to properly converge; therefore only the raw data is shown.

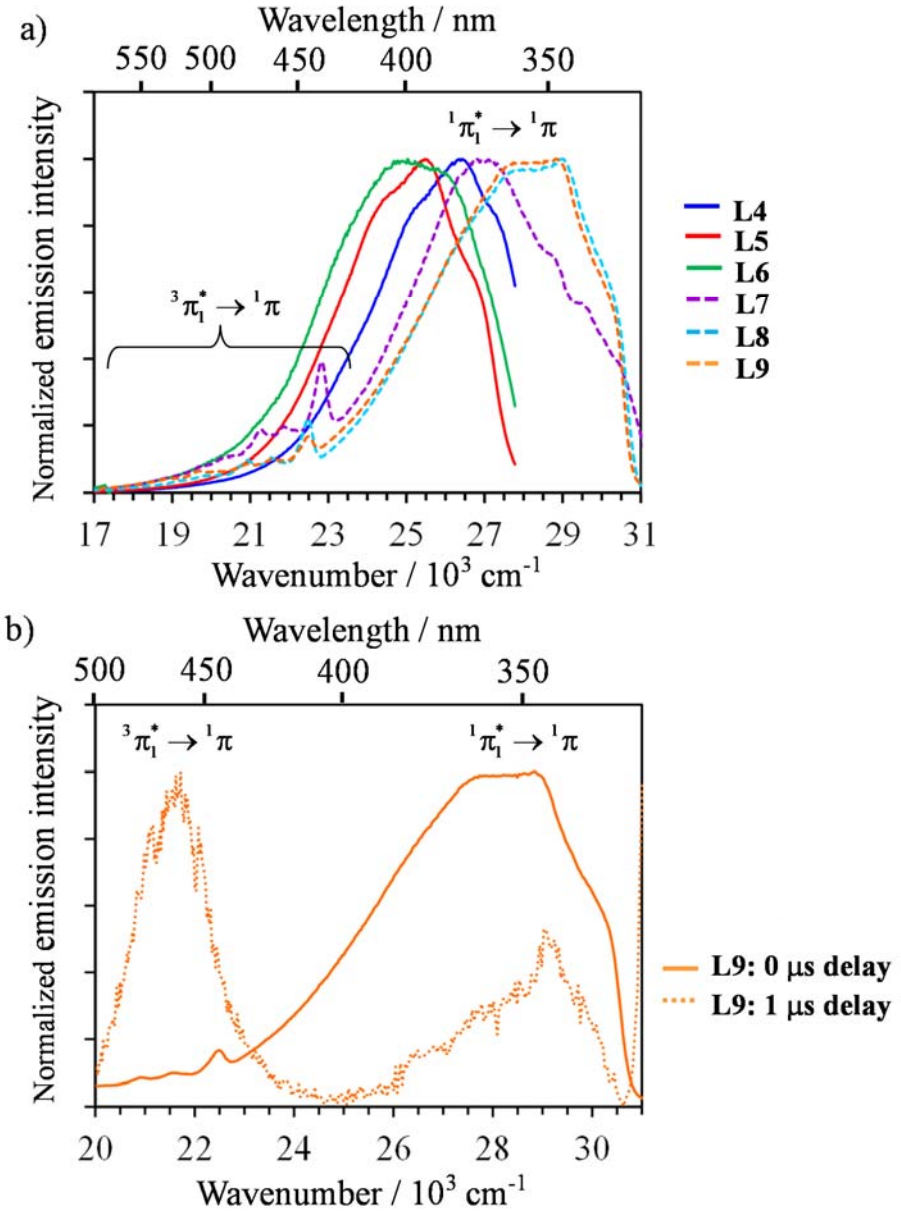

Figure S40 a) Normalized emission spectra recorded for ligands **L4-L6** (λ_{exc} = 330 nm, full traces) and **L7-L9** (λ_{exc} = 280 nm) in frozen acetonitrile (0.3 mM) at 77 K. b) Normalized emission (full trace) and time-gated (1.0 µs delay, dotted trace) recorded for **L9** (λ_{exc} = 280 nm) in frozen acetonitrile (0.3 mM) at 77 K highlighting the weak spin-forbidden $^3\pi_1 \rightarrow {}^1\pi$ transition.

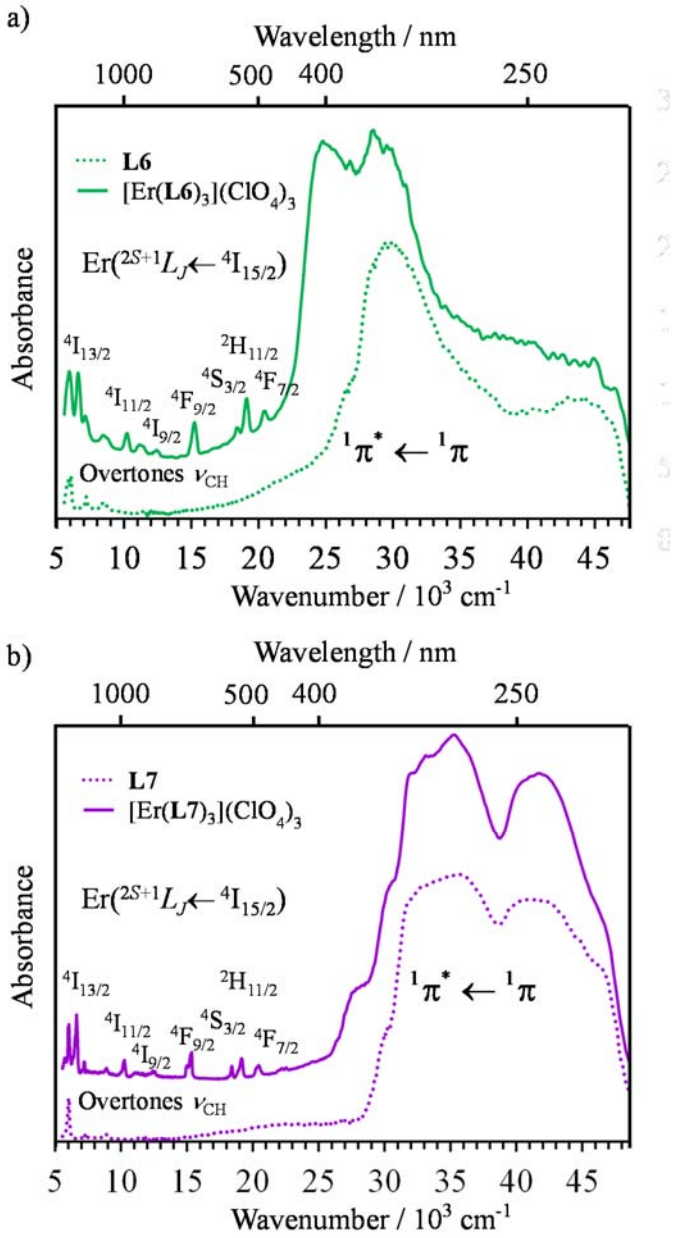

Figure S41 Comparison of the absorption spectra recorded a) ligand **L6** and its triple helical complex $[Er(\mathbf{L6})_3](ClO_4)_3$ (**4**) and b) ligand **L7** and its triple helical complex $[Er(\mathbf{L7})_3](ClO_4)_3$ (**5**) recorded in the solid-state at room temperature. The samples were diluted in MgO (85 wt %).

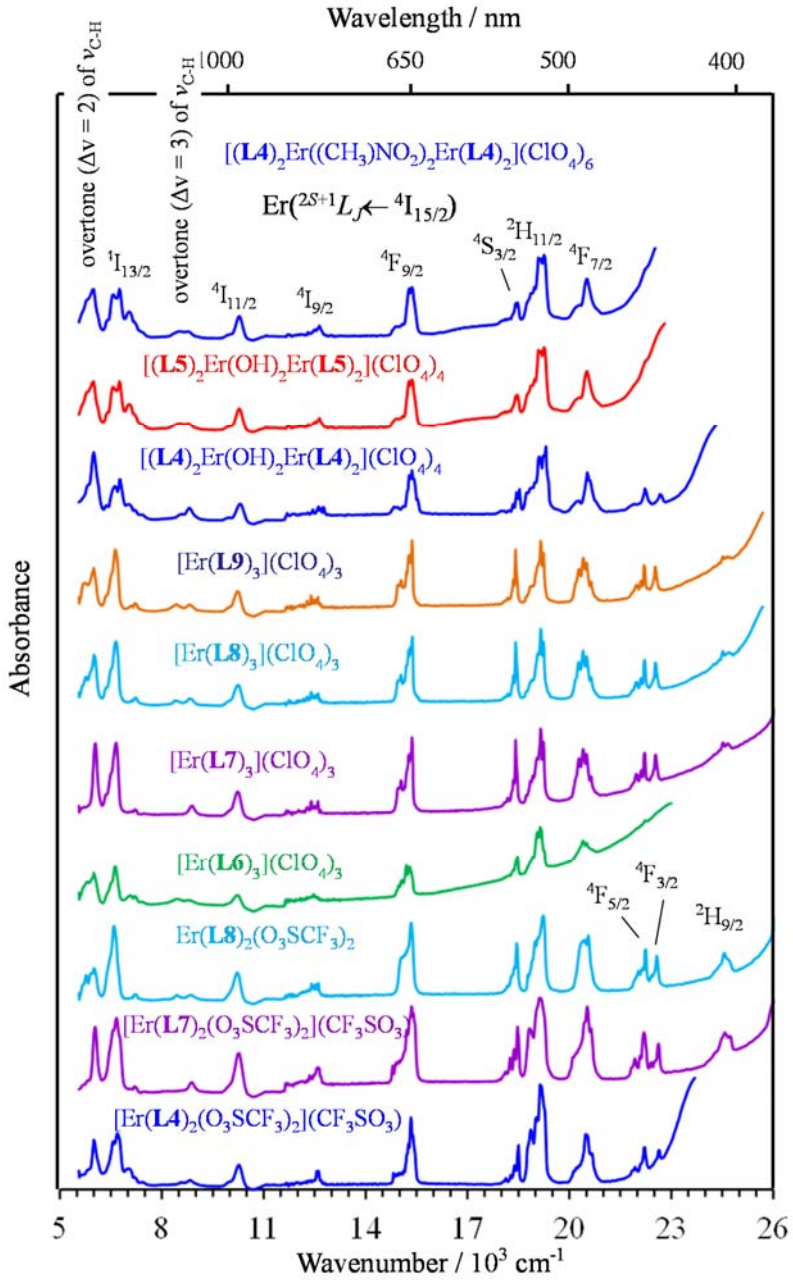

Figure S42 Vis to NIR absorption spectra of the complexes [Er(**L4**)$_2$(CF$_3$SO$_3$)$_2$](CF$_3$SO$_3$)·2CH$_3$CN (**1**), [Er(**L7**)$_2$(CF$_3$SO$_3$)$_2$](CF$_3$SO$_3$)·1.5C$_2$H$_5$CN (**2**),[21a] [Er(**L8**)$_2$(CF$_3$SO$_3$)$_3$] (**3**), [Er(**L6**)$_3$](ClO$_4$)$_3$·1.5CH$_3$CN (**4**), [Er(**L7**)$_3$](ClO$_4$)$_3$ (**5**), [Er(**L8**)$_3$](ClO$_4$)$_3$ (**6**) and [Er(**L9**)$_3$](ClO$_4$)$_3$·1.5CH$_3$CN (**7**) [(**L4**)$_2$Er(OH)$_2$Er(**L4**)$_2$](ClO$_4$)$_4$·2C$_6$H$_5$CN·4CH$_3$CN (**8**), [(**L5**)$_2$Er(OH)$_2$Er(**L5**)$_2$](ClO$_4$)$_4$·C$_6$H$_5$CN·8CH$_3$CN (**9**) and [(**L4**)$_2$Er(CH$_3$NO$_2$)$_2$Er(**L4**)$_2$](ClO$_4$)$_6$·CH$_3$NO$_2$ (**10**) recorded in the solid-state at room temperature and assigned as Er($^{2S+1}L_J \leftarrow {}^4I_{15/2}$) transitions.

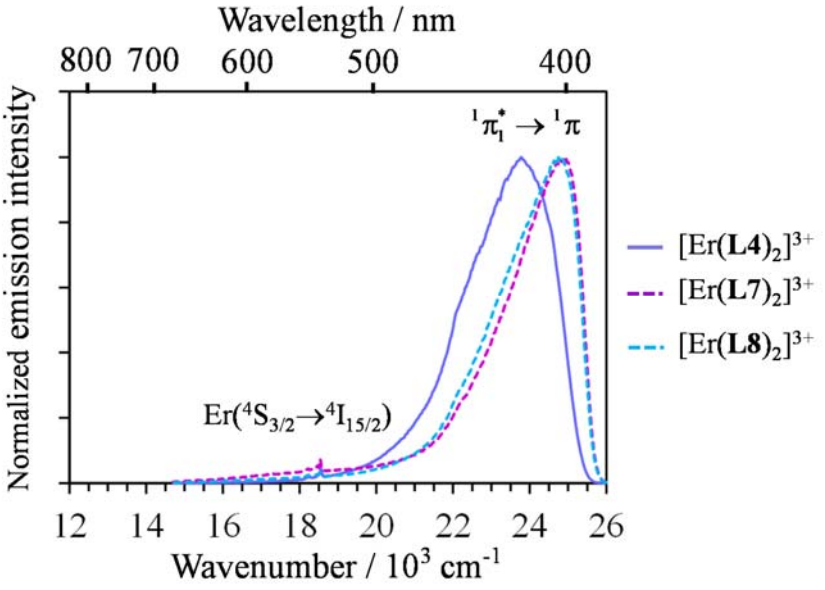

Figure S43 Visible emission spectra recorded for the complexes [Er(**L4**)$_2$]$^{3+}$ (λ_{exc} = 370 nm), [Er(**L7**)$_2$]$^{3+}$ and [Er(**L8**)$_2$]$^{3+}$ (λ_{exc} = 350 nm) in frozen acetonitrile solution (3.0 mM) at 77 K.

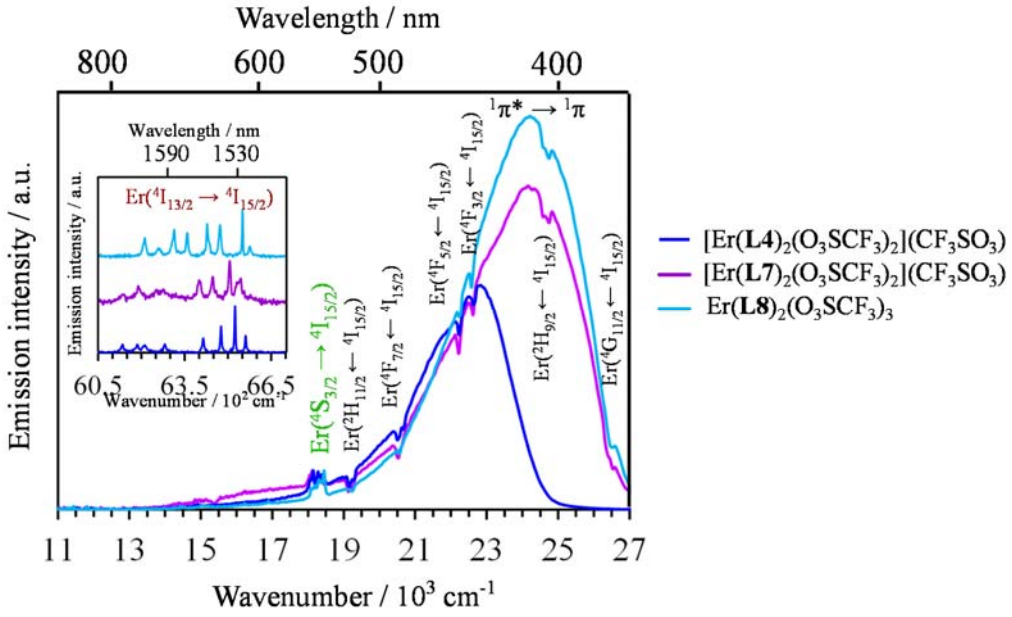

Figure S44 Visible emission spectra recorded for solid-state complexes [Er(**L4**)$_2$(CF$_3$SO$_3$)$_2$](CF$_3$SO$_3$) (**1**), [Er(**L7**)$_2$(CF$_3$SO$_3$)$_2$](CF$_3$SO$_3$) (**2**), [Er(**L8**)$_2$(CF$_3$SO$_3$)$_3$] (**3**) (λ_{exc} = 350 nm) at 7 K. The inset shows the associated near-infrared emission spectra (λ_{exc} = 447 nm, 11 K). The dual emission is assigned with color fonts, while the dips (assigned using black fonts) correspond to Er-centered re-absorption of the residual ligand-centered $^1\pi^* \rightarrow \pi$ emission.

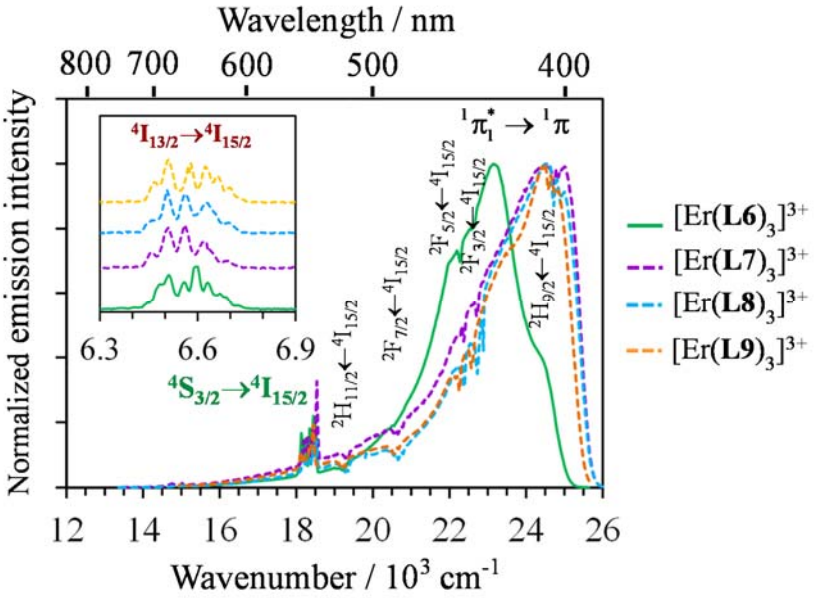

Figure S45 Dual visible (main plot) and near-infrared (inset) emission spectra recorded for the complexes **4** (λ_{exc} = 370 nm) and **5-7** (λ_{exc} = 340 nm) in the solid-state at 77K. The dual emission is assigned using color fonts, while the dips (assigned using black fonts) correspond to Er-centered re-absorption of the residual ligand-centered $^1\pi^*\rightarrow\pi$ emission.

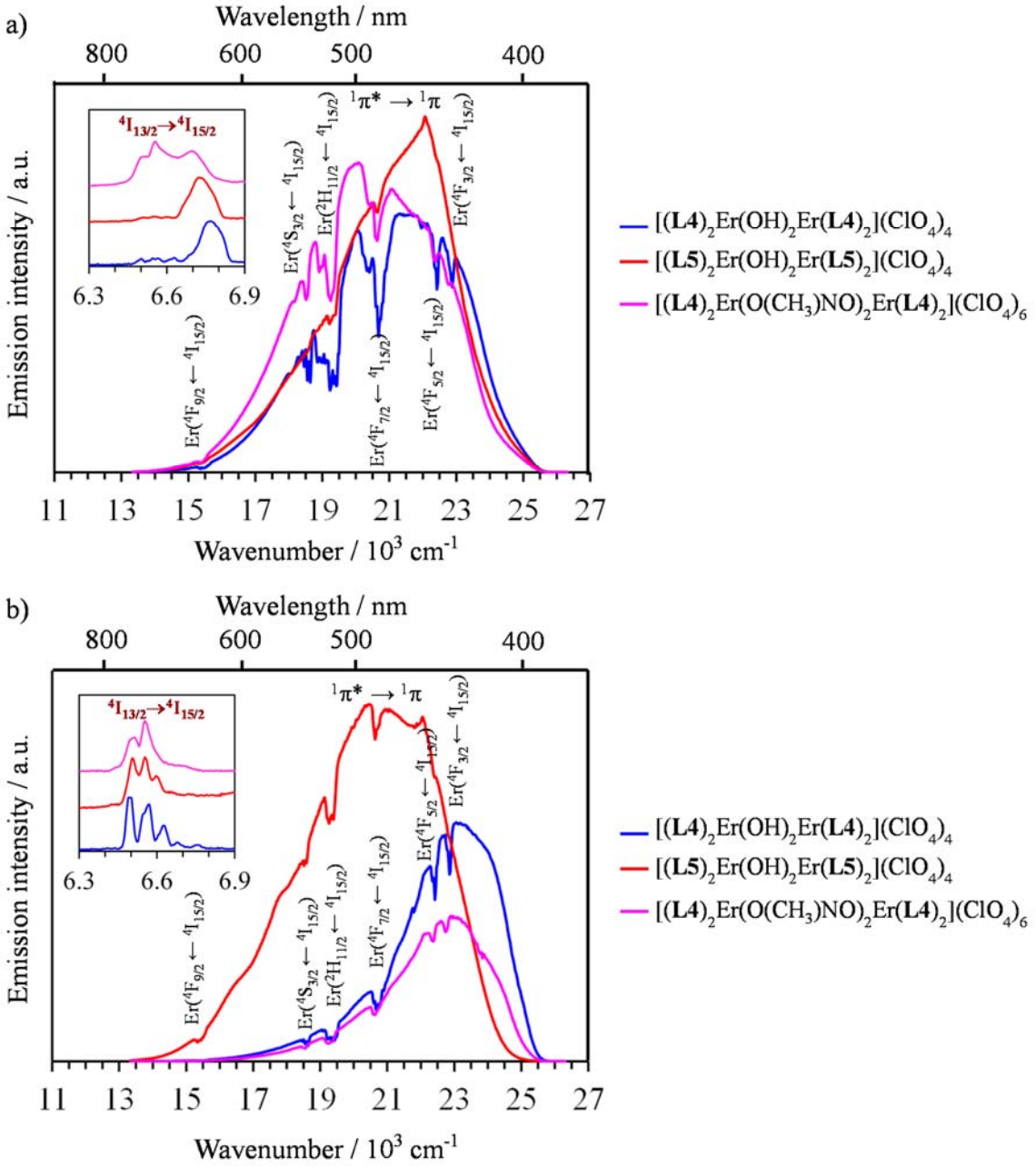

Figure S46 Emission spectra recorded for the dimeric complexes $[(\mathbf{L4})_2Er(OH)_2Er(\mathbf{L4})_2](ClO_4)_4$ (**8**), $[(\mathbf{L5})_2Er(OH)_2Er(\mathbf{L5})_2](ClO_4)_4$ (**9**) and $[(\mathbf{L4})_2Er(CH_3NO_2)_2Er(\mathbf{L4})_2](ClO_4)_6$ (**10**) (λ_{exc} = 370 nm) in the solid-state at a) 298 K and b) 77K. The dips (assigned using black fonts) correspond to Er-centered re-absorption of the residual ligand-centered $^1\pi^* \rightarrow \pi$ emission.